

DOTTORATO DI RICERCA IN
CHIMICA
Ciclo XXXII

Settore Concorsuale 03/B1
Settore scientifico disciplinare CHIM/03

Photoactive tools
for biomedical applications.
From supramolecules to micro-objects.

Presentata da: Benedetta Del Secco

Coordinatore Dottorato
Prof.ssa Domenica Tonelli

Supervisore
Prof.ssa Nelsi Zaccheroni

Co-supervisore
Dr. Enrico Rampazzo

A me stessa

Ad Antonio e Maria

A chi se ne va, ma non lascia.

A chi se lo "meriterebbe"

*A chi fallisce, riprova
e fallisce meglio.*

*A chi, invece di puntare in alto,
sceglie di puntare oltre*

“At the biggest crossroads of life, there is no signage,,

H.E

INDEX

ABSTRACT	1
CAP. 1	1
INTRODUCTION	1
1.1 Nanotechnologies for Theranostic applications	1
1.1.1 Sensing	4
1.1.2 Imaging	5
1.1.3 Delivery	6
1.2 Light trough the biological tissue	10
1.3 NPs and colloids	13
1.3.1 Colloidal stability	14
1.4 Aim of the thesis	17
CAP. 2	22
MOLECULAR CHEMOSENSOR FOR Mg^{2+} DETECTION	22
2.0 Cationic sensing	22
2.1 State of the art	24
2.2 Aim of the work	27
2.3 Synthesis and photophysical characterization	28
2.3 Preliminary tests <i>in vitro</i> .	33
2.4 Conclusion and future steps	37
CAP. 3	40
NANOSTRUCTURED CHEMOSENSORS FOR O_2 DETECTION IN BIOMEDICAL APPLICATIONS	40
3.0 State of the art	41
3.1 Molecular Oxygen: a tool for diagnosis and therapy	42
3.2 Luminescent silica nanoparticles as chemosensors	44
3.2.1 Stöber method	49
3.2.2 Reverse microemulsion method	51
3.2.3 Direct micelle assisted methods	52
3.4 Oxygen chemosensors based on silica nanoparticles	54
3.4.1 Porphyrins and organic phosphorescent molecules	55
3.5 Aim of the work	57
3.6 Results and discussion	58
3.6.1 Optimization of <i>PluS</i> NPs synthesis	58
3.6.2 AIP induced by NPs: Asterisk@NPs	63

3.6.2.1 AIP process	63
3.6.3 Asterisk@NPs: Synthesis and photophysical characterization	64
3.6.3 Oxygen chemosensors: Phorphyrins@NPs	69
3.6 Biological assays@Zurich University	81
3.7 Conclusions and future steps	84
CAP. 4	89
ACTIVE MORPHOLOGICAL COLLOIDS FOR PROBING AND TAILORING INTRACELLULAR ANTIGEN PROCESSING	89
4.0 State of the art	92
4.1 Aim of the work	95
4.2 Synthesis optimization and characterization	95
4.2.1 Hematite cubes	96
4.2.2 Silica Hexapods	99
4.2.3 Swimmers based on TPM spheres and Hematite cubes	108
4.3 Conclusions and future steps	111
CAP. 5	115
BIORESORBABLE ELECTROSPUN NANOFIBER MAT RELEASING DIAGNOSTIC NANOTOOLS, FOR POST-SURGICAL IMPLANTATION	115
5.0 State of the art	115
5.1 Electrospinning	118
5.1.1 PLGA	119
5.1.2 Mechanism of PLGA degradation in DDS	120
5.2 Aim of the work	122
5.3 Results and discussion	123
5.4 Conclusions and future steps	133
CAP. 6	137
LUMINESCENT METALS COMPLEXES AND GOLD NPS AS POTENTIAL BUILDING BLOCKS IN NANOMEDICINE	137
6.1 Rhenium(I) complexes.	138
Effects of the substituents on the terpyridine k ³ N rhenium(I) dicarbonyl complexes in NIR emission	138
6.1.1. Aim of the work	141
6.1.2 Result and discussion	142
6.1.3 Conclusions	145
6.2 Lanthanide (Ln) complexes.	146
Studies of Ln-Ag bimetallic coordination framework.	146
6.2.1 Aim of the work	147
6.2.2 Results and discussion	147
6.3 Gold Nanoparticles.	154

<i>The Role of Onium Salts in the Pro-Oxidant Effect of Gold Nanoparticles in Lipophilic Environments.</i>	154
6.3.1 <i>Aim of the work</i>	155
6.3.2 <i>Results and discussion</i>	156
6.3.3 <i>Conclusions</i>	163
EXPERIMENTAL SECTION	167
APPENDIX	189
LIST OF SYMBOLS & ABBREVIATION	196
LIST OF SCIENTIFIC CONTRIBUTIONS	198
ACKNOWLEDGMENTS	202

ABSTRACT

The research work within the wide field of nanomedicine that is presented in this thesis is centred on the development of new nanostructured multifunctional materials for future theranostic applications. The rationale that it has been followed is inspired to a supramolecular approach, therefore, we have been starting with the study of various components able to play different functions that could be then implemented in more complex multifunctional platform.

I describe the design, preparation and characterization of very different supramolecular, nanostructured and microstructured species suitable to be implemented, in a future, in theranostic agents, but already able to perform useful functions for bio-medical applications (imaging, sensing and drug delivery).

The results will be presented following a sort of 'increasing in dimension' logic, in fact, in the first chapter will deal with luminescent molecular components for sensing, that will be followed by the description of phosphorescent nanostructures and then microstructures, to continue with electrospun composite materials for the delivery in time of active nanoagents. The very last chapter, instead, gathers some interesting results obtained developing basic research on luminescent metal complexes and gold nanoparticles.

In **Chapter 2**, is presented a new luminescent chemosensor for Mg^{2+} detection in mitochondria based on a diaza-18-crown-6 appended with two 8-hydroxyquinoline(8-HQ) derivative. Starting from the knowhow of the group I have worked with it has been synthesized a new species, precisely designed to detect and quantify Mg ions selectively inside mitochondria, thanks to the insertion of two phosphonium moieties on the periphery of the chemosensor. The photophysical characterization will be presented, as well as the results on the efficiency and sensitivity of the new species. The preliminary *in vitro* test (on a human leukemia (HL60) and osteosarcoma tumor (U2Os) cell lines) have allowed to

evaluate the suitable non-toxic concentration to be used for further investigation on the mitochondria target ability of the chemosensor.

In **Chapter 3** is reported a new synthetic strategy based on the micellar assisted method, to prepare silica core/PEG shell nanoparticles doped with phosphorescent emitters such as organic molecules called "asterisks" and metal-porphyrins. It has been obtained very promising nanostructured phosphorescent chemosensors for molecular oxygen, suitable also for two-photon excitation. They present appropriate features for oxygen sensing in the physiological pO_2 range, they are water soluble, stable and biocompatible. The final ambitious step was to optimize the most promising structures for *in vivo* applications. In a pilot test, in collaboration with Professor B. Weber from the University of Zurich, the injection into the tail vein of a sample of metallo-porphyrin doped NPs allowed the phosphorescence intensity decays measurement in mouse brain at increasing depths and the signal was detectable up to 400 μm below the tissue surface.

In **Chapter 4** will be shown the study carried out at the New York University, centred on the synthesis of microstructures suitable to mimic invading microbial pathogens. Their study can allow a full physical-mechanical understanding of how particle morphologies and motilities affect phagosomal antigen degradation. Based on previous achievements, a novel and reproducible method to obtain irregularly-shaped colloids is described, that allows to obtain colloids with dimensions in the range of 10-12 μm . The efficient biotinylation method that it has been also optimized results in synthetic-mimetic materials that are better recognized by primary dendritic cells as shown by a preliminary *in vitro* test. In parallel, there were also prepared other active colloids able to be propelled by the oxygen bubbles formed by a chemical reaction that is UV-light activated in the presence of hydrogen peroxide. These species called 'swimmers' aim to be of help in the elucidation of how particle motilities affect phagosomal antigen degradation by dendritic cells.

Chapter 5 will deal with bioresorbable electrospun nanofiber mat that, if doped with theranostic agents can be used to release the active

species, during their degradation after post-surgical implantation. The fine tuning of the electrospinning parameters was pivotal in order to prepare fibers doped with luminescent targeted nanoparticles that present uniform dimensions and dispersion of the included agents. Photophysical characterization is reported together with a study of the PLGA fibers degradation that proves that the nanoparticle release correlates very well with the degradation profile in physiological conditions. This can allow to tune the release over time simply modulating the polymer composition.

Chapter 6 merged some research works that have been developed on different species that could have, or could take to, interesting properties to be exploited in building block moieties for the design of multifunctional platforms. In particular, the attention has been focused on NIR emitters that are luminescent component of election for medical application *in vivo* due to the maximum depth of penetration in tissues of light falling in the range 650-1350 nm. It has been discussed the results obtained with rhenium(I) and lanthanide metal complex from a photophysical point of view both in solution and in the solid state. Moreover, in this section is also presented a basic study that aims to assess the possible pro-oxidant or antioxidant effects induced by gold nanoparticles, key features determining their safety and suitability for specific applications

CAP. 1

INTRODUCTION

1.1 Nanotechnologies for Theranostic applications

The term “theranostics” was coined to define ongoing efforts in clinics to develop more specific, individualized therapies for various diseases, and to combine diagnostic and therapeutic capabilities into a single agent. The rationale arose from the fact that diseases, such as cancers, are immensely heterogeneous, and all existing treatments are effective for only limited patient subpopulations and at selective stages of disease development. The hope was that a close marriage of diagnosis and therapeutics could provide therapeutic protocols that are more specific to individuals and, therefore, more likely to offer improved prognoses. For this reason, theranostics is also a highly inter-disciplinary field. In fact, with its combining action of diagnosis and therapy, Theranostics works at the intersection of several different scientific fields (Fig.1.0).

The emergence of nanotechnology has offered an elegant pathway to prepare new and effective materials able to merge diagnosis and

therapy. Nanoparticle (NP)-based imaging and therapy have been investigated separately and their single understanding has now evolved to a point enabling the birth of NP-based theranostics. These materials can be seen as nanoplatforms that can co-deliver therapeutic and imaging functions. It adds to the previous paradigm the possibility for imaging to be performed not only before or after, but also during a treatment regimen. Interestingly, that many nanostructured imaging agents could be readily “upgraded” to theranostic ones by integrating therapeutic functions on them. One underlying driving force of such a combination is that imaging and therapy both require enough accumulation of agents in diseased areas. This common targeting requirement brings the two research domains closer and, ultimately, will blur the boundary between them, since many techniques to enhance imaging can, at least in theory, be readily transferred to the therapeutic domain, and vice versa.

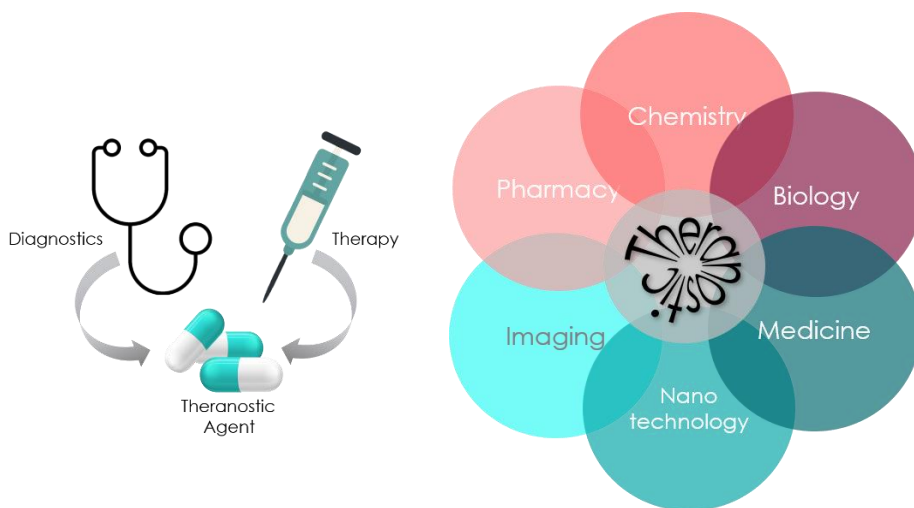


Figure 1.0 Left: cartoon of union between therapy and diagnostic to create a theranostic agent. Right: combination of the multiple field covered by theranostic application

Moreover, nanostructured materials are generally very versatile and allow the application of different targeting strategies to address the desired application. Above all, the NPs systems with multimodal capabilities, in the specific a theranostic agent (Fig 1.0B), offer the opportunity to develop novel strategies for the effective treatment of human diseases that may result in paired or alternative therapeutic options. In recent years, a variety of biomaterial-based multifunctional

nanoparticles have been evaluated for targeted cancer therapeutics and biomedical imaging. The principal characteristics which could occur to the functionalized agent after its modifications are the specific targetability, minimizing toxicity and expanding therapeutic efficiency, the promotion of the intracellular internalization, due to the modification in the pharmacokinetic profile; the functionalization could also bring to the possibility to pursue bioimaging allowing real-time monitoring of the progress of the biological actions and nanoparticle distribution in vivo and, furthermore, work on the biocompatibility and stability of the entire systems, extending residence time in systemic circulation and maintaining therapeutic level of bioactive(s) in the blood.

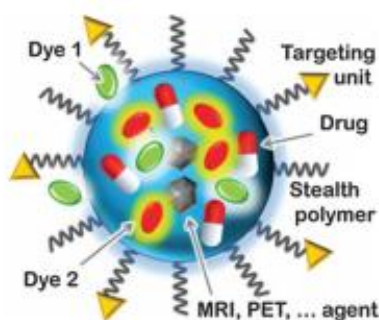


Fig. 1.0B Schematic representation of a multifunctional system for nanomedicine

Imaging nanoparticles and, parallel, nanomaterials for therapeutic application have been deeply investigated in the last years, and the know-how in the field is now exploited in many laboratories worldwide to design theranostic nanoparticles, that is to say nanoplatforms which can allow a close monitoring of the region of interest not only before or after, but also during treatment³⁴.

Liposomes, gold, silver, iron (magnetic) and silica nanoparticles are only few examples of the many substrates investigated nowadays for theranostic purposes. Nanomaterials as diagnostic tools are already in clinical trials in many modern imaging techniques such as: magnetic resonance imaging (MRI), computed X-ray tomography (CT), positron emission tomography (PET), single-photon emission computed tomography (SPECT), ultrasound imaging (US) and optical imaging (OI)³⁵⁻³⁷.

In the case of cancer, it is a common approach to identify a biomarker that is aberrantly expressed on the surface of cancer cells, and then to load its congenial binding vector onto probes/carriers to achieve recognition and tumor homing. To this goal, however, size is a stringent issue since an efficient tumor targeting also depends upon the carrier

1

capability to reach all the areas in the human body, that is to say to cross different tissues and membranes and to present a sufficient persistence to be traced and active. Nanoplateforms, due to their size scale, already present an enhanced-permeability-and-retention (EPR)^{1,2} effect in tumor targeting even if, care must be taken with the particles' surfaces to avoid innate immune system recognition and to secure sufficiently long circulation half-lives for the agents to reach their targets (see sec. 1.1.3 for the details).

At the basis of the development of efficient theranostic agents, there is a deep understanding of three different actions to be merged in one single object: sensing, imaging and delivery.

1.1.1 Sensing

A sensor is a device that detects and responds to some type of input from the physical environment transducing it in a detectable and quantitative way. The specific input could be light, heat, motion, moisture, pressure, or any one of a great number of other environmental phenomena. The output is generally a signal that is converted to human-readable display at the sensor location or transmitted electronically over a network for reading or further processing. I list hereafter some very well-known examples of different sensor devices. a) In a mercury-based glass thermometer, the input is temperature. The liquid contained expands and contracts in response, causing the level to be higher or lower on the marked gauge, which is human-readable. b) An oxygen sensor in a car's emission control system detects the gasoline/oxygen ratio, usually through a chemical reaction that generates a voltage. A computer in the engine reads the voltage and, if the mixture is not optimal, readjusts the balance. c) Motion sensors in various systems including home security lights, automatic doors and bathroom fixtures typically send out some type of energy, such as microwaves, ultrasonic waves or light beams and detect when the flow of energy is interrupted by something entering its path. The active chemical sensing species in a macroscopic device or the sensing molecular species that can be used as such and not integrated in a device are called chemosensors. The action of a

chemosensor, relies on an interaction occurring at the molecular level among the analyte of interest and the receptor that is connected with the signalling moiety, able to generate a detectable variation. Usually they are used for monitoring the activity of a chemical species in a given matrix such as solution, air, blood, tissue, waste effluents, drinking water, etc. The signalling moiety and the recognition one are connected either directly to each other or through a some kind of connector or a spacer⁷⁻⁹ and when the signalling is based on the variation of either the absorption or the emission of light it is generally referred as an optical chemosensor.

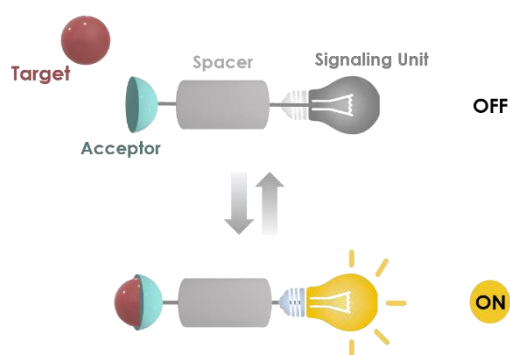


Figure 1.2 schematization of an OFF-ON luminescent chemosensor

Among them, Luminescent ones present many advantages; luminescence is a very sensitive, low cost and rapid technique that is suitable for a wide range of clinical, biological and environmental applications offering a submicrometer spatial and submillisecond temporal resolution. The most

common ones are based on an induced fluorescent intensity variation by the recognition event, but there are other possibilities such as emission wavelength or lifetime changes. In chapter 2 is reported the work on chemosensors able to detect magnesium cations, involved in most important cellular processes and consequently diseases¹⁰, via chelation enhanced fluorescence effect (CHEF effect).

1.1.2 Imaging

In general, imaging is the process of producing an exact picture of the visualized area by scanning it with a detector and, therefore, medical imaging creates visual representations of the body, organs, tissues and of their functions for clinical analysis and intervention. Among all the possible techniques, fluorescent imaging is very convenient being

non-invasive, very sensitive, requiring relatively cheap instrumentation compared to MRI or PET whose handling requires moderate levels of training and protection. Other advantages involve the imaging agents required that present low hazard, low costs and stability (fluorescently molecules can be stored for months differently from radiolabels that decay over a few days¹¹). However, some disadvantages of luminescent imaging agents have to be taken into consideration such as photobleaching, limiting resolving power, parasite quenching effects, and environmental susceptibility and autofluorescence. For these reasons a lot of researcher work is now ongoing worldwide to find solutions taking advantage of all the most recent achievement in the fields of organic synthesis and material science. The goal is also more ambitious since it also involves the possibility to include imaging agents in a more complex platform able to act as a theranostic material and also my research work can be included in this framework.

1.1.3 Delivery

In order to obtain a theragnostic agent, imaging has to be paired by therapy and the most straightforward way is drug delivery. Drug delivery involves a carrier that contains a drug and its administration via implant, injection or ingestion allows for a controlled and localized release. This can take to great advantages with respect to traditional administration of a drug, for example the entire dose for the therapy can be given in only one administration and then gradually released in a controlled way. On the other side the possibility of driving the carrier in a precise site avoids the potential harmful contact of the drug with other tissues and permits to use much reduced drug amounts. Many different ways can be exploited for drug release such as diffusion, degradation, swelling, and affinity-based mechanisms^{12 13}.

Drug delivery technologies can therefore modify drug release profiles, absorption, distribution and elimination with the advantage of increasing the therapy efficacy and safety, together with a patient convenience in terms of time and reduction of the possibility of human mistake in administration. Moreover there are some medications such as peptide and protein, antibody, vaccine and gene based drugs that, in general, may not be delivered using the common routes of

administration that include the enteral (gastrointestinal tract), parenteral (via injections), inhalation, transdermal, topical and oral ones^{14 15}. In fact, they might be susceptible to enzymatic degradation or they cannot be absorbed into the systemic circulation efficiently due to their molecular size and/or charge. For this reason, many protein- and peptide-based drugs have to be delivered by injection or with a nanoneedle array and specific carriers, in these cases, could dramatically improve their therapeutic effectiveness.

Current research efforts in the area of drug delivery include the development of targeted delivery in which the carrier is able to specifically and efficiently recognize a targeted species and it will stop and accumulate only in its presence (for example tumour markers in cancerous tissues), sustained release formulations in which the drug is released over a period of time in a controlled manner, and methods to increase survival of peroral agents which must pass through the stomach's acidic environment. In order to achieve efficient targeted delivery, the designed system must avoid the host's defence mechanisms and circulate for a sufficient time to reach its intended site of action and this is not trivial since it has to be mediated with clearance issues to avoid toxicity.¹⁶ In the case sustained release formulations are required, different species have been tested including liposomes¹⁷, drug loaded biodegradable microspheres¹⁸, drug polymer conjugates¹⁹ and also nanoparticles²⁰. As mentioned before, an important role in the delivery process is played by the EPR effect, which permits the accumulation of macromolecules, and in general of nano scaled objects, in the interstitial of tumor tissues with concentration higher than the blood plasma. In the field of cancer treatment, the EPR effect (Fig. 1.1), studied and proposed by Maeda¹ as an efficient way to hit solid angiogenic tissues (that is to say not only tumors but also inflammatory tissues³) is principally associated with fenestrations formed by the endothelial cells in vasculature. This effect offers one of the most attractive way to gain a selective accumulation of a nanostructure in a tumor tissue. This is an intrinsic property and it is made possible by the abnormal vasculature of the angiogenic tissues together with the longer circulation time of nanoparticles in comparison with single molecules.

1

The selective accumulation of nanostructures is usually localized in the interstitial space⁴.

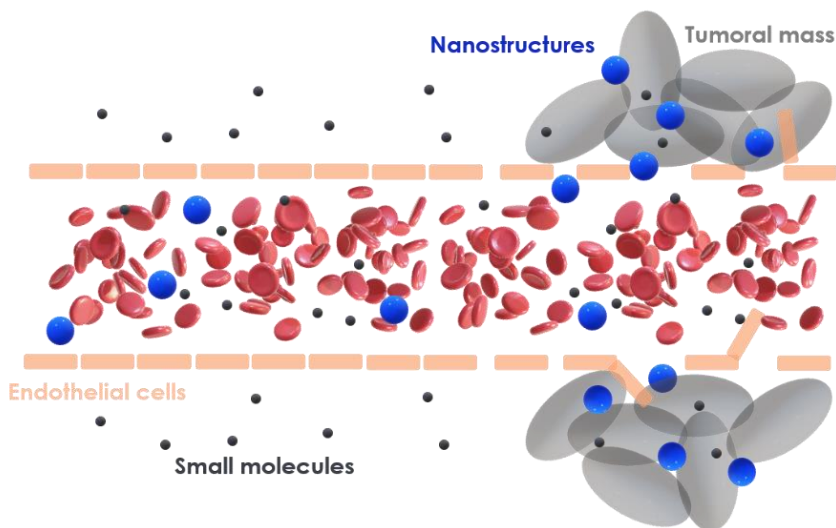


Figure 1.1 Schematic representation of the entrapment of NPs inside a tumor tissue by EPR effect

A key factor for the efficient entrapment in tumoral tissue by EPR effect is the size of the nanostructure. Objects of different sizes present very different circulating times, and this means that with a proper design of the size and shape of the nanoobject it is possible to tune the amount of entrapped material. Objects smaller than 6 nm are excreted too rapidly via urine to accumulate in tumor tissues since they can pass the nephron membranes in the kidneys (this excretion pathway is the best one for optimum body clearance but too fast for an efficient delivery).

Objects bigger than 100-150 nm circulate for a much longer time inside the body, this is helpful for tissue accumulation, but it can result in undesired high toxicity by bioaccumulation. Therefore, the nanostructure size is a very important parameter in the design of targeting materials, but it is not the only one since the nanostructure toxicity depends widely upon the composition, functionalization and properties of its surface. In the framework of medicine, nanomaterials are extensively studied for cancer treatment applications thanks to the possibility given by EPR of their spontaneous accumulation in damaged tissues. Indeed, different therapies are currently in study such as photodynamic and photothermal therapies or local chemotherapy by

drug delivery^{5,6}. Photodynamic and photothermal therapies exploit the nanomaterials to convert, respectively, the light stimuli into the production of reactive species (singlet oxygen, nitrogen oxide...) or into an increase of local temperature, both able to kill the surrounding cells. Nanoparticle-based imaging and therapy are therefore a very promising area and even more nanoparticle-based theranostic agents despite still in their early stages of development. However, the advances in nanotechnology and the need for personalized medicine have already made nanoparticle-based theranostics a research hotspot.

1.2 Light through the biological tissue

It is clear the fact that there is a necessary need of improvements in the detection and, moreover, in the cure of malignant human diseases. It is necessary the development of something non-invasive and specific to understand and directly works on the zone which need to be cured or investigate. Photochemistry should be the perfect solution, both separately with detection using fluorescence or phosphorescent phenomena, and together, using something able to detect and cure in the same time, or, using different ways like delivery systems mentioned before.

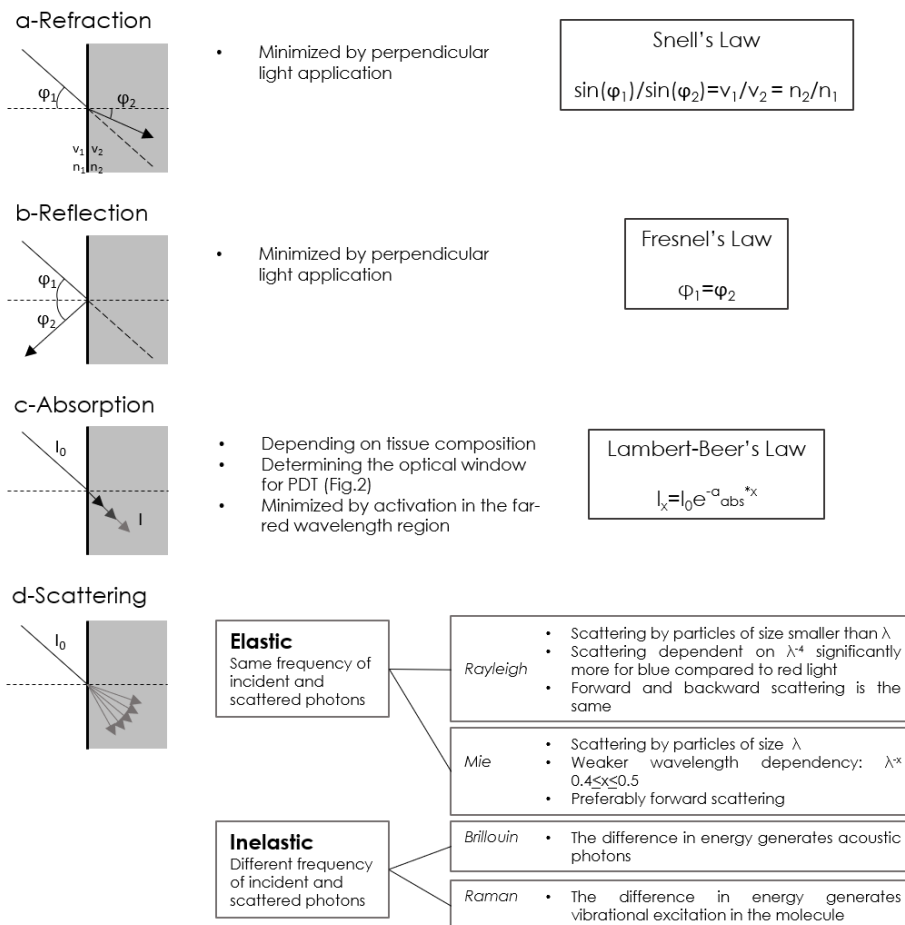


Figure 1.3 Interaction between light and tissue I

When the attention regarding photochemistry want to be moved in biology applications, especially in the interaction between light and human body, some details must be discussed. When the light is propagated through such a medium, are implicated many processes of refraction, reflection, absorption and scattering (Fig. 1.3). Fresnel's law and Snell's law govern reflection from the interface between two media and refraction, respectively, and their impact on the loss of intensity are determined by the relative values of their refractive indices²¹.

When a light beam is applied perpendicular to the interface between the two media it is possible minimize both processes since their proportionality to the angle of incidence. Scattering of light in tissue has the most marked effect on light intensity and directionality.

Scattering causes, together with refraction, a widening of the light beam, resulting in a loss of fluence rate (given as power per unit area of light in $[Wm^{-2}]$) and a change in the directionality of the light beam. Scattering in tissue is quite complex (Fig. 1.3). Inelastic scattering (Brillouin scattering and Raman scattering) does not seem to play an important role in this case. For elastic scattering, neither Rayleigh scattering nor Mie scattering completely describes the effects observed in tissue; here, photons are mainly scattered in the forward direction. The experimentally observed scattering shows weaker wavelength dependence than that predicted by Rayleigh's theory, but the effect is stronger than that given by Mie scattering²². Besides scattering, absorption of light quanta is most relevant for the loss of light intensity with the penetration depth. It is possible mathematically describe the reduction in intensity caused by both processes using an exponential function similar to Lambert–Beer's law. The intensity at a given depth x can be calculated by equation (1), with I_x being the intensity at depth x and I_0 the intensity at the media interface. The parameters a_{abs} and a_{sca} represent the absorption and scattering coefficients, respectively.

$$I_x = I_0 e^{-(a_{abs} + a_{sca})x} \quad 1$$

The most important chromophores in tissue are water, oxyhemoglobin (HbO₂) and deoxyhemoglobin, melanin and cytochromes. The absorption spectra of these molecules define the optical window for use

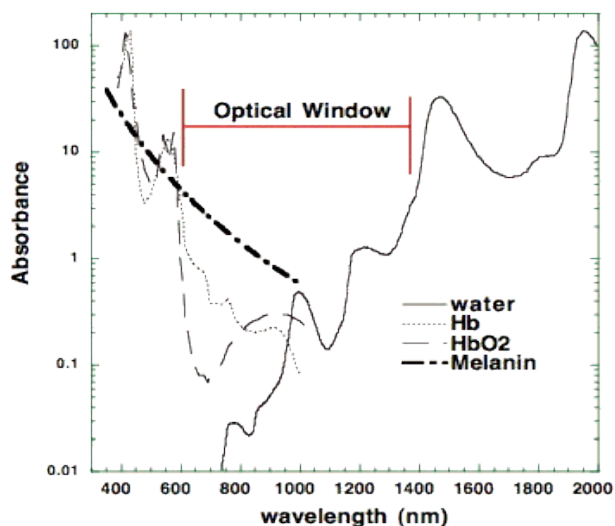


Figure 1.4 The optical window for PDT. Absorption of light by tissue chromophores limits the wavelength range suitable for PDT to about 650-1200 nm

for example of techniques like PDT (explained better in cap 3) in tissue (Fig. 1.4, ^{22,23}).

One should keep in mind that hemoglobin (Hb) and HbO₂ show different absorption in the range of 600– 800 nm, which is commonly used for PDT. In vivo, there might be a significant difference in the amounts of HbO₂ and Hb between non-tumor and tumor tissue

due to a possible lower oxygenation and pH of the latter²⁴. For PDT on solid tumors, the effective penetration depth is of great relevance. It is defined by the depth x , where $I(x)$ decreases to 37% of I_0 ²¹. For clinical treatment with Photofrin, a hematoporphyrin derivative for excitation at 630 nm, the light penetration depth is approximately 3– 5 mm, depending on the tissue²⁵. The use of PSs with absorption peaks at wavelengths >700 nm (or even higher) should, at least, double the penetration depth and thus enable treatment of thicker tumors²⁶. However, the upper limit for the excitation wavelength is given for the minimal energy required for singlet oxygen production. Properly for these reasons, the use of Oxygen as tool for diagnostic and/or therapy should be the principal techniques to investigate for the development of new theranostic agents.

1.3 NPs and colloids

A Nanoparticle (NP) is defined by ISO Technical Specification 80004 as a nano object, with all three external dimensions in the nanoscale, whose longest and shortest axes do not differ significantly, with a significant difference typically being a factor of at least 3. Nanoparticles can exhibit size-related properties significantly different from those of either fine particles or bulk materials²⁷⁻²⁹.

Nanoparticles with a range between 1 and 100 nm in size are synonymous with "ultrafine particles" opposite to "fine particles" sized between 100 and 2,500 nm and "coarse particles" ranging from 2.5 to 10 μm . For the period of the 1970s and 80s, during the first thorough fundamental studies with nanoparticles in the United States by Granqvist and Buhrman³⁰, and in Japan within an ERATO Project³¹, the term utilized was ultrafine particles. In the 90s, the term nanoparticle had become more common, before the National Nanotechnology Initiative was launched in the United States. Sometimes the words nanoparticles and colloids are used with the same meaning but, the terms colloid and nanoparticle are not interchangeable. A colloid is one of the three primary types of mixtures, with the other two being a solution and suspension. A colloid is a solution that has particles ranging between 1 and 1000 nanometers in diameter yet are still able to remain evenly distributed throughout the solution. These are also known as colloidal dispersions because the substances remain dispersed and do not settle to the bottom of the container. In colloids, one substance is evenly dispersed in another. The substance being dispersed is referred to as being in the dispersed phase, while the substance in which it is dispersed is in the continuous phase.

In 1905 Albert Einstein created the mathematic model which describes the phenomenon of the irregular zig-zag motion of the small particles in a solution discovered by Robert Brown in 1827. These erratic particles behavior can be attributed to the collective bombardment of a myriad of thermally agitated molecules in the liquid suspending medium bringing to the impacts between the particles not equal in every direction. As a result, the sol particles show a random trajectory creating the such called Brownian motion or Brownian movement. The Brownian

motion becomes progressively less prominent, as the particles grow in size or the viscosity of the medium increases, indeed, If the particles are larger, their dynamic behavior within the suspension is governed by forces of gravity and sedimentation. Such random motion is visible under ultramicroscopes and for bigger particles even under ordinary microscopes.

A common method of classifying colloids is based on the phase of the dispersed substance and what phase it is dispersed in. The types of colloids include sol, emulsion, foam, and aerosol.

- Sol is a colloidal suspension with solid particles in a liquid.
- Emulsion is between two liquids.
- Foam is formed when many gas particles are trapped in a liquid or solid.
- Aerosol contains small particles of liquid or solid dispersed in a gas.

1.3.1 Colloidal stability

Colloidal dispersions are subject to several kinds of instability. This is due to the attraction and repulsive forces such as Van der Waals forces, electrostatic forces, steric and solvation forces too. All these forces involving in aggregation, coagulation, flocculation or they can stick to surrounding surfaces by deposition and they can separate under gravity bringing to sedimentation or creaming. These mechanisms all can be counteracted by strong electrostatic repulsion, and the strength of that repulsion can be parameterized by the zeta potential (see experimental section for the explanation). In some cases, however, electrostatic interactions can destabilize the dispersion.

In general every particle follow the Lennard-Jones theory³². In particular, for colloidal solutions it has been formulated an extension of LJ theory, the DLVO model (Fig 1.5). This theory is named after Derjaguin, Landau, Verwey, and Overbeek and is the explanation of the stability of colloidal suspension. The theory assumes that the electrostatic double layer forces and the van der Waals forces are independent and therefore can be superimposed or added at each interacting distance for two particles.

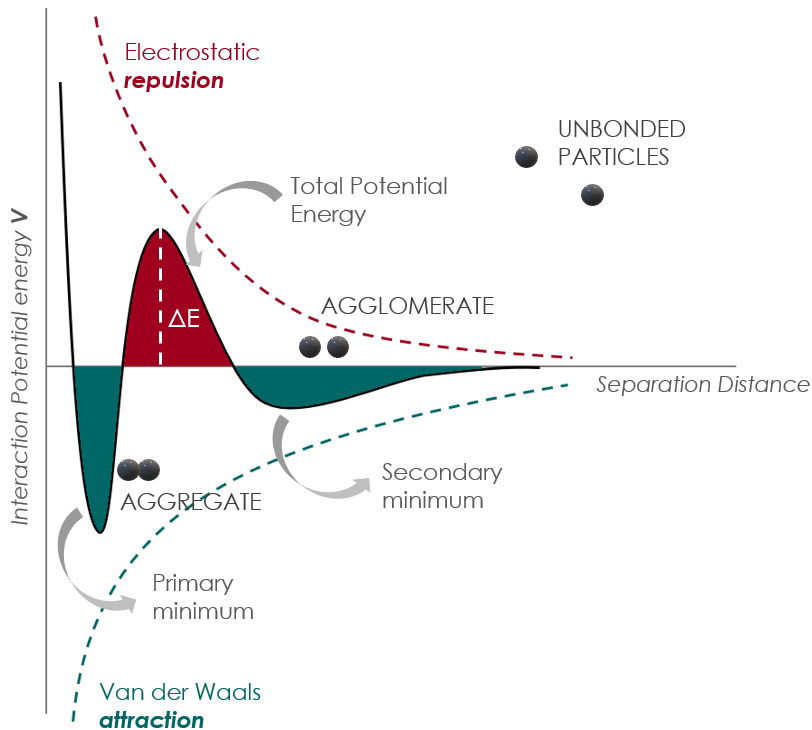


Figure 1.5 Schematization of potential energy graph in DLVO theory

The DLVO theory³³ explains the tendency of colloids to agglomerate or separate by combining two forces described by two curves: electrostatic repulsion due to the so called double layer of counterions, and van der Waals attraction. The total potential energy is described as the sum of the attraction potential and the repulsion potential. When two particles approach each other, electrostatic repulsion increases and the interference between their electrical double layers increases. Meanwhile, the van der Waals attraction increases as they get closer. At each distance, the net potential energy of the smaller value is subtracted from the larger value. The combination of these forces results in a deep attractive shaft, which is referred to as the primary minimum. At maximum energy barrier, repulsion is greater than attraction. Particles rebound after interparticle contact and remain dispersed throughout the medium. The maximum energy needs to be greater than the thermal energy, otherwise, particles will aggregate due to the attraction potential. The height of the barrier indicates how stable the system is. Since particles have to overcome this barrier in order to aggregate, two

1

particles on a collision course must have sufficient kinetic energy due to their velocity and mass. If the barrier is cleared, then the net interaction is all attractive, and as a result the particles aggregate. This inner region is often referred to as an energy trap since the colloids can be considered to be trapped together by Van der Waals forces. For a colloidal system, the thermodynamic equilibrium state may be reached when the particles are in deep primary minimum. At primary minimum, attractive forces overpower the repulsive forces at low molecular distances. Particles coagulate and this process is not reversible. However, when the maximum energy barrier is too high to overcome, the colloid particles may stay in the secondary minimum, where particles are held together weaker than the primary minimum. Particles form weak attractions but are easily re-dispersed. Thus, the adhesion at secondary minimum can be reversible. At larger distances, the energy profile goes through a maximum energy barrier, and subsequently passes through a shallow minimum, which is referred to as the secondary minimum. At each distance, the smaller value is subtracted from the larger value to obtain the net energy. In the regime where there is repulsion, energy can be thought to be an energy barrier.

It is possible work on the surface of the particles modifying the particles double layer, then their stability. The criteria of stability in which is possible to work to obtain a stable system are:

- Salt concentration
- Counter-ion valency
- Z-potential
- Particle size
- Polymeric stabilization

It is possible increase or decrease the energy barrier working on the abovementioned parameters, by changing the ionic or pH environment or adding surfactants to affect the surface charge of the colloid. In this case, zeta potential can be measured to know the stability of dispersion. There are many other effects which are to be considered for sure, but steric stabilization is the most important thing. Adsorbed layer on each particle prevents the particles from coming close enough for van der Waals attraction to cause flocculation. There are no long-range

repulsive forces unlike electrostatic stabilization and the particles are subject to attractive forces until the outer regions of the molecules.

1.4 Aim of the thesis

The research work presented in this thesis can be inserted within the wide field of nanomedicine and it is centred on the development of new nanostructured multifunctional materials for future theranostic applications. The rationale that has been followed in these years has been inspired to a supramolecular approach, therefore, the research started with the study of various components able to play different functions that could be then implemented in more complex multifunctional platforms. Have been designed, prepared and characterized some very different supramolecular, nanostructured and microstructured species suitable to be implemented, in a future, in theranostic agents, but already able to perform useful functions for bio-medical applications (imaging, sensing and drug delivery).

I list hereafter the specific goal pursued in each chapter that describes a different component/material.

Chapter 2: the preparation of a new luminescent chemosensor for Mg^{2+} quantitative detection selectively in mitochondria is the goal of this part of the work. We will realize it functionalizing with two phosphonium moieties the periphery of the chemosensor based on a diaza-18-crown-6 appended with two 8-hydroxyquinoline(8-HQ) derivatives.

Chapter 3 aims to prepare and optimize nanostructured phosphorescent chemosensors for molecular oxygen, presenting the appropriate features for oxygen sensing in the physiological pO_2 range, water solubility, stability and biocompatibility. A new synthetic strategy will be specifically conceived to prepare silica core/PEG shell nanoparticles highly doped with water insoluble phosphorescent emitters such as organic molecules called asterisks and metal-porphyrins. The final ambitious step will be to optimize the most promising structures for *in vivo* applications.

In **chapter 4** will be shown the study carried out at the New York University that aims to allow a full physico-mechanical understanding of how particle morphologies and motilities can affect phagosomal antigen degradation and presentation. To study the influence of morphology the first step is the preparation of irregularly-shaped microstructures suitable to mimic invading microbial pathogens of cells. In parallel, to evaluate the motility impact on phagosomal antigen degradation by dendritic cells I also prepared other active colloids called 'swimmers. Under UV-light activation they are propelled by the oxygen bubbles formed by a chemical reaction that takes place in the presence of hydrogen peroxide.

Chapter 5 Aim of this part of my research is to prepare luminescent nanoparticles bearing a targeting agent for tumor tissues and to explore the possibility to release them from a carrier in a controlled way in view of medical applications. In particular, we want to evaluate if, using the electrospinning method, it is possible to create a bioresorbable mat, containing targeted dye doped PLuS NPs, able to release them in a degradation dependent regime. The goal is to implant the scaffold in a patient after a tumour resect operation to release the theranostic nanoparticles in time during the reabsorption of the fibers, allowing to monitor, and in case to cure, the neighboring tissues.

Chapter 6 merges some research work that on different species that could have, or could take to, interesting properties to be exploited in building block moieties for the design of multifunctional platforms. In particular, we aim to study new NIR emitters based on rhenium(I) and lanthanide metal complexes both in solution and in the solid state, to gain the knowhow for tuning their electronic and photophysical properties. In parallel, we will also carry on a basic study on gold nanoparticles that aims to assess the possible pro-oxidant or antioxidant effects induced by the particles, they are in fact key features to determine their safety and suitability for specific applications.

-
- 1 Y. Matsumura, H. Maeda, *Cancer Res.* **1986**, *46*, 6387 LP.
- 2 R. Duncan, Y.-N. Sat-Klopsch, A. M. Burger, M. C. Bibby, H. H. Fiebig, E. A. Sausville, *Cancer Chemother. Pharmacol.* **2013**, *72*, 417.
- 3 H. Maeda, in *Biomedical aspects of drug targeting*, Springer, **2002**, pp. 211–228.
- 4 Y. Dai, C. Xu, X. Sun, X. Chen, *Chem. Soc. Rev.* **2017**, *46*, 3830.
- 5 J. Xie, S. Lee, X. Chen, *Adv. Drug Deliv. Rev.* **2010**, *62*, 1064.
- 6 Q. Chen, L. Xu, C. Liang, C. Wang, R. Peng, Z. Liu, *Nat. Commun.* **2016**, *7*, 1.
- 7 L. Prodi, M. Montalti, N. Zaccheroni, L. S. Dolci, in *Topics in Fluorescence Spectroscopy*, Springer, **2005**, pp. 1–57.
- 8 J.-M. Lehn, *Science (80-.)*. **2002**, *295*, 2400.
- 9 J. S. Taylor, D. B. Vigneron, J. Murphy-Boesch, S. J. Nelson, H. B. Kessler, L. Coia, W. Curran, T. R. Brown, *Proc. Natl. Acad. Sci. U. S. A.* **1991**, *88*, 6810.
- 10 N. J. Birch, *Magnesium and the Cell*, Academic Press, **1993**.
- 11 M. Forero-Shelton, *Nat. Methods* **2019**, *16*, 293.
- 12 J. S. Patton, P. R. Byron, *Nat. Rev. Drug Discov.* **2007**, *6*, 67.
- 13 M. R. Prausnitz, R. Langer, *Nat. Biotechnol.* **2008**, *26*, 1261.
- 14 J. Hawiger, *Curr. Opin. Chem. Biol.* **1999**, *3*, 89.
- 15 M. L. Bruschi, *Strategies to modify the drug release from pharmaceutical systems*, Woodhead Publishing, **2015**.
- 16 A. L. Marschall, A. Frenzel, T. Schirrmann, M. Schüngel, S. Dübel, *CrossRef PubMed PubMedCentral* **2011**.
- 17 D. C. Litzinger, L. Huang, *Biochim. Biophys. Acta (BBA)-Reviews Biomembr.* **1992**, *1113*, 201.
- 18 R. A. Jain, *Biomaterials* **2000**, *21*, 2475.
- 19 R. Duncan, *Nat. Rev. cancer* **2006**, *6*, 688.
- 20 F. Palomba, D. Genovese, E. Rampazzo, N. Zaccheroni, L. Prodi, L. Morbidelli, *ACS omega* **2019**, *4*, 13962.
- 21 P. N. (2004). I. to biophotonics. J. W. & S. Prasad, *Introduction to biophotonics*.
- 22 M. H. Niemz, *Laser-tissue interactions*, Springer, **2007**.
- 23 A. P. Castano, T. N. Demidova, M. R. Hamblin, *Photodiagnosis Photodyn. Ther.* **2004**, *1*, 279.
- 24
- 25 H.-W. Wang, T. C. Zhu, M. P. Putt, M. G. Solonenko, J. M. Metz, A. Dimofte, J. D. Miles, D. L. Fraker, E. G. M.D., S. M. Hahn, A. G. Yodh, *J. Biomed. Opt.* **2005**, *10*, 1.
- 26 L. O. Svaasand, *Prog. Clin. Biol. Res.* **1984**, *170*, 91.
- 27 G. Valenti, E. Rampazzo, S. Bonacchi, L. Petrizza, M. Marcaccio, M. Montalti, L. Prodi, F. Paolucci, *J. Am. Chem. Soc.* **2016**, *138*, 15935.
- 28 E. ASTM, 2456-06: *Standard Terminology related to Nanotechnology*. ASTM International, 100 Barr Harbor Drive, PO Box C700, West Conshohocken, PA, 19428-2959 USA (2006).

- 29 C. Buzea, I. I. Pacheco, K. Robbie, *Biointerphases* **2007**, 2, MR17.
- 30 L. B. Kiss, J. Söderlund, G. A. Niklasson, C. G. Granqvist, *Nanotechnology* **1999**, 10, 25.
- 31 T. Uyeda, C. Hayashi, A. Tasaki, *Ultra-fine particles: exploratory science and technology*, Elsevier, **1995**.
- 32 J.-P. Hansen, L. Verlet, *Phys. Rev.* **1969**, 184, 151.
- 33 T. L. Moore, L. Rodríguez-Lorenzo, V. Hirsch, S. Balog, D. Urban, C. Jud, B. Rothen-Rutishauser, M. Lattuada, A. Petri-Fink, *Chem. Soc. Rev.* **2015**, 44, 6287.
- 34 J. Xie, S. Lee and X. Chen, *Adv. Drug Deliv. Rev.*, 2010, 62, 1064–1079
- 35 J. Gallo, N. J. Long and E. O. Aboagye, *Chem. Soc. Rev.*, **2013**, 42, 7816.
- 36 N. Lee, S. H. Choi and T. Hyeon, *Adv. Mater.*, **2013**, 25, 2641–2660
- 37 N. Mitchell, T. L. Kalber, M. S. Cooper, K. Sunassee, S. L. Chalker, K. P. Shaw, K. L. Ordidge, A. Badar, S. M. Janes, P. J. Blower, M. F. Lythgoe, H. C. Hailes and A. B. Tabor, *Biomaterials*, **2013**, 34, 1179–1192.

CAP. 2

MOLECULAR CHEMOSENSOR FOR Mg²⁺ DETECTION IN MITOCHONDRIA

2.0 Cationic sensing

Molecular design for the detection of cation has attracted great interest for scrutiny outstanding to its potential applications in biomedical and environmental monitoring¹⁻³. Chemistry of molecular recognition, well known as Host-guest chemistry, is associated with the study of selective recognition of a molecule (guest) by another molecule (host) via the formation of non-covalent interactions, which constitutes the fundamental and traditional concept for the design of cation sensors^{4,6}. The creation of traditional cation sensors generally involves the combination of an ionophore for selective recognition of the target cation, with a chromophore or luminophore to signal the binding events with a respective colorimetric or luminescent response occurring from the alteration of its photophysical properties upon cation complexation. The higher sensitivity of the luminescent sensors respect colorimetric

ones, put them a step forward in their use in quantification in analytical and clinical purpose, where the sensitivity plays a critical role^{2,3}. Supramolecular chemistry, first termed by Lehn who was awarded the Nobel Prize in Chemistry together with Pedersen and Cram for their contribution to this field, combines the fields of host–guest chemistry and the chemistry of molecular assembly to a unified concept^{8,10}. This concept has long been an interest of study in the research field because through the incorporation of different functionalities into the molecular structures (such as ionophores), these systems would respond differently upon the introduction of external stimuli (such as a target cation) and arrange into interesting supramolecular structures. Such characteristic ingenuity endows these systems with versatile potential to be employed in the field of cation detection. Photoinduced electron transfer^{12,13} (PET), photoinduced charge transfer¹⁵ (PCT) and Forster resonance energy transfer¹⁷ (FRET) have been the common mechanisms utilized in the design of traditional cation sensors for governing the signal response of luminophores upon cation-binding. Anyway, many fluorescent probes exhibit cation-induced photophysical changes that cannot be explained along the same lines just mentioned. Interaction of a cation with a fluorophore often leads to changes in radiative, nonradiative and/or intersystem crossing rate constants, and consequently, changes in fluorescence quantum yield and lifetime (whereas shift of spectra is not a general rule). To this category belongs the oxyquinoline-based fluorescent chelators. The first of them is 8-hydroxyquinoline (8-HQ), often called oxine, and its derivatives. The most noteworthy aspect of 8-HQ is its fluorogenic character, i.e. its very low quantum yield in aqueous or organic solutions and the fluorescence enhancement occurring from cation binding. The non/fluorescent character of 8-HQ in neutral water has been satisfactorily explained only recently^{26,27} by the occurrence of excited-state proton transfer reactions coupled to an intramolecular electron transfer. In fact, photoinduced deprotonation of the –OH group and protonation of the heterocyclic nitrogen atom can occur either with surrounding water molecules or intramolecularly, depending on the possible existence of H-bonding between the two functions. Deexcitation of the resulting tautomer occurs mainly via a nonradiative pathway. In contrast, many metal chelates of 8-HQ and derivatives (e.g. Cd, Zn, Mg, Al, Ga, In) present strong yellow–green fluorescence

2

because the above-described photo processes are reduced by a bound cation. However, the changes in electronic distribution upon excitation are likely to weaken the bond between the oxygen atom and the metal ion, thus allowing some charge transfer from the phenolate – O⁻ to the nitrogen atom of the adjacent ring¹².

2.1 State of the art

One of the main protagonist among the divalent cations in the cells is Mg²⁺ being involved in many fundamental processes such as proliferation⁵ and cell death⁷. Magnesium ions have also a role in the regulation of enzymes and other species such as ATP, forming MgATP²⁻ which varies directly with cytosolic Mg²⁺ and plays the effective key role activating protein kinase in a molecular pathway that regulates the initiation of translation in the cells.⁹ Alteration in total or free magnesium levels can have significant consequences for cell metabolism and cell functions. Mg²⁺ biochemistry has been thoroughly studied *in vitro*, nevertheless it has not been achieved yet a fully understanding of cellular magnesium homeostasis. Plasma membrane and organelle transport regulate the cytosolic Mg²⁺ concentration and this level is maintained far from electrochemical equilibrium given by a transport mechanism inside/outside the cells¹¹. Cytosolic free Mg²⁺ levels are reported to be 0.2-1 mM¹⁴¹⁶ representing less than 10% of the total Mg²⁺; the rest is bound or sequestered in different cellular organelles. It has been presumed that cellular magnesium, the free form, is kept constant at the level necessary for cellular metabolic demands and that, in physiological conditions, its concentration does not undergo drastic and rapid changes. The need for a sensitive and reliable tool to measure concentrations and fluctuations of cellular Mg²⁺ becomes very stringent, since available techniques have serious limitations. Atomic absorption spectroscopy is very sensitive and accurate but requires volatilization of the sample and a relatively high number of cells, and it does not discriminate between free and bound forms. On the other hand, *in vivo* NMR spectroscopy allows an accurate measurement of cytosolic free Mg²⁺ but supplies no information on the total Mg²⁺ concentration and its distribution among cellular sub compartments. Electron probe

microanalysis has been exploited to measure Mg^{2+} content in distinct cellular sub compartments in freeze dried cryosections. This technique again does not provide information on free and bound Mg^{2+} and does not allow kinetic measurements of Mg^{2+} fluxes¹⁹. Fluorescent techniques can offer a suitable solution. If properly designed, a fluorescent probe could be the perfect, non-invasive and precise solution. Their application in fluorescence confocal imaging allows dynamic measurements of cellular content and distribution of the targeted ion, allowing analyte mapping in the sample. The available fluorescent probes for intracellular magnesium are mainly derived from those designed for calcium¹⁸, but they retain cross reactivity for Ca^{2+} and dependence on pH. These Mg^{2+} -specific fluorophores are characterized by a K_d in the millimolar range, which is appropriate to measure mainly the free fraction of cellular Mg^{2+} (only 5% of the total). In fact, cytosolic free Mg^{2+} concentrations are in the range of 10^{-4} M, while total cellular Mg^{2+} is up to 100-fold higher. Experimental evidences shows that fluctuations of free intracellular Mg^{2+} concentrations are modest compared to massive changes of total cellular Mg^{2+} ²⁰; thus, modifications of Mg^{2+} availability to influence different biological functions are thought to be accomplished by substantial modifications of the distribution of total Mg^{2+} among cellular sub compartments. In this scenario, a tool able to detect and/or discriminate between free and total Mg^{2+} and between Mg^{2+} content of cytosolic and intracellular sub compartments would be particularly useful. Recently, a new family of magnesium ions binding fluorescent probes named KMGs has been designed, and their application to the study of intracellular Mg^{2+} homeostasis seems promising²². The unavailability of more specific and selective commercial compounds for total magnesium currently represents a technical limitation in the study of the intracellular content and distribution of this cation. Compelling evidence, in fact, demonstrates that cellular magnesium homeostasis is quite unusual: significant fluxes of Mg^{2+} cross the cell membrane in either direction, with consequent major changes in plasma Mg^{2+} levels²¹ which, result in limited variations of free Mg^{2+} intracellular concentration, although large changes in total Mg content within tissues and organelles have been observed²³. This suggests that modifications of magnesium availability that influence different biological functions may be accomplished by

changes in the distribution (binding) of magnesium among cellular ligands and/or sub-compartments rather than by major modifications of the free fraction²⁴. The development of chemosensors able to detect total magnesium *in vivo* and discriminate specific intracellular ligands and/or compartments is particularly appealing. Since a few years, a new class of luminescent chemosensors for different metal cations was designed, synthesized and characterized in collaboration by professors M. Lombardo, L. Prodi and N. Zaccheroni that recently reported a complete study on those for Mg²⁺ ion based on diaza-18-crown-6 appended with two 8-hydroxyquinoline(8-HQ) groups (DCHQ) bearing different substituents²⁵. 8-HQ, that is the second major Mg²⁺ chelating agent after EDTA²⁶, is mostly nonfluorescent in aqueous or organic solutions and undergoes a fluorescence enhancement upon cation binding, which results in an intense yellow–green luminescence signal. Furthermore, the fluorescence of the complexed species depends on the environment and becomes higher as lipophilicity increases²⁷. However, the selectivity of 8-HQ for specific cations is poor and it needs to be improved by appropriate substitution. The study reported a complete synthesis, photophysical characterization and *in vitro* investigation of molecules members of a DCHQ family, with the most efficient one for Mg²⁺-detection being DCHQ5 (Fig 2.1) able to detect the intracellular level of Mg²⁺.

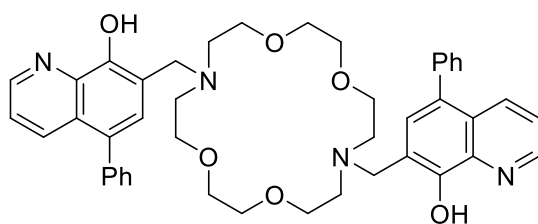


Figure 2.1 Molecular structure of DCHQ5

Mitochondria redistribute cytosolic and mitochondrial Mg²⁺ amount sufficient to change the cytosolic Mg²⁺ concentration ([Mg²⁺]_{cyto}) in response to several physiological stimuli^{28,29}. Recent studies using novel

Mg²⁺ fluorescent probes successfully visualized that mitochondrial Mg²⁺ concentration ([Mg²⁺]_{mito}) dynamically change^{30,31}. However, it is not clear, in cells, how the changes of [Mg²⁺]_{mito} comprehensively affect the cellular energy metabolism in detail. Although regulation of [Mg²⁺]_{mito} has not been elucidated in detail, mitochondrial Mg²⁺ channel MRS2 is known to be a molecular machinery associated with Mg²⁺ influx into mitochondria^{32,33}. Mg²⁺ uptake into mitochondria via MRS2 is essential for

the maintenance of respiratory chain and cell viability. For these reasons it is fundamental to find a specie able to penetrate the mitochondria membranes and to detect the Mg^{2+} concentration directly inside these organelles.

2.2 Aim of the work

The aim of this part of my research work was to functionalize and study a new luminescent chemosensor of the class of DHQC, that is to say a diaza-18-crown-6 appended with two 8-hydroxyquinoline(8-HQ) derivatives, precisely designing it to detect and quantify Magnesium ions selectively inside mitochondria. Starting from the knowhow on DHQC moieties already developed by the group²⁵ we decided to introduce in each 8-hydroxyquinoline component a terminal functional group able to target mitochondria. Many experimental evidences in the literature³⁴ show that phosphonium groups permeate mitochondrial membranes very efficiently and the challenge was to introduce these functions preventing negative drawbacks on both the binding event (receptor-ion interaction and affinity) and on the luminescence variations of the chemosensor in response to metal ion complexation. We chose, therefore, to insert phosphonium functions far from the binding sites at the end of long spacers to avoid their hindrance.

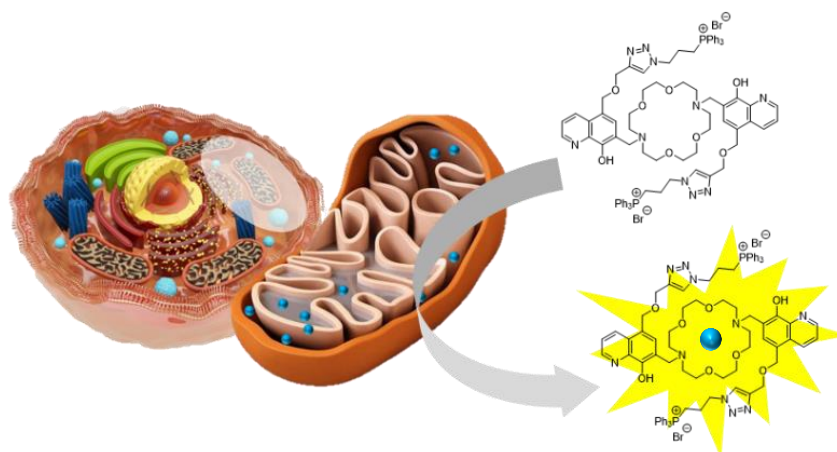


Figure 2.2 schematic representation of mitochondrial Mg^{2+} detection

The nature of these spacers had to be carefully evaluated in order to avoid inducing parasite non-radiative decay pathways that could quench the chemosensor luminescence, resulting in a much lower detection sensitivity. In order to optimize the final new chemosensor, a photophysical characterization of all the derivatized units before the final assembly is needed to verify the possible changes in their recognition and detection ability toward Mg^{2+} . The final chemosensor, instead, must be carefully characterized not only from a photophysical point of view but also *in vitro* (on a human leukemia (HL60) and osteosarcoma tumor (U2Os) cell lines) to test if the derivatization affects the toxicity of the system and/or the cell internalization efficiency.

2.3 Synthesis and photophysical characterization

In collaboration with Prof. M. Lombardo from University of Bologna, was synthesized firstly molecule **2**. Click reaction with $CuBr(PPh_3)_3$ 10% in dry DCM was performed, and deprotection using acidic condition has given to product **2**. Several trials were necessary to find suitable catalyst amount and precise solvent, but with the final conditions the yield is 99% (data reported in the experimental part).

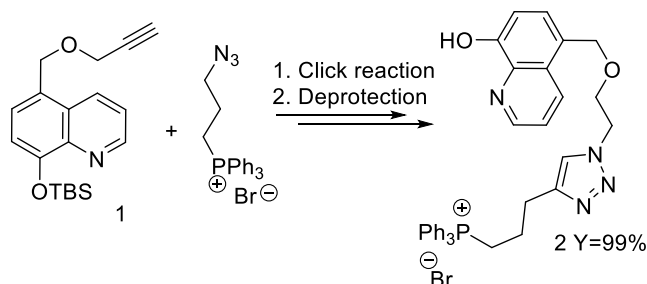


Figure 2.3 Synthesis of molecule 2

At this point has been conducted the first attempt to obtain the chemosensor. The idea, shown in Fig 2.4, was to use a Mannich reaction in a reflux condition. Even in this case were performed many trials not reported here, changing the reaction solvents, Toluene, CH_2Cl and EtOH and following the formation of the product by 1H -NMR analysis.

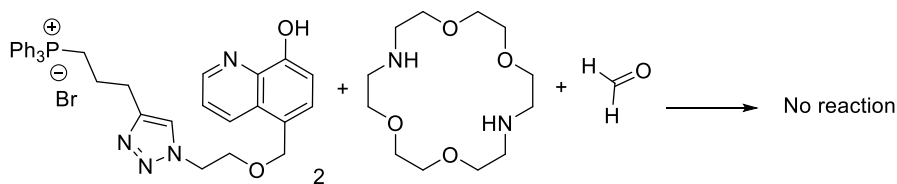


Figure 2.4 first attempt for Synthesis of chemosensor using mannich reaction

The strategy has given no results. Probably the presence of phosphonium group disturbs the reaction, in particular the difficult solubility of product **2** could be the cause. Then, to obtain molecule **4** it was decided to change the reaction pattern, making first the Mannich reaction and, after, to use the click step with phosphonium azide, as shown in Fig. 2.5

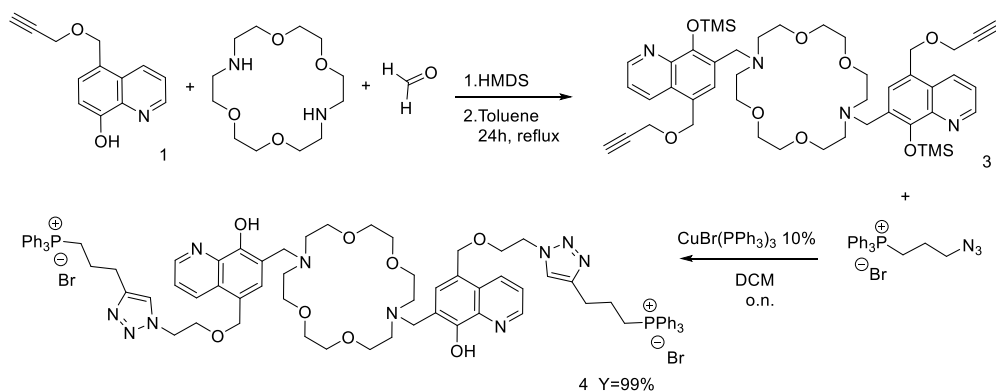


Figure 2.5 Scheme of the complete synthesis to obtain molecule **4**, DHCQPPH₃

This time the synthesis of the sensor **4**, DHCQPPH₃, was well performed. In this way, it is also possible to avoid further purification steps, in fact to the molecule **3** is added directly the catalyst and the azide resulting in a very to a clean ¹H-NMR spectrum of molecule **4 protected** (see experimental section). After a simple evaporation of the solvent under vacuum, **4** is obtained.

The photophysical characterization was performed, first of all, it has been conducted the characterization of the species **3** in order to verify the influence of the derivatization on the complexation and on the photophysical properties of the quinoline. **3** was dissolved in DMF to obtain a 1mM solution then a very small amount of this solution was added to 2.5mL of PBS 0.01M with a pH of 7.4 to mimic the physiological conditions. This procedure was necessary to guarantee the complete

solubilization of **3** since its very low solubility in water. The absorption and fluorescence spectra of **3** are mainly the attended ones for the 8-HQ derivative as it can be seen in Fig. 2.6. The absorption spectrum (Figure 6 on the left) of **3** in PBS 10 mM at pH 7.4, shows an intense band at around 240–250 nm ($\epsilon = 70000\text{--}83000\text{ M}^{-1}\text{ cm}^{-1}$) and a smaller and broader band at around 310–330 nm ($\epsilon = 5200\text{--}9000\text{ M}^{-1}\text{ cm}^{-1}$). The former can be attributed to a $\pi\text{--}\pi^*$ transition, while the latter presents a main charge transfer character with charge density moving from the hydroxyl oxygen atom to the quinoline. ^{35,36}

The titration of molecule **3** was performed using three different salts in order to exclude anion interferences and in particular with MgSO_4 , MgNO_3 and $\text{Mg}(\text{ClO}_4)_2$ obtaining the same results and for this reason I report hereafter only the data relative with MgSO_4 .

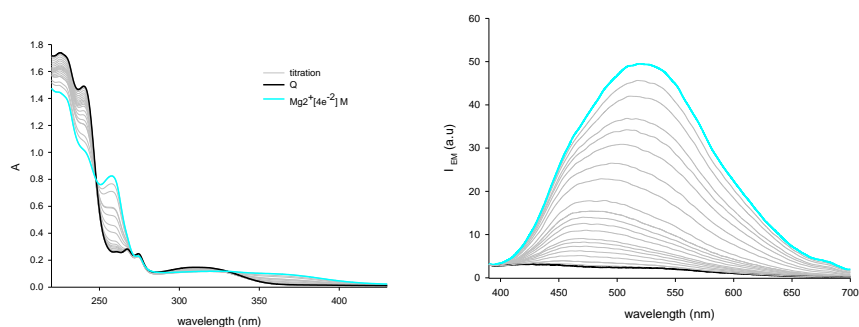


Figure 2.6 absorption (a) and emission (b) spectra of molecule **3** ($29\ \mu\text{M}$) in PBS 10 mM pH 7.4 at room temperature upon addition of increasing amounts of Mg^{2+} ions. $\lambda_{\text{exc}}=328\text{ nm}$ Eq of Mg^{2+} from 0 to 35

The fitting of the data with the program SpecFit³⁷ using a model L:M 1:1, indicate a value of the $\log K_a$ of 2.3 ± 0.04 .

The emission band is large and there is a red shift of 47 nm. This trend is accordant with the expectation, infact there is increasing in fluorescent and a red shift of the maximum in the emission caused by PPT processes (see section 2.0). The obtained results are quite different from the ones reported for the DCHQ chemosensor family, as expected for this single derivatized 'arm'. First of all, the association constant is much lower since in the DCHQ class the complexation is templated by the crown and helped by two side arms. Moreover the emission enhancement after reaching the plateau with the addition of 35 equivalents is only of 50

times, much lower than, for example in DCHQ5. All these results indicate that the derivatization with phosphonium did not significantly affect the quinoline properties, but it does not help metal ion complexation and the bounding with the crown ether is necessary for an efficient recognition. The photophysical characterization of the entire chemosensor was obtained following the same procedure used for **3**.

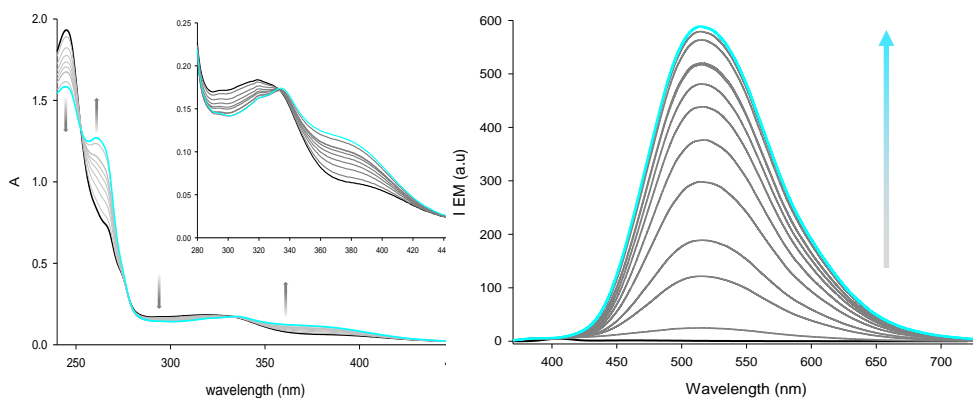


Figure 2.7 Absorption (left) and emission (right) spectra of **4** (25 μ M) in the presence of increasing amounts of Mg^{2+} (from 0 to 35 equivalents) in PBS 1.0 mM pH 7.4. ($\lambda_{\text{exc}}=340\text{nm}$)



Figure 2.8 Photography of increasing in emission of **4** upon addition of crescent amount of magnesium

Mg^{2+} binding causes a dramatic enhancement of the emission spectra up to 300 times the fluorescence intensity of the free ligand that can be appreciated also at naked eye as shown in Fig 2.7. The addition of increasing amounts of Mg^{2+} caused changes in the absorption spectra in line

with the complexation event as already observed for other DCHQ derivatives: the decrease of the bands centred at 240–250 nm and at 310–330 nm and the appearance of new bands around 260–265 and 370–390 nm. These new bands are characteristic of 8-HQ derivatives when the complexation process is accompanied by the deprotonation of the hydroxyl group in position 8^{38,39}. The $\log K_{\alpha}$ is well fitted (data not showed) both for absorption and emission titration giving respectively

2

values 4.5 ± 0.06 and 4.7 ± 0.03 . The quantum yield for the **4** complex is, 0.032. Comparing the results obtained with the previous studies²⁵, the complexation behavior of **4** is quite comparable with the DHCQ family compounds complexed with Mg^{2+} which present a fluorescent quantum yield in the range 6.7×10^{-3} - 3.5×10^{-2} . As for the previous chemosensors of the same class we have studied their selectivity with respect to the other possible competitors i.e Zn^{2+} , Cd^{2+} , Hg^{2+} , Cu^{2+} , Ni^{2+} , Na^+ , K^+ , Ca^{2+} , Fe^{2+} , Fe^{3+} , Al^{3+} and we evidenced that in agreement with previous results also **4** does not complex Na^+ , K^+ , Ca^{2+} , Fe^{2+} , Fe^{3+} ions in the investigated concentration range. Hg^{2+} , Cu^{2+} , Ni^{2+} , were efficiently bonded but formed non-luminescent complexes. All measurements were performed using SO_4^- as counterion and using the same equivalent amount, from 0 to 35. Among all considered metal ions, only Mg^{2+} , and Zn^{2+} and Al^{3+} induced a significant enhancement of the fluorescence of the system. The results for Cd^{2+} Zn^{2+} and Al^{3+} reported an increasing in the emission; respectively, for 35 eq. of salts, the emission of the **4** complexed with Zn^{2+} and Cd^{2+} , is comparable with the **4-Mg²⁺** complex, while with Al^{3+} the data collected were very undetectable due to the precipitation of something in solution (data not-shown). Maybe, gives the very low solubility of the $Al(OH)_3$, it is possible their formation. To be sure, further analysis changing pH value should occur. Anyway, intracellular Zn^{2+} concentration is around 100 times lower than Mg^{2+} and, moreover, most of Zn^{2+} is bound to Zn fingers with particularly high association constant²⁸, cadmium is not presented in non-poisoned cells; for this reasons they can't create competitors for Mg sensing. The selectivity respects to the principal competitors in physiological environment, Na^+ , K^+ , Ca^{2+} was well investigated (Fig. 2.9) All the measurements were performed in PBS 10 mM at pH 7.4 using SO_4^{2-} as counterion.

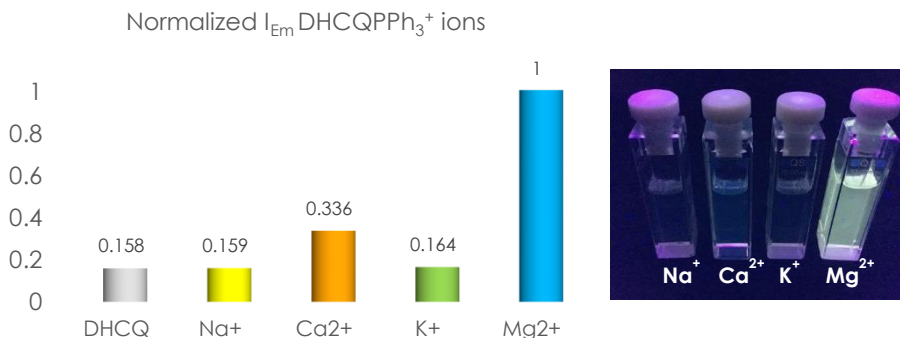


Figure 2.9 Graph of normalized emission intensity of **4** (25 μ M) with Na⁺ Ca²⁺ K⁺ Mg²⁺ and picture of the same samples

As Very interestingly, the complexation behavior of **4** is quite comparable with the DHCQ family compounds complexed with possible cations competitors inside the cells, as shown in chart in Fig. 2.9. These interesting results led to conclude that the new functions introduced in the chemosensor **4** compared to the previous studies on DHCQ family indicate that the derivatization with phosphonium ions does not significantly affects the complexation properties of the chemosensor.

2.3 Preliminary tests *in vitro*.

In collaboration with Prof. Iotti group, we studied the toxicity and internalization of the new probe in cells. In order to establish the maximum non-toxic concentration regime that is possible to use to stain cells we loaded HL60 cells with different concentrations of **4**, and counterstained them with propidium iodide (PI). HeLa is an immortal cell line used in scientific research. It is the oldest and most commonly used human cell line⁴⁰. The line was derived from cervical cancer cells taken on February 8, 1951⁴¹ from Henrietta Lacks, a patient who died of cancer on October 4, 1951. The cell line was found to be remarkably durable and prolific, which warrants its extensive use in scientific research⁴². The analysis of these cells by flow cytometry to discriminate live cells from damaged ones and selectively analyze the intracellular fluorescence of the chemosensors gave very promising results. We tested several concentrations in the range 5–40 μ M in order to identify the best

concentration to obtain a high signal/noise ratio together with a low cytotoxicity.

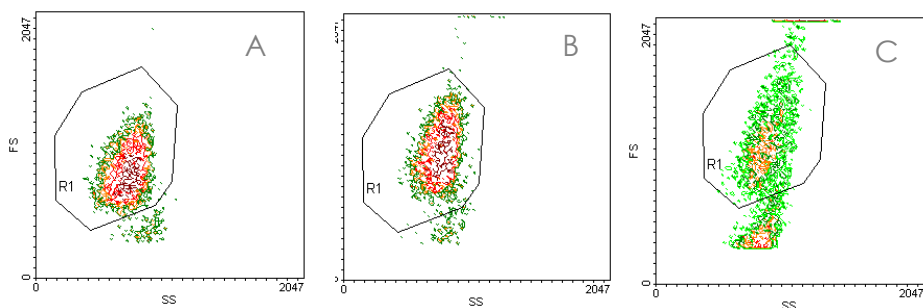


Figure 2.10 A: scatterplots of the control cells; B: HL60 (5×10^5 cell/mL)+4 20 μM; C: HL60 (5×10^5 cell/mL)+4 40 μM

Fig. 2.10 reports information about cells dimension (FS: forward scattering) and internal morphology of the cells (SS: side scattering): if the cells are healthy, all cells should be found in the same area of the graph with respect to the control, while if they are suffering, the size and morphology change, giving a displacement from the coordinates describing the control cells. Fig. 2.10C shows that only 40 μM of **4** induces substantial changes in cell morphology, even if the majority of the cells are still inside the region R1 corresponding to the healthy area. Further analyses were performed to support the non-toxicity of the chemosensor and in Fig. 2.11 are reported cytograms of control HL60 cells and treated with 20 μM of **4** for 30 minutes. All cells were previously treated with PI which reacts only with dead or dying cells and its detection causes the positioning of the cells in the sectors A (dead non-stained cells) or B (dead stained cells). As it can be seen in Fig. 2.11 left, the control cells occupy quadrant C (live non-stained cells) while cells stained with **4** (Fig. 2.11 right) present a high fluorescence and are in great majority in quadrant D (live stained cells). There is, however, a minor percentage of healthy cells that was not efficiently stained and a slightly higher percentage of dead stained cells with respect to the control. These results confirm that **4** stains live cells with a very good efficacy and after about 30 minutes from loading, seems to be well tolerated by the cells

at a loading concentration of 40 μM , which resulted in a good fluorescence signal.

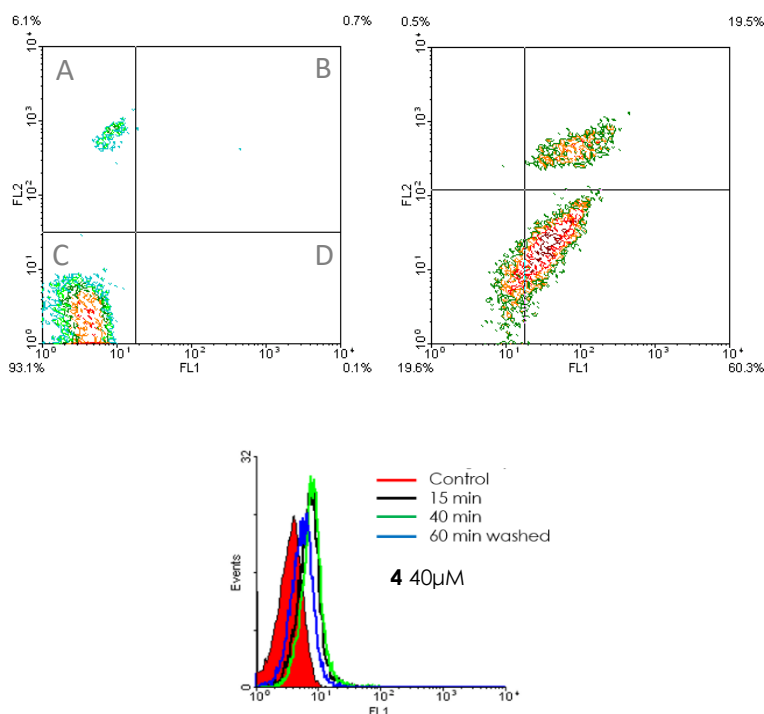


Figure 2.11 Left: cytochrome of control live non-stained cells; right: cytochrome of cells incubated with **4** 20 μM for 30 minutes; centre bottom: fluorescence signal of **4** 20 μM after different incubation time.

Moreover, from Fig. 2.11 centre bottom line blue it is possible to see how the emission signal remains almost unchanged after washing the cells with toxic components used to fix the cells on the glass and that induce their death and a great increase of porosity. This data indicates that **4** remains internalized despite the drastic increase of cell permeation and this could be explained by the possible segregation or the strong interaction of **4** in/with some cellular compartments. It has been speculated that these compartments could be mitochondria and in order to experimentally support this scenario, we performed some preliminary confocal microscopy imaging of mitochondria marked cells.

Preliminary assays were performed on **4** stained osteosarcoma tumoral cells (U2Os) marked with a specific red marker for mitochondria (Mitotracker CMROS). The cells were marked following two different procedures that I will call "pre-fixed" and "post-fixed".

2

In the "pre-fixed" one the Mitotraker and **4** were added simultaneously to the cells for 20 min and then washed and fixed to the glass with 4% of p-formaldehyde in PBS, washed with PBS and analysed after 24h. In "post-fixed" sample, the **4** addition was made after fixation and then they were analysed after 24h.

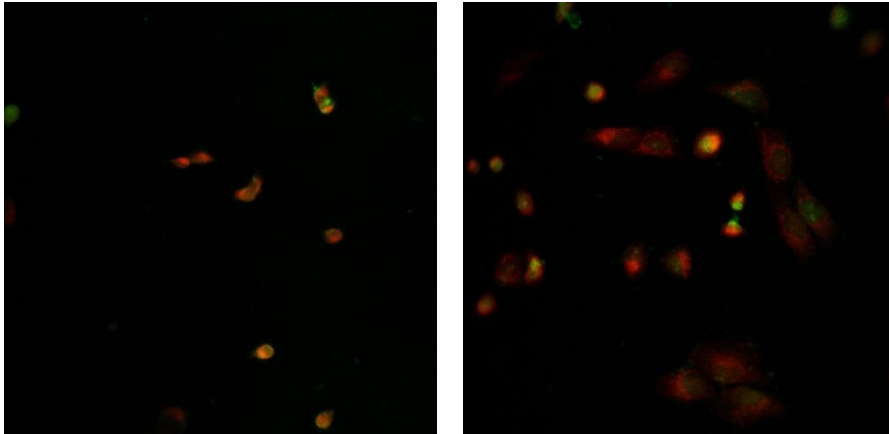


Figure 2.12 Confocal images of U2Os cells stained with **4** and marked with a red Mitotraker. Left "pre-fixed" sample, right: "post-fixed" sample

Fig. 2.12 seems to indicate that staining and marking are more efficient in the "post-fixed" sample. However, the Mitotraker is completely diffuse in all the cell and this is a clear indication that an efficient and selective marking of the mitochondria can be obtained only on live cells when the mitochondria are carrying out their functions and participate to the metabolic activities of the cells. The fixing step causes damages in the cell membranes including mitochondria ones and causes a dispersion of the Mitotraker throughout the cell. In these conditions it is evident that it is not possible to test any selective mitochondria staining of **4** and confocal investigation on live cells are mandatory for this goal. Unfortunately, this technique was not available in our laboratories, but new measurements are now scheduled in the framework of another collaboration of the group that will afford access to the needed technology.

2.4 Conclusion and future steps

During this project, carried out in collaboration with prof. M. Lombardo of the University of Bologna, a new chemosensor for selective intracellular magnesium detection in mitochondria was prepared and fully photophysically characterized. The introduction of the targeting phosphonium groups on the 8-hydroxyquinoline branches of the chemosensor was not trivial and Professor Lombardo developed a new functional total synthetic pattern involving Mannich-type and click reaction steps able to give the chemosensor in very high yield. The photophysical characterization evidenced that the derivatization did not affect the selectivity of the system toward Mg^{2+} in buffered solutions mimicking the physiological environment, and it even increases its sensitivity, in fact, the emission of the complexed specie results higher of up to 300 times with respect to the un-complexed chemosensor in solution.

Preliminary tests on a human leukemia cell line (HL60) in collaboration with Prof. S. Iotti of the University of Bologna, confirmed a very low cytotoxicity of the chemosensor until a concentration of 40 μM and its efficient internalization in live cells. Moreover, cytofluorimetric investigations on cells incubated with **4** 40 μM , then treated with fixing components that highly enhance their permeability and finally washed several times, showed a negligible liking of the chemosensor possibly due to its segregation or strong interaction in/with some cellular compartments. Further confocal investigation on live cells are mandatory in order to collect experimental evidences on the localization of **4** in the cells and on its envisaged selectivity for mitochondria, but unfortunately it was not possible to have access to the necessary instrumentation during my PhD work. These measurements are now scheduled for the next future in the framework of another collaboration of the group.

-
- 1 A. W. Czarnik, in *Fluorescent Chemosensors for Ion and Molecule Recognition*, American Chemical Society, **1993**, Vol. 538, p. 1.
 - 2 A. P. De Silva, H. Q. N. Gunaratne, T. Gunnlaugsson, A. J. M. Huxley, C. P.

- McCoy, J. T. Rademacher, T. E. Rice, *Chem. Rev.* **1997**, 97, 1515.
- 3 J. S. Kim, D. T. Quang, *Chem. Rev.* **2007**, 107, 3780.
- 4 D. J. Cram, J. M. Cram, *Science (80-.)*. **1974**, 183, 803.
- 5 F. I. Wolf, A. Cittadini, *Front Biosci* **1999**, 4, D607.
- 6 D. J. Cram, *Angew. Chemie Int. Ed. English* **1988**, 27, 1009.
- 7 R. Eskes, B. Antonsson, A. Osen-Sand, S. Montessuit, C. Richter, R. Sadoul, G. Mazzei, A. Nichols, J.-C. Martinou, *J. Cell Biol.* **1998**, 143, 217.
- 8 J.-M. Lehn, *Science (80-.)*. **1993**, 260, 1762.
- 9 H. Rubin, ed. by George F. Vande Woude, George B. T. Advances in Cancer Research Klein, Academic Press, **2005**, Vol. 93, pp. 1–58.
- 10 J. Lehn, *Angew. Chemie Int. Ed. English* **1988**, 27, 89.
- 11 A. S. A. Romani, *Front. Biosci.* **2000**, 5, 720.
- 12 B. Valeur, I. Leray, *Coord. Chem. Rev.* **2000**, 205, 3.
- 13 G. J. Kavarnos, *Fundamentals of photoinduced electron transfer*, VCH New York etc, **1993**.
- 14 J. A. Helpen, H. R. Halvorson, in *Measurement and Manipulation of Intracellular Ions*, ed. by Jacob Kraicer, S. Jeffrey B. T. Methods in Neurosciences Dixon, Academic Press, **1995**, Vol. 27, pp. 319–327.
- 15 B. Valeur, I. Leray, in *New Trends in Fluorescence Spectroscopy*, Springer, **2001**, pp. 187–207.
- 16 J. S. Taylor, D. B. Vigneron, J. Murphy-Boesch, S. J. Nelson, H. B. Kessler, L. Coia, W. Curran, T. R. Brown, *Proc. Natl. Acad. Sci. U. S. A.* **1991**, 88, 6810.
- 17 E. A. Jares-Erijman, T. M. Jovin, *Nat. Biotechnol.* **2003**, 21, 1387.
- 18 R. P. Haugland, *The handbook: a guide to fluorescent probes and labeling technologies*, Univerza v Ljubljani, Fakulteta za farmacijo, **2005**.
- 19 M. Bond, G. Vadasz, A. V Somlyo, A. P. Somlyo, *J. Biol. Chem.* **1987**, 262, 15630.
- 20 M. Fathollahi, K. LaNoue, A. Romani, A. Scarpa, *Arch. Biochem. Biophys.* **2000**, 374, 395.
- 21 L. Prodi, M. Montalti, J. S. Bradshaw, R. M. Izatt, P. B. Savage, *J. Incl. Phenom. Macrocycl. Chem.* **2001**, 41, 123.
- 22 H. Komatsu, N. Iwasawa, D. Citterio, Y. Suzuki, T. Kubota, K. Tokuno, Y. Kitamura, K. Oka, K. Suzuki, *J. Am. Chem. Soc.* **2004**, 126, 16353.
- 23 A. Romani, *Arch. Biochem. Biophys.* **2007**, 458, 90.
- 24 V. Covacci, N. Bruzzese, A. Sgambato, A. Di Francesco, M. A. Russo, F. I. Wolf, A. Cittadini, *J. Cell. Biochem.* **1998**, 70, 313.
- 25 A. Sargenti, G. Farruggia, N. Zaccheroni, C. Marraccini, M. Sgarzi, C. Cappadone, E. Malucelli, A. Procopio, L. Prodi, M. Lombardo, S. Iotti, *Nat. Protoc.* **2017**, 12, 461.
- 26 K. Soroka, R. S. Vithanage, D. A. Phillips, B. Walker, P. K. Dasgupta, *Anal. Chem.* **1987**, 59, 629.
- 27 I. Devol, E. Bardez, *J. Colloid Interface Sci.* **1998**, 200, 241.
- 28 O. S en eque, J.-M. Latour, *J. Am. Chem. Soc.* **2010**, 132, 17760.
- 29 R. Yamanaka, Y. Shindo, K. Hotta, K. Suzuki, K. Oka, *FEBS Lett.* **2013**, 587, 2643.
- 30 Y. Shindo, T. Fujii, H. Komatsu, D. Citterio, K. Hotta, K. Suzuki, K. Oka, *PLoS*

- One **2011**, 6, e23684.
- 31 G. Zhang, J. J. Gruskos, M. S. Afzal, D. Buccella, *Chem. Sci.* **2015**, 6, 6841.
- 32 G. Zsurka, J. Gregáň, R. J. Schweyen, *Genomics* **2001**, 72, 158.
- 33 R. Schindl, J. Weghuber, C. Romanin, R. J. Schweyen, *Biophys. J.* **2007**, 93, 3872.
- 34 J. Zielonka, J. Joseph, A. Sikora, M. Hardy, O. Ouari, J. Vasquez-Vivar, G. Cheng, M. Lopez, B. Kalyanaraman, *Chem. Rev.* **2017**, 117, 10043.
- 35 G. Farruggia, S. Iotti, L. Prodi, M. Montalti, N. Zaccheroni, P. B. Savage, V. Trapani, P. Sale, F. I. Wolf, *J. Am. Chem. Soc.* **2006**, 128, 344.
- 36 R. Ballardini, G. Varani, M. T. Indelli, F. Scandola, *Inorg. Chem.* **1986**, 25, 3858.
- 37 R. A. Binstead, A. D. Zuberbuhler, *Chappell Hill, NC* **1996**.
- 38 A. Casnati, F. Sansone, A. Sartori, L. Prodi, M. Montalti, N. Zaccheroni, F. Ugozzoli, R. Ungaro, *European J. Org. Chem.* **2003**, 2003, 1475.
- 39 R. T. Bronson, M. Montalti, L. Prodi, N. Zaccheroni, R. D. Lamb, N. K. Dalley, R. M. Izatt, J. S. Bradshaw, P. B. Savage, *Tetrahedron* **2004**, 60, 11139.
- 40 R. Rahbari, T. Sheahan, V. Modes, P. Collier, C. Macfarlane, R. M. Badge, *Biotechniques* **2009**, 46, 277.
- 41 W. F. Scherer, J. T. Syverton, G. O. Gey, *J. Exp. Med.* **1953**, 97, 695.
- 42 A. Capes-Davis, G. Theodosopoulos, I. Atkin, H. G. Drexler, A. Kohara, R. A. F. MacLeod, J. R. Masters, Y. Nakamura, Y. A. Reid, R. R. Reddel, R. I. Freshney, *Int. J. Cancer* **2010**, 127, 1.

CAP. 3

NANOSTRUCTURED CHEMOSENSORS FOR O₂ DETECTION IN BIOMEDICAL APPLICATIONS

Cells undergo on a variety of biological responses when placed in hypoxic conditions, including activation of signalling pathways that regulate proliferation, angiogenesis and death. Cancer cells have adapted these pathways, allowing tumours to survive and even grow under hypoxic conditions, and tumour hypoxia is associated with poor prognosis and resistance to radiation therapy. Many elements of the hypoxia-response pathway are therefore good candidates for therapeutic targeting and the detection of variations in oxygen levels at the cellular level could take to great step forward for the early diagnoses.

3.0 State of the art

In the so wide chemosensor scenario, the variation in oxygen levels is very often detected taking advantage of metal complexes and in particular metallo-porphyrins¹. Recently many researches are focused on the development of metal-free molecules or nanostructures. A promising class of compounds includes dendrimers, already deeply studied in view of drug delivery applications. Dendrimers are monodispersed, three dimensional, hyperbranched, nanoscaled polymeric architectures with a very high density of surface functional groups. With a definite molecular weight, shape and size, they are suitable species for many and different applications². Dendrimers are composed of three distinct domains, the cores, the dendrons and the terminal functional groups. The space among the branches of a dendrimer molecule forms cavities which are known as dendrimeric crevices and they can host and transport different species. These kinds of structures can mimic natural aggregates, for example natural porphyrin derivatives, including hemes, chlorophylls, and bacteriochlorophylls, are integrated into protein scaffolds that are essential for their biological activities. The development of dendrimer porphyrins has been inspired and prompted by many interesting functions of porphyrin derivatives in biological systems. In particular, their potentialities in oxygen sensing and/or photodynamic therapy (PDT) make them promising moieties to be used both for diagnostic and therapeutic applications especially in cancer fields. This has taken to great efforts in the preparation of dendrimers that are designed to be highly biocompatible, water soluble and even biodegradable.

The exploitation of new complex species for PDT or oxygen sensing has also been favoured by new techniques in the field of in vivo imaging such as Two-Photon (or, more generally, Multiphoton) Laser Scanning Microscopy (2PLSM)³. Its combination with the imaging of the variation of phosphorescence (intensity, lifetime) versus the oxygen concentration could allow to develop a high-resolution oxygen imaging method⁴. 2PLSM is based on the two-photon absorption (2PA) phenomenon⁴, which occurs with high efficiency only at extremely high local instantaneous intensities of the excitation light, i.e., in the focus of an

ultrafast pulsed laser beam. Raster-scanning such a beam in the axial plane at a selected depth (usually no more than 500 μm) within the object permits its effective 3D optical sectioning, provided that the object contains a 2P absorbing luminescent dye. 2PA is typically initiated by lasers operating in the NIR region of the spectrum, where absorption by natural tissue chromophores is diminished, and light can penetrate deeper into the tissue. It has to be also underlined that photodamage, associated with high laser power⁵, is confined in the case of 2PLSM into the immediate vicinity of the focal plane, being minimal along the excitation path, unlike in conventional linear optical methods. A difficulty in using 2PLSM in combination with phosphorescence quenching is that the phosphors for biological oxygen measurements are typically based on metal porphyrins complexes⁶, whose 2PA cross-sections are very low, in the range of a few GM units (Goeppert-Mayer = $10^{-50} \text{ cm}^4 \text{ s photon}^{-1} \text{ molecule}^{-1}$). While in principle phosphorescence of metalloporphyrins can be induced via 2P excitation⁷, for practical applications 2PA cross-sections of biological probes must be considerably higher. Prof. S. Vinogradov from University of Pennsylvania developed an efficient system based on a dendrimer able to overcome this problem^{8,9}. However, these branched moieties present a major drawback that is their demanding synthesis often associated with low yields. Therefore, this research field could undergo a great burst reaching the same results but with material is requiring relatively simple preparation steps with high yields. In the work described in this chapter I report my results in this direction.

3.1 Molecular Oxygen: a tool for diagnosis and therapy

Molecular oxygen O_2 , is at the bases of many natural processes¹⁰. The properties and behavior of oxygen reflect its unique electronic structure. Oddly, oxygen's electronic ground state, $\text{O}_2(X^3\Sigma_g^-)$, presents a triplet spin multiplicity¹¹ while its two lowest excited electronic states, $\text{O}_2(a^1\Delta_g)$ $\text{O}_2(b^1\Sigma_g^+)$, are singlet states (Fig 3.1) . Even though the higher energy $b^1\Sigma_g^+$ state doesn't react with other molecules^{12,13}, at least in solution-phase systems, the $a^1\Delta_g$ state,

commonly called “singlet oxygen”, has a rich chemistry that differs significantly from that of the $X^3\Sigma_g^-$ state¹⁴.

Singlet oxygen stays at the forefront for biological research because its unique reactivity as a synthetic agent¹⁵, as an intermediate in oxygenation reactions of polymers¹⁶ and, perhaps most significantly, forming the so called “reactive oxygen species”, ROS, useful in a range of biologically pertinent systems¹⁷. Singlet oxygen can be produced in a variety of ways¹⁸, a convenient method involves electronic energy transfer from an excited state of a molecule called sensitizer to $O_2(X^3\Sigma_g^-)$, Fig 3.1. Very interestingly, light is not only a useful tool by which singlet oxygen can be produced, but it is also at the basis of convenient methods to monitor events that result in the sensitized formation of singlet oxygen.

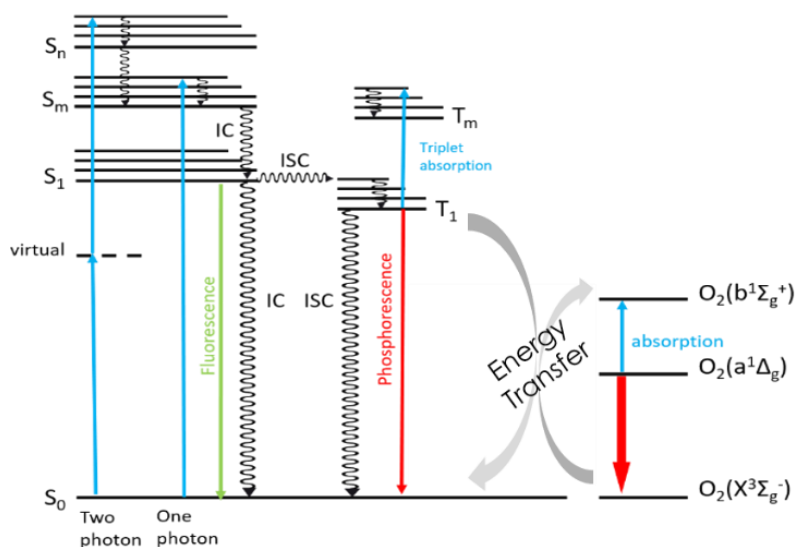


Figure 3.1 Jablonski Diagram illustrating the one- and two-photon-initiated, triplet-state photosensitized production of singlet oxygen

Variations in sensitizer emission are, for example, a very useful method to understand oxygen singlet production or quenching, especially in inhomogeneous systems like biological ones.

Even though Singlet oxygen can be produced upon $O_2(X^3\Sigma_g^-)$ quenching of the S_1 state¹⁸, the lowest energy T_1 state is generally the most efficient singlet oxygen precursor for molecules used as sensitizers and its photophysical characteristics (quantum yield, lifetime, energy) are the

fundamental features to take into account to design a diagnostic or therapeutic tool.

As already mentioned, a powerful, non-invasive, and selective technique useful in the treatment of cancer, and proposed in the last decades also for anti-bacterial applications, is PDT, that in contrast to chemotherapy, presents minor side-effects. The application of PDT in oncology involve a PS which opportunely excited by suitable wavelength by the light, induces a cytotoxic event respect to the tumour tissue. The first step involves an administration of an inert PS to the patient. When the light with a suitable wavelength is irradiated (often using laser sources), the irradiated tissue containing PS is rapidly destroyed. A suitable PS should have many characteristic: well-known composition with high purity level, selectivity to tumoral cell which could be also inducted with the PS functionalization, high yield in cytotoxic species formation, no toxicity in the dark, high efficiency in triplet state formation followed by long lifetimes in that state and high absorption in the red and NIR spectrum zone, which represent the therapeutic window most suitable for the penetration of the tissue (see Introduction). Following the triplet state formation, PS must show as prevalent way of deactivation the formation of the triplet state. In that condition the molecule could interact with the oxygen and forms the cytotoxic species by energy transfer. Activated PSs then, can induce chemical changes in a neighboring molecule via two competing pathways type 1 and type 2¹⁹. Type 1 involves the formation of radical superoxide anion, not so reactive, but able to react with itself to form hydrogen peroxide, which can easily cross the cell membrane. High concentrations of hydrogen peroxide could also bring to very reactive hydroxyl radical, formed by Haber Weiss reaction²⁰. Type 2 reaction instead, is a direct energy transfer to molecular oxygen from the PS, forming singlet oxygen²¹. Both types can occur but generally, type 2 represents the dominant process²².

3.2 Luminescent silica nanoparticles as chemosensors

Silica-based nanostructures represent an extremely versatile and effective platform for the organization of different units^{23,24} in order to obtain diagnostic and/or theranostic tools via a relatively simple

preparation and with high yields. Silica is an innocent matrix from a photophysical point of view, and this allows to obtain luminescent materials simply doping the nanostructure. The photophysical properties of the resulting architectures completely depend upon the included dye and they are mostly determined by two factors: (i) the effect of the nanoenvironment on the behavior of each molecular component²⁵⁻²⁸ and (ii) the strength of the intercomponent interactions.^{23,27,29} Several examples have been reported in the literature that show how luminescent quantum yields and photostability of light emitting molecular species can be improved simply by including them in silica matrix, for example, in the core of a silica nanoparticle (NPs)³⁰. Segregation of the fluorophores strongly reduces their interaction with the solvent as well as their excited-state conformational mobility and their accessibility to the atmospheric oxygen²⁷. The mixture of these factors in most cases inhibits nonradiative decay processes and prevents photoreactions that could cause the irreversible degradation of the dyes. On the other hand, the inclusion could protect some type of molecules from oxygen quenching, often NIR emitting species, enhancing their emission quantum yield (see section 1.1.2). In addition, even if the doping species are water insoluble, the water solubility of silica NPs allows their vehiculation in this solvent. Besides, a very important point is that the doping molecules are segregated in a very small volume and this forces their vicinity. Therefore, the properties of these multichromophoric nano-objects depend, as in the case of rigorously supramolecular systems,²³ on the kind and on the strength of the interactions among the molecular units, either at the ground or at the excited state.³¹ In the simplest case, that is, in absence of any kind of intramolecular interaction, the photophysical features of each NP are simply the combination of those of the trapped molecules. Even this trivial effect has important applicative implication: the presence of many absorbing moieties in a single NP proportionally increases the probability that at least one of them is excited upon irradiation. The molar absorption coefficient of heavily doped NPs is hence often extraordinarily higher than the one of molecular species. This feature, combined with its high fluorescence quantum yields, bestows, on a single NP, a much higher brightness than the one typical of molecular dyes.

Silica NPs are hence, for their high brightness, low intrinsic toxicity of their composition, and optical transparency, ideal for application in fields of high impact such as medical diagnostics and imaging both *in vitro* and *in vivo*³²⁻³⁴.

A further step toward more sophisticated nanosystems with the aim to use them as chemosensors or as theranostic agents requires synthesis able to include many big and hydrophobic molecules in the silica matrix that is usually prepared in water based solvent mixtures.

However, this is worth an effort since there are many advantages in passing from conventional molecular emitters to complex architectures. In this framework, luminescent silica nanoparticles are one of the most interesting and promising systems to be exploited in many fields like energy production and storage, catalysis, and sensing for medical or environmental applications. To obtain sensitive luminescent chemosensors, many requirements must be satisfied. In particular the material should be (photo)chemically stable, should present photophysical properties that do not depend on the environment or on a specific analyte; for marketing in general it should be obtained with an easy synthesis and low cost starting materials, and for their use in the medical field they should be biocompatible, nontoxic and environmental friendly as far as their disposal is concerned.

In more detail luminescent silica nanoparticles have all the crucial features listed hereafter.

- Silica is photophysically inert, i.e. it is transparent to visible light and is not involved in energy- and electron-transfer processes. All the photochemical properties of the luminescent silica nanoparticles are mainly conferred by the doping material and, when present, by the capping agents.
- Silica does not present intrinsic toxicity, and for this reason silica NPs are environmentally friendly and can be suitable for *in vivo* applications because they do not undergo microbial attack.
- Silica nanoparticles can contain many photochemically active species. Thanks to these large amounts of dyes incorporated in a small volume, obtaining a particle with brighter luminescence is easy³⁵ since its extinction

coefficient is equal to the sum of those of the single chromophores.

- The silica matrix protects the active material segregated inside the nanoparticle from external chemicals. Permeability for large species, in fact, is forbidden inside the nanoparticle, while small ones can penetrate with a much-reduced diffusion coefficient. This feature decreases the possibility of undesired photoreactions (the excited state of the dye cannot undergo bimolecular reactions), thus increasing the photostability of the fluorophores inside the nanoparticle, in the same time allows to use them as sensors for small molecules like oxygen.
 - The versatility of the synthesis allows one to design luminescent nanoparticles with chemical properties suitable for the desired applications, including *in vivo* ones. Surface modification with well-known chemical procedures³⁶ allows the optimization of their already good compatibility with water, and with the biological microenvironment (cellular membranes, biomolecules, etc.). It is also possible a simple tuning of the diameter through the control of the synthetic parameters. A fine control of size and functionalization often has a synergic action to obtain long-life systems in which the nanoparticle heads off by RES (Reticulo-Endothelial System) is delayed. RES is a mechanism by which alien particles are removed from blood or lymph by macrophages in vertebrate organisms. The great versatility of the synthetic strategies opens also up the possibility to adapt these materials for very different applications without requiring each time the design of the synthesis from scratch.

These five points make clear how luminescent silica nanoparticles are suitable to be used to engineer efficient fluorescent chemosensors, due both to their intrinsic properties and to their versatility. Anyway, again, all the photophysical properties of luminescent silica nanoparticles are conferred by the doping species, and therefore the photophysical properties of the dyes are the first determining point of

the performance of these systems in sensing and imaging fields. Then, using sol-gel processes³⁷, by tuning parameters such as catalytic conditions and nanoparticle nucleation-growth confinement, a lot of types of silica nanoparticles in solution can be obtained. All these synthetic strategies, however, usually involve TEOS like silica precursor and characteristics such as simplicity, low cost, versatility and control over nanoparticle dimensions. The main synthetic approaches are the Stoeber-Van Blaaderen method and others involving hydrolysis and condensation confinement, known as reverse microemulsions (water-in-oil) ³⁸³⁹ and direct micelle assisted methods (Fig. 2).⁴⁰. Each synthetic approach has advantages and limitations that are transferred to the resulting nanostructures, designed to suit precise applications. It is recommended the use of trialkoxysilane derivatized dyes⁴¹⁴² which prevent the leaching of dye from the particles, especially in biological applications, where the release of hydrophobic dyes, even if not observed in pure water, could be promoted by the proteins and a lipophilic cellular microenvironment. The number of molecular dyes that can be used for doping of NPs is usually quite high depending on the synthetic strategy adopted. Limitations are mainly related to solubility in the reaction batch and to the synthetic accessibility of the trialkoxysilane derivatives. Another important point is the electrostatic interaction among dyes and the silica matrix which generally favors the inclusion of positively charged dye and hampers negatively charged species. In the case of diagnostic applications, the combination of several factors such as the brightness of the system, spatial control over

nanoparticle functionalization and the colloidal stability of the NP suspension determines the suitability of the synthetic method.

In this part of my thesis I have particularly focused my attention on the possibility to overcome the limitations related to solubility of the doping species in the reaction batch. Fig. 3.2 schematizes the most common chemical preparations of silica nanoparticles, but I will describe in detail only the direct micelle assisted methods that is the one that I have followed for the preparation of the materials described in this chapter.

3.2.1 Stöber method

The study of Kolbe, successively developed by Stöber⁴³, to obtain colloidal silica was later implemented by Van Blaaderen to obtain fluorescent NPs, thanks to the incorporation of trialkoxysilane modified dyes⁴⁴. This method is far from dated, thanks to an accessible dimensional range spanning from 10 to several hundreds of nanometers with one-pot procedures, very simple synthetic mixtures (TEOS, water and ammonia), mild conditions, bringing to very monodisperse NPs. In this strategy, ammonia promotes TEOS hydrolysis and NP formation in water using

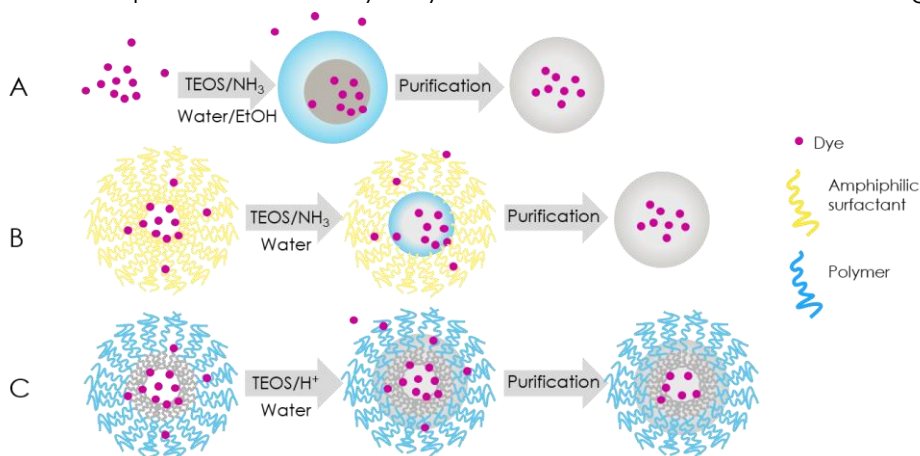


Figure 3.2 Schematic representation of Stöber method A, Reverse microemulsion method B and Micellar assisted method C.

ethanol as the TEOS co-solvent. Controlling the concentrations and ratio between the components its possible set the dimension of the NPs. Covalent doping of the NPs is achieved by using alkoxy silane derivatized dyes, with some limitations due to their solubility in ethanol–water mixtures.

3

Briefly, the Stöber method involves a first hydrolysis step proceeding through a bimolecular nucleophilic substitution (S_n2) on the silicon atom, characterized by a negatively charged, pentacoordinate transition state.^{45,46} The nucleophile involved in this step is OH^- , therefore an increase in the concentration of NH_3 and/or H_2O leads to an increase in the reaction rate. Moreover, since the hydrolysis decreases the electron density on the silicon atom – OH is more electron-withdrawing than OEt – the negative charge of the transition state is more stabilized for each subsequent step; for this reason, the rate-determining step for monomers is the hydrolysis of the first ethoxy group. The condensation step is very similar to hydrolysis: it proceeds through a S_n2 type nucleophilic substitution at the silicon atom, which results in a negatively charged, pentacoordinate transition state; the nucleophile is a deprotonated silanol group, so the reaction rate is still influenced by the concentration of NH_3 and/or H_2O ; and it decreases the electron density on the silicon atom – OSi is more electron withdrawing than OH .

The preparation of the first dye doped silica nanoparticles was possible thanks to van Blaaderen's idea of modifying the structure of fluorophores, by coupling APTES with fluorescein isothiocyanate and rhodamine B isothiocyanate.⁴² The resulting triethoxysilane derivatized molecules are then able to co-condense with TEOS during the nanoparticle growth, yielding systems in which the organic dyes are covalently grafted to the silica matrix. This is a fundamental improvement, because, apart from minimizing leaching issues, allows to reach very high doping levels.

In the Stöber-derived strategies, the presence of deprotonated Si-OH groups on the surface of the NPs usually generates colloidal suspensions that are strongly stabilized by electrostatic repulsion and are characterized by very large negative z-potential values. Functionalization of NPs exploits the presence of the Si-OH groups and is usually carried out in solution, adding alkoxy silane components tailored for different applications. This second step is quite delicate since it often induces aggregation or leads to incomplete surface passivation.

Purification steps are necessary to separate uncondensed dyes, oligomers and condensation catalysts, and to change suspending media when necessary. These strategies may include precipitation-centrifugation, ultrafiltration (UF), size exclusion chromatography (SEC), dialysis or instrumental techniques such as Flow Field Flow Fractionation

(FIFFF)⁴⁷. These last three purification methods involve very mild conditions and consequently stand out for the prevention of NP aggregation.

3.2.2 Reverse microemulsion method

Reverse micelles are formed mixing an appropriate amount of a surfactant and a hydrocarbon. They are capable of housing a limited amount of water forming a macroscopically isotropic reverse microemulsion (water-in-oil), with water cores that can be exploited as nano-containers to confine the Stöber synthetic process. Several protocols have been proposed to give simple way to access to nanoparticle preparation and surface modification in the dimensional range of circa 15–200 nm^{39,48} with the dimension depending largely upon the surfactant type and the surfactant-to-water molar ratio.⁴⁹ The most used method was developed by Arriagada and Osseo-Asare,⁴⁹ and later improved by Tan and co-workers⁵⁰. This process is based on the same described in the previous section; except that the medium where hydrolysis and condensation of TEOS take place, is the core of a reverse microemulsion. Surfactants are amphiphilic long-chain organic compounds, miscible both in hydrocarbons and in water, characterized by two fundamental parameters: the critical micelle concentration (CmC) and the critical micelle temperature (Cmt). Above these threshold values, when they are dissolved in a hydrocarbon solution, they create a macroscopically isotropic dispersion, the orientation of the surfactant molecules is not random: they forms spherical aggregates, where the hydrophilic heads are aligned toward the center, while the hydrophobic tails extend into the bulk oil phase. If water is added to this system, it places itself at the center of these aggregates: these stabilized water droplets then act as small nanoreactors, where the hydrolysis and condensation of TEOS is confined, yielding highly monodisperse, spherical particles with diameters ranging from 20 to 100 nm.

The main drawback of the reverse microemulsion approach is that these work-up procedures usually involve concentration–dispersion steps that can lead to irreversible aggregation.

3.2.3 Direct micelle assisted methods

This approach is based on the use of a surfactant in a water solution where the micellar aggregates (or co-aggregates) act as hydrophobic templates, where the formation of the nanoparticle structure takes place.

On the wave of ORMOSIL⁵¹, and inspired by the work of Liu and co-workers who have described a new kind of core-shell (silica-PEG) nanoparticles as platform for drug-delivery, Prodi et al. have proposed⁵² a synthetic strategy that affords monodispersed and ordered core-shell silica nanoparticles. Such systems allow the inclusion of dye molecules in the silica core and present a stable, biocompatible and water soluble polymeric protective shell. For these reasons these materials appear particularly promising in the development of luminescent probes for *in vitro* and, hopefully, *in vivo* medical and bio-analytical applications. The synthetic strategy is based on the formation of direct micelles of Pluronic® F127 in water. PF127® is a non-ionic triblock copolymer surfactant terminating in primary hydroxyl groups and presenting a PEG-PPO-PEG structure (MW 12600 Da) that is non-toxic. These surfactants have a general molecular formula of PEO_x-PPO_y-PEO_x, with coefficients x and y determining their overall polarity and aggregation behavior in water. In particular, the high molecular weight PF127 surfactant is the most used in the fabrication of silica NPs due to the capability of its aggregates (or co-aggregates) to act as templates in the formation of the NPs.

The subsequent addition of TEOS in acidic (or even neutral) conditions leads to the formation of a silica core following the same steps mentioned in the Stöber approach, due to the fact that, especially before hydrolysis, alkoxy silane are rather apolar species and tend to migrate and accumulate in the central part of the polymeric micelles, the more hydrophobic area where the silicate condensation is promoted. This induces the formation of the silica nanoparticles only inside the micelles, as the condensation proceeds, leading to the entrapment of the surfactant's molecules and to the final silica core-PEG shell architecture, that I will call from here after PlusNPs. (Fig. 2).

To control and avoid the inclusion in the matrix of the whole PEG

segments, or the aggregation through inter-particles polymerization, the introduction in the mixture of a capping agent in due time like DEDMS or TMSCl is needed, to stop the silica condensation.

The addition of the trialkoxysilane derivatized dyes in the reaction mixture leads to their co-condensation with TEOS, resulting in robust and stable luminescent systems. Thus, this method allows the physical or covalent entrapment of dozens of molecules into a small silica core, providing very bright nanosystems. The silanization of the dye and its purification after coupling reaction, represent the most difficult and long step in the NPs synthesis but we have found, as described in paragraph 3.6, an efficient way overcome this issue.

Another great potentiality of this material is the possibility to insert targeting moieties on their surface, including biological relevant species that would account for bio-recognition and bio-specificity, opening the way to several possibilities in biomedical and analytical applications. Modifying the terminal moieties of PF127 its possible to obtain nanoparticles that, as prepared, exhibit functional groups on the surface, such as $-\text{COOH}$, $-\text{NH}_2$, $-\text{SH}$, $-\text{N}_3$, alkynes, that can subsequently undergo different chemical reactions to link the particle to a variety of targeting moieties.

These core-shell nanoparticles are extremely soluble and stable (up to years) in water (or phosphate buffered saline solutions, PBS) in which they maintain an outstanding monodispersity. The strength of this strategy is mainly being a one-pot method, in which very cheap and basically non-toxic components are used even if the synthesis pertains to functionalized nanoparticles. Moreover, the PEG shell boosts the performances of the colloidal system envisaging *in vivo* and *in vitro* bio-analytical applications. The PEG shell provides a stabilizing stealth layer^{53,54} and these colloidal systems retain their stability and monodispersion in simulated physiological or bio-analytical work-up conditions (PBS 1x, bovine serum albumin up to 10 wt%).

Another feature is the ability to host in the outer PEG shell water insoluble materials such as dyes⁵⁵ or chemosensors. In perspective these systems seem to be good candidates for the development in an easy and rapid fashion of chemosensors presenting valuable features like signal amplification due to light harvesting properties.

PLuSNPs were characterized using several experimental techniques, such as TEM and DLS (Dynamic Light Scattering)⁴⁷, AFM measurements⁴⁰. The d_H obtained by DLS is around 25 nm and from TEM is possible estimate the interal diameter of the silica core around 11 nm (Fig 3.3).

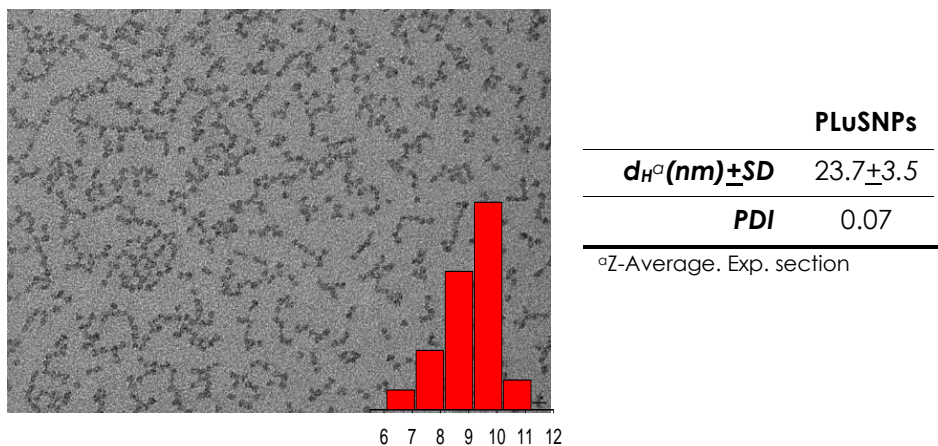


Figure 3.3 TEM image of standard PLuSNPs (scale bar 100 nm) and its DLS measurements in table

¹H-NMR and TGA (Thermo Gravimetric Analysis) were also used for the characterization and they, respectively, showed the outward orientation of the PEG chains and an invariant mass ratio between the organic and inorganic parts of samples subjected to ultrafiltration treatments of different durations (membrane cut-off 100 kDa).

3.4 Oxygen chemosensors based on silica nanoparticles

The design of silica nanomaterials starts from the choice of the synthetic procedure that has to take into account the solubility of the doping and functional moieties needed in the final nanoobject. The research group I worked with, had already demonstrated, for example, that following the Stöber preparation, non-polar dyes spontaneously accumulate in the center of a nanoparticle, especially at high doping concentration regimes, leading to intermolecular interactions, possibly resulting in emission self-quenching and favoring energy or electron transfer processes⁵².

More recently, the research of the group has been focused on silica core/PEG shell nanoparticles obtained through the direct micelle-assisted template synthesis described above, leading to a range of luminescent materials^{47,52} for applications in *in vitro*⁵⁶ and *in vivo*^{57,58} optical and photoacoustic⁵⁹ imaging, as chemosensors⁶⁰ or as electrochemiluminescent probes⁶¹.

In order to design and prepare new oxygen chemosensors based on this preparation the main problem, as already mentioned, is solubility, in fact, phosphorescent Pt and Pd porphyrins are the election doping candidates for optical sensing of oxygen in biological systems⁶². However, porphyrins are known to be difficult-to-solubilize targets, often exhibiting great propensity toward π -stacking and aggregation. On the other hand, porphyrins and their metal complexes form a group of versatile dyes with exceptionally rich optical and electrochemical properties, which present interest for applications in many areas of technology and medicine, from catalysis to biomedical imaging and phototherapy. In order to ensure aqueous solubility, tune the sensitivity of the phosphorescence into the optimal range for biological oxygen detection and simultaneously make porphyrin signals selective for oxygen in complex biological environments, porphyrins need to be incorporated into a protective shell with inert hydrophilic periphery. In this context, Prof. S. Vinogradov⁶³ presented an efficient set of Pt or Pd porphyrin-dendrimers with PEGylated periphery (PEG = polyethyleneglycol) that allow quantitative oxygen measurements *in vivo*.

3.4.1 Porphyrins and organic phosphorescent molecules

As mentioned before, good PSs should work in the range where human tissue are transparent, the photophysical properties of porphyrins and their high synthetic versatility have made them attractive and tunable candidates. Although synthetic routes toward porphyrins lead to relatively low yields, their starting materials are typically inexpensive, and their synthesis is generally straightforward. The synthesis typically requires reaction of pyrrole with the aldehyde of choice to give the appropriate substitution at the meso-positions followed by chromatographic purification to obtain the final product⁶⁴. The

absorption spectra of porphyrins is very typical and two regions can be distinguished: a) the first involves the transition from the ground state to the second excited state ($S_0 \rightarrow S_2$), the corresponding band is called the Soret or B band and the range of absorption is 380-500 nm depending on whether the porphyrin is π - or meso-substituted; b) the second region is due to a weak transition to the first excited state ($S_0 \rightarrow S_1$) in the range between 500-750 nm (the Q bands). The Soret band is characterized by very high molar extinction coefficients of the order of magnitude of $10^5 \text{ M}^{-1} \text{ cm}^{-1}$, while for the weaker, but still considerably intense, Q bands it is of $10^4 \text{ M}^{-1} \text{ cm}^{-1}$. The lower energy Q-bands are the transition of interest for the absorption of light in the tissue transparency window. In addition, porphyrins have been associated with high affinity for tumour sites and efficient formation of ROS⁶⁵. Specifically, cationic porphyrins are widely studied for their water solubility and their strong electrostatic interactions with negatively charged phosphate oxygen atoms of the DNA backbone⁶⁶. This section will focus on the study of 5 different metalloporphyrins synthesized by prof S. Vinogradov group all with phosphorescence emission around 700-850 nm that is quenched by oxygen and suitable for *in vitro/in vivo* tests.

It is much more difficult to find all-organic molecules suitable for this kind of applications, in fact, organic molecules exhibiting phosphorescence at ambient temperatures are rare. Emission from triplet states is usually a prerogative of metal complexes, in which the presence of metal ions enhances spin-orbit coupling and accelerates spin-forbidden transitions. In the case of all-organic molecules, phosphorescence is usually observed only in rigid matrices at low temperatures (e.g. 77 K). In liquid air-equilibrated solutions non-radiative relaxation and/or quenching by molecular oxygen completely outcompete very slow emission from the triplet states of all-organic chromophores, while much faster phosphorescence of metal complexes may still be observable even on air.

In these last years, there has been a burst of interest in non-phosphorescent fully organic molecules in fluid solutions, but can regain emissivity upon rigidification^{9,67-69}. Reducing the mobility of a chromophore by restricting bond rotations, has become one of the most popular strategies to boost triplet emissivity. All-organic phosphorescent

chromophores are subsequently envisioned as luminescent probes, sensors, elements of displays and other components of functional devices. However, the requirement of a rigid environment significantly limits usability of all-organic phosphors. Moreover, for biological applications, transferring organic dyes into aqueous environments either directly in the crystalline form or by embedding into solid polymeric particles presents multiple problems, such as inadequate colloidal stability of the latter and/or their high polydispersity.

Therefore, a biocompatible, easy to synthesize matrix able to constrain molecules and to favor aggregation-induced phosphorescence (AIP) processes would be a perfect solution for the design and preparation of a new generation of oxygen organic chemosensors. We have worked on this topic exploring the potentialities of silica nanoparticles to act as a suitable matrix and we have obtained very promising results discussed in section.

3.5 Aim of the work

The first goal of this part of the thesis was the development of a new optimized synthetic strategy, based on the one already patented by L. Prodi et al., in order to introduce inside the silica core of PluSNPs a high number of dyes, even in case of big and conjugated water insoluble species. The screening of many organic solvents in different percentages will help to reach the goal that is fundamental for the further steps towards the final aim that is the design and preparation of water soluble, stable, biocompatible and efficient molecular oxygen chemosensors for biomedical applications. We will take advantage of two classes of compounds, precisely metal porphyrins and all-organic phosphors, able to interact with O₂ and signal its presence in a quantitative way via light emission quenching.

An efficient preparation method will allow the introduction of all-organic phosphorescent molecules, called *asterisk* and synthesized by prof. Ceroni group, in the PluSNPs to obtain the first water soluble oxygen chemosensor based on all-organic emitters.

Parallel, 5 different metalloporphyrins synthesized by prof. Vinogradov's group will be used as doping agents for PluSNPs that then will be tested

for the same purpose. The porphyrins structures are reported in Fig 3.11 and include both platinum and palladium complexes.

The final ambitious step is to optimize the most promising structures for *in vivo* applications in order to preliminary investigate them in collaboration with Prof. B. Weber of the University of Zurich and his group that has the suitable instrumentation to monitor oxygen dynamics in mouse brain via two-photon phosphorescence lifetime microscopy (2PLM). The key imaging parameters *in vivo* are speed and depth to obtain a fast response to the oxygen changes, while deep imaging is critical because both the most metabolically active and most stroke-prone regions are often located deep in the cortex³⁶ and even in the white matter. The design and optimization of our nanostructured chemosensor will be specifically studied to meet these severe requirements.

3.6 Results and discussion

3.6.1 Optimization of *PluS* NPs synthesis

L.Prodi et al. Patented in 2011⁷⁰ a simple, reproducible and cheap method to synthesize SiNPs using a micelle assisted method. This protocol make use of the A–B–A triblock copolymer surfactant Pluronic® F127, TEOS as silica precursor and acetic acid 1M as reaction medium. Usually the luminescent doping material is composed by triethoxysilane functionalized dyes. The versatility of this approach is huge, since it provides a one-pot strategy to obtain extremely monodisperse NPs with a core–shell silica–PEG structure (hard diameter = 10–12 nm; hydrodynamic diameter = 20–30 nm). In the preparation of luminescent materials, this strategy shows solubility restrictions regarding the doping dye(s), especially in the case of non-polar dyes characterized by an extended planar structure. In particular in the preparation of *PluS* NPs doped with alkoxy silane functionalized porphyrins, and with dyes having an extended aromatic structure, the solubility restrictions bring to poor doping levels and/or to the formation of dye aggregates within the nanoparticle core. In the case of doping dyes like porphyrins, a nanoparticles synthetic protocol able to avoid the purification of the dye after functionalization with the triethoxysilane moieties is desirable, since these molecules can't be purified by standard purification techniques

like precipitation and flash chromatography.

The standard procedure for the synthesis of PluS NPs⁷⁰ involves the use of PF127, NaCl and alkoxy-silanized dye dissolved in acetic acid 1M; TEOS is used as silica precursor. Hydrolysis and condensation of TEOS is performed at 30°C for 3h, and after this time is performed the addition of an endcapping agent like TMSCl to saturate the uncondensed Si-OH groups present on the silica core. PluS NPs purification can be performed by dialysis, ultrafiltration or size exclusion chromatography⁷¹. Previous work showed the possibility to estimate the concentration of nanoparticles obtained by this synthetic protocol⁴⁷.

In the perspective to reduce the solubility limitations showed by few kinds of doping dye during the Pluronic F127 micellar assisted nanoparticle synthesis, we investigate the possibility to perform this synthetic protocol with organic solvent-water mixtures. The first screening of the synthetic conditions was done evaluating the hydrodynamic properties of Pluronic F127 aggregates in the presence of increasing concentrations of selected organic solvents. The screening was performed considering a set of non-nucleophilic, completely water-soluble solvents (DMF, DMSO, 2-butanone, acetonitrile). This last characteristic is necessary to form a homogeneous water mixture during the nanoparticle synthesis, while an inert solvent is useful to perform the in-situ functionalization of the doping agent (dye(s), ligand(s), etc.) with trialkoxysilane moieties. We considered the PF127 concentration usually employed in the 1 M acetic acid synthetic protocol (5.1 mM), and the hydrodynamic behavior of PF127 aggregates in solution in the presence of increasing amounts of an organic solvent was evaluated by DLS measurements.

Table 3.1 DLS data measured for Pluronic F127 micelles ($[F127] = 5.1 \text{ mM}$) in different organic solvent–Acetic acid 1M mixtures

Solvent	Solvent. V/V^a (%)	$d_H \pm SD^b$ (nm)	Pdl	d_H^c (nm)	DCR^d (kcps)
Acetic acid 1 M 2-Butanone	0	18.4 ± 0.4	0.63	6.4 ± 0.2	276 ± 4
	1.3	37 ± 13	0.42	6.6 ± 0.2	225 ± 6
	5.2	20 ± 2	0.64	6.6 ± 0.1	215 ± 6
	12.9	24 ± 6	0.57	6.8 ± 0.1	228 ± 3
	38.7	— ^e	— ^e	— ^e	— ^e
Acetonitrile	1.3	23 ± 0.1	0.80	6.4 ± 0.1	318 ± 14
	5.2	21 ± 3	0.63	6.7 ± 0.1	276 ± 25
	12.9	19 ± 4	0.43	6.5 ± 0.2	244 ± 33
	38.7	21.4 ± 0.1	0.15	17.8 ± 0.2	970 ± 14
DMSO	1.3	19 ± 1	0.65	6.0 ± 0.1	280 ± 10
	3.2	22 ± 2	0.41	9.0 ± 0.3	287 ± 10
	16.1	26 ± 3	0.56	7.1 ± 0.3	315 ± 20
	38.7	19 ± 1	0.49	6.6 ± 0.1	310 ± 10
DMF	1.3	19 ± 5	0.44	6.5 ± 0.2	250 ± 30
	5.2	42 ± 17	0.42	7.0 ± 1	370 ± 70
	12.9	24 ± 14	0.42	7 ± 2	230 ± 30
	38.7	16 ± 3	0.43	7 ± 1	240 ± 60

^a V/V% concentration (the total volume for each solution was 1550 μL). ^b Average hydrodynamic diameter distribution by intensity. ^c Average hydrodynamic diameter distribution by volume. ^d Derived scattering intensity measured by the detector. ^e Data not available because of emulsion formation

Quite surprisingly, these DLS investigations (Table 3.1) showed that with the only exception of 2-butanone, Pluronic F127 aggregates maintain hydrodynamic characteristics quite similar to the aggregates formed in acetic acid 1M in water, up to ~40% V/V concentration of organic solvent. These experiments showed that the presence of organic solvents had only minor effects on the average hydrodynamic diameters of the Pluronic F127 aggregates, and also that in most cases, the scattering intensity (DCR, Table 3.1) produced by surfactant aggregates in organic solvent/water mixture was comparable to the one measured in acetic acid 1M. This last evidence was an indication that the number of Pluronic F127 aggregates and then the number of templates available for the NPs formation was rather constant increasing the amount of organic solvent in reaction medium. These results were used to evaluate the formation of PluS NPs with these new solvent conditions. The first experiments were focused on the synthesis of non-doped silica nanoparticles using TEOS as silica precursor. DLS measurements were performed on PluS NPs purified by dialysis. Table 3.2 provides an overview of these very good results and shows that most of the solvent mixtures were suitable to host the formation of PluS NPs. The only exception is represented by the more concentrated acetonitrile mixture that did not lead to the formation of a colloidal system due to the formation of a precipitate. The NP suspensions obtained in these conditions have a relatively low monodispersity (Pdl = 0.2) in the entire concentration range we tested for each solvent. In particular, the 2-butanone and acetonitrile systems cause the formation of nanoparticles with average hydrodynamic diameters slightly higher than the ones usually obtained in 1 M acetic acid. Probably because of their much higher polarity, DMSO and DMF cause the formation of nanoparticles with average hydrodynamic diameters that are more similar to the ones obtained in the standard acetic acid conditions.

Table 3.2 DLS data measured for Pluronic F127 NPs (PluSNPs) in different organic solvent–Acetic acid 1M mixtures

Solvent	Solvent V/V ^a (%)	$d_H \pm SD^b$ (nm)	PDI	$d_H^c \pm SD$ (nm)
Acetic acid 1 M	0	21.2 ± 0.1	0.13	20.3 ± 0.2
2-Butanone	1.3	30 ± 1	0.13	23.2 ± 0.3
	5.2	36.3 ± 0.4	0.11	30 ± 1
	12.9	26.8 ± 0.4	0.15	23 ± 2
Acetonitrile	1.3	35.4 ± 0.2	0.25	34 ± 2
	5.2	31.3 ± 0.1	0.22	30 ± 1
	12.9	30.6 ± 0.4	0.22	29 ± 2
	38.7	— ^d	— ^d	— ^d
DMSO	1.3	36 ± 1	0.21	20 ± 1
	3.2	17.2 ± 0.3	0.21	15 ± 1
	5.2	26.6 ± 0.3	0.22	21.7 ± 0.4
	12.9	21.6 ± 0.2	0.22	20 ± 2
	16.1	24.0 ± 0.4	0.11	21.0 ± 0.3
DMF	38.7	24 ± 1	0.21	22 ± 1
	1.3	20.7 ± 0.3	0.18	19 ± 1
	5.2	26 ± 1	0.36	22 ± 1
	12.9	22 ± 2	0.22	20 ± 2
	38.7	21 ± 1	0.18	19 ± 2

V/V% concentration (the total volume for each solution was 3100 µL). ^bAverage hydrodynamic diameter distribution by intensity. ^c Average hydrodynamic diameter distribution by volume. ^d Data not available because of precipitation.

3.6.2 AIP induced by NPs: Asterisk@NPs

3.6.2.1 AIP process

Aggregation-induced emission is a phenomenon where a chromophore is not emissive in solution but highly emissive in the solid state or embedded in a rigid matrix. If the chromophore is phosphorescent in the aggregate state, the AIE phenomenon is called AIP. For AIE dyes diluted in solution, the excited state energy is dissipated through intramolecular motions to reduce drastically the emission, while in the aggregate or solid state, the intramolecular motions are restricted. Thus, the non-radiative deactivation pathways are reduced, so that emission is turned on. Although in many examples the contribution of intramolecular rotations has been highlighted in explaining their optical properties, other motions, such as vibrations (including bending, twisting, scissoring, etc.) should also be considered as they all consume the excited-state energy⁷². AIP is slightly different from the general AIE operating mechanisms, because not only restriction of intramolecular motions, which include intramolecular rotations and intramolecular vibrations are valid, but also quenching of the triplet state by dioxygen needs to be considered. The formation of aggregated structures limits the diffusion of dioxygen, thus suppressing this quenching pathway and increasing the phosphorescence quantum yield. This mechanism is common to all phosphorescent compounds, particularly for chromophores exhibiting long-lived phosphorescent excited states. There are several examples of AIP chromophores and we could divide them in metal complexes and organic compounds; in this thesis it will be shown the AIP of organic molecules. One of the strongest AIP chromophore in the solid state is hexakis(p-tolythio)benzene with a quantum yield near 1.0⁷³, a small benzene-cored organic molecule containing six thioether linkages (asterisk). This compound is not emissive in solution but is highly phosphorescent in a solid state or in a rigid matrix at 77 K.

3.6.3 Asterisk@NPs: Synthesis and photophysical characterization

Before the use of the new developed synthetic method of PluSNPs, the asterisk molecule (Fig 3.4), was synthesized after several synthetic steps, and photochemically characterized by M. Villa PhD from

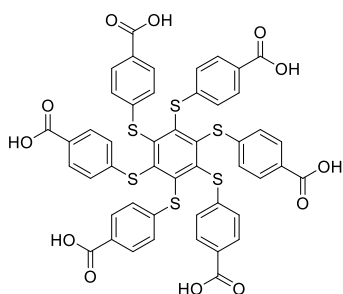


Figure 3.4 Asterisk molecule

P.Ceroni group. The molecule presents a λ_{MaxEM} as powder at 556 nm with a lifetime value of 9.4 μs and an emission quantum yield of 10%. To link covalently the molecule inside the silica core of the NPs, the molecule was modified using a coupling reaction with APTES ((3-Aminopropyl)triethoxysilane) involving CDMT (6-Chloro-2,4-dimethoxy-s-triazine)

and NMM (N-methyl-morpholine) as coupling reagents in DMF (see experimental section for the details). The ethoxysilane functionalized asterisk was precipitated with Et_2O and was characterized by IR spectroscopy (see experimental section). In the IR spectra the C=O stretching frequency change (1682.61 for blue line, 1634.92 for red line) indicated that the carboxylic acid moieties were efficiently converted into amide, since also the acid -OH stretching disappeared, confirming the complete transformation of the carboxylic acid groups (Fig 3.5)(Complete IR spectrum in the experimental section).

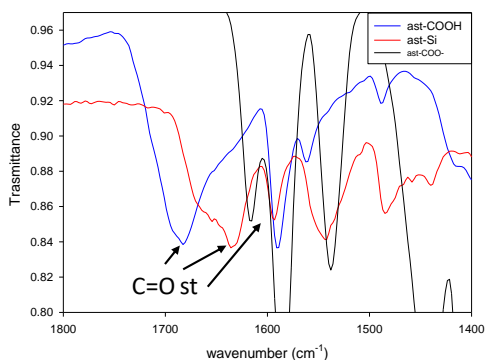


Figure 3.5 FTIR analysis on Silanized asterisk powder (red line), asterisk (blue line), deprotonated Asterisk (black line)

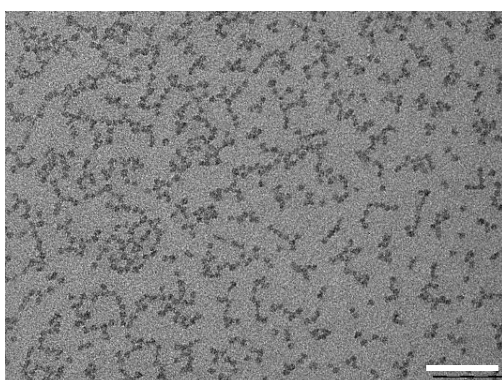
The ethoxysilane derivative of the asterisk was directly introduced inside the PF127 micelles using the modified method previously described, with the maximum possible amount of DMF with the silanization (38.7% v/v) reaction to obtain the silica NPs doped with the molecular asterisk **Asterisk@NPs** presenting different doping levels (0,1%, 0.3%, 0.5%, 1%) of the dye respect to the TEOS mol.



Figure 3.6 Photographs of asterisk@NPs suspension characterized by different doping levels of PhP (left to right: 0,1%, 0.3%, 0.5%, 1%). (left)

The **Asterisk@NPs** were purified by several days of dialysis versus water, obtaining monodisperse Plus NPs.

All doping levels NPs are been morphological characterized by TEM and DLS showed well PDI values in a range of 0.08-0.13 and a d_H range from 21-25 nm (Fig 3.7). TEM is reported only for 1% **Asterisk@NPs** sample because representative of all 4 NPs samples (all silica cores diameters dimension were reconducted by images extrapolation using ImageJ software between 9 and 11 nm).



	$d_H \pm SD$ (nm)	PDI
0.1%	21+1	0.22
0.3%	21.6+0.2	0.18
0.5%^a	23.7+0.4	0.22
1%	22+2	0.39

Figure 3.7 TEM image of Final Asterisk@NPs 1% scale bar 100nm, DLS analysis reported by volume.

These NPs were characterized in water by UV-Vis spectrophotometric analysis. The suspension of NPs in water at the end of the purification have a concentration of 20 μM ^{47,74}. The molar absorption coefficient has been determined by dilution of the stock solution and the number of dyes per NP was calculated by the ratio of the molar absorption coefficient of the **Asterisk@NPs** divided by the molar absorption coefficient of Asterisk molecule (Fig 3.8).

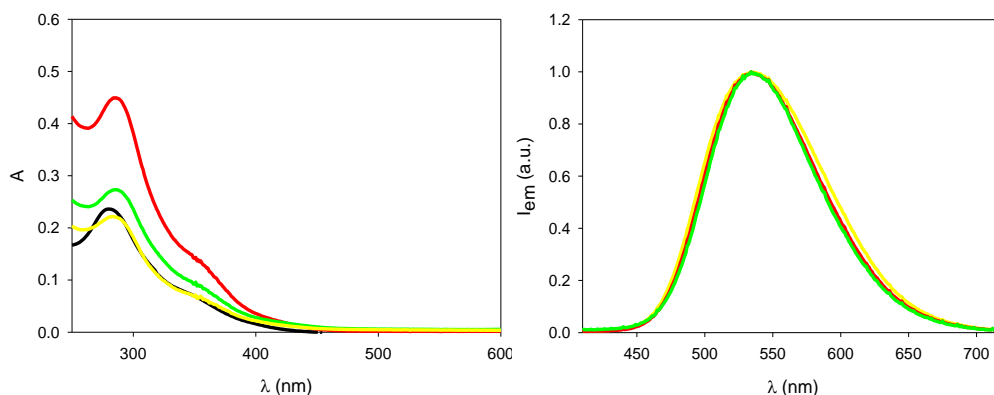


Figure 3.8 Absorption spectra and normalized emission spectra of Asterisk@NPs with 0.3% (yellow), 0.5% (green) and 1% (red) loading and deprotonated form of Asterisk (black) in water

As reported in the published paper⁷⁵, the **Asterisk@NPs** samples show absorption spectra that are very similar to the model compound **Asterisk**. The spectra show a band at 280 nm typical for molecules with phenyl groups as substituents. Also, the emission spectra are identical meaning that the different loading of the NPs doesn't affect the electronic state of the molecular asterisks. The average number of dyes embedded in the nanoparticle and that main photophysical properties for these samples is summarized in table 4. The phosphorescence lifetime of the NPs samples is very similar (14.5-14.8 μs) and the quantum yields are the same (7%) in air-equilibrated solutions. Since all the photophysical parameter are identical except the molar absorption coefficient, the 0.5% and 1% loading are the most interesting samples, obviously for the high number of dye/NP.

Table 3.3 Photophysical properties in air-equilibrated aqueous solution (unless otherwise noted)

	λ_{Max} EM/nm	Dyes/NPs	τ / μs	Φ_{em}
Asterisk@NPS 0.3%	538	19	14.5	7%
Asterisk@NPS 0.5%	540	23	14.8	7%
Asterisk@NPS 1%	536	38	14.7	7%
Asterisk@NPS 1% DEGAS	536	38	38.8	17%
Asterisk <i>in solution</i>	-	-	-	-
Asterisk as a powder ^a	556		9.4	10%

Plus NPs samples characterized by higher doping (1.5% and 2%), were affected by poor colloidal stability and they precipitated during the synthesis or after few days after dialysis. Since the highest value of doping was 1%, and this sample was very stable (more than 1 year), **Asterisk@NPs 1%** has been considered the most interesting system as potential oxygen sensor. The method used was the freeze pump technique; it has been removed oxygen from a sealed solution of **Asterisk@NPs 1%** and an increase of the phosphorescence occur, the quantum yield increases from 7% to 17% as well as the lifetime that increase from 14.7 to 37.4 μs (data not showed). Then the solution is left in air-equilibrated condition and emission spectra are recorded every 5 minutes to observe the decreasing of the emission that return to the initial value.

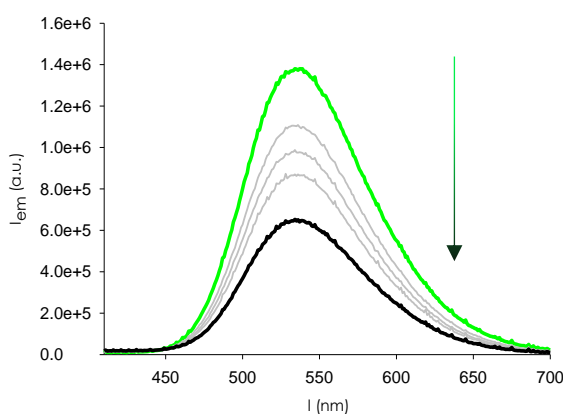


Figure 3.9 Emission spectra recorded every 30 minutes of Asterisk@NPs 1% when oxygen return to atmospheric pressure (air-equilibrated).

The system **Asterisk@NPs** as oxygen sensor, was studied by prof. S. Vinogradov and his group at the University of Pennsylvania (USA) Measurements were performed at two different temperatures: 22°C and 36.6°C (Fig. 3.10). The lifetime of the loaded NPs is recorded at different oxygen concentrations and the lifetime decreases increasing the oxygen concentration based on the Stern-Volmer equation:

$$\frac{\tau_0}{\tau} = 1 + k_q \tau_0 [O_2]$$

The K_q calculated at 22°C is $2 \times 10^7 \text{ M}^{-1} \text{ s}^{-1}$ and at 36.6°C is $1 \times 10^7 \text{ M}^{-1} \text{ s}^{-1}$. These two values are lower than the diffusion limit $1 \times 10^{10} \text{ M}^{-1} \text{ s}^{-1}$ meaning that the diffusion of oxygen to the dye through the PEG shell and into the silica NPs is slowed down. With this system a correlation of the lifetime of **Asterisk@NPs** and the oxygen concentration is possible and the system could have an application in bioimaging.

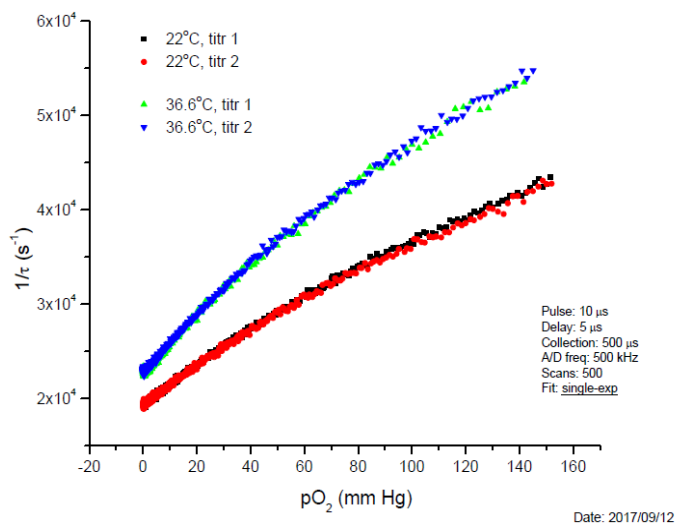


Figure 3.10 Oxygen titration by PhP -NPs 0.5% in aqueous solution

The group of Prof. Vinogradov investigated also the two-photon absorption (2PA) (see experimental section) properties of the system **Asterisk@NPs**. The idea is to use these NPs as dye for the two-photon excitation microscopy and map the oxygen

concentration in a tissue by changes in the lifetime. On system Asterisk@NPs 0.5% two photon absorption is recorded by luminescence intensity measurements⁷⁴¹ and the $\sigma(2)$ was calculated. The NPs show a high cross-section of 1000 GM (Goppert-Mayer, 10^{-50} molecule $\text{cm}^4 \text{s photon}^{-1}$) per nanoparticle at 700nm. The estimated value per dye is ca. 40GM at 700 nm. The system Asterisk@NPs is phosphorescent in air-equilibrated condition and could be used as oxygen sensor in the two-photon excitation microscopy. The oxygen concentration could be correlated to the lifetime of Asterisk (data not showed).

3.6.3 Oxygen chemosensors: Phorphyrins@NPs

The optimization of the synthesis of PluS-NPs in organic solvent/acetic acid mixture, pave the way for the development of new oxygen chemosensors based on Plus NPs doped with phosphorescent dyes characterized by poor solubility in water/surfactant mixtures such as porphyrins. These dyes are good candidates for the development of oxygen chemosensors for biomedical applications, because of their photophysical properties, and were extensively studied by the group of S. Vinogradov (UPenn, US) for the development of porphyrin-core PEGylated dendrimers. Among the solvent that were tested in the synthetic optimization described in paragraph 3.5.2., DMSO and DMF are probably the more interesting and versatile solvents to use. DMF in particular, have very high solubilization capability, and it is very often the solvent of choice to carry coupling reactions with carboxylated porphyrins. This kind of reaction is also needed to convert porphyrins bearing carboxylic groups to their alkoxy silane derivatives. For example, the coupling of carboxylated porphyrin with APTES, can be efficiently achieved using CDMT and NMM as coupling reagents (see experimental section). The possibility to prepare a porphyrin alkoxy silane derivative in situ in DMF, and to use it in the optimized PluS NPs synthesis is an extremely valuable feature, since the purification of alkoxy silane derivatized porphyrin is feasible only with tedious size exclusion or reverse fase chromatographic methods. To test this

approach in collaboration with prof. S. Vinogradov, I tested four different porphyrins to obtain the corresponding doped PluS NPs chemosensor.

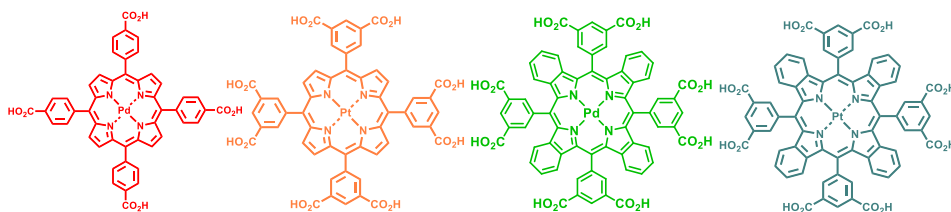


Figure 3.11 PdTCCP PtOCTP, PdOCTBP, and PtOCTBP porphyrins

P1 (PdTCCP), **P2** (PtOCTP), **P3** (PdOCTBP), and **P4** (PtOCTBP) were coupled to APTES following a recipe involving CDMT/NMM as coupling agent (Fig 3.12). The loading limit for these dyes inside the core of the PluS NPs was evaluated using the porphyrin **1**, since it is commercially available. The optimization of the NPs doping and of their brightness is important since too many dyes in each NP bring to self-quenching processes, that can decrease the average phosphorescent lifetime of the system and hence its dynamic range toward the detection of oxygen.

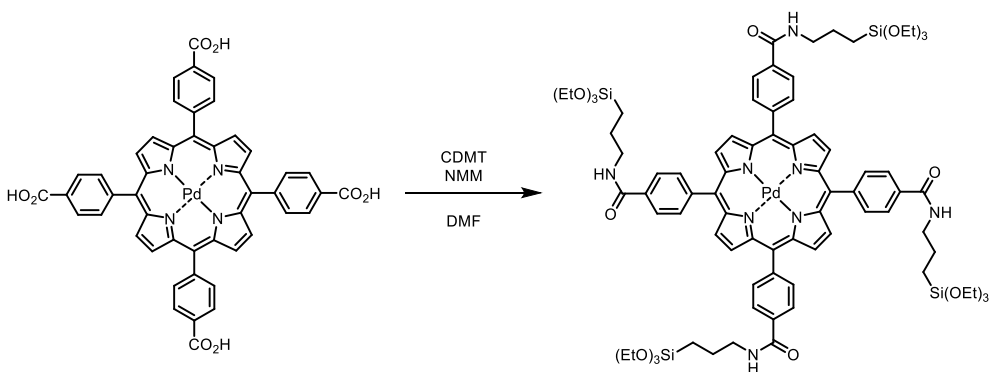


Figure 3.12 Coupling reaction of 1 for silanization

The doping of the NPs was investigated using a 0.1%, 0.5% and 1% in mol respect to the mol of TEOS. The hydrodynamic properties of the samples measured by DLS were good for the less doped samples, while in the higher doping regime precipitation of the nanoparticles occurred during the synthesis or just after dialysis purification. The morphological characterization performed by DLS analysis and by TEM microscopy (Fig. 3.13) showed uniform hydrodynamic diameters

and for the silica core diameters distributions. The doping degree of 0.5% was chosen for the construction of the other chemosensors.

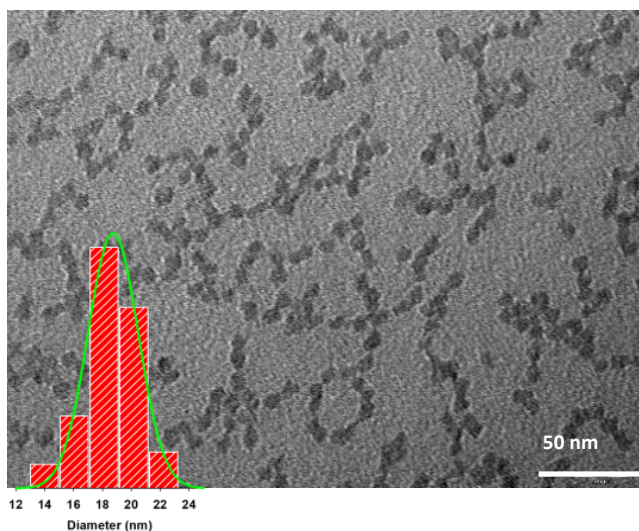


Figure 3.13 TEM and DLS analysis of 2@NPs

This is due to the fact that from DLS measurements, it has been noted the presence of aggregates around 200 nm (data not shown) and the number of the dye/NPs were similar found similar (measured as the ratio of the molar absorption coefficient of the Dye@NPs divided by the molar absorption coefficient of Dye, Table 3.5). The other 3 porphyrins were also silanized using the same synthetic protocol, adapting the number of APTES equivalents to the number of porphyrin carboxylic groups. The NPs synthesis were conducted using DMF (38.7 % v/v)/acetic acid 1M, adding the dye directly in surfactant solution. In Fig 3.13 is reported only the TEM image for the sample 2, because the similarity with the other 3 sample (11.2 ± 0.2 nm).

From TEM analysis it was confirmed the good monodispersity and the size of the silica core is in line with the already mentioned dimension obtained for general PluSNPs. In table 3.4 are reported the data of the d_H for all doped NPs.

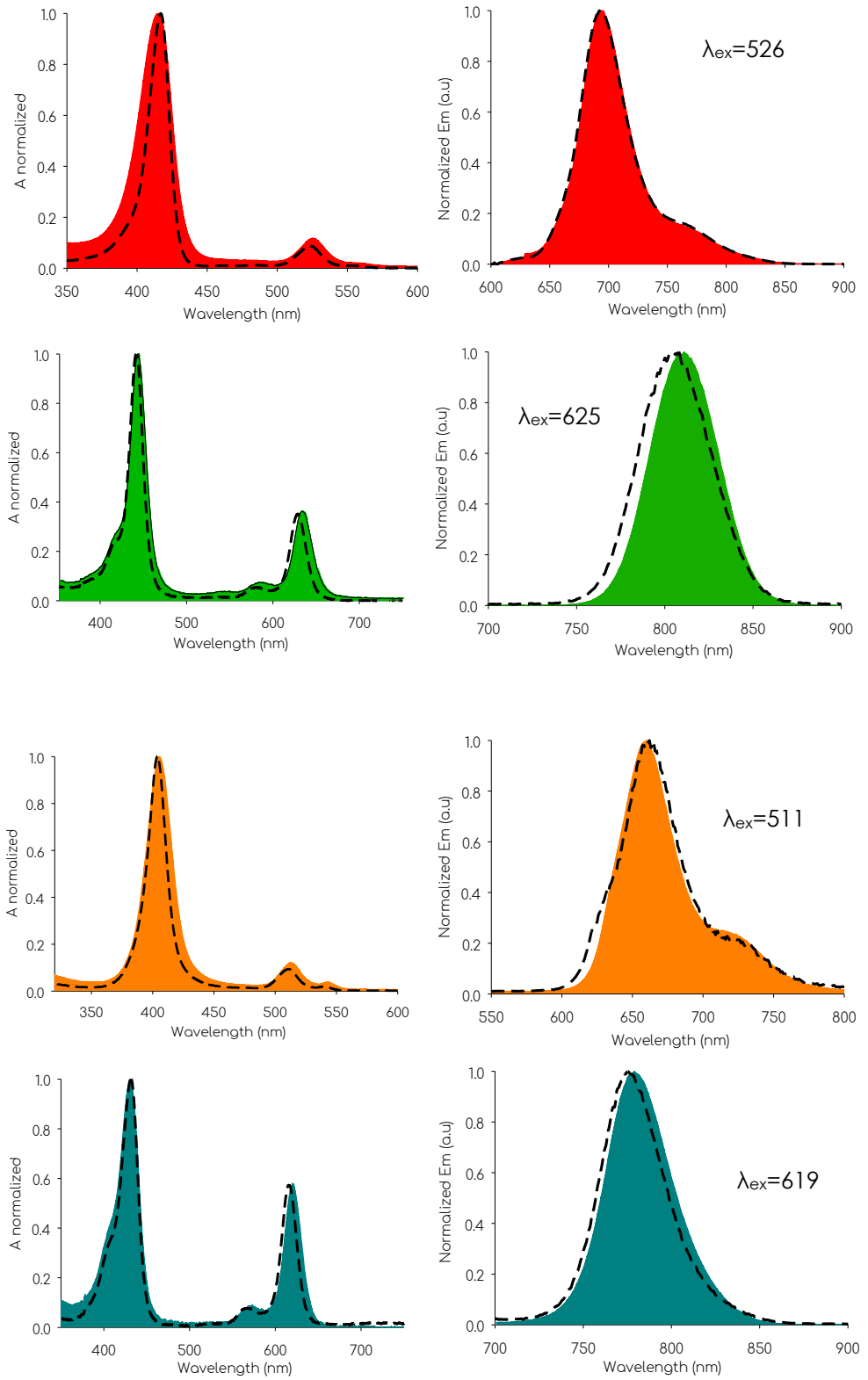
Table 3.4 DLS measurements for all doped NPs

	$d_H \pm SD$ (nm)	<i>PDI</i>	<i>TEM</i> (core d)
P1	21.7 \pm 6.1	0.14	12.1 \pm 0.4
P2	19.8 \pm 6.2	0.35	11.8 \pm 0.3
P3	26.9 \pm 7.1	0.36	11.2 \pm 0.2
P4	24.1 \pm 5.4	0.24	9.9 \pm 0.1

^aAverage hydrodynamic diameter distribution by volume

3
Once again, the DLS measurements are aligned with the classical d_H dimension expected for this type of NPs. The morphological characterization confirmed that the porphyrins dyes don't influence the synthesis. Then, it has been conducted the entire photophysical characterization in Fig. 3.14 are reported normalized absorption and emission spectra of NPs in water (filled spectra) and of respective porphyrins (dotted line) in THF solutions.

Figure 3.14 normalized absorption and emission spectra of all NPs in water (filled spectra) and of respective porphyrins (dotted line) in THF solutions.



From the normalized absorption and emission spectra it is possible to estimate how the behavior of the porphyrins free in solution is well maintained when they are bound inside the core of the NPs, in fact the shape of the peak in every case is very similar only a little bit enlarged in absorption for the NPs, due to their scattering in solution. Furthermore, despite the large number of dyes entrapped covalently inside the silica core (Tab 3.5), the absorption spectra of the NPs are very superimposable with the respective spectra of the dye free in solution.

A comparison between the phosphorescent properties of the porphyrin doped PluSNPs in aerated and deaerated conditions was made comparing air equilibrated PluS NPs samples or nanoparticles suspension deaerated by the *freeze pump* technique. The quantum yield of the PluS NPs samples has been measured and compared to the quantum yield of the corresponding carboxylated porphyrin in solution in deaerated and aerated conditions (Tab 3.5).

Table 3.5 Photophysical characterization of the 1@NPs 2@NPs 3@NPs 4@NPs and of the 1 2 3 4 complexes free in solution of THF

	P1	P1@NPs	P2	P2@Nps	P3	P3@NPs	P4	P4@NPs
λ_{abs} (nm)	415	406	401	401	438	439	429	429
ϵ_1 ($10^4 \text{ cm}^{-1}\text{M}^{-1}$)	39	2 90	24	4 70	12	1 90	12	230
λ_{abs} (nm)	526	526	511	511	625	629	615	619
ϵ_2 ($10^4 \text{ cm}^{-1}\text{M}^{-1}$)	3,5	375	19,5	52,5	4,6	75	7,9	1 05
I_{phosp} (nm)	688	703	654	664	805	810	773	778
N° Dye	--	11	--	27	--	17	--	14
Φ_{EM} DEGAS	2.3%	0.7%	1.8%	1%	1.3%	0.2%	2.4%	1.6%
Φ_{EM}	0.1%	0.3%	0.2%	0.5%	0.06%	0.15%	0.16%	0.4%
T DEGAS (ms)	0.310	0.091	0.026	0.053	0.193	0.153	0.046	0.040
T (ms)	-	0.030	0.001	0.002	0.008	0.063	0.010	0.017
B degas (ϵ_1)	8 970	20 300	4 320	47 000	1 560	38 000	2 880	36 800
B (ϵ_2)	3 90	8 700	480	23 500	72	2 850	192	920

^aBrightness (B) defines as $\epsilon \cdot \Phi^{76}$

In general, the shape and position of the absorption and of the fluorescence bands of the dyes in the NPs are very similar (as shown in Fig 3.14 and table 5) to the ones of the free luminophores in THF solution (as could be expected for a transition mostly $\pi-\pi^*$ in nature) presenting only very small red shifts, evidencing once again that the behavior of the dyes don't change once internalized inside the silica core. Each NP entraps several dyes (in a range from 11 to 27), and this confers a very high absorption coefficient and overall brightness to these materials. Comparing the emission quantum yields of the deaerated solution of the dyes dissolved in THF respect their behavior inside NPs in water solution, it is clear how the results were very interesting. Indeed, as shown better in Fig 3.15 below, it is obvious how porphyrins inside NPs maintains their increasing in phosphorescence in deaerated solutions (full cylinders) and are quenched in emission when the oxygen was equilibrated again in solutions. It was not granted, because the dyes could have different response to the oxygen due to their position inside the silica core.

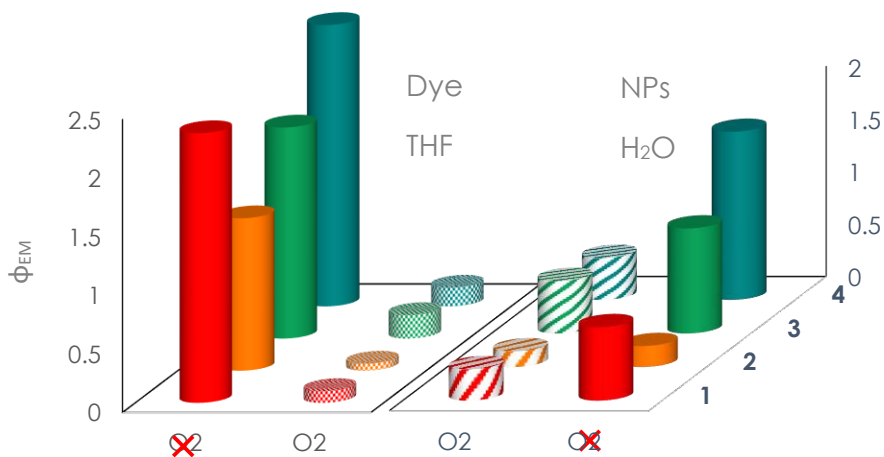


Figure 3.15 Chart of comparison between Dye free in solution aerated and deaerate, respect Dye@NPs deaerated/aerated.

The emission quantum yield for the NPs were in general low than the respective dye free in THF solution (see table 3.5), but this fact could depend from the structure of the NPs: infact, firstly the shell, then the silica core, could make more difficult the diffusion of the oxygen inside the NP. This hypothesis is confirmed also from the behavior of the oxygenated

solutions. Undeniably, most important effect to evaluate is the differences between aerated solutions: the fluorophores free in solution are completely quenched by the presence of the oxygen, while when they are inside the silica core of the NPs, they present visible phosphorescence, even maintaining their increasing when deaerated from the O₂. This is a powerful result for a chemosensor, because its possibility to be phosphorescence since the administration and increase its emission when in hypoxic environment.

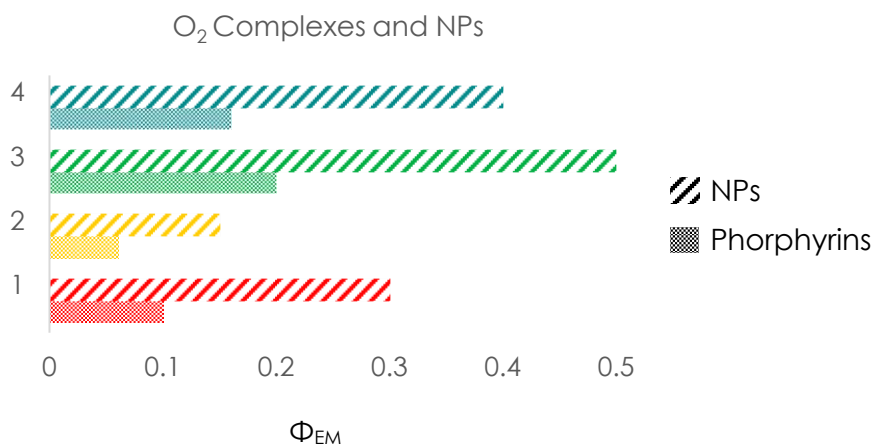


Figure 3.16 Comparison between NPs and corrispective phorphyrins in aerated condition

These very promising preliminary results were finally used to produce a Plus NPs oxygen chemosensor containing a much more sophisticated metal porphyrin, developed by Prof. Vinogradov. Porphyrin core dendrimer containing this porphyrin (PtTAPIP, Fig. 3.17) were recently developed for in vivo imaging on mouse, using a two-photon laser scanning fluorescence microscopy technique (2PLSM)³ in collaboration with Prof. B. Weber at University of Zurich. The alkoxyisane derivative of PtTAPIP was obtained by amide coupling with APTES using CDMT/NMM, as already described.

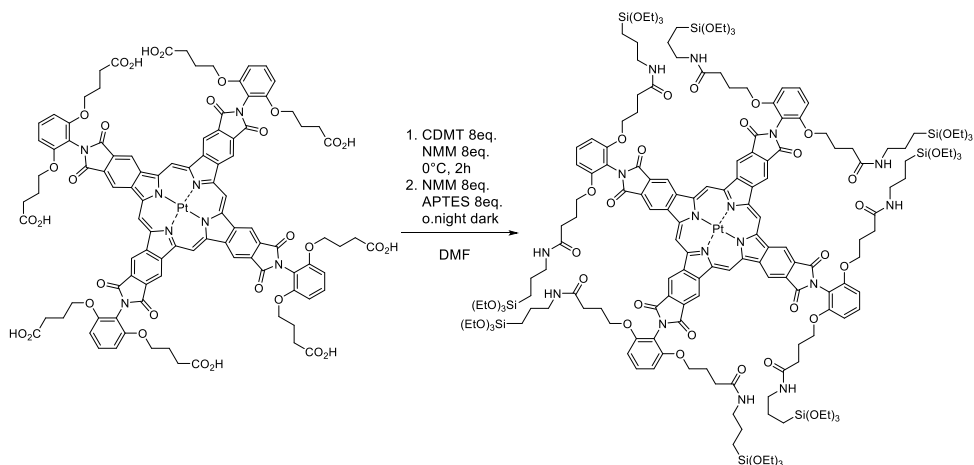


Figure 3.17 Schematic representation of PtTAPIP silanization synthesis

The ethoxysilane derivative of PtTAPIP was directly used for the PtSNPs synthesis using a DMF/acetic acid 1M mixture (% v/v), with amount of dye corresponding to doping level of 0.1, 0.5, 1.0% mol. All the systems after synthesis and dialysis purification showed good hydrodynamic characteristics (Fig. 3.18).

Loading	$d_H \pm SD$	PDI
0.1%	21.6 \pm 5.5	0.131
0.3%	19.4 \pm 5.5	0.294
0.5%	19.6 \pm 6	0.174



Figure 3.18 DLS values for 3 different NPs@PtTAPIP batches in different loading of dye respect TEOS mol (left). Visible monodispersity of NPs in all three synthesis

From the photophysical point of view however, these samples showed a low enhancement in emission when in deaerated condition, due to self-quenching processes occurring within the nanoparticles. Infact the increasing in emission in deoxygenated solution respect to the oxygenated was worst respect to the all other 4 chemosensors studied (data non shown). In the Fig. 3.19 is reported a practical visualization of the ratio between $\Phi_{EmDeaerated}/\Phi_{EmAerated}$ **PtTAPIP@NPs 0.5%, 0.3%** and **0.1%** and **P4@NPs** for comparison which shows the low response of that PtTAPIP@NPs systems respect the abovementioned 4 chemosensors. This phenomenon is probably caused by the formation of porphyrin aggregates.

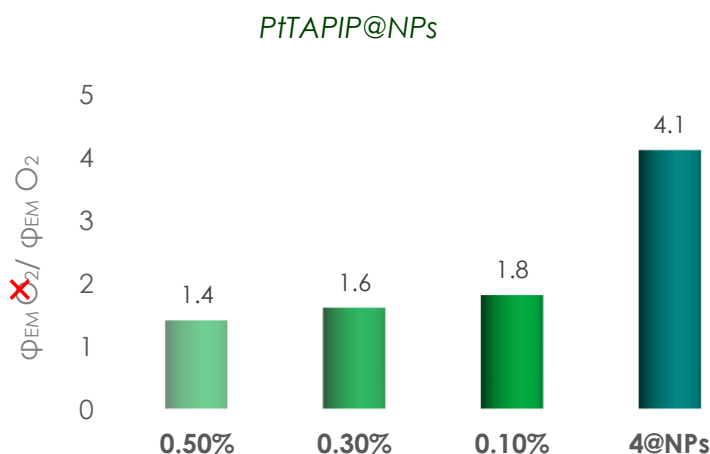


Figure 3.19 Ratio between emission quantum yield deaerated/aerated for PtTAPIP@NPs 0,5%, 0,3% and 0,1% in loading respect TEOS mol (green bars)

For this reason, a set of samples with lower doping levels were synthesized, in order to increase the emission properties of the systems. In these new samples the level of doping of the silanized PtTAPIP respect to the TEOS mol was decreased to 0.05% mol and 0.025% mol. The morphology was again characterized by TEM and DLS measurements giving good results in terms of monodispersity as shown in Fig 3.20.

Table 3.6 DLS measurements of PtTAPIP@NPs 0.05% and 0.025% loaded

Loading	$d_H \pm SD$	PDI
0.05%	25.7±4.1	0.09
0.025%	24.8±5.2	0.10

^aAverage hydrodynamic diameter distribution by volume

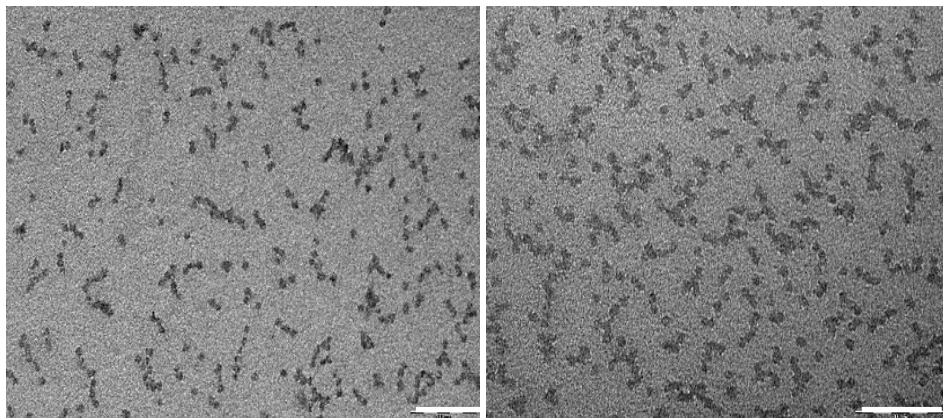


Figure 3.20 TEM analysis of PtTAPIP@NPs left 0.05% and 0.025% loading right. Scale bar 100nm

The conformational analysis confirmed by TEM the monodispersity and the core dimension around 11 nm, followed by a DLS data reporting d_H around 25 nm for both different batches.

The photophysical characterization was performed in the new PtTAPIP@NPs less doped and showed in Fig 3.21.

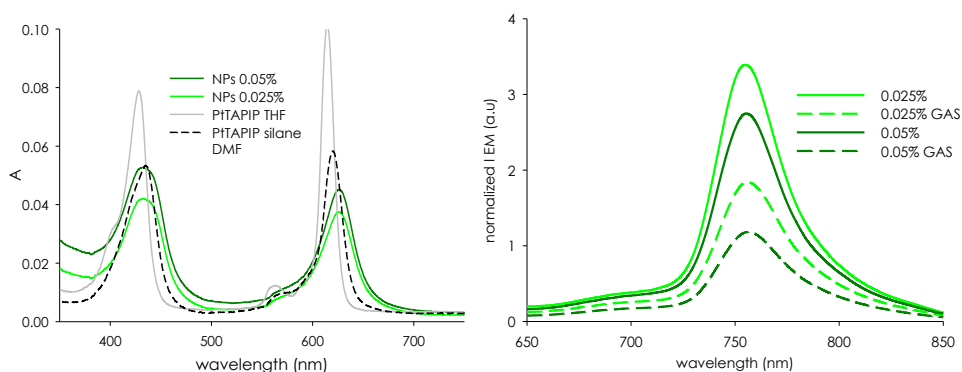


Figure 3.21 LEFT: Absorption spectra of PtTAPIP@NPs 0.05% dark green, 0.025% light green; PtTAPIP free in THF solution gray line and in dotted black silanized PtTAPIP in DMF. RIGHT: Emission spectra of PtTAPIP@NPs aerated solution dotted line, PtTAPIP@NPs deaerated solution solid line (light green 0.025% dark green 0.05%). The value of doping are in mole respect to the mol of the TEOS

The absorption spectra of the PtTAPIP@NPs for both loading levels show a little blue shift (<10nm) respect to the PtTAPIP free in THF and silanized, results in trend with the change of the solvent. The decreasing of loading percentage clearly has led to less aggregates, which caused a

brightness increase when they are in deoxygenated solution. Infact the $\Phi_{EmDeareated}/\Phi_{EmAreated}$ values were increased to 2.0 for PtTAPIP@NPs 0.05% mol and to 2.4 for PtTAPIP@NPs 0.025% mol respect to the data reported in Fig 3.18.

In collaboration with Prof. S. Vinogradov were performed oxygen titrations in the less doped sample, which presented best emission as shown in Fig 3.21 and good $\Phi_{EmDeareated}/\Phi_{EmAreated}$. All experiments were performed using a solution of NPs in phosphate buffer 20 mM 0.1 μ M, pH 7.1-7.2. A small volume of the stock solution of NPs was added to the buffer, equilibrated on air under gentle stirring, until the phosphorescence lifetime and the readings of the oxygen electrode became stable. Fig 3.22 reports the comparison among 3 different titrations on the sample 0.025%.

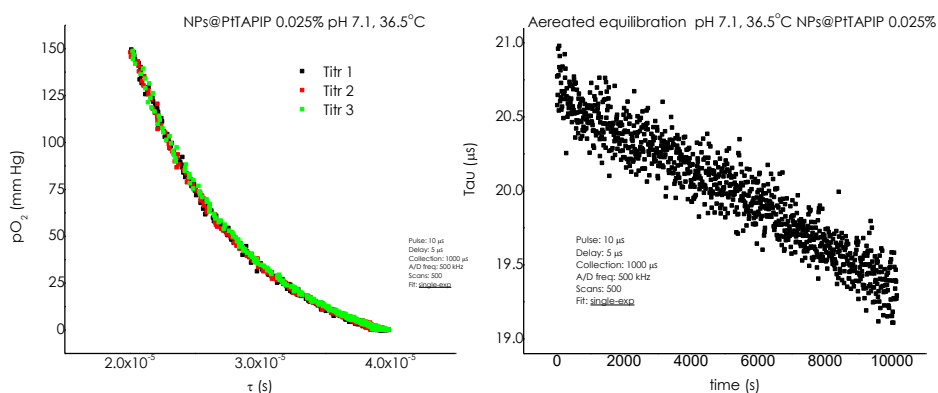


Figure 3.22 Oxygen titration of PtTAPIP@NPs 0.025% in aqueous solution (left), fluctuations of lifetimes values measurements over the time.

Fig 3.22 shows a reproducible behavior, but a quite limited dynamic range for the measurements, that is strongly influenced by the value of the pristine lifetime in oxygenated conditions. As it is possible to see from the Fig 3.22 right, the lifetime in physiological conditions has a drift around 2 μ s which is considerable value for *in vivo* experiments. Even in the presence of this limitation, the probe was tested *in vivo* to compare it with the previous studies by Prof. S. Vinogradov group concerning the same porphyrin but as PEG-dendrimers⁷⁷.

3.6 Biological assays@Zurich University

Professor Vinogradov in collaboration with prof. B. Weber from the Neuroscience Center of the University of Zurich (Switzerland) have recently proposed a new fully PEGylated dendritic oxygen probe that enables oxygen microscopy in tissues. Quantitative imaging of oxygen distributions in tissue is fundamental to get information about metabolism in normal and diseased states. As proof of principle, they monitored oxygen dynamics for days *in vivo* after inducing micro-stroke by occlusion of a single capillary in a mouse brain. To this goal, they optimized a setup based on two-photon phosphorescence lifetime microscopy (2PLM) to perform measurements of oxygen *in vivo* with micronscale resolution in 3D. The results were extremely promising, however, the method's potential to be fully realized needs a great step forward in the current phosphorescent probe technology. In fact, present phosphorescent probes are often non-biocompatible and/or require great synthetic efforts.

It has been therefore investigated if the doped PluSNPs described in this chapter, and in particular PtTAPIP@NPs, could be a valid alternative as phosphorescent probes for the same application, being much more versatile platforms, relatively easy and cheap to prepare and biocompatible. I joined the Professor Weber's group for a few days, and we performed some *in vivo* experiments following the same procedures already tested for the previous PEGylated dendritic oxygen probe prepared by professor Vinogradov.

The key imaging parameters *in vivo* are speed and depth, since a fast response to the oxygen changes and deep imaging are critical⁷⁸. Moreover, intravascular measurements are much less invasive than extravascular ones, since the probe can be injected far away from the measurement site (e.g., into the tail vein) and it distributes throughout the entire body. Generally, its concentration in the measurement medium (blood plasma) is uniform, facilitating accurate comparison of the signals acquired at different imaging depths.

The first investigation that we performed aimed to determine if PtTAPIP@NPs injected into the tail vein would allow the signal monitoring in time, in mouse brain, without having to inject the probe directly into the imaged region. The most important feature to measure was the possibility to detect the signal in depth and until which depth. We did preliminary tests injecting PtTAPIP@NPs in a concentration of circa 10 μ M

and only few minutes were needed to perform the measurements *in vivo* in the brain. Quite remarkably this first attempts were done using a very high particle concentration (the solution was almost dense), nevertheless it did not cause any evident negative consequence to the mouse and it was urinary excreted very efficiently in circa 24 hours. A first (not exhaustive) investigation of the mouse health in the next days after injection indicates a benign nature of the probe, in line with all the experimental evidences collected until now on the non-toxic nature of PLuS NPs⁵⁶.

The phosphorescence intensity decays measured e Cortical Surface at increasing depths (Fig. 3.23) show that the phosphorescence signal of this probe is detectable up to 400 μm below the tissue surface. This value is lower in comparison with the 600 μm of the PEGylated dendritic oxygen probe prepared by professor Vinogradov, but higher than the 300 μm previously possible with other probes. It has to be underlined that this is really remarkably for a very first attempt with a non-optimized NP and protocol. These data are very encouraging for the development of these materials as very promising probes for *in vivo* oxygen detection. Unfortunately, as mentioned in the previous paragraph, the first formulation of the PtTAPIP@NPs presented a drift in the lifetime in physiological conditions of a non-negligible value for *in vivo* applications (circa 2 ms). Further quantitative investigation *in vivo* with this NP sample was prevented by this limitation. However, a parallel research effort has been devoted to the optimization of the synthetic steps of the PtTAPIP@NPs and very preliminary results show a good stability of the phosphorescent lifetime signal in the new particles with the modified formulation (data not show in this thesis) that will be tested in due course.

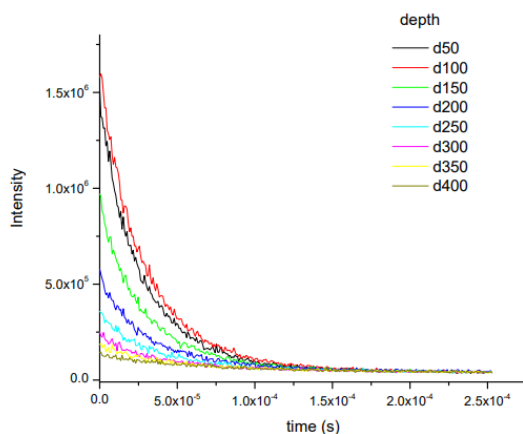


Figure 3.23 phosphorescence decays changed with depth in the diving artery

3.7 Conclusions and future steps

The achievements described in this chapter are more than one starting from a new synthetic path that allows to prepare luminescent silica NPs in organic solvent–water mixtures by using a template-assisted method based on Pluronic F127 micelles. We found that Pluronic F127 aggregates maintain their hydrodynamic properties in water mixtures containing a large amount (up to 40% v/v) of water-soluble organic solvents such as DMSO, DMF, acetonitrile or 2-butanone and, consequently, their capability to act as templates for the formation of silica NPs with uniform size, with a hydrodynamic diameter of 25–30 nm. We have demonstrated the feasibility of this approach for the fabrication of silica NPs doped with doping dyes presenting high hydrophobicity and high propensity for aggregation. With this method, it is possible to perform functionalization of the dye with alkoxy silane groups in a strong solubilizing solvent such as DMF, and to directly use this reaction mixture in a one-pot procedure, avoiding the problematic step of purification and isolation of the luminescent silanized species.

This important result has taken to the preparation of very promising nanostructured phosphorescent chemosensors for molecular oxygen via emission quenching, including sensing coupled to two-photon excitation. They are based on different active units but all of them

present appropriate features for oxygen sensing in the physiological pO_2 range.

The first one described is based on persulfurated asterisks that are an example of all-organic chromophores with luminescence induced by environment rigidification. Inclusion of the asterisks into the core of PLuS NPs provides a useful method for switching on their phosphorescence at room temperature and take the all-organic phosphorescent chromophores in water. This system may be an alternative to commonly used oxygen probes based on metal-containing chromophores.

The second class of oxygen chemosensors that I have prepared and studied contains different metallo-porphyrin dyes. These NPs present properties that are compatible with oxygen sensing in biological environments, i.e., high colloidal stability, appropriate brightness, and efficient shielding from oxygen. They were tested in solution giving very promising results in terms of sensitivity and maintaining a residual luminescence that would allow their contemporary imaging. Very interestingly, a pilot test, in collaboration with Professor B. Weber from the Neuroscience Center of the University of Zurich, injecting into the tail vein PtTAPIP@NPs allowed the phosphorescent signal monitoring in time, in mouse brain, without having to inject the probe directly into the imaged region. A very high particle concentration solution was injected nevertheless it did not cause any evident negative consequence in the mouse and the NPs were urinary excreted very efficiently in circa 24 hours, an evidence in favor of their benign nature. The phosphorescence intensity decays were measured at increasing depths and the signal was detectable up to 400 μm below the tissue surface. This value is higher than the 300 μm previously possible with other probes (with the only exception of the one recently prepared by professor Vinogradov and already presented in this chapter), a remarkable achievement for a very preliminary test using not yet optimized NPs and protocols.

These data are very encouraging for the further development of these materials as probes for *in vivo* oxygen detection.

Chapter based on results published in the papers *J. Phys. Chem. C* 2019, 123, 49, 29884-29890 and *Photochem. Photobiol. Sci.*, 2019, 18, 2142-2149

-
- 1 T. V Esipova, S. A. Vinogradov, *J. Org. Chem.* **2014**, 79, 8812.
 - 2 D. A. Tomalia, H. Baker, J. Dewald, M. Hall, G. Kallos, S. Martin, J. Roeck, J. Ryder, P. Smith, *Polym. J.* **1985**, 17, 117.
 - 3 J. M. Mayrhofer, F. Haiss, D. Haenni, S. Weber, M. Zuend, M. J. P. Barrett, K. D. Ferrari, P. Maechler, A. S. Saab, J. L. Stobart, M. T. Wyss, H. Johannssen, H. Osswald, L. M. Palmer, V. Revol, C.-D. Schuh, C. Urban, A. Hall, M. E. Larkum, E. Rutz-Innerhofer, H. U. Zeilhofer, U. Ziegler, B. Weber, *Biomed. Opt. Express* **2015**, 6, 4228.
 - 4 S. A. Vinogradov, L. W. Lo, W. T. Jenkins, S. M. Evans, C. Koch, D. F. Wilson, *Biophys. J.* **1996**, 70, 1609.
 - 5 U. K. Tirlapur, K. König, C. Peuckert, R. Krieg, K.-J. Halbhuber, *Exp. Cell Res.* **2001**, 263, 88.
 - 6 O. S. Finikova, T. Troxler, A. Senes, W. F. DeGrado, R. M. Hochstrasser, S. A. Vinogradov, *J. Phys. Chem. A* **2007**, 111, 6977.
 - 7 E. G. Mik, T. G. van Leeuwen, N. J. Raat, C. Ince, *J. Appl. Physiol.* **2004**, 97, 1962.
 - 8 T. V Esipova, H. J. Rivera-Jacquez, B. Weber, A. E. Masunov, S. A. Vinogradov, *J. Am. Chem. Soc.* **2016**, 138, 15648.
 - 9 R. P. Briñas, T. Troxler, R. M. Hochstrasser, S. A. Vinogradov, *J. Am. Chem. Soc.* **2005**, 127, 11851.
 - 10 R. Carter, *J. R. Soc. Med.* **2003**, 96, 46.
 - 11 R. S. MULLIKEN, *Nature* **1928**, 122, 505.
 - 12 R. D. Scurlock, B. Wang, P. R. Ogilby, *J. Am. Chem. Soc.* **1996**, 118, 388.
 - 13 M. Bodesheim, R. Schmidt, *J. Phys. Chem. A* **1997**, 101, 5672.
 - 14 C. S. Foote, *Acc. Chem. Res.* **1968**, 1, 104.
 - 15 W. Adam, D. V Kazakov, V. P. Kazakov, *Chem. Rev.* **2005**, 105, 3371.
 - 16 E. S. Gonçalves, P. R. Ogilby, *Langmuir* **2008**, 24, 9056.
 - 17 M. J. Davies, *Biochem. Biophys. Res. Commun.* **2003**, 305, 761.
 - 18 J. M. Fernandez, M. D. Bilgin, L. I. Grossweiner, *J. Photochem. Photobiol. B Biol.* **1997**, 37, 131.
 - 19 K. Plaetzer, B. Krammer, J. Berlanda, F. Berr, T. Kiesslich, *Lasers Med. Sci.* **2009**, 24, 259.
 - 20 J. P. Kehr, *Toxicology* **2000**, 149, 43.
 - 21 C. S. Foote, *Photochem. Photobiol.* **1991**, 54, 659.
 - 22 K. R. Weishaupt, C. J. Gomer, T. J. Dougherty, *Cancer Res.* **1976**, 36, 2326 LP.
 - 23 5924 Descalzo, A. B., Martnez-Mez, R., Sancenn, F., Hoffmann, K., and Rurack, K. *Angew. Chem., Int. Ed.* 2006, 45, .
 - 24 R. Pinalli, M. Suman, E. Dalcanale, *European J. Org. Chem.* **2004**, 2004, 451.
 - 25 D. R. Larson, H. Ow, H. D. Vishwasrao, A. A. Heikal, U. Wiesner, W. W. Webb, *Chem. Mater.* **2008**, 20, 2677.
 - 26 L. M. Rossi, L. Shi, F. H. Quina, Z. Rosenzweig, *Langmuir* **2005**, 21, 4277.
 - 27 E. Rampazzo, S. Bonacchi, M. Montalti, L. Prodi, N. Zaccheroni, *J. Am. Chem. Soc.* **2007**, 129, 14251.

- 28 M. Montalti, L. Prodi, N. Zaccheroni, G. Battistini, S. Marcuz, F. Mancin, E. Rampazzo, U. Tonellato, *Langmuir* **2006**, *22*, 5877.
- 29 H. Yu, M. Chen, P. M. Rice, S. X. Wang, R. L. White, S. Sun, *Nano Lett.* **2005**, *5*, 379.
- 30 J.-M. Lehn, *Chem. – A Eur. J.* **1999**, *5*, 2455.
- 31 M. Grabolle, M. Spieles, V. Lesnyak, N. Gaponik, A. Eychmüller, U. Resch-Genger, *Anal. Chem.* **2009**, *81*, 6285.
- 32 A. Burns, H. Ow, U. Wiesner, *Chem. Soc. Rev.* **2006**, *35*, 1028.
- 33 L. Wang, C. Lofton, M. Popp, W. Tan, *Bioconjug. Chem.* **2007**, *18*, 610.
- 34 W. Wu, S. Zhou, *Nano Rev.* **2010**, *1*, 10.3402/nano.v1i0.5730.
- 35 A. Pedone, G. Prampolini, S. Monti, V. Barone, *Chem. Mater.* **2011**, *23*, 5016.
- 36 D. Genovese, M. Montalti, L. Prodi, E. Rampazzo, N. Zaccheroni, O. Tomic, K. Altenhöner, F. May, J. Mattay, *Chem. Commun.* **2011**, *47*, 10975.
- 37 L. L. Hench, J. K. West, *Chem. Rev.* **1990**, *90*, 33.
- 38 S. Zanarini, E. Rampazzo, L. Della Ciana, M. Marcaccio, E. Marzocchi, M. Montalti, F. Paolucci, L. Prodi, *J. Am. Chem. Soc.* **2009**, *131*, 2260.
- 39 R. P. Bagwe, C. Yang, L. R. Hilliard, W. Tan, *Langmuir* **2004**, *20*, 8336.
- 40 S. Zanarini, E. Rampazzo, S. Bonacchi, R. Juris, M. Marcaccio, M. Montalti, F. Paolucci, L. Prodi, *J. Am. Chem. Soc.* **2009**, *131*, 14208.
- 41 A. Van Blaaderen, A. Imhof, W. Hage, A. Vrij, *Langmuir* **1992**, *8*, 1514.
- 42 N. A. M. Verhaegh, A. van Blaaderen, *Langmuir* **1994**, *10*, 1427.
- 43 W. Stöber, A. Fink, E. Bohn, *J. Colloid Interface Sci.* **1968**, *26*, 62.
- 44 A. Van Blaaderen, A. Vrij, *Langmuir* **1992**, *8*, 2921.
- 45 A. van Blaaderen, A. Vrij, *J. Colloid Interface Sci.* **1993**, *156*, 1.
- 46 B. L. Cushing, V. L. Kolesnichenko, C. J. O'Connor, *Chem. Rev.* **2004**, *104*, 3893.
- 47 E. Rampazzo, S. Bonacchi, R. Juris, M. Montalti, D. Genovese, N. Zaccheroni, L. Prodi, D. C. Rambaldi, A. Zattoni, P. Reschiglian, *J. Phys. Chem. B* **2010**, *114*, 14605.
- 48 R. P. Bagwe, L. R. Hilliard, W. Tan, *Langmuir* **2006**, *22*, 4357.
- 49 F. J. Arriagada, K. Osseo-Asare, *J. Colloid Interface Sci.* **1995**, *170*, 8.
- 50 X. Zhao, R. P. Bagwe, W. Tan, *Adv. Mater.* **2004**, *16*, 173.
- 51 R. Kumar, I. Roy, T. Y. Ohulchanskyy, L. N. Goswami, A. C. Bonoiu, E. J. Bergey, K. M. Trampusch, A. Maitra, P. N. Prasad, *ACS Nano* **2008**, *2*, 449.
- 52 M. Montalti, L. Prodi, E. Rampazzo, N. Zaccheroni, *Chem. Soc. Rev.* **2014**, *43*, 4243.
- 53 M. Montalti, L. Prodi, E. Rampazzo, N. Zaccheroni, *Chem. Soc. Rev.* **2014**, *43*, 4243.
- 54 S. Kim, H. Huang, H. E. Pudavar, Y. Cui, P. N. Prasad, *Chem. Mater.* **2007**, *19*, 5650.
- 55 S. Kim, T. Y. Ohulchanskyy, H. E. Pudavar, R. K. Pandey, P. N. Prasad, *J. Am. Chem. Soc.* **2007**, *129*, 2669.
- 56 E. Rampazzo, R. Voltan, L. Petrizza, N. Zaccheroni, L. Prodi, F. Casciano, G. Zauli, P. Secchiero, *Nanoscale* **2013**, *5*, 7897.
- 57 E. Rampazzo, F. Boschi, S. Bonacchi, R. Juris, M. Montalti, N. Zaccheroni,

- L. Prodi, L. Calderan, B. Rossi, S. Becchi, A. Sbarbati, *Nanoscale* **2012**, *4*, 824.
- 58 M. Helle, E. Rampazzo, M. Monchanin, F. Marchal, F. Guillemin, S. Bonacchi, F. Salis, L. Prodi, L. Bezdetnaya, *ACS Nano* **2013**, *7*, 8645.
- 59 S. Biffi, L. Petrizza, C. Garrovo, E. Rampazzo, L. Andolfi, P. Giustetto, I. Nikolov, G. Kurdi, M. B. Danailov, G. Zauli, P. Secchiero, L. Prodi, *Int. J. Nanomedicine* **2016**, *11*, 4865.
- 60 E. Rampazzo, S. Bonacchi, R. Juris, D. Genovese, L. Prodi, N. Zaccheroni, M. Montalti, *Chem. – A Eur. J.* **2018**, *24*, 16743.
- 61 G. Valenti, E. Rampazzo, S. Bonacchi, L. Petrizza, M. Marcaccio, M. Montalti, L. Prodi, F. Paolucci, *J. Am. Chem. Soc.* **2016**, *138*, 15935.
- 62 W. L. Rumsey, J. M. Vanderkooi, D. F. Wilson, *Science (80-.)*. **1988**, *241*, 1649.
- 63 T. V. Esipova, S. A. Vinogradov, *J. Org. Chem.* **2014**, *79*, 8812.
- 64 J. S. Lindsey, I. C. Schreiman, H. C. Hsu, P. C. Kearney, A. M. Marguerettaz, *J. Org. Chem.* **1987**, *52*, 827.
- 65 H. G. Jeong, M. S. Choi, *Isr. J. Chem.* **2016**, *56*, 110.
- 66 E. Stulz, *Acc. Chem. Res.* **2017**, *50*, 823.
- 67 A. Y. Lebedev, A. V. Cheprakov, S. Sakadzic, D. A. Boas, D. F. Wilson, S. A. Vinogradov, *ACS Appl. Mater. Interfaces* **2009**, *1*, 1292.
- 68 T. V. Esipova, A. Karagodov, J. Miller, D. F. Wilson, T. M. Busch, S. A. Vinogradov, *Anal. Chem.* **2011**, *83*, 8756.
- 69 O. S. Finikova, A. Y. Lebedev, A. Aprelev, T. Troxler, F. Gao, C. Garnacho, S. Muro, R. M. Hochstrasser, S. A. Vinogradov, *ChemPhysChem* **2008**, *9*, 1673.
- 70 S. Bonacchi, D. Genovese, R. Juris, M. Montalti, L. Prodi, E. Rampazzo, N. Zaccheroni, *Angew. Chemie Int. Ed.* **2011**, *50*, 4056.
- 71 M. Soster, R. Juris, S. Bonacchi, D. Genovese, M. Montalti, E. Rampazzo, N. Zaccheroni, P. Garagnani, F. Bussolino, L. Prodi, *Int. J. Nanomedicine* **2012**, *7*, 4797.
- 72 J. Mei, Y. Hong, J. W. Y. Lam, A. Qin, Y. Tang, B. Z. Tang, *Adv. Mater.* **2014**, *26*, 5429.
- 73 G. Bergamini, A. Fermi, C. Botta, U. Giovanella, S. Di Motta, F. Negri, R. Peresutti, M. Gingras, P. Ceroni, *J. Mater. Chem. C* **2013**, *1*, 2717.
- 74 M. Montalti, L. Prodi, N. Zaccheroni, A. Zattoni, P. Reschiglian, G. Falini, *Langmuir* **2004**, *20*, 2989.
- 75 M. Villa, B. Del Secco, L. Ravotto, M. Roy, E. Rampazzo, N. Zaccheroni, L. Prodi, M. Gingras, S. A. Vinogradov, P. Ceroni, *J. Phys. Chem. C* **2019**, *123*, 29884.
- 76 L. Prodi, *New J. Chem.* **2005**, *29*, 20.
- 77 T. V. Esipova, M. J. P. Barrett, E. Erlebach, A. E. Masunov, B. Weber, S. A. Vinogradov, *Cell Metab.* **2019**, *29*, 736.
- 78 B. Weber, A. L. Keller, J. Reichold, N. K. Logothetis, *Cereb. cortex* **2008**, *18*, 2318.

CAP. 4

ACTIVE MORPHOLOGICAL COLLOIDS FOR PROBING AND TAILORING INTRACELLULAR ANTIGEN PROCESSING

Is the shape of synthetic microarchitecture important for the interactions with human cellular membranes? This is the question at the basis of my research project that I carried out during my internship at the New York University under the supervision of Prof. S. Sacanna. The project in which is inserted the part that I have developed is based on the collaboration among three different groups, Prof. Geert Van Den Bogaart from Department of Tumor Immunology Radboud University Medical Center (Netherlands), Prof. Shashi Thutupalli from Simons Centre for the study of living machines Tata Institute for Fundamental Research (India), Prof. Stefano Sacanna from department of chemistry University of New York (USA). The main aim of the project is to study the relationship among phagocytosis processes and the shape/morphology of complex architecture in the cells of the immune system. Phagocytosis is the

process that occurs when the cell uptakes objects of an unconventional size and morphology. The immune system needs to cope with a wide range of pathogens that can be different in terms of size, shape and mobilities. These pathogenic antigens are taken up by phagocytosing immune cells, including dendritic cells, for degradation by metabolic enzymes within the lumen of phagosomes. Dendritic cells can then activate antigen-specific killer and helper T cells, by presenting pathogen-derived peptide fragments in major histocompatibility complexes (MHC) to the T cells¹. The response of the immune system to artificial micrometre scaled objects is also very useful to the development the design and synthesis of efficient theranostic carriers². Beside the drug/probe carrier suitability, the complex synthetic microarchitectures are also very useful to mimic the dynamic and the biochemistry of pathogens, such as bacteria, which usually are similarly sized.

This project will demonstrate that the morphology of microarchitected carriers, both for imaging, sensing or diagnostic, can play a key role for the cellular internalization and immune response. The main part of the research that I carried out at NYU has been focused on the design and preparation of complex monodisperse microarchitectures with magnetic and fluorescent features. The microarchitectures are then tested in biological assays. The project conveys four new concepts to the fields of phagocytosis, cell biology, biophysics, and immunology:

1-Phagocytosis. A major technical innovation will be the generation of active colloids of non-trivial morphologies bearing antigenic proteins as phagocytic cargoes. These will be fuelled by H₂O₂ using light-activated hematite or platinum catalyst-based chemical engines³⁻⁸. H₂O₂ is produced in large amounts within the phagosomal lumen by the dendritic cells to kill ingested pathogens and to promote antigen preservation for MHC presentation⁹⁻¹⁵.

2-Cell biology. Membrane regions of high curvature are recognized by many proteins and lipids involved in membrane fusion and fission or tethering of the cytoskeleton to membranes^{16,17}. However, up to now, the cell biological mechanisms of antigen processing have almost exclusively been studied with spherical model particles. Irregularly-

shapes and forces exerted by particles could induce membrane deformations and thereby affect phagosome maturation for the degradation of antigen.

3-Biophysics. While it is widely recognized that metabolic activity drives transport of organelles within cells, the interplay between cellular crowding, activity and transport is poorly understood. We will create novel technological and conceptual tools to address the dynamics of phagosome transport in crowded intracellular environments, both *in vivo* and *in vitro*. High organellar and macromolecular crowding could lead to spontaneous flows, anomalous transport and directional orientation of anisotropic and morphologically diverse colloids¹⁸⁻²⁰.

4-Immunology. It is well-known, but not mechanistically understood, that pathogens can evade immune degradation by altering their shape by forming elongated hyphens²¹. Nevertheless, the influence of pathogen morphology on immune responses has been largely neglected, and by far most studies focus on pathogen-generated effector molecules/toxins that hijack host cell structure and function²². Also underappreciated is that pathogens can exert intra-phagosomal forces to circumvent immune clearance, as shown for *Candida albicans* which perforates the phagosomal membrane by forming hyphen²³. Mimicking these processes by using H₂O₂ as a fuel or active irregularly shaped colloids is a novel approach, which will allow to answer a key open question in immunology: is the phagocyte able to discern whether the ingested pathogen is dead by sensing mechanical cues? This project will also enable particle design for triggering fast/strong or slow/weak immune responses, with potential applications in vaccination and drug delivery.

The collaboration with the abovementioned three different groups, gives the possibility to investigate deeply the phagocytosis process with an interdisciplinary approach which combines three different moments: a first section is carried out by Prof. Sacanna group that will synthesize micrometer-sized colloids with distinct irregular morphologies and in this framework is also inserted the research work that I developed in his laboratories. These colloids will be equipped with platinum and light-activated hematite catalyst based chemical engines that can propel the particles by converting H₂O₂ into oxygen. The H₂O₂ required for

4

fueling the active colloids is produced in large amounts (molar concentrations) for prolonged times (hours) after antigen uptake by dendritic cells (in contrast to macrophages and neutrophils)⁹⁻¹¹. This H₂O₂ normally serves to kill the ingested pathogens¹³ and to preserve antigenic peptides for T cell presentation^{9-11,14,15}. Secondly, *in vitro* experiments conducted by Prof. S. Thutupalli will be used to quantify the mechanics of the active colloids in crowded environments. By studying the motion of the particles in well-defined densely packed suspensions, we will elucidate how colloid shapes and motilities affect migration in complex crowded cellular environments. By encapsulating colloids with a range of curvatures in artificial membranes, we will determine how forces and shapes affect the spatial organization of lipids and exogenously added proteins. These experiments will be combined with *in vivo* experiments by Prof. Van Den Boogart group with dendritic cells, aimed at identifying the locations of membrane fusion and fission on phagosomes bearing active irregularly shaped colloids and their transport within cells. The organization of the phagosomal membrane and cytoskeletal arrangements will be resolved by super-resolution microscopy. We will coat the particles with model antigenic proteins to determine how particle shape and motilities affect antigen degradation, activation of dendritic cells, and antigen presentation to T cells.

4.0 State of the art

Many synthetic strategies for the preparation of complex architectures have been developed by Prof. Stefano Sacanna and his research group to obtain and engineer active irregularly shaped colloids with a range of curvatures and symmetries, as phagocytic cargo mimicking pathogens. At the interface between chemistry, physics and material science, the Sacanna laboratory (SS Lab) has pioneered synthetic methods to create active colloidal building blocks and defined general self-assembly principles (Fig. 4.1A)^{8,24}. By combining classic sol-gel chemistry with a recently developed micro-emulsification methodology²⁵, the SS lab can synthesize biocompatible colloidal particles with a wide range of morphologies. These particles will be further investigated in this project, coated with light-activated hematite

or platinum catalyst based chemical engines for H₂O₂-fuelled motility^{3-8,26} and conjugated to fluorophores and/or model antigens. The particles can incorporate semiconductor or magnetic oxides (e.g., TiO₂ or Fe₂O₃) to allow for external manipulation using magnetic and light fields.

Several different particles were synthesized and tested with dendritic cells (Fig. 4.1A). These particles are composed of amorphous silica and organo-silica hybrids (e.g., 3-(trimethoxysilyl)propyl methacrylate), and between 2 and 8 μm in size. With the laboratory of Professor Geert Van Den Bogaart (GB laboratory), they were able to show that various particles are readily phagocytosed by blood-isolated dendritic cells and do not affect cell viability (Fig. 4.1B-D). Moreover, the SS laboratory already developed a protocol for the biotinylation of the colloids, which is non-trivial given that the biotin influences colloid formation. This biotinylation facilitates the conjugation of the colloids to antigen proteins and fluorophores by avidin-based interactions (Fig. 4.1E).

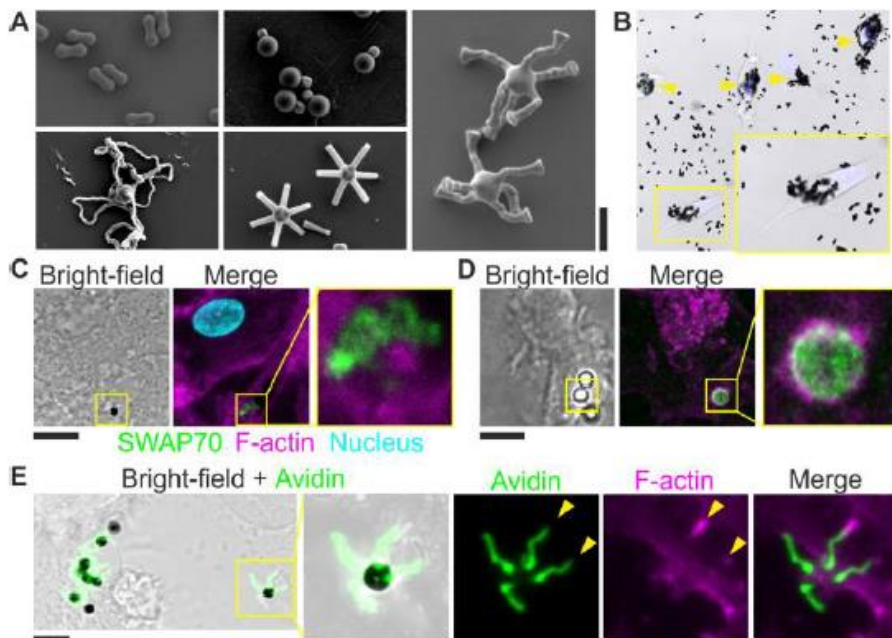


Figure 4.1. Proof of concept: phagocytosis of irregularly shaped particles. **A.** Scanning electron microscopy image of irregularly-shaped colloids. Scale bar, 3 μm. **B.** Bright-field microscopy image of dendritic cells ingesting peanut-shaped particles from panel A (top-left image). **C.** Fluorescence microscopy image of dendritic cell pulsed with the spider hexapod-shaped colloids from panel A (right image) with immunolabeling for actin

(magenta) and the early phagocytic marker SWAP70 (green). Cyan: DAPI. Scale bar, 5 μm . **D.** Same as panel B, but now for latex beads (from ref²⁷). **E.** Same as panel C, but now for hexapod shaped colloids with biotinylation. The spike protrusions were labelled with streptavidin-Alexa fluor 488 (Avidin) to increase their visibility. Scale bars, 5 μm .

Although the first range of particles synthesized by Sacanna group are already very promising, there are still several modifications required for the prosecution of the research:

1. coating of the differently shaped colloids with metal catalyst-based chemical engines for H_2O_2 -fuelled motility.
2. increase the size range of the particles to approximately 10 μm ;
3. increase the density of the biotin coating.
4. generate particles with a range of curvatures and symmetries.

The Sacanna laboratory will work on the localized application of the metal catalyst-based chemical engines to the irregularly shaped colloids (aim 1). Platinum or hematite triggers the decomposition of H_2O_2 when suspended in an aqueous peroxide solution, and the oxygen formed leads to phoretic or bubble propulsion^{3-8,26}, but this has never been applied to generate forces in living cells. Sacanna group will also attempt to synthesize larger particles (aim 2). The size range of the current particles (2-8 μm) is still somewhat too small for the microscopy planned in *in vivo/in vitro* tests. A larger size (more than 10 μm) is desirable for better resolving particle orientation within cells, heterogeneities of the phagosomal membrane, sites of membrane trafficking, and the arrangement of the cytoskeleton. Moreover, the density of biotin on the current particles is still relatively low and a higher density would facilitate addressing the rates of antigen degradation and presentation (aim 3). Finally, the SS Lab should generate more different shapes of colloids (aim 4). For instance, if it will be found that a certain curvature promotes tethering of phagosomes to the actin cytoskeleton, SS Lab will design particles with this curvature on one side allowing polar attachment of the cytoskeleton. In this part has been inserted the research work that I present in this chapter.

4.1 Aim of the work

The goal of the entire project is to determine how the geometry and mechanics of phagocytic cargoes affect the cellular processes underlying phagosomal antigen degradation and presentation by dendritic cells. Together, the combination of colloid chemistry, *in vitro*

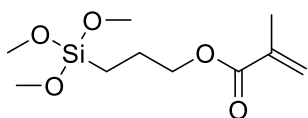


Figure 4.2 TPM structure

and *in vivo* experiments will allow a full physico-mechanical understanding of how particle morphologies and motilities affect phagosomal antigen degradation and presentation. The idea involves the use of a

combination between inert and magnetic materials, in that specific case the use of SiO₂ and hematite, in order to obtain active colloids able to mimic external pathogens and in the same time, able to respond to a specific external input. In particular, the aim of the part of the research that I developed at NYU during a six months period, will be to carry out the following 4 modifications:

1. coating of the differently shaped colloids with metal catalyst-based chemical engines for H₂O₂-fuelled motility.
2. obtain particles in a size range of approximately 10 μm;
3. get a high density of the biotin coating.
4. generate particles with a range of different curvatures and symmetries.

During this limited period, it will be also tried the first biological assays to verify the biotinylation and the cellular uptake by dendritic cells.

4.2 Synthesis optimization and characterization

In order to obtain some of the above-mentioned different types of colloidal material (aim 4), two different types of silica precursors have been used. The first one, TEOS, has been already discussed in chapter 3, but there is a need to quickly introduce 3-(Trimethoxysilyl)propyl methacrylate (TPM) (Fig. 4.2) Despite all micellar assisted method seen until now, this type of architectures are based on the use of modified Stober method. Infact, the preparation of TPM spheres begins with the spontaneous formation of TPM emulsion droplets in water²⁵. This

phenomenon has been described previously for different alkoxy silanes in water under alkaline conditions. Since TPM can be polymerized at its methacrylate moiety, these emulsion droplets can also be used to fabricate solid colloidal particles, which has been used in the past to image Pickering emulsions^{25,28} as well as to make complex and anisotropic particles^{29–31}. Since TPM will hydrolysed and subsequently self-condense in water³², hydrolysis and self-condensation reactions are believed to be the driving forces for the formation of a TPM emulsion^{25,33}. The rates of these processes highly increase with the pH of the solution³²; the reported first-order rate constant for hydrolysis at pH 9 is 1.2 h, which means that 90% of the TPM monomers are already hydrolyzed after 2 h. Indeed, Sacanna et al.³⁴ confirmed the release of methanol during TPM emulsion formation by ¹HNMR, which indicates that the TPM is at least partially hydrolyzed in the emulsification process.

4.2.1 Hematite cubes

The fundamental part in the growth of anisotropic objects is the formation of very monodisperse structures that present precise angles. An example is constituted by the shaping of hematite (mixed iron oxides) cubes that has been carefully investigated including detailed reports on their physical behaviour.³⁵ These mixed iron oxides-based microstructures not only are functional to act as magnetic cores for the precise growth of arms depending on their planar faces (Fig 4.3²⁹), but also for the development of monodisperse pathogen mimetics.

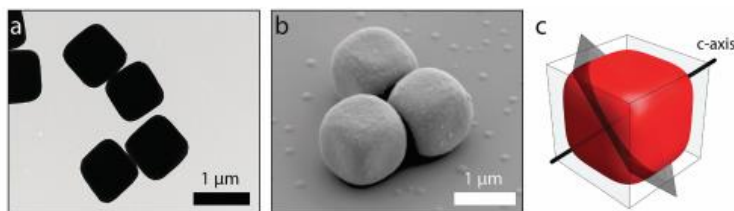


Figure 4.3 TEM, SEM and rendering images of hematite cubes

In any case size distribution of these cubes has to be as narrower as possible since it can affect the formations of different silica arms and the photochemical-induced propulsion in solution. In general, the synthesis of these objects involves the use of condensed ferric hydroxide gel.

Briefly, $\text{FeCl}_3 \cdot 6\text{H}_2\text{O}$ and NaOH were mixed in water thoroughly and aged inside the oven for days in a sealed Pyrex bottle. The final hematite cubes were isolated by repeated sedimentation and resuspension in deionized (DI) water. Tuning the incubation temperature and duration time is possible to obtain cubes different in size.

The synthesis is very sensitive to humidity since the high hygroscopicity of $\text{FeCl}_3 \cdot 6\text{H}_2\text{O}$ and the highly reactive reagents involved, this is not trivial and needs to develop the correct operative skills. As shown in Fig. 4.4, I obtained the cubes after several initial trials, fixing temperature of the oven at 100°C and duration time of the incubation to 8 days. Thanks to the SEM imaging it has been possible to evaluate the degree of purity of the synthesis, and the dimension of the cubes.

The cubes obtained have been used then as core building blocks both to obtain the hexapods as pathogen mimic (paragraph 4.2.2) and the swimmers (paragraph 4.2.3).

It has to be underlined that the synthesis has been modified to tailor the size of cubes (from 500 nm to $1\ \mu\text{M}$), in order to investigate the most suitable dimension for our aims.

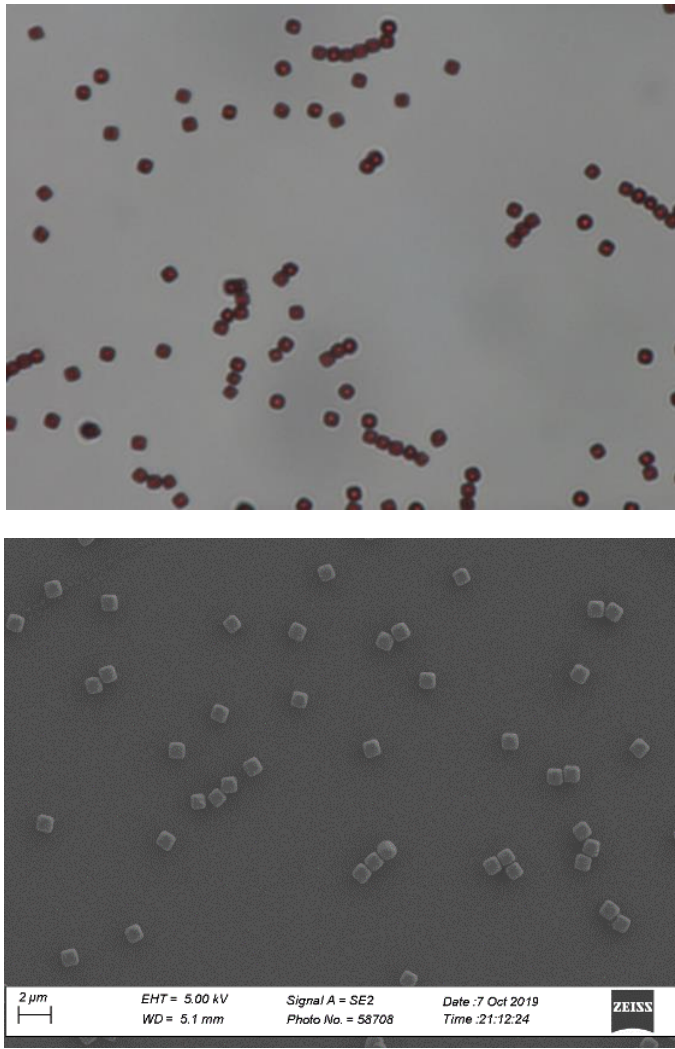


Figure 4.4 Optical microscope image (UP) and SEM image (BOTTOM) of hematite cubes dimension 1 μm

4.2.2 Silica Hexapods

The focus of this work is the construction of anisotropic mimetic of pathogens as mentioned in 4.0 part. The main synthetic strategy shown in Fig 4.5 is to re-create a six arms colloids with magnetic core²⁹ starting from hematite cubes, increasing their dimension until almost 10 μM in order to pursue the aim 2 of the project mentioned in the introduction.

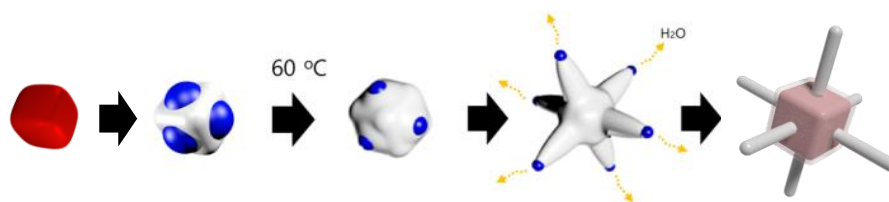


Figure 4.5 Rendering of the Synthesis of hexapods with magnetic hematite core

The water droplet formed on the surface of the seed particle acts as a confined microreactor for the formation of silica rods. To obtain multiple silica rods instead of a single silica rod, there is the need to control the number of droplets operated on hematite cubic seeds.

Typically, for the water-pentanol emulsion, PVP polymers (10 wt %) are first dissolved in 1-pentanol, and then ethanol and studied amount of water are mixed, which yields a homogeneous solution. At this point Cubes were added in precise concentration since the water droplets and hematite cubes are comparable in size so they have to be in a controlled stoichiometry (for six arms hexapods each face of the cube has a single water droplet). Then, when additional water with sodium citrate in order to stabilize the emulsion, are mixed with the homogeneous solution, it becomes slightly opaque, which indicates that water-in-pentanol emulsion droplets were formed by phase separation. It was verified that the single emulsion droplet covered a cubic seed initially, but it could be divided into six small droplets due to the increase of interfacial tension when ammonia is introduced. After this step, the reaction mixture was kept in the oven for 5 minutes and TEOS was added. The reaction has been left to room temperature overnight.

The first attempts, as showed a representative SEM images in Fig 4.6, showed how the recipe was good in terms of formation of six arms around hematite cubes but the synthetic pattern didn't match with our purpose: monodispersity and big size. Infact too many silica big materials are present in solution after purification.

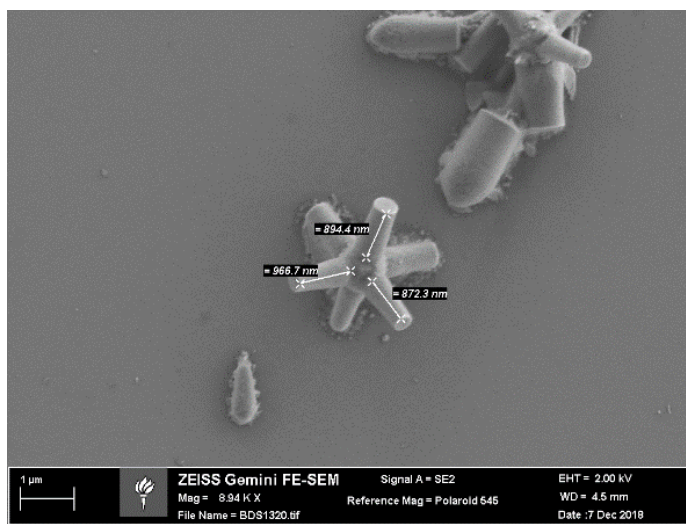


Figure 4.6 representative SEM image of the first hexapods synthesis. Hematite Cubes 500 nm

The synthesis is very sensitive to a lot of parameters such as changing in temperature, reactor dimensions, stirring way, freshness of the reagents used, and obviously, operator skill. I worked on the previous recipe²⁹ working in all these parameters, keeping constant the adding order and the quantity reported on the previous work, in order to optimize the reproducibility of the synthesis. A final recipe has been found in the use of 8mL vial, strong hand shaking after every add, dramatic increasing of the temperature after the adding of NH_3 putting the reactor in the oven for 5 min, faster adding of TEOS followed by gentle hand shaking, left to RT overnight. To improve in the monodispersity issue, I have decided to use bigger cubes despite as reported in the literature. This because the main synthetic issues are related to the purification based on steps of centrifugation of the solution followed by using magnet close to the vial to catch and separate the magnetic objects from the silica growth randomly not attached to the hematite. The use of centrifuge at high rpm values for long time could led to the broken of the arms; this validate the

choice to use bigger hematite cubes since their major density followed by the stronger magnetism. So, to simplify the purification, and, to increase the size of the final hexapods microstructure, the synthesis has been carried out with cubes of 1 μm nm as seeds instead of 500 nm. The bigger hematite cubic seeds allowed to obtain clean hexapods structures. The recipe as developed gave amazing results in terms of monodispersity and reproducibility of the hexapods synthesis (Fig 4.7).

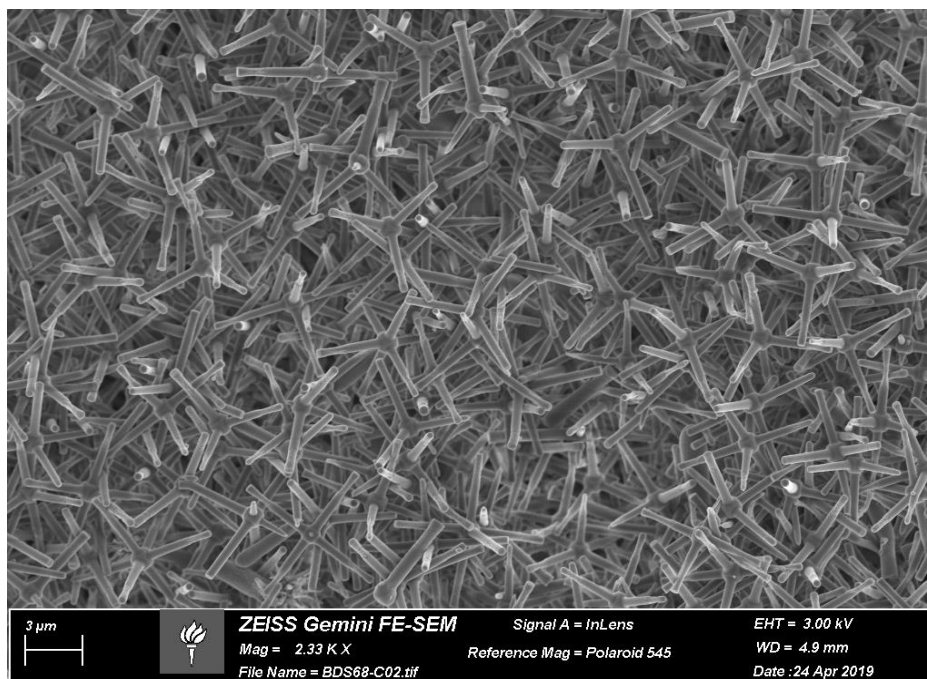


Figure 4.7 Hexapods of circa 6 μm with hematite cubes core.

At this point I worked only in the parameters directly involved in the formation of the arms. Infact I modulated the ratio between TEOS amount and water, looking for the possible relationship between them and the arm's length. Since that the total concentration of cubes was fixed at 0.04% w/v inside the reaction batch, DI water was kept fixed at 280 μL and the quantity of TEOS was varied from 25% to 70% v/v respect to the amount of water. Varying the water amount could be risky, as expressed before, since the water amount can negatively affect the droplet formation around the cubes.

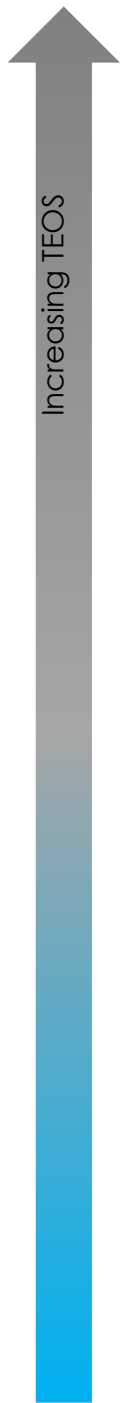
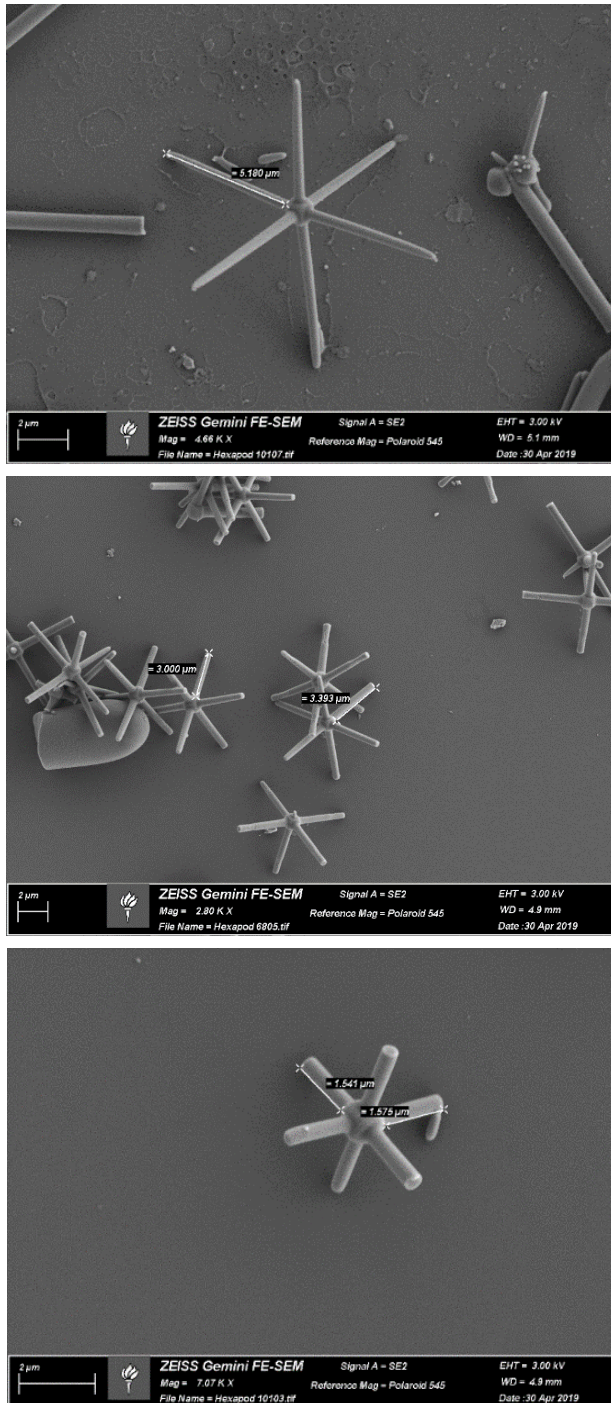


Figure 4.8 SEM images of 28%, 50%, 70% (from bottom to up) volume of TEOS respect to the water volume

As shown in Fig 4.8, the increasing in volume of TEOS is strictly correlated with the increase of the length of the arm, and it is possible to create a perfect ratio between amount of silica precursor and size of the hexapods from 4 to 11 μM .

Given the excellent results, it has been tried to obtain hexapods with hollow cubes instead magnetic ones since their possible comparison on the future biological tests. The reaction to obtain hollow structures starting from hematite cube has been reported by L.Rossi et al²⁹. Briefly mixture of absolute ethanol, water, tetramethylammonium hydroxide and PVP-stabilized hematite cubes was mechanically stirred and sonicated in a 2 L round bottom flask. The silica deposition was started by adding a mixture of TEOS and ethanol to the flask in repetitive portions. Next a solution of PVP in EtOH was added to the flask to prevent aggregation induced by dye molecules at the silica surface. Finally, the flask was sonicated for at least 2 more hours and stirred overnight. To remove unreacted molecules the dispersion was washed several times via centrifugation in ethanol. After centrifugal transfer of the silica coated particles to water, the hematite cores were dissolved by adding hydrochloric acid (37% wt) to a final concentration of 5 M. Once obtain hollow cubes, there is the possibility to proceed with the hexapods synthesis using them as seeds instead hematite cubes. The problems in the use of this way to obtain silica hollow hexapods are the already commented purification steps that would be useless. As matter of fact, the use of magnet will be worthless, and the centrifugation step doesn't discriminate this low difference in density between hollow hexapods and silica material randomly create during the reaction. In order to overcome this problem and avoid all the difficult and long synthetic step to obtain silica hollow cubes, the idea was work directly in the already formatted hematite hexapods. The silica shouldn't have problem in acidic condition necessary to dissolve hematite, hence it could be possible destroy the hematite putting the hematite hexapods directly in a concentrated HCl solution. For this reason, the etching has been carried out involving the use of a 9M solution of HCl, directly to the fresh formed hexapods with hematite core. As reported in the Fig 4.9, also from the changing in colour of the bulk of the solution is clear, the batch changed from red to white in 1h at 80°C.

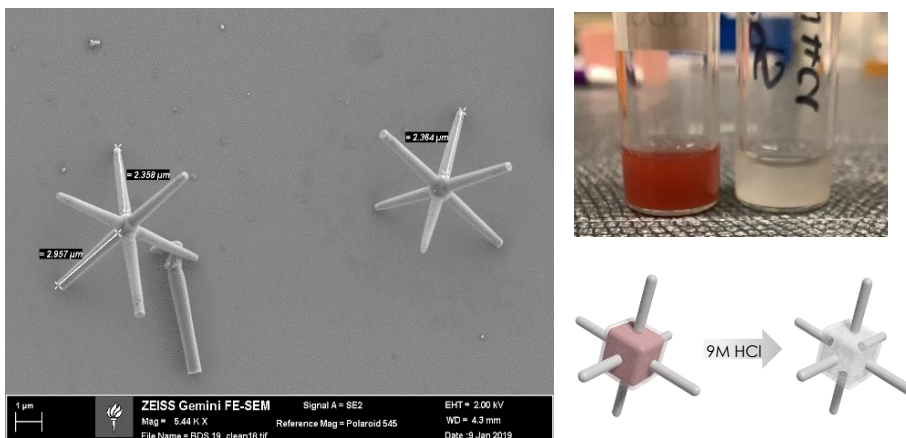


Figure 4.9 SEM image of Silica hollow hexapods (left), Picture of the batches of red hematite core hexapods and silica hollow hexapods (right up), rendering of the schematization of the reaction.

In this way, it has been obtained hollow hexapods, avoiding the previous complicated steps of the hematite cubes coverage, and the impossible purification of the hexapods that it would have had to afford if they had used cubes of single silica as seeds, instead of magnetic cores.

The following step will be performed in the hematite hexapods core in order to be fast in the purification step. Once well investigation on the synthetic pattern, it will be possible use the same procedures in the hollow silica hexapods.

As mentioned in the introduction, part of this work involved also non-trivial biotinylation step of the microstructures, which facilitates the conjugation of the colloids to antigen proteins and fluorophores by avidin-based interactions. However, It has been experimentally found that biotin tents to influence colloid formation. During the studies it has been also demonstrated that the synthesis of this type of material is very sensitive to every change of the precursor. It has been tried to investigate if it was possible to introduce a modified silane like APTES directly to the reaction mixture useful for the biconjugation. In this way it would have been possible to couple the arms of the hexapods with biotine. The resulted modification has led to a very irregular morphology of the hexapod. Indeed, as shown in Fig 4.10, the hexapods look deformed. It may also happen using very low amount of APTES respect to the TEOS (1% in mol).



Figure 4.10 Hexapods with 1% amount in mol of APTES respect to the TEOS

To overcome this deformation, it has been decided to don't modify the synthesis but in order to have bio-conjugable hexapods the reactive moiety has been introduced after the purification once the structure is perfectly formed. To verify the possibility of the modification of the arms, it has been introduced a fluorescent tag to the structure. It has then performed a labelling with RhodamineB-silane. The fluorescent labelling has occurred starting from clean hexapods in EtOH and silane rhodamine B previous synthesized using IST-Rhodamine B coupled with APTES. Thus, the fluorescent functionalization has been useful to demonstrate the possibility to carry on reaction on the hexapods without affecting their morphology. In Fig 4.11 are reported the optical microscope images of the labelled hexapods, which show that they maintain their morphology after the reaction, and their obtained fluorescence, indices of the successful of the reaction.

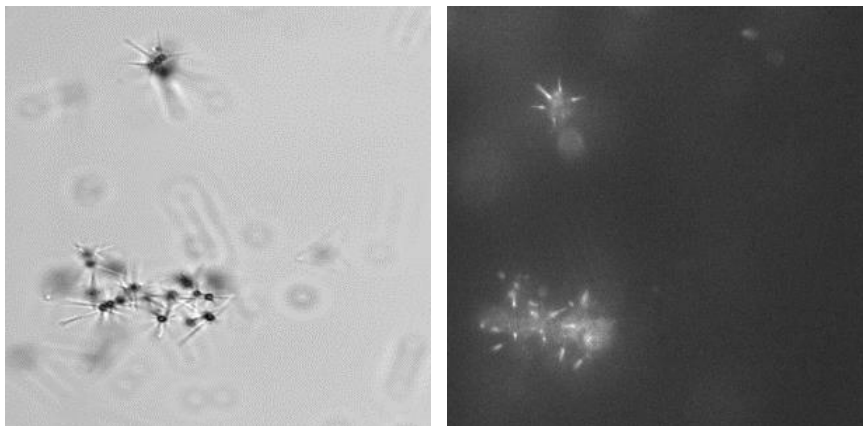


Figure 4.11 Optical images under microscope of Hexapods bright field (left) and Rhodamine fluorescence (right)

Once proved the suitability of functionalization of the formed hexapods, the biotinylation has been carried out with PEG-Biotine-Silane. Thanks to the peg linker it has been possible to obtain biotinylated microarchitectures since the uncondensed silica of the arms could hydrolyze with the silane of the PEG-biotine without perturbing the morphology of the silica arms. The formulated protocol starts simply diluting 100 μL of concentrated clean hexapods in EtOH, then add 600 μL Biotine-PEG-Silane 6 mg/mL and kept the solution under gently stirring overnight.

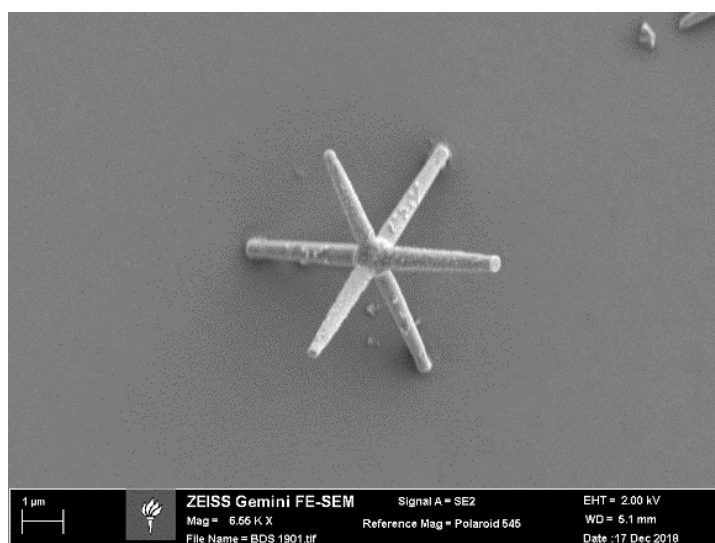


Figure 4.12 SEM image of Hexapod with hematite core after biotinylation

The Hexapods were then collected by magnet and SEM images in Fig 4.12 showed how the biotinylation hasn't affect at all the hexapods morphology.

The presence of biotinylation on the hexapods surface has been proved staining them with a fluorescent streptavidin (AF488/647) in the group of Prof. Van der Bogaart. In Fig 4.13 is reported the green fluorescence given by the complex biotinylation-streptavidin, and, furthermore, the blue emitting antigen Anti-streptavidin antibody complex with streptavidin, index of the perfect recognizing of the biotinylated hexapods.

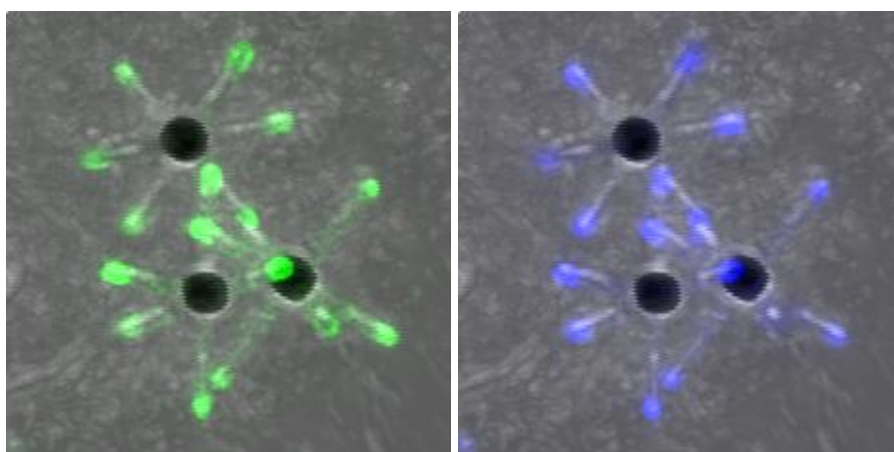


Figure 4.13 In green biotinylated-Hexapods with streptavidin, in blue biotinylated-Hexapods with streptavidin with anti-streptavidin antibody

The emission localized at the extremities of the arms should be due to the easier accessibility by the PEG-biotinylation-silane respect to the internal part of the exapods, and, moreover, because the tips could present not hydrolyzed silane which could better react with silane moiety of the PEG-Biotinylation. The hexapods functionalized with PEG biotinylation have been then tested in cellular internalization assay. The preliminary test with the monocyte-derived dendritic cells (moDC) showed in Fig 4.14, display the good internalization of the hexapods.

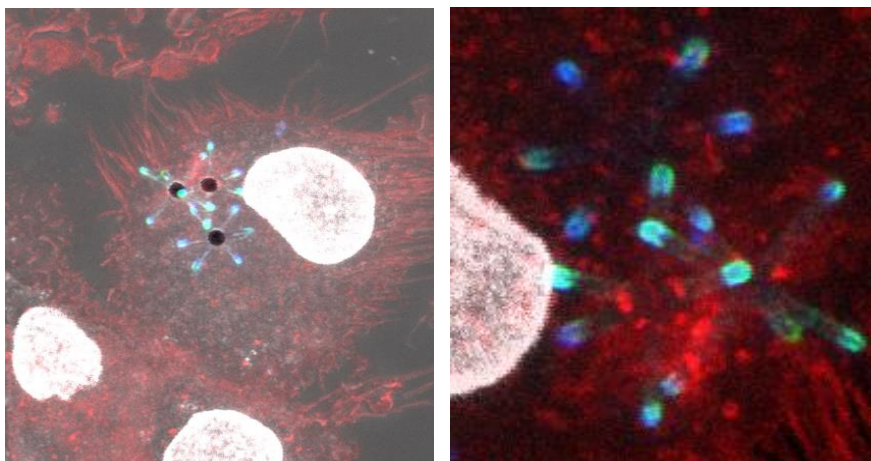


Figure 4.14 Phagocytosis by moDC. Red: F-Actin gray:DAPI,green/blue: Streptavidin and anti-streptavidin antibody.

The hexapods are internalized within the phagosome by human monocyte-derived dendritic cells. It could be established that even particles with very unusual shapes can be taken up by dendritic cells. Further measurements have to be performed, but the first analysis show how the improvements in size is good for the biological characterization (aim 2).

4.2.3 Swimmers based on TPM spheres and Hematite cubes

I have been involved also in the design and preparation of active colloids able to move fuelled by hydrogen peroxide (swimmers) and activated by light. This structure can be used to understand the movements and trajectories when they would find themselves “under attack” of reactive oxygen species formed by dendritic cells during phagocytosis.

In this paragraph it will be described the synthetic approach for the formation of swimmers as spherical particles of TPM including hematite cubes used as seeds. Usually the synthesis of hybrid architectures is quite complicated²⁹ and I spent many efforts to optimize and simplify the preparation without compromising the swimming features and monodispersity.

The synthesis involves a water solution containing hematite cubes where 0.1% of NH_4OH is added together with increasing amounts of TPM. The process is a variation of the Stöber method, where droplets of oily TPM are hydrolysed in basic condition; the main difference from the reference method involving only silica (see chapter 3), is that there are hematite cubes embedded inside.

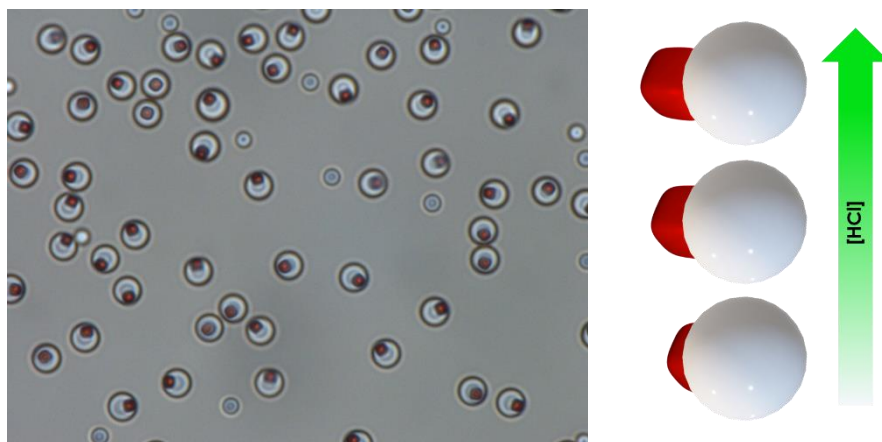


Figure 4.15 Optical microscope capture of cubes inside TPM spheres before acidic depletion left, rendering of depletion of the cubes increasing acidic conditions

Different reaction times from 40 min to 2 h were explored since the final dimension depends upon this parameter: the longer the time of reaction the bigger the size. The dimension of the resulting particles was checked with optical microscope. As shown in Fig 4.15, the particles result quite monodisperse. The particles have been used then to evaluate the effect of the addition of different amounts of HCl on the controlled dissolution of the TPM droplet. The study has been carried out to estimate the correct conditions to obtain the desired ejection of the cubes with respect to the spheres. In fact, we proved that exists a correlation between the ejection level and the concentration of the acid used: higher concentrations of acid lead to a bigger depletion, until the complete collapse of the sphere (at HCl 0.1M). After obtaining the controlled dissolution of the dimension of the “TPM head”, AIBN radical initiator is used to polymerize the methacrylate part of the TPM. The Swimmers have been kept in the oven at 100°C for 24 hours and collected by centrifugation and using a magnet to select only the ones containing the hematite tail. The SEM images reported in Fig. 4.16 have confirmed different level of the ejection of the cubes respect to the

sphere, for two different samples containing different amounts of acid (0-0,08 M) and therefore validating the synthetic approach.

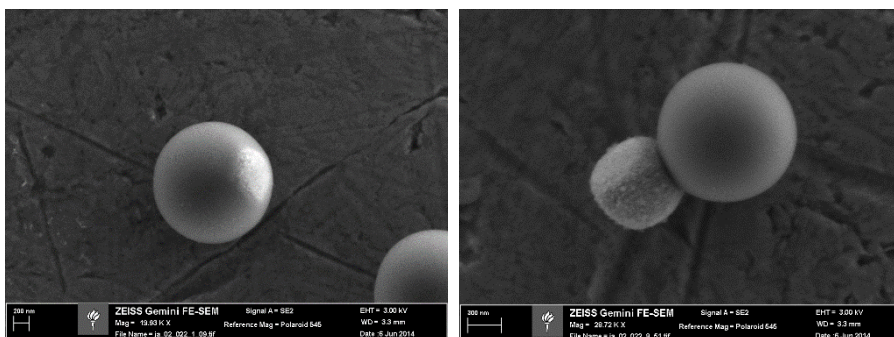
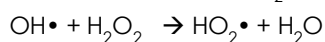
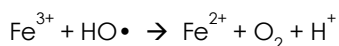
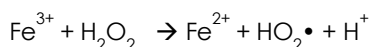
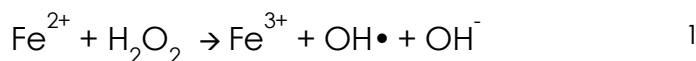


Figure 4.16 Fully inserted cube inside TPM particles (left), complete ejected cube from TPM sphere (right)

After the synthesis of the swimmers the experiments have been focused on the description of their motion in solution upon exposition of UV light. The formed swimmers were collected with centrifuge and put in a solution of H₂O₂ 10% v/v in water and then recovered inside a glass capillary and settled in an optical microscope under blue UV-light. The swimmers follow initially the normal Brownian motion, but when blue light is turned on, the Fenton reaction 1 starts. Fenton reaction is reported below:



This reaction takes to the formation of molecular oxygen on the surface of hematite cubes creating bubbles that act as a driving force for the swimmers 'pushing' them. The next step will be to study the trajectory of the swimmers, anyway, the new understanding obtained are steps forward in the rotor construction and fuelled synthetic micro colloids.

4.3 Conclusions and future steps

With the aim to understand phagosomal membranes, in particular how factors as pathogen morphologies, mechanical properties or intracellular motilities and forces affect phagosomal processing within immune cells, mimetic of external pathogens were developed using silica and magnetic hematite cubes. Moreover, to mimic pathogens with non-regular shapes I also prepared irregular shaped microobjects like hexapods and circular ones. I succeeded in optimizing the synthesis of hexapods to obtain a procedure that allows the modulation of the arm's length. I also developed a functional protocol for their easy biotinylation that allowed via the use of PEG-biotine moieties the PEGylation of the hexapods to favour their cell internalization. Preliminary *in vitro* experiments were performed with the monocyte-derived dendritic cells (moDC) and they evidenced that this was a successful strategy, in fact, the hexapod uptake was confirmed proving that even particles with very unusual shapes and size can be cell internalized. Together with *in vitro* tests, the future steps would be the establishment of how particle shape and curvature affect the recruitment of intracellular markers guiding phagosomal membrane conversion.

Parallely, I also synthesized particles called 'swimmers' that are propelled by the formation of molecular oxygen bubbles during their reaction with hydrogen peroxide activated by light. These active colloids are formed by a tail constitute of a hematite cube and a spherical head obtained by the condensation of TPM. The optimization of the synthesis has taken to the formation of swimmers with tuneable dimensions and their motion under the activation of light was studied with an optical microscope. These structures can be used to understand the movements and trajectories that they would follow when "under attack" of reactive oxygen species formed by dendritic cells during phagocytosis. I was able to observe and record the change in motion of the swimmers from a normal Brownian motion, under the activation of the Fenton reaction by light and consequent bubbles formation that 'push' them. The next step will be to study the trajectories of the swimmers.

-
- 1 J. M. Vyas, A. G. Van der Veen, H. L. Ploegh, *Nat. Rev. Immunol.* **2008**, *8*, 607.
- 2 R. Xu, G. Zhang, J. Mai, X. Deng, V. Segura-Ibarra, S. Wu, J. Shen, H. Liu, Z. Hu, L. Chen, *Nat. Biotechnol.* **2016**, *34*, 414.
- 3 T. D. Gough, J. R. Howse, R. A. L. Jones, A. J. Ryan, **2009**.
- 4 W. Gao, A. Pei, J. Wang, *ACS Nano* **2012**, *6*, 8432.
- 5 S. Wang, N. Wu, *Langmuir* **2014**, *30*, 3477.
- 6 R. Golestanian, T. B. Liverpool, A. Ajdari, *Phys. Rev. Lett.* **2005**, *94*, 220801.
- 7 W. Wang, W. Duan, S. Ahmed, T. E. Mallouk, A. Sen, *Nano Today* **2013**, *8*, 531.
- 8 J. Palacci, S. Sacanna, A. P. Steinberg, D. J. Pine, P. M. Chaikin, *Science (80-.)*. **2013**, *339*, 936.
- 9 A. Savina, C. Jancic, S. Hugues, P. Guermonprez, P. Vargas, I. C. Moura, A.-M. Lennon-Duménil, M. C. Seabra, G. Raposo, S. Amigorena, *Cell* **2006**, *126*, 205.
- 10 F. Kotsias, E. Hoffmann, S. Amigorena, A. Savina, *Antioxid. Redox Signal.* **2013**, *18*, 714.
- 11 A. R. Mantegazza, A. Savina, M. Vermeulen, L. Pérez, J. Geffner, O. Hermine, S. D. Rosenzweig, F. Faure, S. Amigorena, *Blood* **2008**, *112*, 4712.
- 12 I. Dingjan, L. M. Paardekooper, D. R. J. Verboogen, G. F. von Mollard, M. ter Beest, G. van den Bogaart, *Eur. J. Cell Biol.* **2017**, *96*, 705.
- 13 M. Vulcano, S. Dusi, D. Lissandrini, R. Badolato, P. Mazzi, E. Riboldi, E. Borroni, A. Calleri, M. Donini, A. Plebani, *J. Immunol.* **2004**, *173*, 5749.
- 14 J. M. Rybicka, D. R. Balce, S. Chaudhuri, E. R. O. Allan, R. M. Yates, *EMBO J.* **2012**, *31*, 932.
- 15 E. R. O. Allan, P. Tailor, D. R. Balce, P. Pirzadeh, N. T. McKenna, B. Renaux, A. L. Warren, F. R. Jirik, R. M. Yates, *J. Immunol.* **2014**, *192*, 4989.
- 16 H. T. McMahon, E. Boucrot, *J Cell Sci* **2015**, *128*, 1065.
- 17 S. Suetsugu, S. Kurisu, T. Takenawa, *Physiol. Rev.* **2014**, *94*, 1219.
- 18 D. S. Banks, C. Fradin, *Biophys. J.* **2005**, *89*, 2960.
- 19 N. Fakhri, A. D. Wessel, C. Willms, M. Pasquali, D. R. Klopfenstein, F. C. MacKintosh, C. F. Schmidt, *Science (80-.)*. **2014**, *344*, 1031.
- 20 C. Riedel, R. Gabizon, C. A. M. Wilson, K. Hamadani, K. Tsekouras, S. Marqusee, S. Pressé, C. Bustamante, *Nature* **2015**, *517*, 227.
- 21 L. P. Erwig, N. A. R. Gow, *Nat. Rev. Microbiol.* **2016**, *14*, 163.
- 22 A. Jimenez, D. Chen, N. M. Alto, *Annu. Rev. Cell Dev. Biol.* **2016**, *32*, 373.
- 23 C. G. J. McKenzie, U. Koser, L. E. Lewis, J. M. Bain, H. M. Mora-Montes, R. N. Barker, N. A. R. Gow, L. P. Erwig, *Infect. Immun.* **2010**, *78*, 1650.
- 24 M. Youssef, T. Hueckel, G.-R. Yi, S. Sacanna, *Nat. Commun.* **2016**, *7*, 12216.
- 25 C. van der Wel, R. K. Bhan, R. W. Verweij, H. C. Frijters, Z. Gong, A. D. Hollingsworth, S. Sacanna, D. J. Kraft, *Langmuir* **2017**, *33*, 8174.
- 26 Y. Wu, Z. Wu, X. Lin, Q. He, J. Li, *ACS Nano* **2012**, *6*, 10910.
- 27 D. Genovese, M. Montalti, L. Prodi, E. Rampazzo, N. Zaccheroni, O. Tomic, K. Altenhöner, F. May, J. Mattay, *Chem. Commun.* **2011**, *47*, 10975.

- 28 S. Sacanna, W. K. Kegel, A. P. Philipse, *Phys. Rev. Lett.* **2007**, 98, 158301.
- 29 L. Rossi, S. Sacanna, W. T. M. Irvine, P. M. Chaikin, D. J. Pine, A. P. Philipse, *Soft Matter* **2011**, 7, 4139.
- 30 S. Sacanna, W. T. M. Irvine, P. M. Chaikin, D. J. Pine, *Nature* **2010**, 464, 575.
- 31 Y. Liu, K. V Edmond, A. Curran, C. Bryant, B. Peng, D. G. A. L. Aarts, S. Sacanna, R. P. A. Dullens, *Adv. Mater.* **2016**, 28, 8001.
- 32 D. A. Kurtz, K. R. Brereton, K. P. Ruoff, H. M. Tang, G. A. N. Felton, A. J. M. Miller, J. L. Dempsey, *Inorg. Chem.* **2018**, 57, 5389.
- 33 T. M. Obey, B. Vincent, *J. Colloid Interface Sci.* **1994**, 163, 454.
- 34 S. Sacanna, L. Rossi, A. P. Philipse, *Langmuir* **2007**, 23, 9974.
- 35 L. Rossi, J. G. Donaldson, J.-M. Meijer, A. V Petukhov, D. Kleckner, S. S. Kantorovich, W. T. M. Irvine, A. P. Philipse, S. Sacanna, *Soft Matter* **2018**, 14, 1080.

CAP. 5

BIORESORBABLE ELECTROSPUN NANOFIBER MAT RELEASING DIAGNOSTIC NANOTOOLS, FOR POST-SURGICAL IMPLANTATION

5.0 State of the art

The loss or failure of an organ or tissue is a frequent and devastating problem in health care, occurring in millions of patients every year. Organ or tissue damage is currently treated by transplantation from another donor individual or performing a surgical reconstruction by transferring tissue from another healthy area of the human body to the diseased one. Although these approaches have saved and improved the quality of millions of lives, they remain imperfect solutions and there is still a lot of room for improvement. In this framework, tissue engineering (TE) represents a new and promising pathway to help in the resolution of some of the problems associated to the traditional strategies currently adopted¹. The field of tissue engineering has

noticeably increased over the last decade, offering nowadays the chance of new treatments for many disease states. This research area involves researchers in a multitude of disciplines, including cell biology, imaging, biomaterials science, chemistry and medicine. The aim of tissue engineering is to restore, maintain, or improve tissue functions that are defective or have been lost by different pathological conditions, by either developing biological substitutes or reconstructing tissues². In addition to clinical applications, other uses include drug testing for efficacy and toxicology as well as basic studies on tissue development and morphogenesis³. However, in the most frequent paradigm of tissue engineering, isolated living cells are used to develop biological substitutes for the restoration or replacement of organ/tissue functions.

The development of biomaterials for surgical implants has evolved through three stages, each of them with a distinctly different objective. The goal of the first generation of biomaterials was to achieve a proper combination of functional properties to match those of the replaced tissue without deleterious response by the host. They were intended to be bioinert, that is, to elicit minimal response from the host tissue. Consequently, a second generation of biomaterials was developed, whose goal was to be bioactive, that is, able to stimulate a nontrivial but desired – and therefore controlled-reaction with the tissue in which they were implanted. This second generation of materials also included the development of biodegradable and bioresorbable materials. Nowadays, it has been developed a third generation of biomaterials, intended to be not only bioactive and resorbable, but also being able to stimulate specific cell response at molecular level, like cell proliferation and differentiation³. In this chapter the attention will be focused on the second generation, in the study of release matter from biodegradable mat. Both synthetic polymers and biologically derived (or natural) polymers have been extensively investigated as biodegradable polymeric biomaterials⁴, mainly because it is easy to control both their macro and microstructure. Furthermore, they offer multiple advantages of biocompatibility, chemical versatility and biological properties, which are necessary for the application of tissue engineering and organ substitution. Their properties depend on the composition, structure and arrangement of the constituting macromolecules. Synthetic polymers

are highly useful since their properties can be tailored for specific applications. They are usually cheaper, can be produced in large quantities and have a long shelf life. PLGA has been widely investigated for medical uses, such as suture materials⁵¹, bone fixation⁵⁰, implants, prosthetic devices⁴⁸, surgical sealant films and depot drug delivery systems⁴⁹. Recently electrospun PLGA nano- and microfibers have also been studied for bone regeneration, wound dressing, and tissue engineering^{5,6}. Besides its biodegradability and biocompatibility, the reason why this polymer is particularly attractive is the potential for controlled drug release^{7,8}. Although numerous studies have utilized PLGA to prepare electrospun nano- and micro-fibers for controlled-release purposes, not much is known yet about how the polymer solution properties influence the quality of electrospun PLGA fibers. With Electrospinning, it is possible to fabricate fibrous polymer scaffolds with fiber diameters ranging from several microns down to several nanometres. Electrospinning has been widely investigated for producing scaffolds for tissue engineering^{9,10}, drug delivery systems¹¹, wound dressings¹², artificial organs¹³ and vascular grafts¹⁴. It is a versatile, cost effective, and simple process for making micro- or nanoscale fibers by exposing polymer solution/melt to a high voltage¹⁵. A stable liquid jet can be discharged from the tip of the Taylor cone¹⁶ when the voltage is increasing to break the balance between Coulombic repulsion and surface tension. A whip-like motion of the liquid jet between the capillary tip and the grounded collector is formed. If there is sufficient chain overlap and entanglements of the polymer molecules in the solution, with a lateral electric force, and this motion results in thinning of the jet and formation of micro- or nanoscale fibers. The electrospun fibers have been found to be a good mimic for the structure of the extracellular matrix (ECM) of the body¹⁷⁻¹⁹. The electrospun fibrous mats, with a high pore volume with variable pore sizes, can enhance cell differentiation, adhesion, and proliferation²⁰. Different materials, such as synthetic or naturally derived polymers, can be processed alone or in combinations to promote various biological or physicochemical properties, such as biodegradation, biocompatibility, mechanical strength, hydrophobicity, or hydrophilicity, needed for different application purposes¹⁶.

5.1 Electrospinning

ES is one of the most used techniques to fabricate polymeric fibers²¹ due to its versatility that allows the use of a great variety of polymers and the inexpensive nature of the ES basic apparatus. To start a brief description of the technique it is necessary to mention the many parameters²² that influence ES that can be divided in three main groups: a) environmental parameters like relative humidity (RH) and temperature²³, b) solution parameters related to the used solvent mixture²⁴ and to the viscosity of the solution and c) operative parameters which are related to the applied voltage, needle to collector distance and feed rate of the solution through the metallic needle. To obtain good quality fibers the first data to consider is the molecular weight of the used polymer and the solution viscosity since they govern the so-called physical entanglements²⁵. Macromolecular chains dissolved into a mixture of solvents arrange into a random coil structures, and the presence of physical interconnections among them, i.e. physical entanglements, are mandatory in order to obtain a constant and continuous flow of macromolecules during the ES process necessary to successfully produce fibers²⁶. Due to the entanglement interaction importance most of the polymers employed for the ES process present high molecular weight, usually way over tens of kilo Daltons.

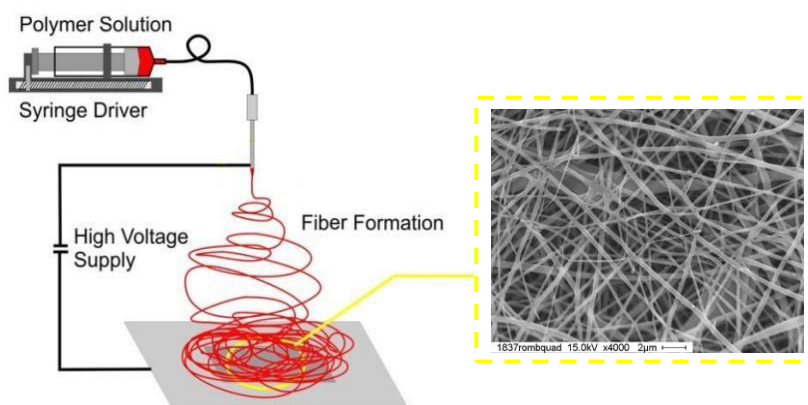


Figure 5.1 Schematization of Electrospinning methods and SEM image of electrospun fibers of PLGA

ES is an electrostatically driven process and it's based on the feeding of a polymeric solution through a capillary tube into a high electric field

(Fig. 5.1). When the solution reaches the electrified needle, it is subject to forces produced by the magnetic field, once these forces overcome the surface tension of the polymeric solution it leads to the formation of the so-called Taylor cone. After that a small and thin fluid jet is ejected and the fiber starts forming. The applied voltage leads to a whipping motion that has two main effects it allows stirring the fibers and, in the meantime, it promotes solvent evaporation and let the dry fibers to be collected over a grounded collector. This technique gives the possibility to control not only the fibers dimensions but also their architecture, obtaining fibers as random oriented, aligned, core shell, hallow and even with more complex structures²⁷. The 3D structures of the ES fibrous systems, known in tissue engineering as scaffolds, are highly porous made up of fibers with high surface to volume ratio. This allows to greatly mimic the extracellularmatrix well-supporting cell activities involved in tissue regeneration processes²⁸. Coupling this with the possibility to obtain new generations of scaffolds that can act as drug carriers, providing a controlled release of drugs while promoting the tissue regeneration, might represent a big step forward in the field of tissue engineering^{10,29}. In this context electrospinning can be considered a powerful and versatile tool to be applied to meet all the requirements for advanced medical applications that nowadays are of central interest for the scientific community. Noteworthy, the polymer, copolymer or blend of polymers used for this kind of applications must be first of all biocompatible and then present the suitable chemical and mechanical characteristics for each single application. Among all the possible choices

5.1.1 PLGA

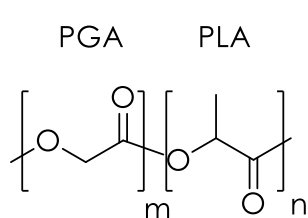


Figure 5.3 PLGA structure

Poly lactic-co-glycolic acid (PLGA) is a biodegradable and biocompatible copolymer approved by Food and Drug Administration (FDA) for food and medicine applications. Its synthesis involves the ring-opening co-polymerization of two different monomers, the cyclic dimers (1,4-dioxane-2,5-diones) of glycolic acid and lactic acid.

During polymerization process, successive monomeric units (of glycolic

or lactic acid) are linked together in PLGA by ester formation, thus yielding a linear, aliphatic polyester as a product³⁰.

PLGA degrades by hydrolysis of its ester bonds in the presence of water. It has been shown that the time required for degradation of PLGA is related to the monomers' ratio used in the preparation: the higher the content of glycolide units, the lower the time required for degradation as compared to predominantly lactide materials. An exception to this rule is the copolymer with 50:50 monomers' ratio which exhibits the faster degradation (about two months)³¹. This tunability in degradation has made it very advantageous for the production of many medical devices, such as, grafts, sutures, implants, prosthetic devices, surgical sealant films, micro and nanoparticles³². PLGA undergoes hydrolytic degradation producing lactic acid and glycolic acid, that under normal physiological conditions, are by-products of various metabolic pathways in the body. Lactic acid is metabolized in the tricarboxylic acid cycle and eliminated as carbon dioxide and water. Glycolic acid is metabolized in the same way, and also excreted through the kidney³³. Since the body can metabolize the products of its degradation, there is minimal systemic toxicity associated PLGA in medical application. It has also been reported that the acidic degradation of PLGA reduces the local pH low enough to create an autocatalytic environment³⁴, involving in a pH variation which increase the rate of the degradation.

5.1.2 Mechanism of PLGA degradation in DDS

There are various factors which affect the release of drug from the PLGA-based Drug Delivery Systems (DDS). The drug release from PLGA-based DDS has been beautifully reviewed by Fredenberg et al³⁵. The main mechanisms of drug release from PLGA-based DDS are three: (i) transport through water-filled pores, (ii) transport through the polymer, and (iii) dissolution of the encapsulating polymer. The last mechanism does not involve transport of drug from DDS, as in this case the drug is automatically exposed to the dissolution medium due to erosion of the polymer. The contact of PLGA with the medium causes its rapid absorption, hence creating water pockets which can be considered as

pores. In the initial phase this absorption is slow but becomes more and more efficient^{36,37} and it causes hydrolysis of PLGA. Hydrolysis leads to formation of degradation products, which then diffuse out of the polymer matrix creating small pores that, increasing in size with the proceeding of the reaction, finally coalesce to form bigger ones³⁷. The release profile of drug from PLGA-based DDS is rarely found to be monophasic, commonly is biphasic or triphasic. A DDS with colloidal nature, often shows altered release profile from a Fickian diffusion profile and a sigmoidal profile to a zero-order profile^{38,39}. In the case of triphasic release profile showing DDS, the first phase is often termed as burst release, which is attributed to the presence of untrapped drug present as adsorbed layer on the surface of particle, either nanoparticles or microparticles, or drug layer present close to the surface which is easily accessed by hydration of particle. The second phase is slow due to slow diffusion of drug from dense polymer matrix and absence of multiple larger pores. The third phase shows faster drug release as compared to the second one, which is attributed to the presence of larger pores and progressive degradation of the polymer^{40,41}.

5.2 Aim of the work



Chart 1 Description of the project idea

Aim of this part of my research was to prepare luminescent nanoparticles bearing a targeting agent for tumor tissues and to explore the possibility to release them from a carrier in a controlled way in view of medical applications. In particular, this project is inserted in a wider and more complex one in collaboration with prof. L. Focarete group of the University of Bologna.

This part includes the first pilot attempts in view of the engineerization of a multicomponent biodegradable material able to release theranostic targeted NPs *in situ* in a postsurgical event. The idea is to implant the material in a patient after a tumour resect operation to release the theranostic nanoparticles in time during the reabsorption of the scaffold, allowing to monitor, and in case to cure, the neighboring tissues.

The core of my study will be to evaluate if, using the electrospinning method, it is possible to create a bioresorbable mat, containing targeted dye-doped PLuS NPs, able to release them in a degradation dependent regime.

In chart 1 it is highlighted the sequence of the steps followed in this study: a) the preparation of luminescent targeted nanoparticles, b) the insertion of these nanotools in a polymer matrix during electrospinning, c) the study of the particle release process and its correlation to the degradation of the matrix.

First of all I synthesized luminescent core-shell silica NPs covalently doped in the core with Rhodamine B (previously silanized⁴²) and functionalized on the surface with a complementary peptide to a peptidic chain over-expressed by hepatic cancer cells⁴³. The NPs, both decorated or not with the target moieties, were introduced in a biocompatible and biodegradable poly-lactic-co-glycolic acid (PLGA) mat and its

degradation carefully monitored by different methods. The photophysical characteristics of the particles make it also possible to directly follow their release monitoring fluorescence in the incubation water.

5.3 Results and discussion

First step was to prepare PlusNPs presenting rhodamine B as dye, in order to be able to follow the release using its fluorescence. In order to covalently bind the dye inside the core of PlusNPs, rhodamine B was modified by the use of piperazine⁴² and, successively, coupled with silica moiety as shown in Fig. 5.3, to obtain silane derivatized molecule.

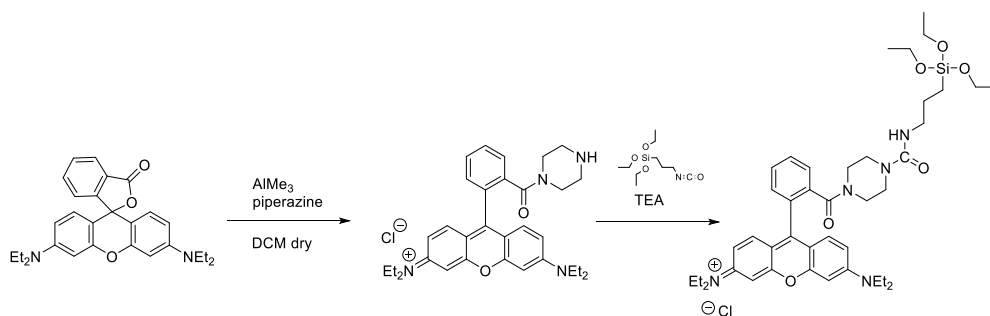


Figure 5.3 Synthesis of Rhodamine B silane

RhB@NPs, were synthesized co-condensing Rhodamine B (0,25% amount respect to the mol of the TEOS) (Fig. 5.3) together with TEOS in the micelle assisted preparation step (see cap 3). The NPs were morphologically characterized by TEM and DLS analysis showing a good monodispersity and size completely in line with the attended measures for this synthetic procedure (see Fig. 3.3 in cap3). The photophysical characterization of the NPs was carried on and compared with the behavior of Rhodamine B in solution in water (Fig. 5.4):

The absorption and emission spectra doesn't change significantly: from the comparison between the profile of Rhodamine B free in solution and inside the NPs it is possible to see how, for the absorption spectra, the ratio peak/shoulder stay constant in the RhB@NPs profile, index of a

very weak formation of the dye aggregates, it is present only a red shift with the same shape of 14 nm.

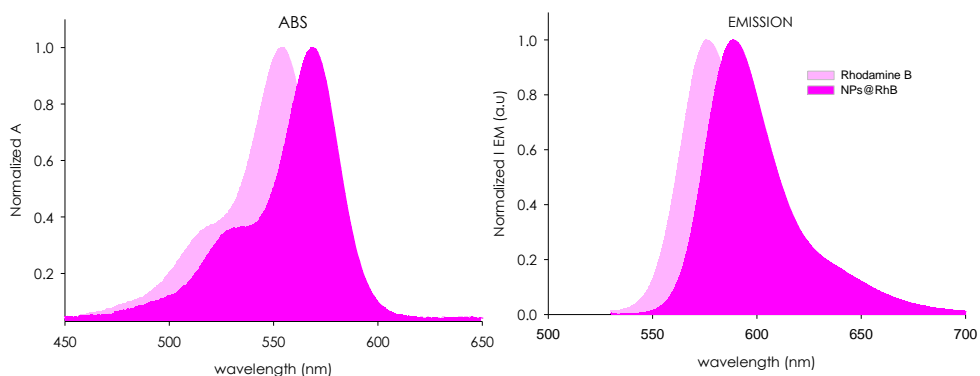


Figure 5.4 Normalized Absorption and emission spectra of RhB and NPs@RhB

In the emission spectra there is the same red-shift and, as demonstrated also from the low differences in their emission quantum yield (Tab. 5.1), the self-quenching of the dyes is not dramatic, as observed when this type of dye is constrain in a very little space. These data are in agreement of the calculated low number of dye/NP; from molar extinction coefficient and quantum yield of Rhodamine, indeed, it was also possible to obtain the number of dye/NP, almost 5 clearly from the ratio between the ϵ values, and calculate the NPs brightness⁴⁴.

Table 5.1 Photophysical data of RhB free in water and RhB@NPs in water

	RhB	NPs
ϵ	104 000	476 923
$\Phi_{EM}(H_2O)$	31% ⁴⁵	25%
B^a	32 240	119 230

^aBrightness (B) defines as $\epsilon \cdot \Phi$ ⁴⁴

The following step of insertion of the NPs in the polymer solution to obtain doped fibers with good characteristics was not trivial and required many attempts by Prof. Focarete group, in order to find the suitable solvent mixture and component concentrations. They studied the perfect solvent mixture to use due to the insolubility of NPs in only DCM solvent, in order to obtain good electrospun mat. Several parameters were changing working in humidity levels and temperature finding the perfect electrospinning condition using 35% w/v of PLGA 50:50, 2% NPs $W_{NPs}/W_{polymer}$ in DMF/DCM 70:30. Potential 18 Kv, distance needle-collector 20 cm, RT and Rh 70-73% with a flux speed of 0.8 mL/h.

Exploiting this acquired knowhow, It has been decided to use PLGA 50:50 as polymer due to its well-known degradation mechanism that, for its ratio, presents the shortest time degradation of the series (circa 2 months) that is compatible with the type of application of this work purpose.

In order to study the NPs release it has been followed the degradation of two mats electrofilated in the same exact conditions but one doped with the nanoparticles (RhB@**NPsmat**) and the other one non-doped (**plainmat**). We used different techniques, in collaboration with the group of prof. M. L. Focarete, to monitor the degradation in time, measuring GPC, TGA and DSC variations and the weight loss of the two samples left in PBS 10mM (pH7.4) for 50 days. In order to correlate the release of the NPs with these degradation data we quantified, in the same time scale, the presence of Rhodamine B via spettrophotometric and spettrofluorimetric measurements in the incubation solution. In particular, the incubation medium was removed, investigated, kept in a vial and replaced with an exactly same volume of clean PBS 10mM, initially each day and then with a lower frequency.

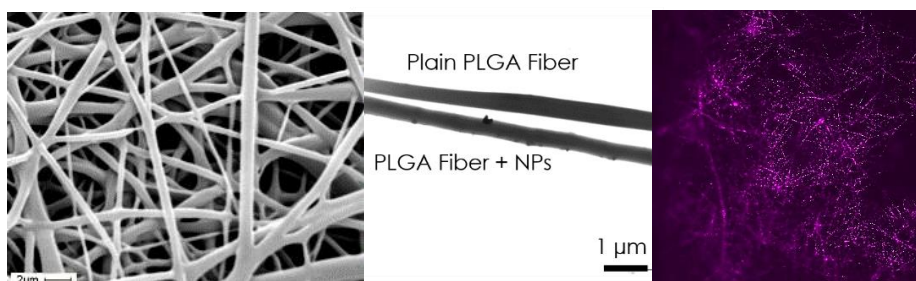


Figure 5.5 (left) SEM image of electrospun NPs@RhB inside PLGA fibers, (centre) TEM image of Plainmat fiber and fiber of RhB@NPsmat, (right) Confocal image of RhB@NPsmat †

For each sample we measured the absorption and emission spectra of the RhB contained in the NPs but, due to the higher sensitivity of the technique the emission data were less error affected. We therefore calculated the percentage of the NPs released monitoring the emission intensities variations in the emission maximum at 535 nm. The concentration of the NPs released was calculated respect to the sum of the initial loading of the RhB@**NPsmat**. A calibration line (data not shown) was defined preparing 7 different solutions with increasing amount of RhB@**NPs**, and measuring their emission. From the equation of the

extrapolating line plotting the emissions of the RhB@**NPs** respect to the NPs concentration is possible to calculate the perfect concentration of the NPs. In this way, it was possible calculate the initial level doping of the RhB@**NPs***mat* melting a weighted piece in DMF and measuring it emission. By the interpolation with the line was possible to estimate the total weight percentage of RhB@**NPs** loaded equal to 1.4%. From cumulative sum of the release calculated using the same procedure for any solutions, was possible to create the cumulative release shown in Fig. 5.6

In Fig. 5.6 are displayed the trend in gray of the degradation and the tendency of the release of the NPs in pink, From the graph is clear how the both lines during the time have the same trend. This is also visible from the SEM image collected at the same time from both doped and **plainmat** (Fig. 5.6. bottom.). This means that the release of the NPs is only due to the degradation of the PLGA and not to a leaking from the pores, furthermore, working on the modulation of the release times is possible to modulate the release times. This was an extremely important results because means that the insertion of NPs on the mat doesn't affect it degradation, and moreover, modulating the percentage of the composition of the polymer used, it is possible modulating directly the time of NPs release.

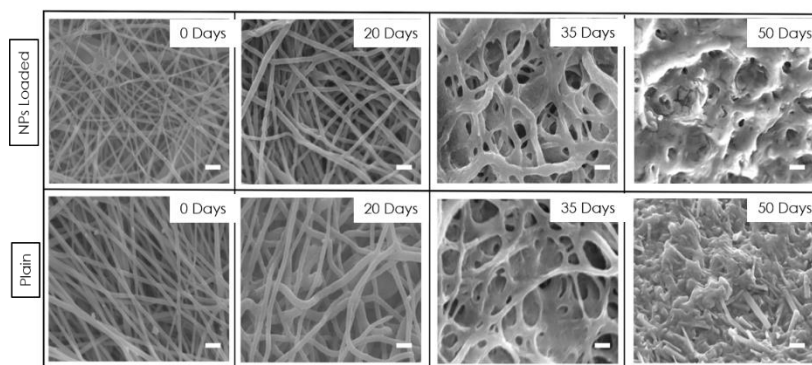
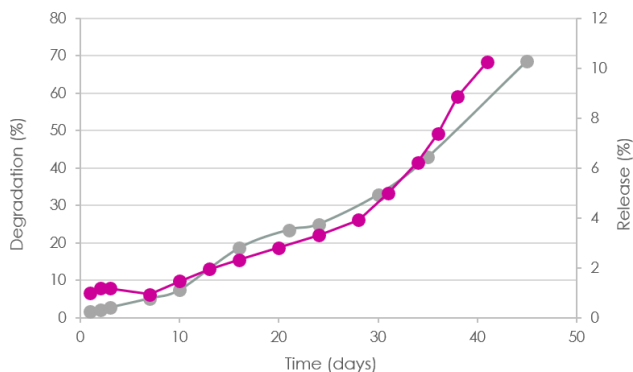


Figure 5.6 up: graph of the release on NP@RhB from NP@RhBmat (pink line) and degradation of the plainmat (gray line); bottom, SEM of the degradation of **plain mat** and RhB@NPsmat

At this stage of the work it has been investigated the influence of the modification of the NP surface on the doping and release in and from the polymeric matrix. We therefore proceeded with the modification of the outer shell of the NPs with a target moiety and in particular with a TTP (Tumor target peptides) that is able to specifically recognize a marker on the tumoral cells surface (such as membrane receptor) and driving drugs (in our case the NP) on the tumor tissue and to accumulate it there. For example, RGD⁴⁶ or NGR peptides link integrins or receptors on the membrane, usually overexpressed in tumoral tissue. We chose a specific sequence CGIYRLRS that recognizes a peptide sequence over expressed specifically by hepatic cancer cells. These sequence was derived by comparative phage display bio-panning on fresh surgical samples of hepatic metastases versus matched normal liver biopsies and proved to be selective for the stromal and the epithelial components of the metastasis⁴³.

In order to functionalize the NPs@**RhB** outer shell, we first modified the terminal part of PF127 used to form the micelles templating the synthesis of the NPs. We introduced an active site able to act as a reagent in a coupling reaction and in particular a carboxylic function. The synthetic procedure is shown in Fig. 3 and summarized hereafter: to a PF-127 and

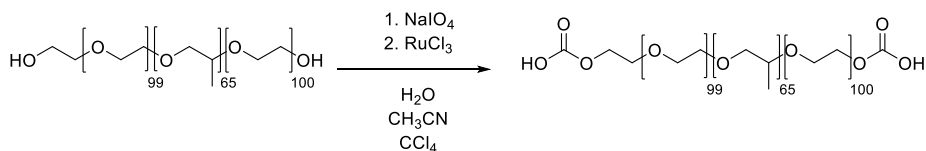


Figure 5.7 Schematization of PF127 functionalization

NaIO₄ mixture were added water, acetonitrile and carbon tetrachloride after RuCl₃ was added to the resulting biphasic solution and the reaction mixture was stirred overnight at RT, followed by repeated extractions with CH₂Cl₂. The reunited organic phases were dried over Na₂SO₄, filtered and evaporated to yield the final product in a yield, product that was characterized by NMR (see experimental section).

The RhB@NPs**COOH** synthesis was carried out as already reported (see cap 3) but using 70% of PF127 and 30% of COOH functionalized PF127. The resulting NPs, after dialysis, were again characterized by TEM (Fig. 5.8) and DLS analysis, showing a core around 9.5 nm and a d_H around 27 nm with a very good monodispersity (PDI=0.06±0.02), completely in line with the morphology of the non-derivatized NPs.

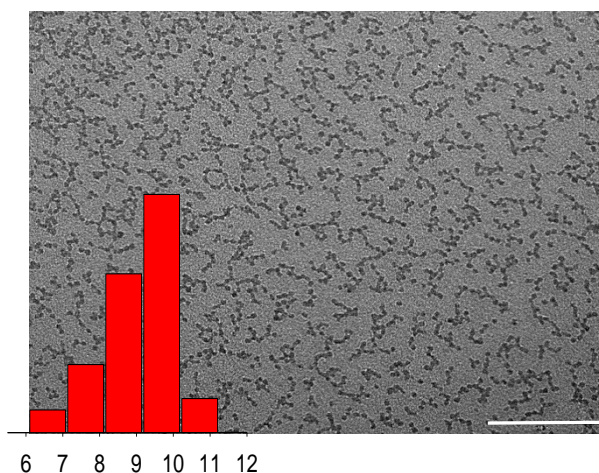


Figure 5.8 TEM image of RhB@NPsCOOH. Scale bar 200 nm

Photophysical characterizations shown in table 5.2 did not present any significant difference from the data obtained for the previous NPs and the average number of dye/NP resulted again 5.

Table 5.2 Photophysical data for RhB@COOHNPs and rhodamine B in water

	RhB	RhB@COOHNPs
λ_{Abs}	568	584
λ_{Em}	577	589
ϵ	104 000	470 437
$\phi_{EM}(H_2O)$	31%	24%
brighthouse	32 240	112 902

^aBrightness (B) defines as $\epsilon \cdot \Phi^{44}$

The further surface coupling reaction to introduce peptide CGIYRLRS (Fig. 5.9) was performed in borate buffer pH=8 with EDC.HCl and sulfo-NHS and the peptide was added (see experimental section). The solution was left stirring overnight at room temperature and purified dialysis over 2 days.

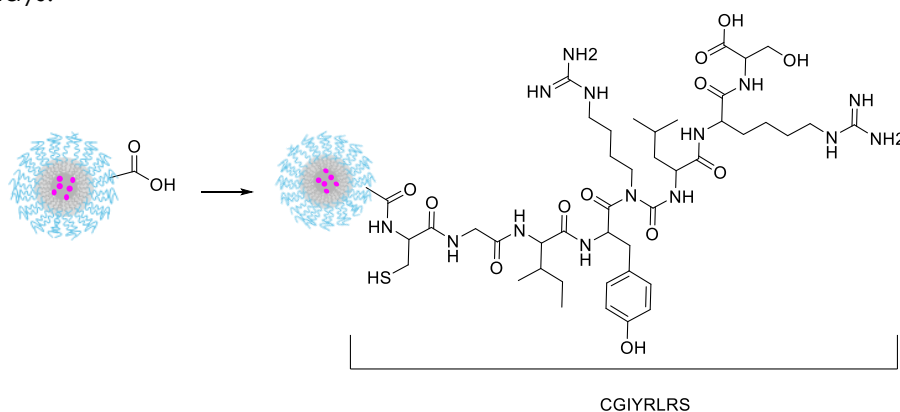


Figure 5.9 Schematic representation of coupling reaction between RhB@NPsCOOH and peptide

To investigate the number of peptide/NP present in the final product, that I will call for here after RhB@NPsPEP, we measured the zeta potential (ζ -potential) and we used the so called fluorescamine assay.

Table 5.3 ζ -potential of NPs with different shell modification

Sample	ζ-potential (mV)
<i>RhB@NPs</i>	-6.12±0.05 ^a
<i>RhB@NPsCOOH</i>	-7.04±0.09
<i>RhB@NPsPEP</i>	-2.51±0.02

^afrom literature pH 7.4⁴

The values of ζ -potential give a clear indication of the successful functionalization of the surface revealing a lowering of the value with the insertion of the carboxylic groups and a much less negative potential with after the functionalization with the peptides. This was reasonably expected for *RhB@NPsPEP* where CGIYRLRS presents positive sites, and its coupling decreases the number of the free -COOH sites. However, these values don't allow a precise quantification of the average number of peptides on the surface of each NP and for this we used the well-known fluorescamine assay. Fluorescamine (4-phenylspiro-(furan-2(3H),1'-phthalan)-3,3'-dione), is a non-fluorescent molecule that undergoes a chemical reaction in the presence of primary amines to give a fluorescent product; De Bernardo et al. demonstrated it is possible to quantify the number of the reacted amines measuring the emission signal of the reaction product⁴⁷. In order to prevent the detrimental amine protonation, the pH value must be controlled to and De Bernardo et al. suggest as the best pH range 8/8.5 for the quantification of amines in peptides and 8.5/9.5 for proteins. The quantum yield of the formed adduct, instead, is not depending on the environment, and it is constant in the pH range from 4.5 to 10.5. It has been decided to work at pH 8 that was obtained using a borate buffer solution.

As a first step, it has been made a calibration curve using butylamine that was added in increasing volumes to 5 different solution of DMSO containing inert *RhB@NPs* to simulate the same environment of the measurements on *RhB@NPsPEP*. After 150 minutes of reaction were recorded the the emission spectra ($\lambda_{exc} = 380$ nm) in a diluted solution in borate buffer (pH=8) (details in Experimental section).

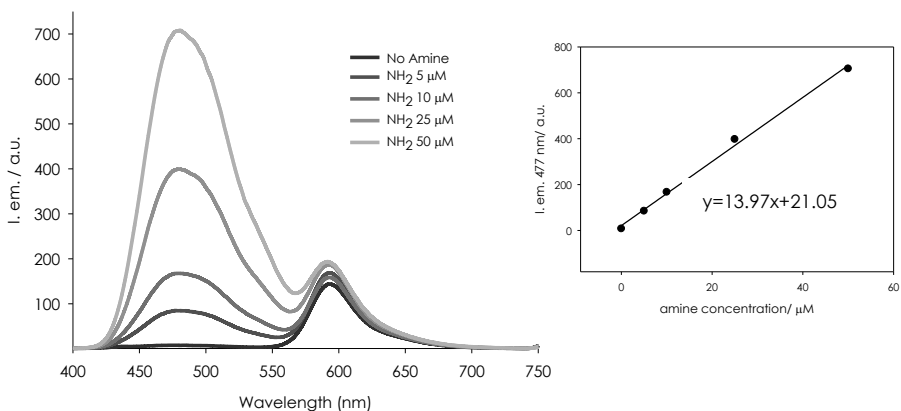


Figure 5.10 Emission spectra of the solutions of fluorescamine and NPs in DMSO with higher concentration of butylamine (left), calibration line obtained $R^2=0.9998$ (right)

Plotting the emission of the fluorescamine respect to the concentration of butylamine it was possible obtain a calibration line. From the line equation extrapolation, the obtained solution of RhB@**NPsPEP** was analyzed by emission of the rhodamine B and it was possible to determine the number of the amine in solution, in particular the arg.inine residues, and from this data the average number of peptides present on the surface of each NPs. This number resulted to be 6 peptides per NP.

With the aim to make a comparison between the release of RhB@**NPsCOOH** and RhB@**NPsPEP**, two new mats were electrospun: RhB@**NPsCOOHmat** and RhB@**NPsPEPmat**. The nanofibers of PLGA 50:50 w/w were obtained using the same procedure and parameters described above for RhB@**NPs**. The obtained mats presented good fibers of the same dimensions and aspect of the scaffolds prepared with the other particles (SEM Fig. 5.11 right) and again with a very good distribution, as reported for the RhB@**NPsPEPmat** in Fig. 5.11 only inside and along all the length of the fibers .

The characterization for RhB@**NPsCOOHmat** gave the same results, for this reason is not reported. From the extrapolation of the calibration line as explained above (see experimental section for the details), it resulted that the NPs loading for RhB@**NPsCOOHmat** was 1.34%, while for RhB@**NPsPEPmat** lower than expected, resulting in 0.64% respect to the total weight (PLGA+NPS). This could be due to the fact that the bioconjugation reaction occurs in water in very diluted conditions and to take the NPs in the DMF/DCM mixture used for the electrospinning they must be concentrated using ultracentrifuge equipped with 100K filters, the repetitive step of concentration of the NPs may have caused a loss of NPs leading to an overestimate initial NP concentration used. This step will be optimized in the future but the important data for the purpose of this study is the real initial loading amount to be able to calculate the percentage of released nanoparticles.

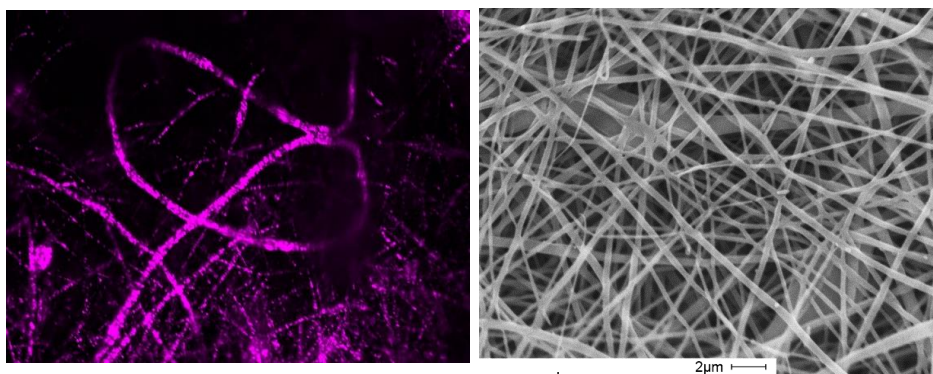


Figure 5.11 Confocal image and SEM image of RhB@PEPNPsmat

Following the same procedure used for RhB@**NPs** and the same measurement techniques, RhB@**NPsPEP** and RhB@**NPsCOOH** release were followed putting the scaffolds in PBS 10mM (pH 7.4) at 37°C. Collecting periodically the PBS of incubation and replacing it with the same volume of a new solution, it was possible to quantify, measuring the emission at 535 nm, the cumulative percentage of the released NPs, from the sum of the NPs quantity released during the time respect to their calculated total weight loaded. In the graph in Fig. 5.12 are reported the 3 different trends: in gray the degradation of the mat (already explained above), in pink the RhB@**NPsCOOH** release, and in green the release of the RhB@**NPsPEP**.

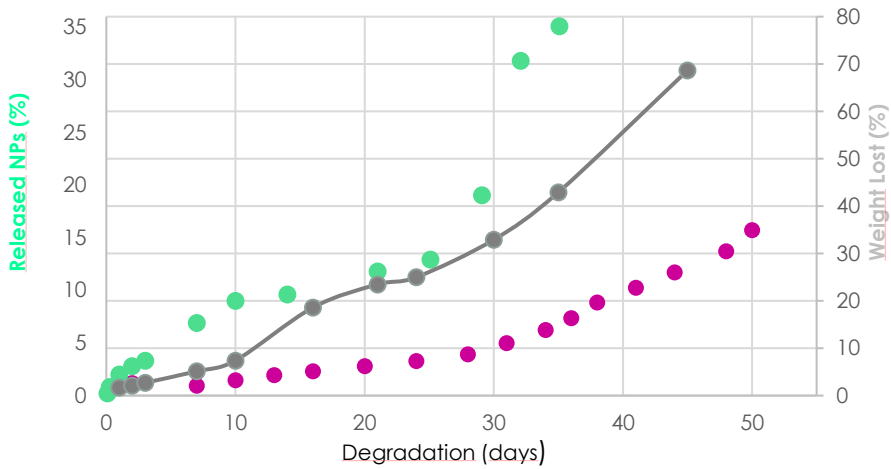


Figure 5.12 release of the NPsPEP@RhB green line, release of NPs@RhB pink line, degradation of the plainmat in gray.

The gray line it was already discussed before in Fig. 5.6; The pink line is the release of the RhB@**NPsCOOH**; the kinetic of the release is slow, the amount of NPs release in the first 10 days is less than 5% but in line with the result for the RhB@**NPs** showed in Fig. 5.6. Differently, the total amount of the release is 40% respect to the other NPs (Fig. 5.6). The green data are the ones obtained for the release of RhB@**NPsPEP**. The kinetic of the release is a little bit faster, infact in the first 336 hours (14 days) were released less than 10% of loaded RhB@**NPsPEP** with an initial burst of 4% after the first incubation day. However, a very interesting evidence is that the release of the RhB@**NPsPEP** is higher in percentage at any time with respect to the release of the RhB@**NPsCOOH** and even more than RhB@**NPs**. This could tentatively be due to the fact that the PLGA interacts with the PF127 of the NPs favouring their retention, in the RhB@**NPsCOOH** and even better for RhB@**NPsPEP** the presence of the COOH for the first one, and quite bulky peptide groups for the second one, could partially impede this interaction facilitating the release.

5.4 Conclusions and future steps

During this work carried out in collaboration with Prof. ML. Focarete from the University of Bologna, we were able to obtain an electrospun nanofiber mat of PLGA that is a biocompatible and biodegradable polymer, doped with luminescent PLuS NPs bearing or

not target moieties on their surface. In particular, after many attempts, we found the correct electrospinning parameters to obtain the PLGA fibers doped at a high degree and presenting the NPs homogeneously dispersed. The characteristic luminescence of the Rhodamine B doped NPs allowed the measuring of the emission intensity in the incubation water of the mat and the direct calculation of the number of particles released in time. All the experimental evidences indicate that the release of the NPs correlates very well with the degradation of the PLGA fibers in physiological conditions. This is a very important result since, being possible to modulate time profile of the degradation changing the polymer composition, it is consequently possible to tune the release of the eventual theranostic agent over time. Furthermore, the functionalization of the outer shell with a metastasis-specific peptide for hepatic cancer cells has shown that any modification of the outer shell of the NPs influences the interaction among the polymer and the nanoparticles themselves. This has again a non-negligible influence on the release and, in particular, the hindering peptide, decreasing the PEG-PLGA affinity, results in the same release profile in time but presenting a percentage of released NPs higher than the one of the non-targeted NPs at all times.

These very promising results will push further this research line and the next step will be to insert in the PluSNPs a therapeutic agent, such as an active species to allow photothermal therapy, transforming the particles in theranostic targeting agents. These new nanotools will be then inserted in a mat and tested *in vitro* experiments.

-
- 1 J. Xie, S. Lee, X. Chen, *Adv. Drug Deliv. Rev.* **2010**, *62*, 1064.
 - 2 B. Sumer, J. Gao, **2008**.
 - 3 M. Montalti, L. Prodi, E. Rampazzo, N. Zaccheroni, *Chem. Soc. Rev.* **2014**, *43*, 4243.
 - 4 E. Rampazzo, R. Voltan, L. Petrizza, N. Zaccheroni, L. Prodi, F. Casciano, G. Zauli, P. Secchiero, *Nanoscale* **2013**, *5*, 7897.
 - 5 S. A. Stewart, J. Domínguez-Robles, R. F. Donnelly, E. Larrañeta, *Polymers (Basel)*. **2018**, *10*, 1379.
 - 6 E. J. Lee, B. K. Huh, S. N. Kim, J. Y. Lee, C. G. Park, A. G. Mikos, Y. Bin Choy,

- Prog. Mater. Sci.* **2017**, *89*, 392.
- 7 B. D. Weinberg, E. Blanco, J. Gao, *J. Pharm. Sci.* **2008**, *97*, 1681.
- 8 Q. Xu, J. T. Czernuszka, *J. Control. Release* **2008**, *127*, 146.
- 9 J. A. Matthews, G. E. Wnek, D. G. Simpson, G. L. Bowlin, *Biomacromolecules* **2002**, *3*, 232.
- 10 R. L. Dahlin, F. K. Kasper, A. G. Mikos, *Tissue Eng. Part B Rev.* **2011**, *17*, 349.
- 11 J.-Z. Du, X.-J. Du, C.-Q. Mao, J. Wang, *J. Am. Chem. Soc.* **2011**, *133*, 17560.
- 12 T. J. Sill, H. A. von Recum, *Biomaterials* **2008**, *29*, 1989.
- 13 J. Venugopal, S. Low, A. T. Choon, A. B. Kumar, S. Ramakrishna, *J. Biomed. Mater. Res. Part A An Off. J. Soc. Biomater. Japanese Soc. Biomater. Aust. Soc. Biomater. Korean Soc. Biomater.* **2008**, *85*, 408.
- 14 A. Ratcliffe, *Matrix Biol.* **2000**, *19*, 353.
- 15 N. Bhardwaj, S. C. Kundu, *Biotechnol. Adv.* **2010**, *28*, 325.
- 16 Y. Christanti, L. M. Walker, *J. Nonnewton. Fluid Mech.* **2001**, *100*, 9.
- 17 B. Dhandayuthapani, Y. Yoshida, T. Maekawa, D. S. Kumar, *Int. J. Polym. Sci.* **2011**, 2011.
- 18 X. Zhu, W. Cui, X. Li, Y. Jin, *Biomacromolecules* **2008**, *9*, 1795.
- 19 W. Li, C. T. Laurencin, E. J. Caterson, R. S. Tuan, F. K. Ko, *J. Biomed. Mater. Res. An Off. J. Soc. Biomater. Japanese Soc. Biomater. Aust. Soc. Biomater. Korean Soc. Biomater.* **2002**, *60*, 613.
- 20 D. Kai, M. J. Tan, M. P. Prabhakaran, B. Q. Y. Chan, S. S. Liow, S. Ramakrishna, X. J. Loh, *Colloids Surfaces B Biointerfaces* **2016**, *148*, 557.
- 21 A. Greiner, J. H. Wendorff, *Angew. Chemie Int. Ed.* **2007**, *46*, 5670.
- 22 G. R. Mitchell, *Electrospinning: principles, practice and possibilities*, Royal Society of Chemistry, **2015**.
- 23 S. De Vrieze, T. Van Camp, A. Nelvig, B. Hagström, P. Westbroek, K. De Clerck, *J. Mater. Sci.* **2009**, *44*, 1357.
- 24 L. Wannatong, A. Sirivat, P. Supaphol, *Polym. Int.* **2004**, *53*, 1851.
- 25 R. P. Wool, *Macromolecules* **1993**, *26*, 1564.
- 26 S. L. Shenoy, W. D. Bates, H. L. Frisch, G. E. Wnek, *Polymer (Guildf)*. **2005**, *46*, 3372.
- 27 W. E. Teo, S. Ramakrishna, *Nanotechnology* **2006**, *17*, R89.
- 28 M. M. Stevens, J. H. George, *Science (80-.)*. **2005**, *310*, 1135.
- 29 A. Tamayol, M. Akbari, N. Annabi, A. Paul, A. Khademhosseini, D. Juncker, *Biotechnol. Adv.* **2013**, *31*, 669.
- 30 C. E. Astete, C. M. Sabliov, *J. Biomater. Sci. Polym. Ed.* **2006**, *17*, 247.
- 31 N. Samadi, A. Abbadessa, A. Di Stefano, C. F. Van Nostrum, T. Vermonden, S. Rahimian, E. A. Teunissen, M. J. Van Steenberghe, M. Amidi, W. E. Hennink, *J. Control. Release* **2013**, *172*, 436.
- 32 V. Pavot, M. Berthet, J. Rességuier, S. Legaz, N. Handké, S. C. Gilbert, S. Paul, B. Verrier, *Nanomedicine* **2014**, *9*, 2703.
- 33 G. Crotts, T. G. Park, *J. Microencapsul.* **1998**, *15*, 699.
- 34 B. S. Zolnik, D. J. Burgess, *J. Control. Release* **2007**, *122*, 338.
- 35 S. Fredenberg, M. Wahlgren, M. Reslow, A. Axelsson, *Int. J. Pharm.* **2011**, *415*, 34.
- 36 K. G. H. Desai, K. F. Olsen, S. R. Mallery, G. D. Stoner, S. P. Schwendeman,

- Pharm. Res. **2010**, *27*, 628.
- 37 N. Faisant, J. Akiki, F. Siepmann, J. P. Benoit, J. Siepmann, *Int. J. Pharm.* **2006**, *314*, 189.
- 38 C. Berklund, M. King, A. Cox, K. K. Kim, D. W. Pack, *J. Control. release* **2002**, *82*, 137.
- 39 N. Peppas, *Pharm. Acta Helv.* **1985**, *60*, 110.
- 40 S. E. Bae, J. S. Son, K. Park, D. K. Han, *J. Control. Release* **2009**, *133*, 37.
- 41 B. Han, S. Gao, X. Zhang, H. Tian, H. Wang, Z. Shang, *J. Appl. Polym. Sci.* **2010**, *117*, 2754.
- 42 T. Nguyen, M. B. Francis, *Org. Lett.* **2003**, *5*, 3245.
- 43 M. Soster, R. Juris, S. Bonacchi, D. Genovese, M. Montalti, E. Rampazzo, N. Zaccheroni, P. Garagnani, F. Bussolino, L. Prodi, *Int. J. Nanomedicine* **2012**, *7*, 4797.
- 44 L. Prodi, *New J. Chem.* **2005**, *29*, 20.
- 45 D. Magde, G. E. Rojas, P. G. Seybold, *Photochem. Photobiol.* **1999**, *70*, 737.
- 46 S. Kunjachan, R. Pola, F. Gremse, B. Theek, J. Ehling, D. Moeckel, B. Hermanns-Sachweh, M. Pechar, K. Ulbrich, W. E. Hennink, *Nano Lett.* **2014**, *14*, 972.
- 47 S. De Bernardo, M. Weigele, V. Toome, K. Manhart, W. Leimgruber, P. Böhlen, S. Stein, S. Udenfriend, *Arch. Biochem. Biophys.* **1974**, *163*, 390.
- 48 *J Bone Miner Res* **2005**, *20*, 848
- 49 *Wound Rep Reg* **2016**, *24*, 223–236
- 50 *Int. J. Mol. Sci.* **2014**, *15*, 3640-3659
- 51 *J.Arthroscopic and Related Surgery*, **2010**. *26*, 821

CAP. 6

LUMINESCENT METALS COMPLEXES AND GOLD NPS AS POTENTIAL BUILDING BLOCKS IN NANOMEDICINE

This last chapter of my thesis merges some research work that I have developed on different species that could have, or could take to, interesting properties to be exploited in building block moieties for the design of multifunctional platforms for applications in nanomedicine. In particular, it has been focussed the attention on NIR emitters that are luminescent component of election for medical application *in vivo* due to the range 650-1350 nm of the so called *biological optical window*, that indicates where light has its maximum depth of penetration in tissues. In the framework of two different collaborations, I have studied rhenium and lanthanide metal complex from a photophysical point of view both in solution and in the solid state.

Moreover, besides luminescent components useful as signalling units, medical applications need therapeutic ones and, among them, gold nanoparticles have an important role since functionalized gold nanoparticles with controlled geometrical and optical properties are widely studied for laser phototherapy of cancer cells and for the targeted delivery of drugs, DNA and antigens. I present here a basic study that aims to assess the possible pro-oxidant or antioxidant effects induced by gold nanoparticles. In fact, nanoparticles are often found to be toxic, and one of the most frequently reported mechanisms of nanoparticle toxicity is the generation of free radicals. Therefore, the elucidation of the possible pro-oxidant activity of nanoparticles is among the key features determining their safety and suitability for specific applications.

6.1 Rhenium(I) complexes.

Effects of the substituents on the terpyridine k^3N rhenium(I) dicarbonyl complexes in NIR emission

There is always a need to expand the range of already known luminescent tools suitable for a large number of applications in different field and the NIR emitters are of particular interest for energy, telecommunication and medical purposes, for example the NIR region is the one of interest for *in vivo* applications.

Professor G. Hanan with his group designs, prepares and characterizes since many years a wide range of NIR emitting metal complexes¹⁻³, and in the latest period he moved his attention in particular on Re-complexes⁴. Since the first report on this subject in the early 1970s,¹ low spin d_6 polypyridyl rhenium(I) carbonyl complexes have drawn the interest of the scientific community. Their photophysical and electrochemical properties have been thoroughly studied and applied in a multitude of the fields such as solar energy harvesting devices⁵ and solar to chemical energy conversion⁶, light emitting devices⁷ as well as photodynamic therapy and cellular imaging^{8,9}. G. Hanan et al⁴ recently

focused their attention on tri-coordinated terpyridine complexes as they offer a suitable geometry for predictable assembly depending on the facial or meridional arrangement of the ligands. In a recent report, Dempsey et al. working with a Re bipyridine complex successfully pushed their absorption to the red, matching the $\kappa_3\text{N}$ terpyridine values, by modifying the nature of the ligands completing the coordination sphere¹⁰. The simplicity of the synthesis of the Re precursors and their supramolecular architecture as well as the ease of fine-tuning of the optical properties by varying the bidentate ligand certainly contributed to the ascension in popularity of this class of compounds.

However, the $\kappa_3\text{N}$ terpyridine based complex $[\text{Re}(\text{CO})_2(\text{py})(\kappa_3\text{N}-4\text{pytpy})]^+$ (with py standing for pyridine and 4pytpy being 4'-(4-pyridyl)-2,2':6',2''-terpyridine), published by professor Hanan, is the only case presenting a near-infrared emission band at room temperature, with a maximum around 940 nm⁴.

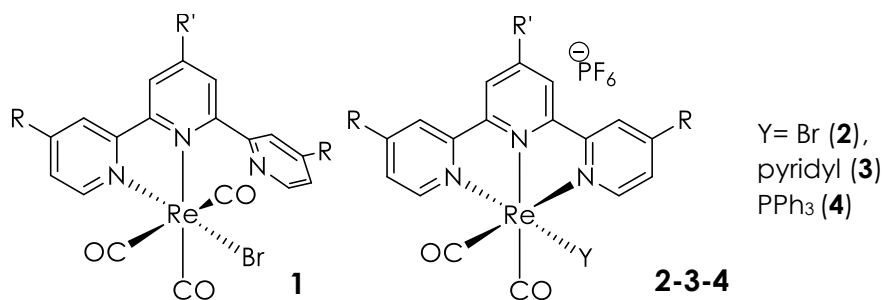


Figure 6.1 structures of complexes that compose the series called here **1**, **2**, **3** and **4**.

Inspired by this very interesting result, they decided to investigate the effect of varying substituent and ancillary ligand on the emission of $\kappa_2\text{N}$ and $\kappa_3\text{N}$ terpyridine rhenium complexes in order to gain a better understanding of the parameters influencing their electronic properties. To this goal, they prepared four series of compounds (numbered as **1** to **4**), with different ancillary ligands, that are schematized in Fig. 6.1. Each series is composed by complexes that differ for the substituent of the terpyridine ligand as shown in Fig.6.2.

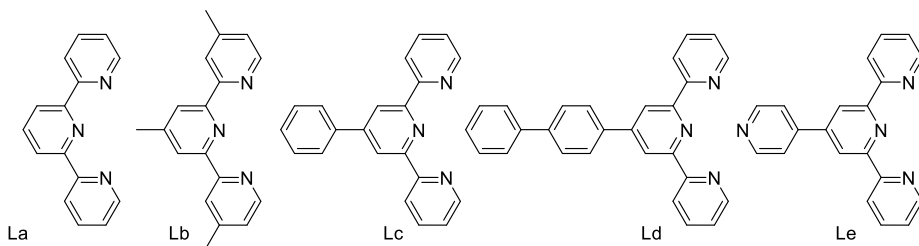


Figure 6.2 Substituted terpyridine ligands used in the different rhenium complexes series.

First Prof. Hanan group performed DFT calculations on all the complexes and they showed how the conversion of 1a-e into 2a-e causes a significant increase in energy for the higher occupied levels. The found trend was expected since the replacement of a strongly π -accepting CO ligand by the terpyridine ligand should lead to the destabilization of the metal centered π orbitals, how showed in Fig 6.3.

Moreover, they found a stabilization of LUMO levels increasing the conjugation of the terpyridine once in its meridional coordination mode. The LUMO of complexes 1a-e is delocalized over the coordinated bipyridine-like moiety and the increase in conjugation does not really affect its energy while the LUMO+1 and LUMO+2 involve individual pyridine ring and the extended conjugation modifies their relative energies. Going from the neutral 2a-e to the cationic complexes 3a-e and 4a-b leads to an overall stabilization by several hundred meV similarly when looking at the unoccupied levels but with a stronger impact on the occupied levels from the triphenylphosphine in 4a-b compared to the pyridine in 3a-e.

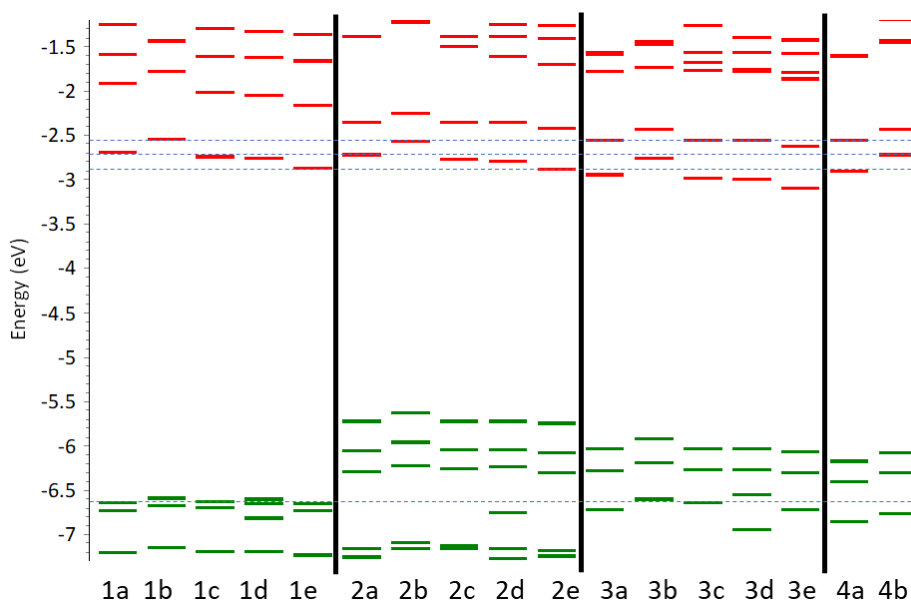


Figure 6.3 Partial energy diagram centered on frontier orbitals for all complexes modeled in an acetonitrile continuum by DFT (PBE0/LanL2DZ). LUMO levels red, HOMO in green

My contribution in the framework of this research has been to photophysically characterize all the complexes.

6.1.1. Aim of the work

The aim of my contribution in this work in collaboration with Professor G. Hanan is the careful and exhaustive photophysical characterization of different $\kappa_2\text{N}$ and $\kappa_3\text{N}$ terpyridine Re(I) carbonyl complexes of general formula $[\text{Re}(\kappa^x\text{N-Rtpy})(\text{CO})_y\text{L}]^{n+}$. By varying the coordination modes of terpyridines ligands, their substituent and the nature of the axial ligands in these complexes, it is possible to tune their electronic and photophysical properties as theoretical calculation had predicted.

The photophysical characterization of the $\kappa^3\text{N}$ terpyridine rhenium complexes shown in Fig 6.4 and their comparison with the DFT calculation results will help to gain a better understanding of the parameters involved in their NIR emission. The good correlation of the

results could demonstrate the possibility to finely tune the properties of these complexes via simple structural variations, opening up a path to the design of application specific complexes.

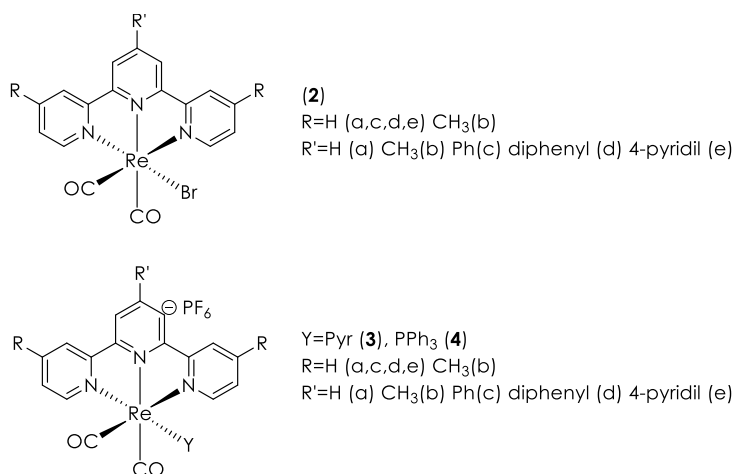


Figure 6.4 structures of the complexes of the series 2, 3 and 4

6.1.2 Result and discussion

The synthesis of all the complexes shown in fig 1 was carried on in Montreal following the synthetic procedures already reported in literature^{11,12}. I describe here the photophysical characterization of the compounds reported in Fig. 6.5 while the ones of the series 1, k²N terpyridine complexes, are not present in this thesis because already studied in a previous research and presenting the emission in the UV-VIS range. The spectroscopic characterization of series 3 and 4 were performed in CH₃CN solution while this was not possible for series 2 due to the very low solubility of these complexes that are neutral. Thus, the measurement for series 2 were performed in DMSO. For all compounds, the measurements were conducted on solutions with a concentration of 5 x 10⁻⁵ M. The absorption spectra of all the series are reported in Fig 6.5.

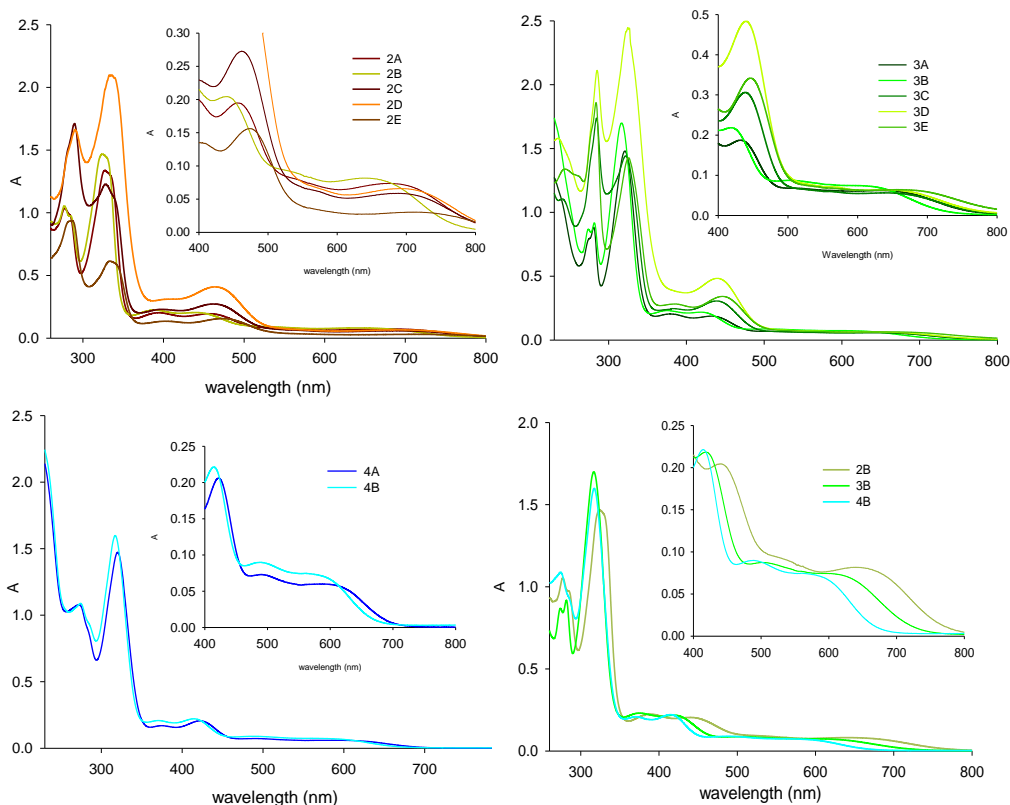


Figure 6.5 Absorption spectra of respectively, series 2 (in DMSO) , 3 and 4 (in CH₃CN) Absorption spectra of series b.

All the $\kappa^3\text{N}$ complexes absorption spectra present three large transitions bands in the visible region between 400 nm and 700 nm as it can be seen by the insets of Fig. 6.5. The replacement of the bromide by pyridine going from series **2** to series **3** leads to a blueshift of these bands of some tens of nanometers, and the triphenylphosphine complexes **4** present an even larger blueshift. The transitions in the visible correspond in all cases to Metal-Ligand to Ligand Charge Transfer (MLLCT). The various substituents allow for fine-tuning of the absorption maxima, the more electron rich ligand **Lb** leading to higher wavelengths in all cases while the aromatic substituents on the 4' position for **Lc**, **Ld** and **Le** cause a slight redshift compared to **La**. The 4-pyridyl in **Le** presents a stronger effect, in agreement with its higher electron withdrawing properties.

The emission spectra were recorded exciting all compound at 440 nm and using a Ge detector that presents a high sensitivity in the NIR range.

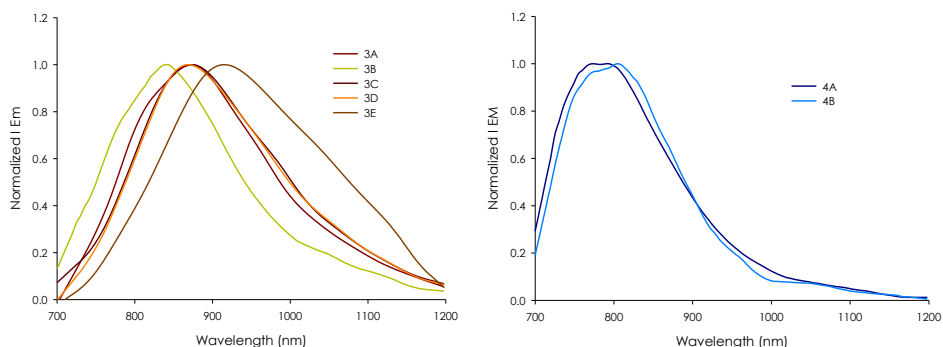


Figure 6.6 Emission spectra of complexes of series 3 and 4

In table Table 6.1 are reported the wavelength of the emission maxima and the corresponding emission quantum yields (Φ_{EM}) for all the investigated complexes. The species of the **2** series are all non-emissive, the presence of bromide could be envisaged to have a role in this, even if TD-DFT predicted an emission below 900 nm. Exchanging the bromide ligand for pyridine or triphenylphosphine we obtain series **3** and **4** that, instead, show emission in the NIR region with maxima in the range 780-940nm as reported in table 6.1. The emission wavelengths vary depending on the substituent in the 4' position of the terpyridine presenting the lower wavelength for the electron rich ligand **Lb** and the most red-shifted maxima for the electron poor ligand **Le**.

Table 6.1 Data of quantum yield emission of series 2, 3 and 4 complexes

	2a-e	3a	3b	3c	3d	3e	4a	4b
λ_{EM}	-	870	840	876	865	940	800	782
$^a\Phi_{EM}$ (%)	-	0.13	0.18	0.13	0.11	0.02	0.71	0.4

^a calculated respect standard IR125 ¹³

The quantum yield of these complexes are quite unexpectedly higher in comparison with other neutral κ^2N complexes already studied. This could be explained by the change in the nature of the emissive state, as supported by theoretical calculations made by the group of Prof. Hanan. Indeed, while the κ^2N -tpy halide complexes have a complex mix of MLCT, LLCT and LC contributions in their lowest transition, in the κ^3N

complexes, the lowest transition are purely metal-ligand-to-ligand (MLLCT) in nature, the density being transfer from the $\{\text{Re}(\text{CO})_2\}$ fragment to the terpyridine ligand π^* orbital.

6.1.3 Conclusions

The results reported in this section demonstrate the structure-properties relationship in a series of carbonyl rhenium(I) complexes based on substituted terpyridine ligands of general formula $[\text{Re}(\kappa^x\text{N-Rtpy})(\text{CO})_y\text{L}]^{n+}$. In these compounds, the terpyridines can adopt both bidentate ($\kappa^2\text{N}$) and tridentate ($\kappa^3\text{N}$) coordination modes associated with three or two carbonyls, respectively. The experimental evidences show that the $\kappa^3\text{N}$ complexes' absorption profiles present three large bands covering the whole visible range between 400 and 800 nm. The substituents on the tpy ligand influence the position of the absorption maxima, the more electron rich ligand **b** leading to higher wavelengths in all cases. The aromatic substituents on the 4' position for **c**, **d** and **e** cause a redshift compared to **La**, the 4-pyridyl having a stronger effect, in agreement with its higher electron withdrawing properties.

It was interesting to note that no emission is observable with Br^- as axial ligand L but when L is changed from the halide to pyridine or triphenylphosphine, these cationic complexes become near-infrared emitters. The emission maxima are in the range between 840-950 nm for the pyridine compounds and 780-800 nm for the triphenylphosphine ones. The quantum yields are unusually high for this class of complexes with values between 0.02 and 0.7 %. Theoretical calculations made in Montreal indicate that this could be attributed to a change in the nature of the excited state going from a $\kappa^2\text{N}$ -tpy halide complexes presenting MLCT, LLCT and LC contributions in their lowest transition, to $\kappa^3\text{N}$ complexes where the lowest transition are purely metal-ligand-to-ligand (MLLCT) in nature.

All these results demonstrate that it is possible to finely tune the properties of these complexes via simple structural variations, opening a path to the design of application specific complexes including the biomedical ones that very often require NIR emission properties.

6.2 Lanthanide (Ln) complexes. Studies of Ln-Ag bimetallic coordination framework.

In the past decades metal–organic frameworks (MOFs) have emerged as a new class of porous materials showing great potential in building fluorescent materials^{7–10} as well as gas adsorption/separation^{14–16}, heterogeneous catalysis¹⁷, drug delivery¹⁸, and other applications¹⁹. MOFs are constructed from organic ligands and inorganic metal nodes, possessing high porosity and large internal surface areas. The structure of MOFs is not only tunable through designing the organic ligand and choosing metal clusters, but also can be modified via postsynthetic modifications^{20,21}. Recently, rigid MOFs have been demonstrated to be able to fix fluorescent ligands and exhibit excellent fluorescence properties²², making MOFs effective candidates having potential to design and construct various fluorescent materials. Fluorescent MOFs have been widely evaluated for chemical sensing²¹, optoelectronic/electrochemical devices^{23–25}, light-emitting devices and biomedicine²⁰. Combination of lanthanide metalloligands and transition metal ions in one MOF could represent a suitable way for isolating new convenient materials with interesting luminescent properties for different applications. The research on luminescent LnMOFs has been focused on their visible emission features, whereas emissive NIR LnMOFs (usually Ln³⁺ = Yb³⁺, Nd³⁺ and Er³⁺) are barely studied, mainly because: (i) most ligands are poor sensitizers of Yb³⁺, Nd³⁺ and Er³⁺, with molar absorption coefficients typically lower than 10 L mol⁻¹ cm⁻¹, 2 and (ii) the energy gap between the first excited emitting state and the fundamental level is quite small (ca. 5400 and ca. 6500 cm⁻¹ for Nd³⁺ and Er³⁺, respectively) and easily matched by the C–H, C–C, O–H, and N–H vibrations of the organic framework, which provide suitable non-radiative channels. In order to investigate the possibility to work in the range of NIR emission. Among the investigation on the possibility to obtain new suitable species based on lanthanide Metalloligands it was studied their use in the assembly of Ln-Ag bimetallic coordination framework.

6.2.1 Aim of the work

The goal of this project, published in collaboration with Prof. L. Carlucci, was the preparation and successively the characterization both photophysical and by X-ray of $\text{NEt}_4[\text{Ln}(\text{L}^1)_4]$ [$\text{Ln} = \text{Eu}$ (**1a**, **1a***), La (**1b**), Nd (**1c**), Tb (**1d**)] . $\text{NEt}_4[\text{Ln}(\text{L}^2)_4]$ [$\text{Ln} = \text{Eu}$ (**1e**), Nd (**1f**)]. The high flexibility in the stereochemistry of these metalloligands allows for the formation of a new type of secondary building unit (SBU) in the reaction with silver cations. This SBU consists of a “pincer-like” moiety, in which a silver cation coordinates to two central carbon atoms of two different diketonate ligands of the same metalloligand. The different polymeric products could be organized on the basis of the number of these SBUs. Accordingly, species with 0, 1, and 2 “silver-pincers” per ML have been obtained. Were then also synthesized and characterized the assembled lanthanide-silver coordination networks with the $[\text{Ln}(\text{L}_1)_4]$ – Metalloligands; in particular 1D Coordination Networks $[\text{Ln}(\text{L}^1)_4\text{Ag}]$ [$\text{Ln} = \text{Eu}$, La , Nd , and Tb (**2a–2d**)] and 2D Coordination Networks $[\text{Ln}(\text{L}^1)_4\text{Ag}]$ [$\text{Ln} = \text{Eu}$, La , and Nd (**3a–3c**)]. In particular, for what concern the aim of my work, it has been deeply study the entire characterization of the abovementioned MOF, especially the role of the silver ion in the coordination network structures.

6.2.2 Results and discussion

After all synthetic work reported in the paper²⁶ and the entire X ray characterization made by Prof. L. Carlucci, there were performed all photophysical characterization. In particular the studied species were: $\text{HL}^1 \text{NEt}_4[\text{Eu}(\text{L}^1)_4]$ (**1a**), $1\text{D}-[\text{Eu}(\text{L}^1)_4\text{Ag}]$ (**2a**), $2\text{D}-[\text{Eu}(\text{L}^1)_4\text{Ag}]$ (**3a**), $2\text{D}-[\text{Eu}(\text{L}^1)_4\text{Ag}_2]\text{PF}_6$ (**4a**), $\text{NEt}_4[\text{La}(\text{L}^1)_4]$ (**1b**), $\text{NEt}_4[\text{Nd}(\text{L}^1)_4]$ (**1c**), $1\text{D}-[\text{Nd}(\text{L}^1)_4\text{Ag}]$ (**2c**), $2\text{D}-[\text{Nd}(\text{L}^1)_4\text{Ag}]$ (**3c**), $\text{NEt}_4[\text{Tb}(\text{L}^1)_4]$ (**1d**), HL^2 , $\text{NEt}_4[\text{Eu}(\text{L}^2)_4]$ (**1e**) and $\text{NEt}_4[\text{Nd}(\text{L}^2)_4]$ (**1e**). In fig. 7 are reported the structures of HL^1 and HL^2 .

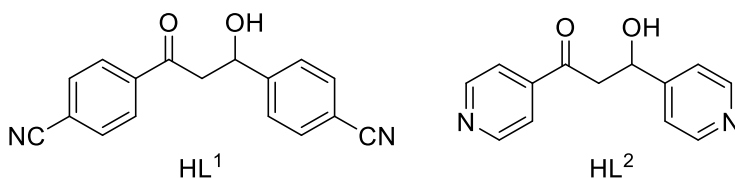


Figure 6.7 structures of HL^1 and HL^2

The high flexibility in the stereochemistry of these metalloligands allows for the formation of a new type of secondary building unit (SBU) in the reaction with silver cations. This SBU consists of a “pincer-like” moiety, in which a silver cation coordinates to two central carbon atoms of two different diketonate ligands of the same metalloligand.

To clarify the studied structures is reported below the schematic representation of the silver pincer-like SBUs observed in two polymer families described below. One silver pincer-like SBU (top) is formed by one ML and one silver cation interacting with the central carbon atoms of two diketonate ligands. Such neutral SBU is present in polymeric families **2** and **3**. Two silver pincer-like SBUs (bottom) are formed by one ML and two silver cations, each of which interacts with the central carbon atoms of two diketonate ligands. Such cationic SBU is present in polymeric family **4**.

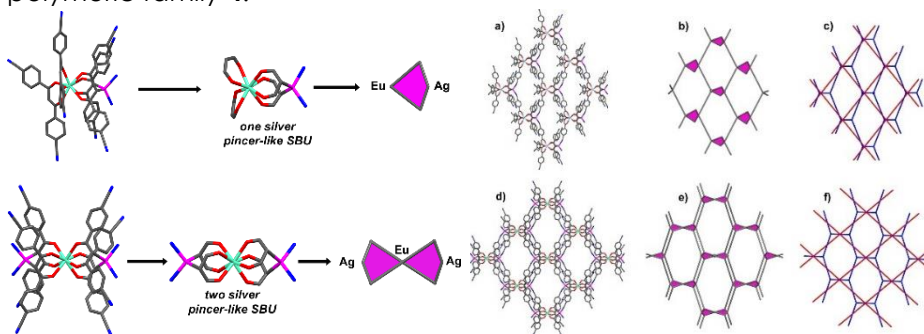


Figure 6.8 left: Schematic representation of the silver pincer-like SBUs observed for polymeric families **2**, **3** and **4**. One silver pincer-like SBU (top) is formed by one ML and one silver cation interacting with the central carbon atoms of two diketonate ligands (**2** and **3**). Two silver pincer-like SBUs (bottom) are formed by one ML and two silver cations, each of which interacts with the central carbon atoms of two diketonate ligands (**4**). Right: Comparison of the two families of 2D polymeric structures (**3** in the upper row and **4** in the lower row). In the left column (a and d) the molecular drawings; in the middle column (b and e) the corresponding schematic drawings, in which the different types of SBU have been highlighted in pink; and in the right column (c and f) the simplified networks obtained by considering the silver and lanthanide atoms as nodes (in blue) or the SBUs as nodes (in red).

The entire photophysical characterization was performed and resumed in table 6.2. All the monomeric lanthanide complexes $NEt_4[Ln(L)_4]$ were characterized both at room temperature and at 77 K in dichloromethane solution.

Table 6.2 Photophysical Properties of the Ligands, the Metalloligands, and the Heterometallic Coordination Networks ^a

Compound	Abs Max (nm)	Em Max (nm)	Lifetimes (μS)
HL¹	255, 352	405	3 ns
1a	252, 368	615	41, 21 pw
2a		615 pw	20 pw
3a		615 pw	15 pw
4a		615	20 pw
1b	256, 365	380 ^b	2 ns ^b
1c	256, 367	893, 1065	c
2c		894 _{pw} , 1070 _{pw}	c
3c		894 _{pw} , 1070 _{pw}	c
1d	256, 367	390 ^b	2 ns ^b
HL²	243, 338	400	5 ns
1e	290, 350	615	140, 480 _{pw}
1f	255, 367	890, 1064	c

^a All the values determined in dichloromethane solution at room temperature, apart from the ones in round brackets, determined at 77 K, and the ones with the subscript "pw", measured for the microcrystalline powders. b Data relative to the LC emission. c Not possible to measure with our instrumentation

All the solid measurements were performed constrain the solid powder between two glass slides and were recorded the emission spectra.

As presented in Tab 6.2, **HL¹** presents absorption maxima at 255 and 352 nm and a large and not structured fluorescence band centered at 405 nm at room temperature (both in solution and in the solid state) with a low emission quantum yield ($<10^{-4}$). This band has been attributed to a spin allowed fluorescence transition because of its energy and excited state lifetime. Similar characteristics are visible also for **HL²**, but with slightly higher absorption energies and emission that is at 400 nm in solution, with a similar quantum yield to **HL¹**.

A first parameter to be observed is the energy of the ligand-centered states in the complexes. Due to their low intrinsic absorption, a high brightness for lanthanide ions is possible only if there is an efficient antenna effect through the light excitation of suitable ligands, together with and an efficient energy transfer process to the metal-centered states of the metal ions. With this aim, we carefully characterized the lanthanum complex **1b** since La^{3+} , presenting the close shell electronic configuration of xenon, does not usually have metalcentered (MC) emission bands²⁷. The absorption spectrum of the complex presents the features of the ligand absorption profile, but with a shift in the lower wavelength band to 365 nm, as expected upon metal complexation. Since the absorption spectrum of **1b** is superimposable with those of all the other complexes with **HL¹**, similar complexation environments are supposed to be for all the **1a-1d** species (Fig 6.9)

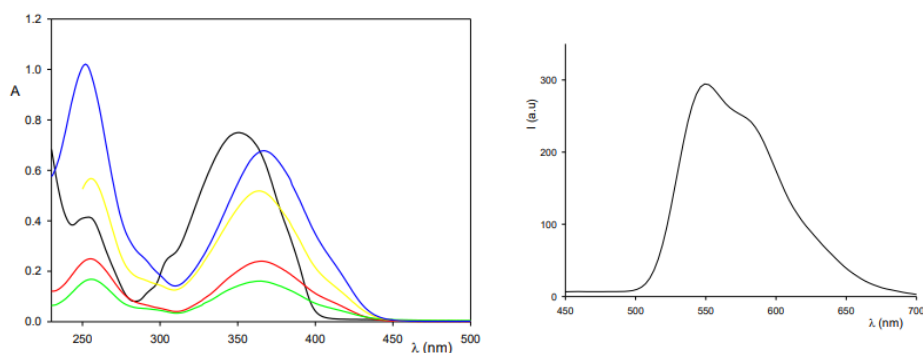


Figure 6.9 left: Absorption spectra in CH_2Cl_2 of the free ligand **HL¹** (black) and of the metallogligands **1a** (blue), **1b** (green), **1c** (yellow), **1d** (red). Right Emission spectrum in CH_2Cl_2 at 77 K of **1b**, λ_{ex} 350 nm

A broad fluorescence band at ca. 380 nm is visible for the emission spectrum of **1b** at room temperature, with a lifetime of 2 ns, while at 77 K a lower-energy (555 nm), longer-lived (2.2 ms) band is present, attributable to a ^3LC transition. According to these data, it is notable that the ^3LC state (19250 cm^{-1}) is lower in energy than the MC^5D_4 state of the Tb^{3+} ion, suggesting that the ligand HL^1 is not able to sensitize the typical MC emission of this ion. Indeed, **1d** does not present no typical MC emission is present from **1d** in solution, even at low temperature.

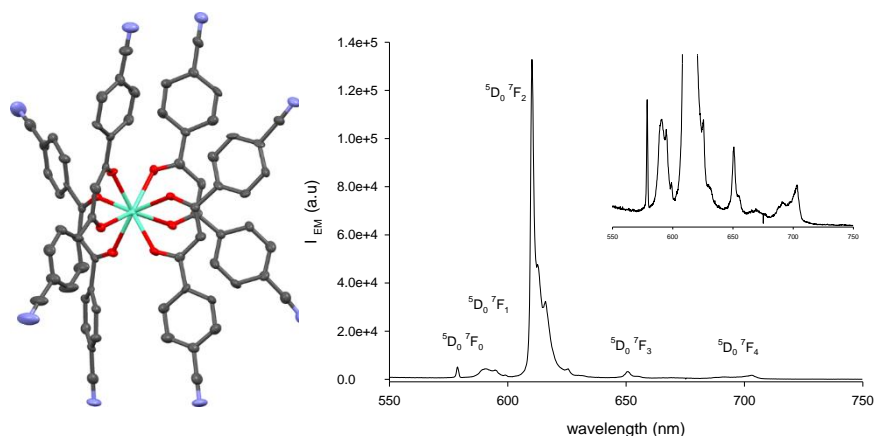


Figure 6.10 left: View of the europium the tetra-chelate complex in the crystal structure **1a**. Hydrogen atoms have been omitted for clarity. Right: Emission spectra of **1a**

The emission spectrum of compound **1a** reveals the typical MC bands of the europium ion (Fig. 10), and it is possible to observe the $0\text{ D}_5 \rightarrow 7\text{ F}_j$ transitions with j from 0 to 4. The presence of the forbidden $0\text{ D}_5 \rightarrow 7\text{ F}_0$ and $0\text{ D}_5 \rightarrow 7\text{ F}_3$ transitions and, above all, the high value of the ratio between the $0\text{ D}_5 \rightarrow 7\text{ F}_2$ and $0\text{ D}_5 \rightarrow 7\text{ F}_1$ intensities are in line with a low symmetry environment of the Eu^{3+} ion, lacking an inversion center, in agreement with the geometry observed in the crystal structure (Fig. 10 left). For this case, the energy of the ^3LC transition is compatible with a good energy transfer from the ligand to the metal center. However, low values were observed for the measurements of its lifetime (Table 6.2) an unexpected result for similar compounds (lifetimes in the range of hundreds of microseconds), evidencing the presence of favorable nonradiative deactivation pathways. The energy of the MC state is close to the one of the ^3LC transition, so that the sensitization of the MC state is possible but with the establishment of a thermally activated equilibrium

between the two states. This assumption is supported by a 10-fold increase of the emission lifetime observed at low temperature (77 K). The neodymium complex **1c** is also efficiently populated by the ligand, presenting the typical IR bands at 893 and 1065 nm with an interesting emission quantum yield of ca. 2%. The luminescence spectra of the two complexes **1e** and **1f** are very similar to those observed for their L1 homologues, but with a longer lifetime (Table 6.2), probably due to the higher energy of its ³LC state, a condition that would shift the above-mentioned equilibrium in favor of the europium MC state. Due to the lack of luminescence of the lanthanum and terbium complexes, it was possible to characterize only the ¹D and ²D polymers containing europium (**2a**, **3a**, and **4a**, Figure 6.11) and neodymium (**2c** and **3c**)

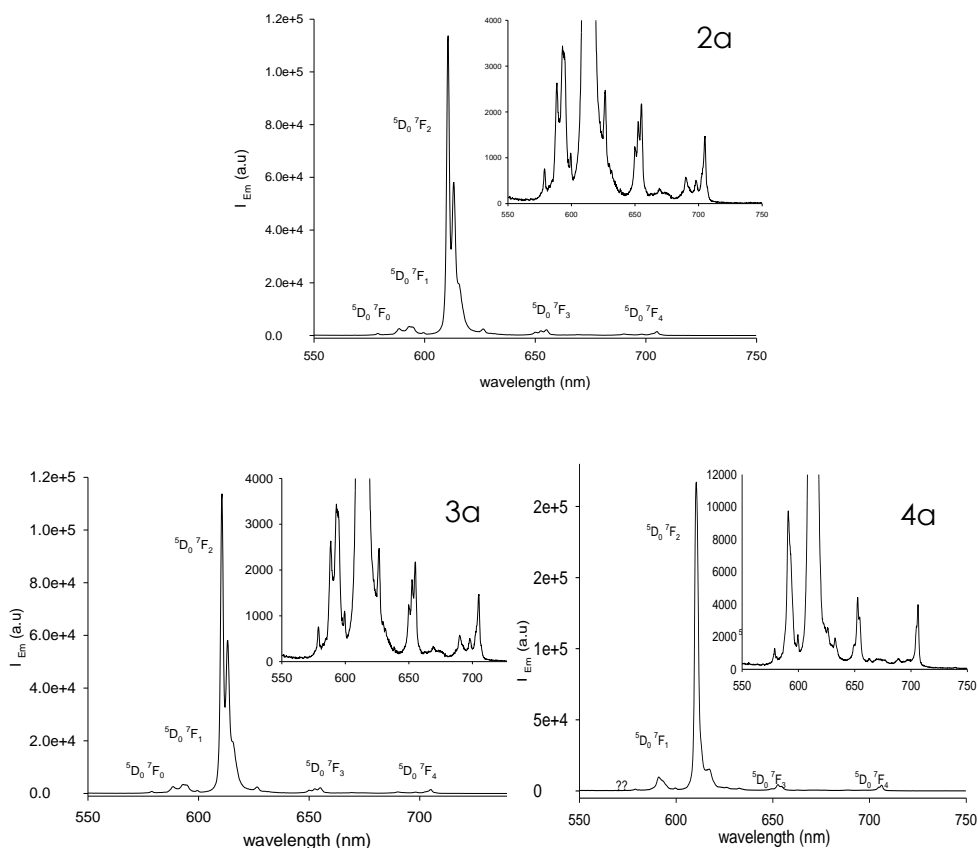


Figure 6.11 Emission spectra of 2a, 3a and 4a

As a general remark, both the microcrystalline powders and the single crystals were characterized, with identical results obtained (data not

showed). A comparison between the data obtained for the metalloligands and the corresponding silver–lanthanide coordination networks showed that no significant change the photophysical behavior of this specie was observed in the presence of the silver centers. This means that the presence of silver pincer-like secondary building units does not add other efficient nonradiative deactivation pathways for the excited states. Furthermore, the series of 2D structures containing europium and bearing different counteranions (**4a–4c**) presents again analogous characteristics and the data are not reported in Table 6.1.

6.2.3 Conclusions

In this work we explored the use of two new tetrakis-chelate Ln–MLs, containing the 1,3-disubstituted diketonate ligands HL1 and HL2, in order to prepare HMOFs by reaction with silver cations. It was found that this approach gives good results only using the metalloligands based on the 4-cyanophenylsubstituted diketonate HL1, obtaining different families of 1D and 2D HMOFs. The photophysical characterization of the ligands and the metalloligands evidenced that lanthanum and terbium complexes are not emissive while the europium ones present quite low intensities and lifetimes due to similar energies of the MC and ^3LC states that give rise to a thermally activated equilibrium. However, the sensitization of neodymium complexes is very efficient. The heterometallic coordination networks have similar photophysical behavior evidencing that, both in 1D and 2D structures, the presence of silver ions does not add other efficient nonradiative deactivation pathways. The results here presented point out some of the features of the lanthanide metalloligands and of their interaction with silver cations that could be fruitfully employed in the development of new HMOFs with tailored structures and properties.

6.3 Gold Nanoparticles. *The Role of Onium Salts in the Pro-Oxidant Effect of Gold Nanoparticles in Lipophilic Environments.*

Free radicals are highly unstable due to unpaired electrons. In the body, they are either produced by the natural metabolic process or by oxidative stress caused by toxins^{28,29}. At high concentrations, radicals and radical derived reactive species are all hazardous to living systems and damage the body at cellular level³⁰. Free radicals are scavenged or removed by molecules known as antioxidants³¹. The protective role of antioxidants against free radicals has been widely studied³² for promoting the development of antioxidants for the treatment of diseases associated with oxidative stress. Nanoparticles can potentially influence autoxidation in various ways, depending on their ability to generate or trap radicals, displaying pro-oxidant or antioxidant effects, respectively (Scheme 1)³³. Nanoparticles are often found to be toxic, and one of the most frequently reported mechanisms of nanoparticle toxicity is the generation of free radicals^{34–37}. Therefore, the supposed pro-oxidant activity of nanoparticles is among the key features determining their safety and suitability for specific applications. With the aim to develop novel nano-antioxidants^{33,38,39}, we were interested to know if gold nanoparticles (AuNPs) can be used as inert carriers of small active molecules without having an intrinsic pro-oxidant activity, which would contrast with the desired radical trapping effect. Interestingly, a promising radical trapping ability in a model system (i.e., toward the 2,2'-diphenylpicrylhydrazyl radical) has been already shown for thiol-capped AuNPs bearing α -tocopherol⁴⁰ or salvianic acid¹⁵ pendants. Despite the availability of many studies that addressed the problem of the toxicity of AuNPs³⁵, little is known about the stability of AuNPs in solution under autoxidation conditions, that is, in the presence of oxygen, of an oxidizable substrate and of different hydroperoxides. In particular, hydroperoxides accumulate during autoxidation experiments and can be involved in the initiation step (Fig. 6.12) by the Fenton reaction, already reported in Cap. 4. Differently from the aim seen before, now is fundamental for its radical production by iron and copper

NPs^{41,42} as the reaction between dissolved or surface metal ions and hydroperoxides produces hydroxyl radicals (HO•).

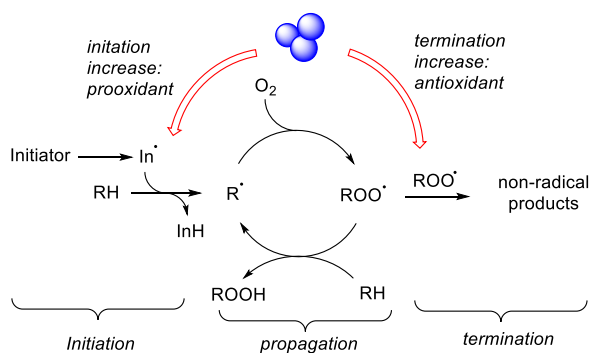


Figure 6.12. Effect of nanoparticles on the autoxidation of an organic substrate (RH).

Surprisingly, also gold nanoparticles, have been reported to induce radical formation in the presence of hydroperoxides, and have been mentioned as mimics of peroxidase enzymes, which catalyze the radical production inside the

cell for specific functions⁴³. Then, there is a possible initiating role of AuNPs in the autoxidation reaction; this is an effect, however, apparently depending on the surface functionalization (NPs passivated with strong ligands are less active) and on the reaction conditions (low pH and intense light)⁴³. The ability of AuNPs to catalyze the homolytic decomposition of hydroperoxides may pose a serious obstacle to their use in real systems, as hydroperoxides are ubiquitously found in small amounts in most oxidizable materials and are formed every time that a peroxy radical is quenched by a chain-breaking antioxidant. Despite the fact that most materials requiring stabilization toward oxidative degradation are lipophilic (edible oils, fuel, lubricants, etc.), there are no reports in the literature about the pro-oxidant behavior of AuNPs in lipophilic (apolar) environments. With this work, we aim at filling this gap of knowledge by studying, in a quantitative fashion, the pro-oxidant activity of thiol-capped AuNPs in apolar solvents, as well as the role of thiols and surfactants used in the preparation of nanoparticles, so to pave the way to their rational use as scaffolds for the development of liposoluble nano-antioxidants.

6.3.1 Aim of the work

Given the potential use of based AuNPs as inert scaffolds for the design of novel nano-antioxidants, the aim of this published work in

collaboration with Prof. R. Amorati and L. Valgimigli, is to investigate if relatively inert thiol-capped gold nanoparticles have a role in the induction of the radical formation in the presence of hydroperoxides. In particular I synthesized dodecanethiol-capped AuNPs (~5 nm), prepared via the Brust-Schiffrin method which involve transfer agent tetraoctylammonium bromide (TOAB) left from the synthesis and decreased on repeated washing of the nanoparticles, and, parallelly, I synthesized AuNPs (~9 nm) prepared via the Ulman method without onium salts. In collaboration with Prof. R. Amorati group it has been examined the pro-oxidant activity of the first one (**AuNPs1**) with different levels of TOAB impurities taken off from the solution by successive washing, comparing with the second one (**AuNPs2**) synthesized without any trace of transfer agent. Moreover, alternative onium phase-transfer agents Oct₄NBF₄, Hex₄NBF₄, Hex₄NPF₆ were comparatively investigated⁴⁴.

6.3.2 Results and discussion

Firstly, AuNPs were synthesized. As mentioned before, to be able to effort the behaviour of the amount of TOAB in the NPs, it was necessary to follow two different synthetic method to obtain Gold NPs, Brust-schiffrin method which involve the phase transfer and Ullman method which don't involve the use of phase transfer.

*AuNPs via Brust and Schiffrin method*⁴⁵.

For the preparation of the gold nanoparticles we slightly modified the original procedure proposed by Brust et al.⁴⁵ based on a two-phase method. Briefly, a water solution of H₂AuCl₄·3H₂O were stirred with toluene solution of TOAB. The TOAB amount is half of the one reported in the original paper, this change was introduced to try to decrease his persistence as an impurity after purification of the product, as discussed later. After the complete transfer of the [AuCl₄] anion to the organic phase, confirmed by the colour change from yellow to colourless and from colourless to deep red, 1-dodecanethiol was added to the organic phase. The separation of the two phases, followed by the addition of NaBH₄ water solution (0.35 M) to the organic one, lead to a quick colour change to deep purple due to gold reduction and formation of metal nanoparticles. The mixture was stirred for 1 hour at room temperature

before particle purification (see detailed synthesis in the experimental section). The organic phase was separated, and ethanol slowly added to obtain particle precipitation. The NPs were then collected by centrifugation and redissolved in 8 ml of toluene. TEM analysis allowed to measure an average diameter of 4.5 ± 0.5 nm (Fig. 6.13A).

AuNPs through a modified Ulman method⁴⁶:

Shortly, $\text{HAuCl}_4 \cdot 3\text{H}_2\text{O}$ was dissolved in distilled THF resulting in a pale yellow color. 1-dodecanethiol was added and left overnight in the dark. The reduction was then initiated with a one-shot addition of LiAlH_4 in THF (instead of lithium triethylborohydride used in the Ulman method) and with successively add every 30 min over two hours until gas evolution ceased. The solution was again stirred overnight in the dark. The nanoparticles were cleaned by three cycles of precipitation by using EtOH followed by centrifugation and re-dispersion in THF. TEM analysis allowed to measure an average diameter of 9.0 ± 0.3 nm (Fig. 6.13B), which is perfectly in agreement with the data obtained by DLS, ($d_H=8.5$ nm, $\text{PDI}=0.3$) and with the UV/Vis spectrum ($\lambda_{\text{max}}=516$ nm)⁴⁷ (data not showed).

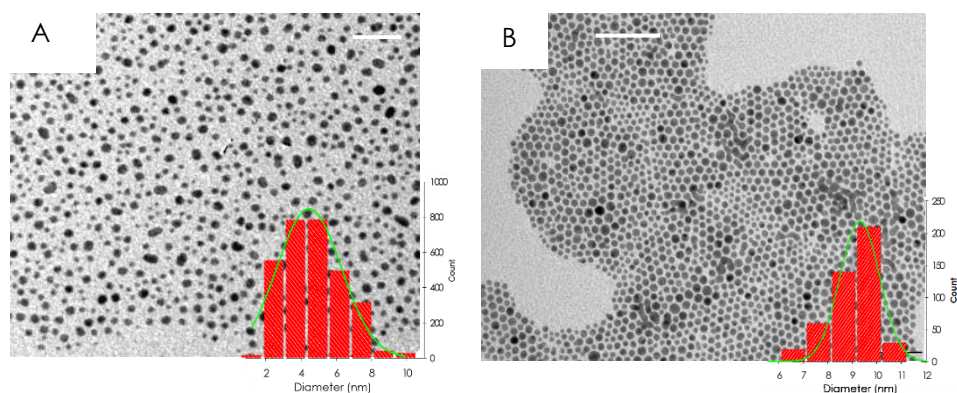
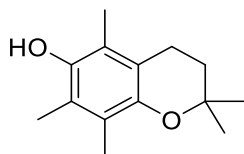


Figure 6.13 TEM images and size distribution analysis (inset) of: A) AuNPs synthesized by the Brust-Schiffrin method and deposited from toluene scale bar 20 nm; B) AuNPs via Ulman method and deposited from THF, scale bar 80 nm

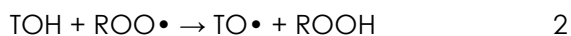
Then, it was quantified the prooxidant activity of AuNPs by measuring their ability to initiate the autoxidation using the styrene substrate as standard oxidizable, in the presence of hydroperoxides. The autoxidation was initiated by mixing the AuNPs with the azoinitiator 2,2'-azobisisobutyronitrile (AIBN) for the positive control and tert-butyl

hydroperoxide ($t\text{BuOOH}$), for the rest of the measurements, in the apolar solvent chlorobenzene. Measuring the kinetics of O_2 consumption with an automatic gas recording apparatus³⁸ it was possible to calculate the rate of autoxidation. Styrene is a peculiar oxidizable substrate because it mainly forms a polyperoxide (i.e. phenylethane units joined by a peroxy O-O linkage), rather than hydroperoxides and this avoids autocatalysis due to hydroperoxide accumulation during the autoxidation⁴⁸.

The rate of production of free radicals (R_i) could be obtained by using the reference antioxidant 2,2,5,7,8-pentamethyl-6-hydroxychromane (TOH), structural analogue of α -tocopherol lacking the phytyl chain, which is able to strongly inhibit the autoxidation of styrene by reactions 2 and 3.



TOH



The rate of initiation R_i was determined experimentally by using Equation (4), where n is the stoichiometric coefficient of the antioxidant, that is, the number of radicals trapped by each antioxidant molecule (for TOH, $n=2$), and t is the length of the inhibited period.

$$R_i = n[\text{antiox}]/t \quad 4$$

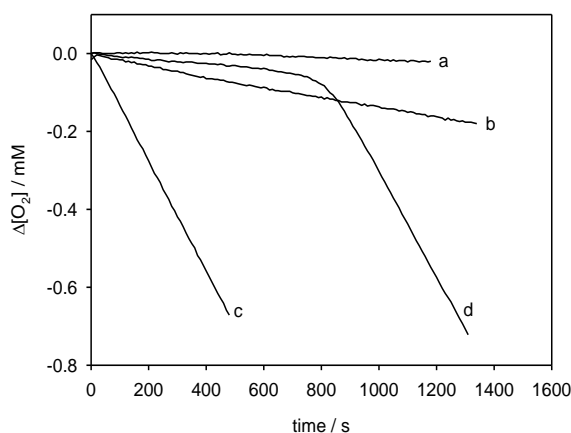


Figure 6.14 Oxygen consumption measured during styrene autoxidation in chlorobenzene at 30 °C in the presence of (a) dodecanethiol-capped AuNPs (0.86 nM); (b) $t\text{BuOOH}$ (3.8 mM); (c) AuNP and $t\text{BuOOH}$; (d) AuNP, $t\text{BuOOH}$ and TOH (1.3 μM).

Were performed then, measurements of O₂ consumption during the autoxidation of the styrene in chlorobenzene at 30°C in 4 different solutions: in presence of **AuNPs1** 0.86nm, with tBuOOH 3.8 mM, , AuNPs1 and tBuOOH and the last one with AuNPs1 and tBuOOH and TOH 1.3 μM (Fig 6.14).

AuNP1 obtained by the Brust-Schiffrin method, taken alone, do not initiate the autoxidation of styrene in chlorobenzene, while tBuOOH provide a slow initiation due to its self-decomposition (lines a and b, respectively). Instead, when AuNPs and tBuOOH are mixed together, a linear decrease of O₂ concentration is observed (line c), indicating a clear pro-oxidant activity. When the reference antioxidant TOH (1.3 μM) was added to the oxidizing mixture, the O₂ consumption was inhibited for about 800 seconds (line d), to start again upon consumption of the antioxidant, when the oxidation rate was the same as that observed in the absence of inhibitor. This experiment clearly indicates that the O₂ consumption is due to the on-setting of styrene autoxidation as the effect of radical production by the contemporary presence of tBuOOH and protected AuNPs. From the duration of the inhibited period, a Ri value $3.1 \times 10^{-9} \text{ M s}^{-1}$.

Among these results, the experiments were repeated at different reactant concentrations, showing a fair linear dependence on [tBuOOH] and [AuNPs1] (Fig 6.15)

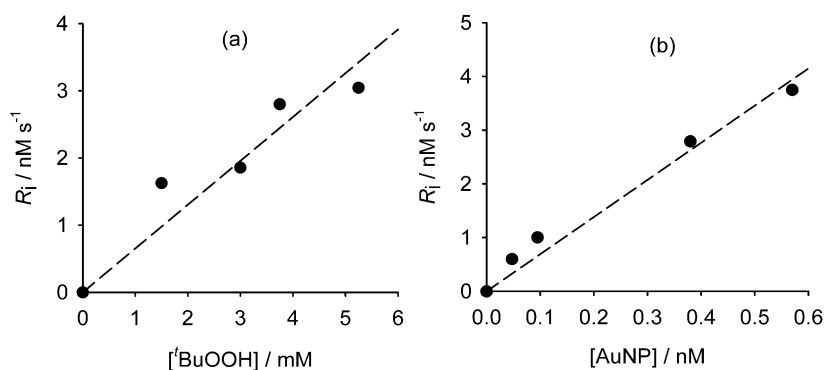


Figure 6.15 Rate of radical production after mixing dodecanethiol-capped AuNPs and tBuOOH in chlorobenzene (30°C), as a function of the reactant concentrations. Graph (a): [AuNPs] = 0.86 nM; Graph (b): [tBuOOH] = 3.8 mM.

To clarify the mechanism of initiation, we investigated all the parameters that can affect the pro-oxidant behavior of AuNP1, together with the effect of each component used in the synthesis. There was performed a photophysical characterization by UV/Vis spectra of the AuNPs mixed to tBuOOH before and after the reaction (data not showed) which not reveal any significant change, indices that the radical production is not associated to coalescence or dissolution of the AuNPs. In analogy, the R_i values recorded for reactions occurring in the dark or under ambient light were the same (data not showed).

Continuing with the investigation of the influence on the pro-oxidant behavior of the species used during the synthesis of the it was mixed C₁₂H₂₅SH (capping agent of AuNPs1) and tBuOOH we didn't seen any radical formation (see Table 6.1), while mixing of TOAB and tBuOOH induced substantial radical generation, as shown in Figure 6.16A. Therefore, a calibration line was performed mixing increasing amount of TOAB (until 6 μ M).

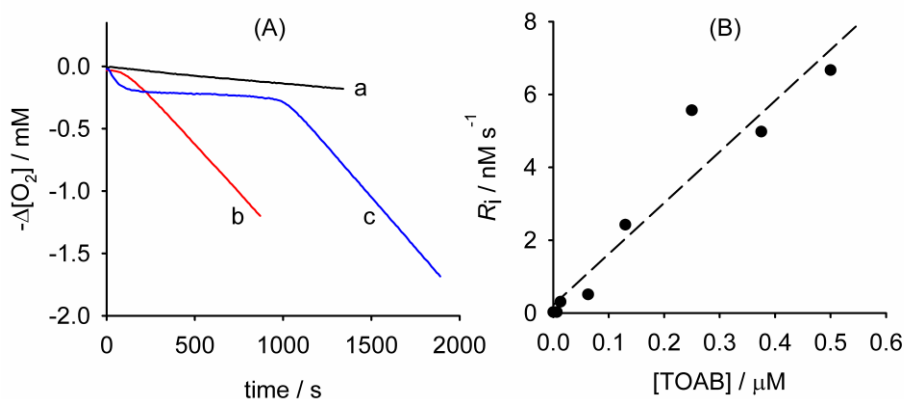


Figure 6.16 Graph(A): Oxygen consumption measured during styrene autoxidation in chlorobenzene at 30 °C in the presence of: (a) tBuOOH; (b) tBuOOH and TOAB; (c) tBuOOH, TOAB and TOH. [tBuOOH] = 3.8 mM; [TOAB] = 3.8×10^{-7} M; [TOH] = 2.5×10^{-6} M. Graph (B): Rate of radical production observed after mixing TOAB and tBuOOH (3.8 mM).

From the Fig 6.16 is clear how TOAB is a very powerful hydroperoxide decomposer, being effective even at submicromolar concentrations. After these results it was better investigate the behaviour of the TOAB together with the AuNPs1. It is known that AuNPs synthesized by this method retain a significant amount of TOAB [30] (the phase-transfer

reagent used in the synthesis) as an impurity, but it was also hypothesized that it could help the stability of the system. The content of TOAB can be substantially decreased by consecutive cycles of precipitation with ethanol–centrifugation–solubilization in toluene or by Soxhlet extraction. The experiments of O₂ consumption were then performed in **AuNPs1** washed 3 times, in order to eliminate any trace of species which could influence the reaction, and the Ri for every solution is reported in table 6.3. In particular the NPs were collected by centrifugation (6188 g for five minutes) and were re-dissolved in toluene (8 mL). Half of the volume was used and called **BS1w** (Brust–Schiffrin one washing step) while ethanol was added to the other half to make the particles precipitate again. The process was, in fact, repeated to have a second washing step and a third washing step indicated, respectively, in the text with **BS2w** and **BS3w**. In this contest were also used the **AuNPs2** which don't present any trace of phase transfer.

Table 6.3 Pro-oxidant activity of dodecanethiol-capped AuNPs in the presence of ^tBuOOH (3.8 mM) in chlorobenzene from the rate of radical initiation (R_i), and estimated TOAB molecules per nanoparticle.[†]

	^t BuOOH mM	R _i / 10 ⁻⁹ M s ⁻¹	N _{TOAB} / N _{NP}
<i>blank</i>	3.8	0.03±0.02	
<i>C₁₂H₂₃SH (45 mM)</i>	3.8	<0.01	
<i>AuNPs1 BS1w (0.86 nM)^b</i>	-	<0.01	
<i>AuNPs1 BS1w (0.86 nM)^b</i>	3.8	2.8±0.2	230±16
<i>AuNPs1 BS2w (0.86 nM)^b</i>	3.8	0.18±0.02	12±1
<i>AuNPs1 BS3w (0.86 nM)^b</i>	3.8	0.20±0.02	13±1
<i>AuNPs2 Ulm (0.3 μM)^c</i>	3.8	0.27±0.06	-

^b The concentration of 0.86 nM corresponds to 5.2x10¹¹ AuNP per mL solution. ^c 1.8x10¹⁴ AuNP per mL solution.

From the data exposed in table 6.3 is clear that the pro-oxidant activity of the AuNPs drastically decreases after the second washing cycle, remaining approximately constant with the third cycle. The Ri values decreased about 10-fold, from 2.8x10⁻⁹ to 1.8x10⁻¹⁰ Ms⁻¹. This lower value, however, is still 6-fold larger than that due to the spontaneous decomposition of ^tBuOOH, indicating a residual pro-oxidant activity that could be ascribed either to traces of TOAB still present, or to an intrinsic

activity of the thiol-capped gold surface. Comparing the AuNP1 after a different number of washing cycles, there was no significant difference, it can be concluded that some persistent impurity of TOAB is left on the surface. Indeed, Schiffrin et al. reported that a persistent impurity of 1.33% by weight cannot be removed by repeated washing⁴⁹. Considering the size of our particles, such amount would correspond to about fifteen molecules of TOAB per nanoparticles. Lastly, when **AuNPs2** were mixed to tBuOOH, however, these nanoparticles showed no pro-oxidant activity. The concentration useful to see comparable value of Ri with the **BS3W** is obtained only using them in a concentration 300-fold larger. It can be, therefore, concluded that the intrinsic pro-oxidant behavior of thiocapped AuNPs is negligible under our conditions. The number of TOAB per Au nanoparticle was estimated assuming that gold spheres of 2.25 nm of radius (TEM data) constitute our samples, with a gold density of 19.32 g/cm³ and that each thiol terminating capping agent occupies an average area of 21 Å². We could calculate the surface area, the volume and consequently the weight of each gold core (9.22 x 10⁻¹⁹g). The number of thiols on each NP resulted circa 300, therefore, adding the weight of the organic part to the particle core we could calculate a total weight of 1.02 x 10⁻¹⁸ gr for each NP. For a 0.86 nM concentration of NPs, assuming that the persistent TOAB could be the 1.33% of the total weight⁴⁹, we obtained a TOAB concentration of 1.29 x 10⁻⁸ M after repeated washing. These data yield an attended number of TOAB/NP of 13.

Moreover, further measurements were performed in order to study the activity of different ammonium ions, having Cl⁻ as counterion. In particular we set to investigate alternative phase-transfer agents that could, in case, be used to replace TOAB it in the Brust–Schiffrin synthesis. As the bromide ion had been indicated in some studies as the cause of oxidative instability of thiol-protected gold nanoparticles, surfactants having the relatively more inert BF₄⁻ and PF₆⁻ counterions were considered with different chain length. Data, reported on the paper⁴⁴, showed how the length have weak influence in the pro-oxidant activity and as expected the replacing with PF₆⁻ and BF₄⁻ counterions giving less behavior pro-oxidant, but it never disappear.

6.3.3 Conclusions

In order to evaluate the the Pro-oxidant activity of AuNP in apolar solvents, were synthesized **AuNP1** (gold Nps Synthesized by Brust–Schiffirin method) and it has been measured the consumption of O₂ given by the reaction between the styrene and initiator tBuOOH and TOH as reference antioxidant in presence of **AuNPS1**. Studing deeply all species involved in the reaction, it was found that mixing of TOAB and tBuOOH induced substantial radical generation. It has been demonstrated than the TOAB which is present in the **AuNPs1** synthesized using Brust-Schiffin, play a fundamental role in their pro-oxidant activity. Infact, AuNPs were washed over 3 times giving 3 differents batch **BS1W**, **BS2W** and **BS3W** presenting a numero of TOAB/NPs respectively 221, 12 and 13. The rate Ri of the consumption of the oxygen decrease drastically with the number of the TOAB. Furthermore, **AuNPs2** (synthesized by Ullman method) which don't present any trace of phase transfer, infact showed pro-oxidant activity comparable with **BS3W** only by using them at a 300-fold larger concentration. It is possible to conclude that TOAB has a strong catalytic hydroperoxide-decomposing activity in apolar solvents, being active at sub-micromolar concentrations. We have shown that, besides TOAB, also other onium salts with different polar heads and alkyl tails catalyze the production of free radicals when mixed to hydroperoxides. Such initiating effect of onium salts is one possible reason of the long known toxicity of AuNPs stabilized by these compounds^{50,51}. For instance, the cytotoxicity of CTAB (cetyltrimethylammonium bromide)-capped nanorods on human colon carcinoma cells (HT-29) is caused by the free CTAB in solution, and it is strongly reduced by different capping agents⁵². As the apolar organic system studied herein is representative of the bio-membrane interior, our results suggest that AuNPs can release onium salts in phospholipid bilayers, thereby promoting lipid peroxidation associated with the loss of integrity and function. We believe this awareness will prove very valuable in the design of novel less-toxic nanomaterials.

Chapter results reprinted also in the published papers Cryst. Growth Des. 2019, 9, 5376 and T. Auvray, B. Del Secco, A. Dubreuil, N. Zaccheroni*, G. S. Hanan* In depth study of the electronic properties of NIR emissive κ 3N terpyridine rhenium(I) dicarbonyl complexes under submission work

- 1 A. K. Pal, S. Serroni, N. Zaccheroni, S. Campagna, G. S. Hanan, *Chem. Sci.* **2014**, 5, 4800.
- 2 A. K. Pal, N. Zaccheroni, S. Campagna, G. S. Hanan, *Chem. Commun.* **2014**, 50, 6846.
- 3 B. Laramée-Milette, F. Lussier, I. Ciofini, G. S. Hanan, *Dalt. Trans.* **2015**, 44, 11551.
- 4 B. Laramée-Milette, N. Zaccheroni, F. Palomba, G. S. Hanan, *Chem. Eur. J.* **2017**, 23, 6370.
- 5 L. Veronese, E. Q. Procopio, T. Moehl, M. Panigati, K. Nonomura, A. Hagfeldt, *Phys. Chem. Chem. Phys.* **2019**, 21, 7534.
- 6 Y. Kuramochi, O. Ishitani, H. Ishida, *Coord. Chem. Rev.* **2018**, 373, 333.
- 7 T. Klemens, A. Świtlicka-Olszewska, B. Machura, M. Grucela, E. Schab-Balcerzak, K. Smolarek, S. Mackowski, A. Szlapa, S. Kula, S. Krompiec, *Dalt. Trans.* **2016**, 45, 1746.
- 8 S. Hostachy, C. Policar, N. Delsuc, *Coord. Chem. Rev.* **2017**, 351, 172.
- 9 F.-X. Wang, J.-H. Liang, H. Zhang, Z.-H. Wang, Q. Wan, C.-P. Tan, L.-N. Ji, Z.-W. Mao, *ACS Appl. Mater. Interfaces* **2019**, 11, 13123.
- 10 D. A. Kurtz, K. R. Brereton, K. P. Ruoff, H. M. Tang, G. A. N. Felton, A. J. M. Miller, J. L. Dempsey, *Inorg. Chem.* **2018**, 57, 5389.
- 11 J. Hawecker, J.-M. Lehn, R. Ziessel, *J. Chem. Soc. Chem. Commun.* **1983**, 536.
- 12 B. A. Frenzel, J. E. Schumaker, D. R. Black, S. E. Hightower, *Dalt. Trans.* **2013**, 42, 12440.
- 13 C. Würth, M. Grabolle, J. Pauli, M. Spieles, U. Resch-Genger, *Nat. Protoc.* **2013**, 8, 1535.
- 14 R.-B. Lin, S. Xiang, H. Xing, W. Zhou, B. Chen, *Coord. Chem. Rev.* **2019**, 378, 87.
- 15 L. Du, S. Suo, G. Wang, H. Jia, K. J. Liu, B. Zhao, Y. Liu, *Chem. Eur. J.* **2013**, 19, 1281.
- 16 C.-X. Chen, Z.-W. Wei, J.-J. Jiang, S.-P. Zheng, H.-P. Wang, Q.-F. Qiu, C.-C. Cao, D. Fenske, C.-Y. Su, *J. Am. Chem. Soc.* **2017**, 139, 6034.
- 17 Y. Cui, Y. Yue, G. Qian, B. Chen, *Chem. Rev.* **2011**, 112, 1126.
- 18 G. Kumar, R. Gupta, *Chem. Soc. Rev.* **2013**, 42, 9403.
- 19 H. Ow, D. R. Larson, M. Srivastava, B. A. Baird, W. W. Webb, U. Wiesner, *Nano Lett.* **2005**, 5, 113.
- 20 L. Jiao, Y. Wang, H. Jiang, Q. Xu, *Adv. Mater.* **2018**, 30, 1703663.
- 21 M. Sakamoto, K. Manseki, H. Ōkawa, *Coord. Chem. Rev.* **2001**, 219, 379.
- 22 Y. Zhang, S. Yuan, G. Day, X. Wang, X. Yang, H.-C. Zhou, *Coord. Chem. Rev.* **2018**, 354, 28.

- 23 X. Feng, Y. Feng, N. Guo, Y. Sun, T. Zhang, L. Ma, L. Wang, *Inorg. Chem.* **2017**, *56*, 1713.
- 24 B. D. Chandler, J. O. Yu, D. T. Cramb, G. K. H. Shimizu, *Chem. Mater.* **2007**, *19*, 4467.
- 25 B. D. Chandler, D. T. Cramb, G. K. H. Shimizu, *J. Am. Chem. Soc.* **2006**, *128*, 10403.
- 26 M. Visconti, S. Maggini, G. Ciani, P. Mercandelli, B. Del Secco, L. Prodi, M. Sgarzi, N. Zaccheroni, L. Carlucci, *Cryst. Growth Des.* **2019**.
- 27 Q. Zhao, X.-M. Liu, H.-R. Li, Y.-H. Zhang, X.-H. Bu, *Dalt. Trans.* **2016**, *45*, 10836.
- 28 Q. Chen, E. J. Vazquez, S. Moghaddas, C. L. Hoppel, E. J. Lesnefsky, *J. Biol. Chem.* **2003**, *278*, 36027.
- 29 W. Droge, *Physiol. Rev.* **2002**, *82*, 47.
- 30 V. Lobo, A. Patil, A. Phatak, N. Chandra, *Pharmacogn. Rev.* **2010**, *4*, 118.
- 31 S. Cailliet, G. Lorenzo, J. Côté, J.-F. Sylvain, M. Lacroix, *Food Nutr Sci*, 337–347.
- 32 I. Margail, M. Plotkine, D. Lerouet, *Free Radic. Biol. Med.* **2005**, *39*, 429.
- 33 C. Viglianisi, V. Di Pilla, S. Menichetti, V. M. Rotello, G. Candiani, C. Malloggi, R. Amorati, *Chem. Eur. J.* **2014**, *20*, 6857.
- 34 A. Nel, T. Xia, L. Mädler, N. Li, *Science (80-.)*. **2006**, *311*, 622.
- 35 J. J. Li, D. Hartono, C.-N. Ong, B.-H. Bay, L.-Y. L. Yung, *Biomaterials* **2010**, *31*, 5996.
- 36 E. Burello, A. P. Worth, *Nanotoxicology* **2015**, *9*, 116.
- 37 G. Zerbi, A. Barbon, R. Bengalli, A. Lucotti, T. Catelani, F. Tampieri, M. Gualtieri, M. D'Arienzo, F. Morazzoni, M. Camatini, *Nanoscale* **2017**, *9*, 13640.
- 38 L. Valgimigli, A. Baschieri, R. Amorati, *J. Mater. Chem. B* **2018**, *6*, 2036.
- 39 M. Massaro, R. Amorati, G. Cavallaro, S. Guernelli, G. Lazzara, S. Milioto, R. Noto, P. Poma, S. Riela, *Colloids Surfaces B Biointerfaces* **2016**, *140*, 505.
- 40 Z. Nie, K. J. Liu, C.-J. Zhong, L.-F. Wang, Y. Yang, Q. Tian, Y. Liu, *Free Radic. Biol. Med.* **2007**, *43*, 1243.
- 41 M. A. Voinov, J. O. S. Pagán, E. Morrison, T. I. Smirnova, A. I. Smirnov, *J. Am. Chem. Soc.* **2010**, *133*, 35.
- 42 H. L. Karlsson, P. Cronholm, J. Gustafsson, L. Moller, *Chem. Res. Toxicol.* **2008**, *21*, 1726.
- 43 W. He, Y.-T. Zhou, W. G. Wamer, X. Hu, X. Wu, Z. Zheng, M. D. Boudreau, J.-J. Yin, *Biomaterials* **2013**, *34*, 765.
- 44 A. Baschieri, B. Del Secco, N. Zaccheroni, L. Valgimigli, R. Amorati, *Chem. – A Eur. J.* **2018**, *24*, 9113.
- 45 M. Brust, M. Walker, D. Bethell, D. J. Schiffrin, R. Whyman, *J. Chem. Soc. Chem. Commun.* **1994**, 801.
- 46 C. K. Yee, R. Jordan, A. Ulman, H. White, A. King, M. Rafailovich, J. Sokolov, *Langmuir* **1999**, *15*, 3486.
- 47 W. Haiss, N. T. K. Thanh, J. Aveyard, D. G. Fernig, *Anal. Chem.* **2007**, *79*, 4215.
- 48 G. W. Burton, T. Doba, E. Gabe, L. Hughes, F. L. Lee, L. Prasad, K. U. Ingold, *J. Am. Chem. Soc.* **1985**, *107*, 7053.

- 49 C. A. Waters, A. J. Mills, K. A. Johnson, D. J. Schiffrin, *Chem. Commun.* **2003**, 540.
- 50 L. Dykman, N. Khlebtsov, *Chem. Soc. Rev.* **2012**, 41, 2256.
- 51 N. Khlebtsov, L. Dykman, *Chem. Soc. Rev.* **2011**, 40, 1647.
- 52 A. M. Alkilany, P. K. Nagaria, C. R. Hexel, T. J. Shaw, C. J. Murphy, M. D. Wyatt, *small* **2009**, 5, 701.

EXPERIMENTAL SECTION

Chemicals

All reagents, solvents and chemicals were purchased from Sigma-Aldrich, Fisher or Alfa-Aesar and used directly unless otherwise stated (purity: reagent or analytical grade). Peptide sequence presented in chapter 5 was purchased by Sigma-Aldrich.

Common purification methods

Normal flash chromatography was performed for molecular part, dialysis steps and/or centrifugation for nanomaterials e micromaterials. Dialysis was performed vs. water at room temperature under gentle stirring with regenerated cellulose dialysis tubing purchased by Sigma Aldrich, mol wt. cut-off > 12 KDa, avg. diameter 33 mm).

Photochemical & Instruments

Electronic absorption spectra

For the acquisition of electronic absorption spectra, a double beam spectrophotometer UV/Vis Perkin Elmer Lambda-45 was used. The spectra were recorded at 25°C using 1 cm quartz cells.

The components of the spectrophotometer are: source: formed by two lamps, a tungsten filament lamp which works between 1100 nm and 320 nm and a deuterium lamp operating between 320 nm and 190 nm; monochromator: a diffraction lattice; sample: a solution of the sample contained in a cuvette, generally of quartz; reference: the solvent, contained in a second cuvette; a photomultiplier tube detector; chopper, a mechanical device which allows the light to be alternatively transmitted through the sample and the reference, or to be suppressed in order to measure the dark current of the photomultiplier used as detector; mirrors. The amount of the absorbed light is provided by the difference of the intensity of incident light I_0 and the intensity of transmitted light I_t and it is expressed as transmittance T :

$$T=I_t/I_0$$

or as absorbance A :

$$A=-\log_{10}T=\log_{10}(I_0/I_t)$$

From the registered spectra moreover it is possible to determine the probability of every transition by calculating the molar absorption coefficient ϵ , expressed in $M^{-1} \text{ cm}^{-1}$, according to Lambert-Beer law:

$$A= \epsilon c l$$

where A is the absorbance of the sample, c is the molar concentration of the sample, and l is the optical path length of the cuvette (usually 1 cm).

Emission and excitation spectra

The registration of the emission and excitation spectra was performed using a spectrofluorimeter Perkin Elmer LS55 and a spectrofluorimeter Fluorolog 3 ISA Jobin Yvon – Spex, Instruments S.A.

These instruments consist of a xenon lamp source, pulsed in the case of Perkin Elmer LS55, continuous-wave in the case of Fluorolog 3; two monochromator excitation light and for emission light; two photomultipliers, one in order to correct the signal as a function of the emission spectrum of the lamp, and the second, for the detection of the emission signal of the analyte; sample lock and a chopper. The slits

determine the bandwidth of the excitation and emission light. In order to register an emission spectrum, the excitation monochromator must be positioned at a determined wavelength, which normally relates to the absorption maximum or lower wavelengths, and a scan with the emission monochromator is performed. Solutions having an absorbance lower than 0.1 at the excitation wavelength have to be used so that the relation between the emission intensity and the concentration is linear. In order to register an excitation spectrum, the emission monochromator is positioned at a fixed wavelength which generally corresponds to the emission maximum or higher wavelengths, while the excitation monochromator scans the spectrum region in which the sample absorbs. If we want to obtain a correct spectrum, we need a solution of sample possessing an absorbance lower than 0.1 all over the wavelength range chosen to register the excitation spectrum. In this way the registered emission intensity is directly proportional to the absorbance value, and the obtained spectrum results proportional to the absorption one (this is strictly true if the species follows Kasha's rule).

Luminescence quantum yield assessment

For solid samples, emission quantum yield was calculated from corrected emission spectra registered by an Edinburgh FLS920 spectrofluorimeter equipped with a barium sulfate coated integrating sphere (4 in.), a 450W Xe lamp (λ excitation tunable by a monochromator supplied with the instrument) as light source, and a R928 photomultiplier tube, following the procedure described by De Mello et al⁴. In all other cases, same instruments seen above for emission spectra were used.

The luminescence quantum yield ϕ_l , defined as the ration between the number of emitted photons and the number of photons absorbed by a species in the same time and for a determined excitation wavelength. For the evaluation of luminescence quantum yield with a relative method there is a necessity of a reference, a known ϕ_l . The species used as a reference should emit in the same spectral region in which the sample emits so that emission spectra are obtained in the same experimental conditions. For the assessment ϕ_l of we adopted the

following experimental procedure¹: the absorption spectra of the sample and of the reference were registered and, when possible, isosbestic points were used as excitation wavelength for the registration of emission spectra.

Excited state lifetime measurements technique

Time-resolved phosphorescence measurements were carried out using a custom-made fiber-optic phosphorometer constructed around a multichannel data acquisition board (USB NI-6361, National Instruments) operating at 2 MHz frequency. The excitation sources in the instrument are light-emitting diodes (LED's) (LedEngin, LZ1), and the detector is an avalanche photodiode module (C12703, Hamamatsu). The luminescence decays were analyzed using non-linear least-squares method. The IRF of the instrument is 1 ns (FWHM). All the custom software (hardware control, data collection and processing) was written in C/C++ (Qt, Nokia). Routine data analysis was performed using Origin 7.0 (OriginLab).

Dynamic light scattering

Hydrodynamic diameter

DLS measurements were performed using a *Malvern Instruments DLS ZetaSizer Nano-ZS* (Fig E1) equipped with a 633 nm laser diode. Samples were housed in disposable polystyrene cuvettes of 1 cm optical path length, using water as solvent.

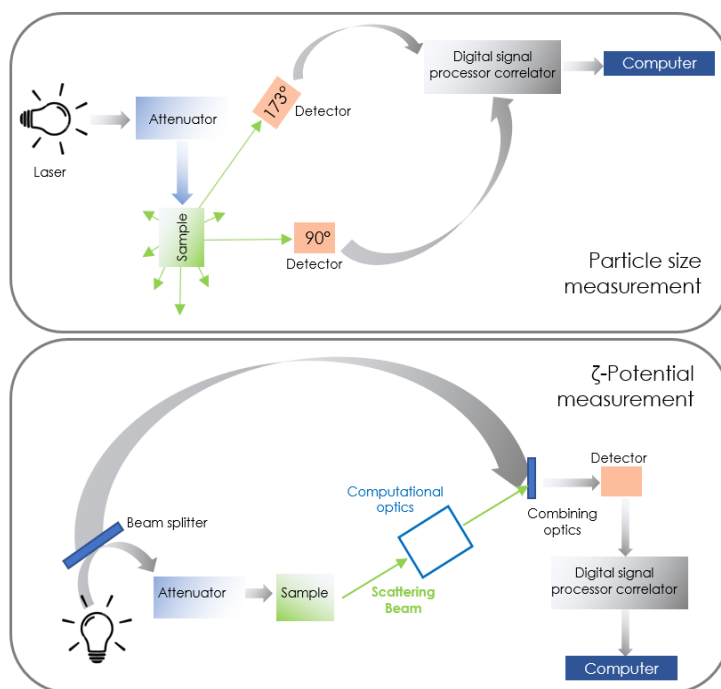


Figure E1 blocks scheme of DLS instrument

With this instrument it is possible to determine the dimension and the Z-potential of the particles having a diameter between 1 nm and 10 μm .

Its components are:

- Laser: He-Ne laser ($\lambda_{\text{exc}} = 633 \text{ nm}$), that lights the sample.
- Cell: it contains the sample.
- Detector: positioned at 173° or at 90° with respect to the incident laser beam, it registers the lightscattered by the sample.
- Attenuator: it modulates the intensity of the laser beam.
- Correlator: it compares the output signals as a function of time
- Nano Software: it translates the information, by providing the dimensions of the several populations of particles present in the sample.

The DLS technique allows the measurements of submicrometric particles. It exploits the study of Brownian motions to determine the hydrodynamic diameter of particles suspended in solution. The higher the dimensions, the lower the particle speed of displacement: as a consequence the

smallest particles move more rapidly. It is necessary to know the viscosity and the temperature of the system for DLS measurements and in particular the system has to be kept at a constant temperature in order to avoid internal convection currents that can affect the measurements. *Stokes-Einstein* equation defines the dimensions of a particle from its translational diffusion coefficient,

$$d(H) = kT / 3\pi\eta D$$

where $d(H)$ is the hydrodynamic diameter expressed in m, k is Boltzmann constant in $J \cdot K^{-1}$, T is the absolute temperature, η is the viscosity in $Kg \cdot m^{-1} \cdot s^{-1}$ and, D is the diffusion coefficient in $m^2 \cdot s^{-1}$. The obtained diameter is a value referred to particles dispersed in a fluid, so it is reported as hydrodynamic diameter, which is defined as the diameter of a rigid sphere that diffuses at same speed of the particle. Its value is not only dependent of the particle dimensions, but also of the concentration and the kind of ions present in the dispersant. Some changes in the superficial structure are able to influence the diffusion speed and as a consequence the hydrodynamic diameter of the particle: for example, a polymeric shell covering a nanoparticle can reduce the diffusion speed and thus enhancing its hydrodynamic diameter. The charge and the concentration of ions in the dispersant also influence the diffusion speed of the particle: an increase of the ionic strength causes a decrease of the hydrodynamic diameter. According to Rayleigh approximation, the light scattering of the particles irradiated by the laser is mainly isotropic if the particles have dimensions that are negligible with respect to the wavelength used (generally less than $\lambda/10$) about 60 nm if a He-Ne laser is used). With this hypothesis the scattered light intensity I becomes directly proportional to the sixth power of the particle diameter d and inversely proportional to the fourth power of the incident light wavelength λ :

$$I \propto d^6$$

$$I \propto \lambda^{-4}$$

The proportionality to d^6 specifies that the ratio between the scattering intensity of a particle having a diameter of 50 nm and that of one having a diameter of 5 nm is equal to 1 million. The proportionality to λ^{-4} indicates that a high scattering intensity is obtained using short wavelengths. If we imagine that a stationary state is reached, we would observe a speckle pattern after the laser irradiation (Figure E2 left).

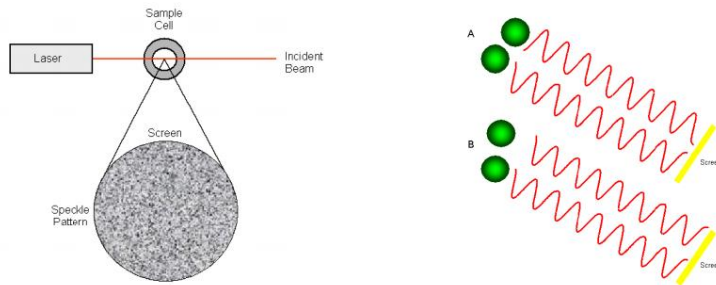


Figure E2 left representation of speckle pattern right destructive interference of scattered light of different particles

The black zones are due to the effect of a destructive interference of scattered light of different particles (Fig. E2 right). Observing the system from a dynamic point of view, that is considering that Brownian motion occurs, the single points of the pattern are in continuous motion.

The correlator is necessary to measure the frequency spectrum of these intensity fluctuations. It compares the signals by measuring their degree of similarity in a determined time range. For a random process, such as diffusion, it is not possible to correlate two signals that are temporally distant, that is when δt is in the order of milliseconds (Figure 3). On the other hand, if δt is in the order of microseconds to nanoseconds, it is possible to observe that the signal intensity at the time t is correlated with the signal in the subsequent instant $t + \delta t$.

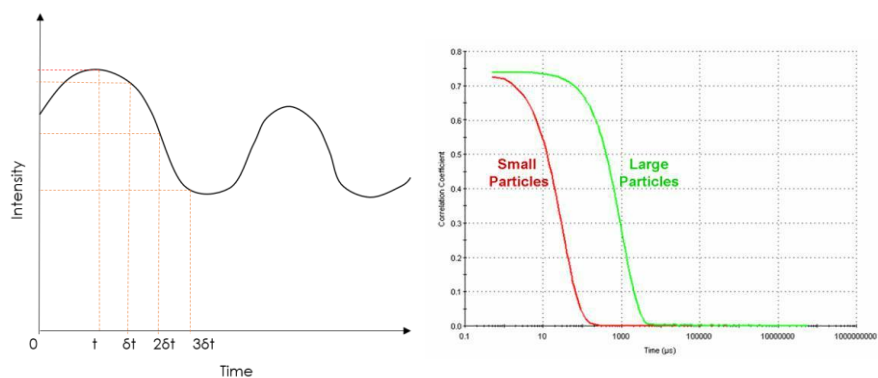


Figure E3 intensity fluctuations of the scattered light as a function of time

If the particles are big, the signal slowly fluctuates, and the correlation persists for a long-time interval. On the other hand, if the particles are small, they rapidly move and the correlation decreases more quickly. In Fig. E3 the differences in the shape of the correlogram as a function of particle dimensions is shown: the left correlogram represents a sample containing big particles and it is characterized by a slow decay; the right one relates to small particles and it is characterized by faster decay. The hydrodynamic diameter is obtained from the correlogram mainly by using two approaches:

- Monoexponential fitting of the correlation function in order to obtain the average dimension (Z-average diameter) and an estimate of the width of the distribution (Polydispersity index, PDI);
- Multiexponential fitting of the correlation function in order to obtain the particle size distribution.

The particle size distribution is obtained from the relative scattering intensity graph of the several particle size classes (intensity size distribution). It is also possible to obtain this distribution as a function of particle volume, or particle number. Let us consider, for example, a sample containing two populations of spherical particles having a diameter of 5 and 50 nm respectively and present in the same number (Fig E4). As far as the number of particles is concerned, the graph consists of two peaks, one at 5 nm and the other at 50 nm, with a 1:1 ratio. If we

convert the number distribution in volume distribution, the two peaks ratio is 1:1000, because the volume of a sphere is equal to $\frac{4\pi}{3} \left(\frac{d}{2}\right)^3$.

If we switch to intensity distribution, the ratio becomes equal to 1:10⁶ according to Rayleigh approximation.

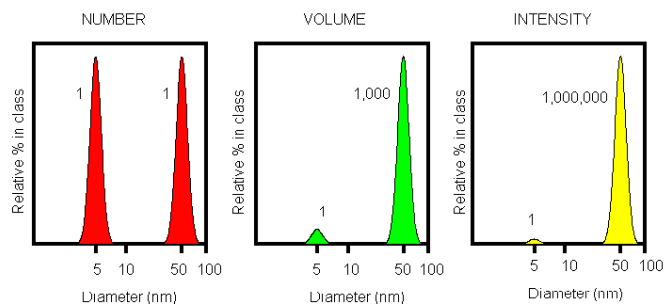


Figure E4 Number, volume and intensity distribution of a sample containing spherical particles of 5 and 50 nm diameter in equal number

In output are obtained data:

- Hydrodynamic volume
- Correlation function
- PDI, polydispersity index is the index of a hypothetical width of a monomodal gaussian distribution

$$PdI = \left(\frac{\sigma}{Z_{avg}} \right)^2$$

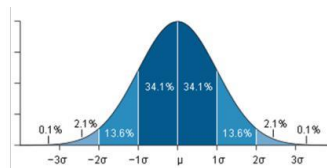


Figure E5 PDI equation and gaussian distribution

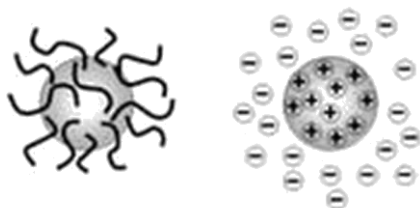
Finally it is important to underline that sample absorbing and/or emitting at the analysis wavelength are not suitable for DLS technique.

ζ-Potential

SiNPs *ζ*-Potential values were determined using a Malvern Nano ZS instrument. Samples were housed in disposable polycarbonate folded capillary cell (750 μL, 4 mm optical path length). Electrophoretic

determination of ζ -Potential was made under Smoluchowski approximation in aqueous media at moderate electrolyte concentration.

The Z-potential is a physical property shown by every particle in solution and it is fundamental to formulate a stable colloidal suspension. There are two fundamental mechanisms that influence the stability of a colloidal system: Steric repulsion which involve the absorption on the Ps surface of the polymers added in solution to prevent the Ps contact.



Electrostatic Stabilization: this is the effect between Ps interaction due to the charged species distribution in the system.

Figure E6 schematization of steric (left) and electrostatic (right) stabilization

Every mechanism has its advantages, but focusing on Electrostatic Stabilization, there is a need to consider that the presence of an overall charge on the surface of the particle influences the distribution of the ions around it, resulting in an increasing amount of the counterions close to its surface. This leads to a double electric layer formation around any Ps. The liquid layer which surrounds the particle has 2 parts, the internal one (Stern layer) which has the ions well attracted and the external one (diffuse layer) where are the weakly attracted ions. In the diffuse layer there is an imaginary edge which contains the entire particle. This means that the ions inside this double layer move with the particle when it moves in solution, while the external ions stay with the solution bulk. The difference between this double layer and the bulk of the solution is the ζ -Potential. The ζ -Potential is calculated by measuring the electrophoretic mobilities (the movement of a charged particle) with respect to the solution under the influence of an applied electric field)

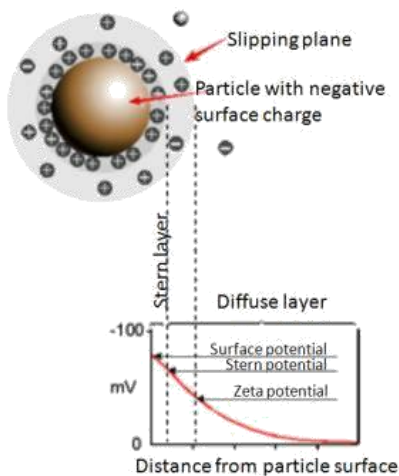


Figure E7 representation of charged layers around the NP's surface

where is used a capillary cell equipped with electrodes capable to accept the applied potential, resulting in a movements of the Ps towards proper electrode, measuring its speed. The particle speed in electric field unit is defined as its electrophoretic mobility. The Z-Pot is linked with electrophoretic mobility by Henry equation

$$U_e = \frac{2 \cdot \varepsilon \cdot \zeta \cdot f(ka)}{3 \cdot \eta}$$

Where U_e is the electrophoretic mobility, ζ is ζ -Pot, ε is the dielectric constant, η is the viscosity and $f(ka)$ is the Henry function. The Malvern Zeta sizer instrument uses the combination of the Doppler laser velocimetry and phase analysis light scattering (PALS) in a patented technique called M3-PALS to measure the electrophoretic mobility.

TEM

The instrument used for the TEM analysis is a Philips CM 100 TEM operating at 80 kV. For TEM investigations, a holey carbon foil supported on conventional copper microgrids was dried under vacuum after deposition of a drop of NP solution diluted with water (1:50). We obtained the size distribution by analysing images with a block of several hundreds of NPs using software ImageJ.

In this instrument, the beam of electrons from the electron gun is focused into a small, thin, coherent beam by the use of the condenser lens. This beam is restricted by the condenser aperture, which excludes high angle electrons. The beam then strikes the specimen and parts of it are transmitted depending upon the thickness and electron transparency of the specimen. This transmitted portion is focused by the objective lens into an image on phosphor screen or charge coupled device (CCD) camera. Optional objective apertures can be used to enhance the contrast by blocking out high-angle diffracted electrons. The image then passed down the column through the intermediate and projector lenses, is enlarged all the way. The image strikes the phosphor screen and light is generated, allowing the user to see the image. The darker areas of the image represent those areas of the sample that fewer electrons are transmitted through while the lighter areas of the image represent those

areas of the sample that more electrons were transmitted through. As the electrons pass through the sample, they are scattered by the electrostatic potential set up by the constituent elements in the specimen. After passing through the specimen they pass through the electromagnetic objective lens which focuses all the electrons scattered from one point of the specimen into one point in the image plane.

SEM

The SEM instrument used is MERLIN Zeiss Type FESEM, field emission scanning electron microscope. Software used is SmartSEM v5.06.

The scanning electron microscope uses a focused beam of high-energy electrons to generate a variety of signals at the surface of solid specimens. The signals that derive from electron-sample interactions reveal information about the sample including external morphology (texture), chemical composition, and crystalline structure and orientation of materials making up the sample. In most applications, data are collected over a selected area of the surface of the sample, and a 2-dimensional image is generated that displays spatial variations in these properties. Areas ranging from approximately 1 cm to 5 microns in width can be imaged in a scanning mode using conventional SEM techniques (magnification ranging from 20X to approximately 30,000X, spatial resolution of 50 to 100 nm). The SEM is also capable of performing analyses of selected point locations on the sample; this approach is especially useful in qualitatively or semi-quantitatively determining chemical compositions (using EDS), crystalline structure, and crystal orientations (using EBSD). The design and function of the SEM is very similar to the EPMA and considerable overlap in capabilities exists between the two instruments. The difference in the FESEM is that the beam gun in SEM is thermoionic and in FESEM is electromagnetic. thus, in FESEM the electron beam is more powerful.

CONFOCAL microscopy

For *cap2* biological assay the microscope used is Nikon d-eclipse C1 equipped with lasers 405, 488 and 543 nm.

OPTICAL MICROSCOPE

The used microscope is Leica DMI3000B equipped with lens 100x/1.4-0.7

2PLSM² using 2PA

It was performed at University of Zurich, follow the ref for a very exhaustive explanation of the instrument and technique.

The two-photon absorption is a nonlinear optic phenomenon where two photons are absorbed simultaneously to populate the excited state of the dye.

The probability of two photon absorption (2PA) depends on the $\sigma^{(2)}$, the 2PA cross-section, the ability of the chromophore to absorb light via 2P mechanism and Φ the photon flux by the equation:

$$\alpha = \sigma^{(2)}\Phi^2$$

The probability α have a quadratic dependence of rate on flux, this means that higher number of photons need to be focused in a small volume to have an observable two photon absorption. This property is used in the two-photon excitation microscopy, where using a high-power femtoseconds focused laser is possible to have two photon excitation only in the focal spot increasing greatly the resolution compared to confocal microscopy.

Synthesis of 2

	Cat	Solvent	Time&T	Yield
I	Cu(PPh ₃) ₃ Br 5%	DCM	O.N, rt	74%
II	Sodium Ascorbate 2% CuSO ₄ H ₁₀ O ₅ 1%	H ₂ O/t-Bu (1:1)	48h, rt	65%(desililated product)
III	Cu(PPh ₃) ₃ Br 10%		O.N, rt	99%
IV	Cu(PPh ₃) ₃ Br 10%		O.N, rt	55%

Molecule 1 (1.1 eq.) is solubilized in dry DCM together with the catalyst. The reaction is left stirring overnight and the product of the reaction is direct used for the purification step by flash chromatography DCM-MeOH (9:1-7:3) **¹H NMR** (400 MHz, CDCl₃) δ 8.93 (s, 1H), 8.50 (s, 1H), 8.41 (s, 1H), 7.75 (m, 9H), 7.66 (m, 7H), 7.46 (d, J = 8.0 Hz, 1H), 7.12 (d, J = 7.7 Hz, 1H), 5.01 (t, J = 6.4 Hz, 2H), 4.92 (s, 2H), 4.69 (s, 2H), 3.91 (m, 2H), 2.34 (s, 2H), 1.06 (s, 9H), 0.29 (s, 6H).

Synthesis of 3

1 (2 eq.) crownether and p-formaldehyde (3 eq) were added in a dry toluene and left the reaction refluxing for 24h. The product **3** is collected by rotavapor Y=90% **¹H NMR** (400 MHz, CDCl₃) δ=8.90 (dd, J = 4.1, 1.6 Hz, 2H), 8.44 (dd, J = 8.6, 1.7 Hz, 2H), 7.43 (dd, J = 8.5, 4.2 Hz, 2H), 7.17 (d, J = 6.8 Hz, 2H), 4.92 (s, 4H), 4.19 (d, J = 2.4 Hz, 4H), 4.02 (s, 4H), 3.73 (t, J = 5.4 Hz, 8H), 3.64 (s, 8H), 2.97 (t, J = 5.4 Hz, 8H), 2.52 (t, J = 2.4 Hz, 2H). **HPLC-MS** (ESI): Rt: 6.23-7.47-5.63 min, m/z calcd [M+H]⁺:713.35, found: 713.0.

Synthesis of 4

HDMS (20 eq) and **3** were added in a dry flask and kept in reflux conditions for 24h. Under Argon flux were added dry DCM, (3-Azidopropyl) triphenylphosphonium Bromide (1.9 eq) and Cu(PPh₃)₃Br 10% mol. The reaction was left stirring overnight and the product was collected by rotavapor. Y=90% **¹H NMR** (4010MHz, CDCl₃) δ 8.75 (d, J = 4.0 Hz, 2H), 8.40 (d, J = 8.4 Hz, 2H), 8.28 (s, 2H), 7.71 (m, 30H), 7.38 (m, 2H),

4.98 (d, J = 6.2 Hz, 4H), 4.90 (s, 4H), 4.67 (s, 4H), 3.89 (s, J = 21.0 Hz, 8H), 3.63 (m, 8H), 2.87 (s, 8H), 2.32 (s, 4H), 0.31 (s, 18H), 0.05 (s, 12H).

Trials for first attempt (Fig 2.4):

<i>Trial</i>	<i>Mol 1</i>	<i>Crown</i>	<i>p-formaldehyde</i>	<i>Solvent</i>	<i>Yield</i>
I				Toluene	0%
II	2 eq	1 eq	2 eq	CH ₃ Cl	0%
III				EtOH	0%

Cap 3

Dye silanization (40 mg, 1 eq.) was dissolved in a 20 mL scintillation glass vial with 4 mL of DMF. CDMT (31.6 mg, 1 eq x every COOH.), NMM (37.6 μ L, 2eq x every COOH) and APTES (42.1 μ L, 1eq x every COOH.) were added to this solution. Upon the addition of NMM and APTES, a red slurry formed and quickly dissolved. The reaction mixture was stirred overnight in the dark. The mixture reaction containing the conjugate dye-APTES was directly used for the nanoparticle synthesis without further purification.

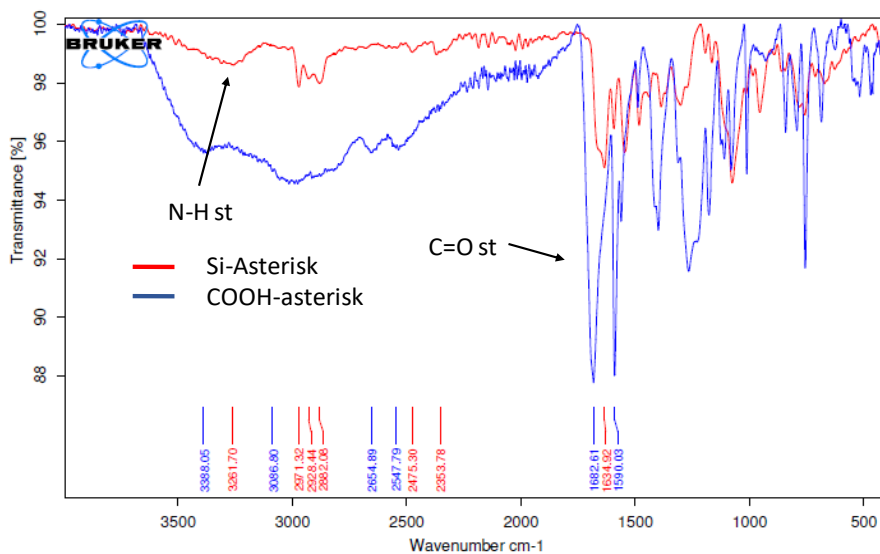
Purification silanized compound: It is possible to obtain clean silanized dye for further analyses using a precipitation in ether. This method doesn't allow to obtain the powder for the quantum yield calculation but is useful for the complete characterization of the solid dye, otherwise impossible to purify. A large amount of cold ether is put in a round flask and kept under stirring. A very small amount of product is dropped into the ether very slowly. (the ratio between ether and dye should be 1/20 vol/vol). The precipitation starts visibly by naked eyes and the powder is collected by rotavapor.

NPs Synthesis A precise amount of silanized porphyrin dye mixture (obtained by silanization batch) was added to a mixture of 100 mg of Pluronic F127, NaCl (68.6 mg), organic solvent and 1 M acetic acid. The total volume of the organic solvent and 1 M acetic acid was 1.55 mL.

Various volumes of porphyrin dye mixtures were added to obtain the desired NPs doping level (0.5%, indicated as %mol of dye vs. mol TEOS). The mixture was then solubilized under magnetic stirring at 25 °C, and TEOS (180 μ L, 0.80 mmol) was added to the resulting homogeneous solution followed by TMSCl (10 μ L, 0.08 mmol) after 180 min. The mixture was kept under stirring in the dark for 24 h at 25 °C before dialysis. The dialysis purification was carried out against water and finally diluted to a total volume of 10 mL with water.

Asterisk IR spectrum: Blue line Asterisk molecule cm^{-1} =3388.05, 3086.80, 2654.89, 2547.79, 1682.61, 1590.03

Red line silanized Asterisk molecule cm^{-1} = 3261.70, 2971.32, 2928.44, 2882.08, 2475.30, 2353.78, 1634.92.



Cap 4

HEXAPODS SYNTHESIS: For hexapods on hematite cubes with 1 μ m of edge length, PVP (1.0 g, $M_n = 40$ kg/mol) powders were dissolved in 1-pentanol (10 mL) by magnetic stirring at 80 °C for 12 h. Once the PVP powders were completely dissolved, anhydrous ethanol (1 mL), distilled water (280 μ L), hematite cube suspension (2.5 wt %, 200 μ L), and sodium citrate aqueous solution (0.18 M, 100 μ L) were added into 1-pentanol

solution with PVP and mixed for a minute handly. Then, ammonia (28 wt % in water, 200 μ L) was mixed by hand shaking, and TEOS (x μ L) was introduced into the mixture. After all ingredients were mixed by hand shaking, the bottle was left to age for 12 h. Then, powders were collected by ultracentrifuge at 3000 rpm for 30 min and redispersed in ethanol, which was repeated twice. For matchstick-like particles, we repeated the same experimental procedures but with more distilled water (200 μ L). For matchstick-like particles with a 570 nm hematite cube, more hematite cubes (4 wt %) were used as seeds.

X= 80 μ L for 1.5 μ m arm length, 140 for 1.5 μ m arm length, 200 for 5 μ m arm's length

BIOTINYLATION: The formulated protocol starts diluting 100 μ L of concentrated clean hexapods in EtOH in a 1 ml centrifuge Eppendorf. Then ere added 600 μ L Biotine-PEG-Silane 6 mg/mL previously dissolved in EtOH and kept the solution under gently stirring overnight

STREPTAVIDIN RECOGNITION (made by the collaborators at university of Netherland GB group): Protocol details reported: the biotinylated hexapods were washed 3 times in water, 5 min-1000 rpm. Alexa Fluor 647-Streptavidin was added (50ug/mL). The incubation time was 2h15min. The particles were washed 3 times in water 5 min 1000 rpm and 100 μ L of PBS were added together with rabbit anti-streptavidin antibody (poly Rabbit, Novus, NB100-175) 25ug/mL.

SWIMMERS In 100 ml of water were dissolved 3mg of hematite cubes (previously dissolved and sonicated in 1 mL of water) where 0.1% of NH_4OH is added together. At this point 1 mL of TPM is added and the reaction was left stirring for 1 hour. After the sphere dimension check under optical microscope HCl is added. For complete ejection of the cubes were added 700 μ L of HCl. Decreasing the volume of HCl is possible to modulate the ejection of the cubes. After that 10 mg of AIBN were added to the solution and it was left in the oven overnight at 100°C. The purification was performed by several steps of centrifugation in water and 3 steps were performing using a magnet to collect only the magnetic spheres.

The mobility of the swimmers was evaluated using a glass capillary filled with the clean swimmer solution together with a 10uL of Hydrogen peroxide. The capillary is linked with the common microscope glass by a transparent glue which close the extremities of the capillary. Under optical microscope was evaluated the “swimming” behavior turning on the blue light. When the light is turned on the Fenton reaction starts, and the swimmers starts to move. When the light is turned off, they stop to swim and continue to move just by the Brownian motion.

Cap5

Rhodamine B piperazine amide³. A 2.0 M solution of trimethyl aluminum in toluene (22.6 mL, 45.2 mmol) was added dropwise to a solution of piperazine (7.8 g, 91 mmol) in 35 mL of CH₂Cl₂ at room temperature. After one hour of stirring a white precipitate was observed. A solution of rhodamine B base (10.0 g, 22.6 mmol) in 20 mL of CH₂Cl₂ was added dropwise to the heterogeneous solution. Gas evolution was observed during the addition period. After stirring at reflux for 24 h, a 0.1 M aqueous solution of HCl was added dropwise until gas evolution ceased. The heterogeneous solution was filtered, and the retained solids were rinsed with CH₂Cl₂ and a 4:1 CH₂Cl₂/MeOH solution. The combined filtrate was concentrated, and the residue was dissolved in CH₂Cl₂, filtered to remove insoluble salts, and concentrated again. The resulting glassy solid was then partitioned between dilute aqueous NaHCO₃ and EtOAc. After isolation, the aqueous layer was washed with 3 additional portions of EtOAc to remove residual starting material. The retained aqueous layer was saturated with NaCl, acidified with 1 M aqueous HCl, and then extracted with multiple portions of 2:1 iPrOH/CH₂Cl₂, until a faint pink color persisted.

The combined organic layers were then dried over Na₂SO₄, filtered, and concentrated under reduced pressure. The glassy purple solid was dissolved in a minimal amount of MeOH and precipitated by dropwise addition to a large volume of Et₂O.

¹H NMR (400 MHz, CD₃OD): δ 1.25-1.38 (t, 12, J=7.5), 3.20 (br s, 4), 3.68-3.80 (m, 12), 7.13-7.34 (d, 2, J=2.5), 7.52-7.58 (dd, 2, J=2.6, 10.0), 7.31-7.38 (d, 2, J=9.5), 7.7.53-7.57 (m, 1), 7.81-7.85 (m, 3)

Rhodamine silanization (40 mg, 1 eq.) was dissolved in a 20 mL scintillation glass vial with 4 mL of DMF. CDMT (31.6 mg, 1 eq x every COOH.), NMM (37.6 μ L, 2eq x every COOH) and APTES (42.1 μ L, 1eq x every COOH.) were added to this solution. Upon the addition of NMM and APTES, a red slurry formed and quickly dissolved. The reaction mixture was stirred overnight in the dark. The mixture reaction containing the conjugate dye-APTES was directly used for the nanoparticle synthesis without further purification.

RhB@NPs Synthesis Solid silanized Rhodamine (0.025% in mol of TEOS), NaCl (68.6 mg) and 100mg of PF127 were dissolved in 3.1 mL of 1M acetic acid solution. The mixture was then solubilized under magnetic stirring at 25 °C, and TEOS (180 μ L, 0.80 mmol) was added to the resulting homogeneous solution followed by TMSCl (10 μ L, 0.08 mmol) after 180 min. The mixture was kept under stirring in the dark for 24 h at 25 °C before dialysis. The dialysis purification was carried out against water and finally diluted to a total volume of 10 mL with water.

PF127-COOH PF-127 (1.0 mmol) and NaIO₄ (8.2 mmol) were placed in a 250-mL round-bottom flask. Water (60 mL), acetonitrile (24 mL), and carbon tetrachloride (21 mL) were added to this mixture; RuC₁₃ (0.044 mmol) was added to the resulting biphasic solution and the reaction mixture was stirred overnight at RT, followed by repeated extractions with CH₂Cl₂. The reunited organic phases were dried over Na₂SO₄, filtered, and evaporated. **¹H NMR** (300 MHz, CDCl₃, 25°C, δ ppm): 4.02–4.04 (d, 4H, -CH₂COOH); 3.73–3.77 (t, 4H, -OCH₂CH₂OCH₂COOH); 3.52 (s, -OCH₂CH₂O-) and 3.39–3.42 (m, -OCH₂C-CH₃O-) ~ 922H; 3.26–3.29 (m, -OCH₂CHCH₃O-) 65H, 1.00-1.02 (d, -OCH₂CHCH₃O-) ~ 195H;

Peptide coupling The functionalization of NP-COOH with the peptidic sequence CGIYRLRS was carried out by mean of a one-step coupling reaction. To 3 mL of a 20 μ M aqueous solution of NP-COOH were added 30 μ mol and 60 μ mol of 0.2M aqueous solution of EDC HCl and sulfo-NHS, respectively. 10 mL of a 2 mg/mL solution of peptide in borate buffer 0.01 M (pH= 9.0) was then added and the mixture was left under magnetic stirring at room temperature over-night. The solution was purified by dialysis versus Milli-Q water for 36 hours. The resulting functionalized

nanoparticles were characterized by DLS and photophysical measurements.

Peptide quantification: The number of peptides per nanoparticle was quantified adapting the well reported fluorescamine assay (4-phenylspiro-(furan-2(3H),1'-phtalan)-3,3'-dione). In order to avoid the hydrolysis of fluorescamine by water, the standard solutions for the calibration curve were prepared in dimethyl sulfoxide (Table E1, line equation and extrapolation pg 129).

Table E1 Solutions used to make calibration line

Conc. Butylamine (μM)	NPs (μL)	DMSO (μL)	Fluorescamine (μL)
0	96	400	40
2	96	400	40
5	96	400	40
10	96	400	40
25	96	400	40

For the quantification of the number of the peptide around the NPs, 96 μL of a 15 μM aqueous solution of unfunctionalized Rhodamine-doped nanoparticles was diluted in 400 μL of DMSO and 40 μL of 10 mM solution in dimethyl sulfoxide of fluorescamine was added. After the addition of 2 mM solution of butylamine (used as standard) in the final range of concentration 11-137 μM , the reaction was left under stirring for 150 minutes at room temperature. The final mixtures were diluted in 3 mL of borate buffer (pH = 9), conditions that cause the hydrolysis of the unreacted fluorescamine. Fluorescence spectra were recorded in the 400-750 nm range ($\lambda_{\text{exc}} = 380 \text{ nm}$) and the emission intensities were plotted versus butylamine concentration, in order to obtain a calibration curve. Following the same procedure, the NPs-peptide sample was analysed. The fluorimetric titration gave an average of 6 peptide sequences per nanoparticles.

Degradation of the mat: 2g of electrospun mat was dissolved in 50mL of PBS buffer 0.1M at 37°C. The PBS is removed entirely constantly, and the mat dried by the vacuum pump. At this point the weight of the mat is

registered and SEM picture was performed. It is put again in 50 mL of fresh PBS. This action has been repeated for 50 days.

Nanoparticles quantification in the electrospun PLGA mat: A 20 μM (corresponding to 160 $\mu\text{g}/\text{mL}$) aqueous solution the Rhodamine-doped nanoparticles (used as standard) was diluted in DMF in the range 28-96 $\mu\text{g}/\text{mL}$ concentration. Fluorescence measurements were carried out in the range 550-750 nm ($\lambda_{\text{exc}}=535$ nm) and a calibration curve was obtained. A small piece of electrospun PLGA was dissolved in DMF and fluorescence measurements were carried out as reported above. The fluorimetric titration gave an average loading of 0.64% w/w of the peptide nanoparticles and 1.3% of unfunctionalized nanoparticles.

Cap 6

Gold NPs

Modified Ulman synthesis: 200 mg of $\text{HAuCl}_4 \cdot 3\text{H}_2\text{O}$ was dissolved in a vial with 5 mL of distilled THF resulting in a pale yellow color. 125 μL of 1-dodecanethiol was added under nitrogen atmosphere and left overnight in the dark. The reduction was then initiated with a one-shot addition of 500 μL of LiAlH_4 in THF in three repetitions, every 30 minutes until gas evolution ceased. The solution was again stirred overnight in the dark. The nanoparticles were cleaned by three cycles of precipitation by using EtOH followed by centrifugation at 2000 rpm for 5 minutes and re-dispersion in THF.

AuNPs via Brust and Schiffrin method. A water solution of $\text{HAuCl}_4 \cdot 3\text{H}_2\text{O}$ (30 mM) were stirred in a round flask with toluene solution of TOAB (50 mM). After the complete transfer of the $[\text{AuCl}_4]$ anion to the organic phase, confirmed by the colour change from yellow to colourless and from colourless to deep red, 1-dodecanethiol (170 mg) was added to the organic phase. The separation of the two phases, followed by the addition of NaBH_4 water solution (0.35 M) to the organic one, lead to a quick colour change to deep purple due to gold reduction and formation of metal nanoparticles. The mixture was stirred for 1 hour at room temperature before particle purification by centrifugation 2500

rpm for 5 minutes. EtOH was added in different amount dependently on the desired excess of TOAB.

- 1 G. A. Crosby, J. N. Demas, *J. Phys. Chem.* **1971**, 75, 991.
- 2 J. M. Mayrhofer, F. Haiss, D. Haenni, S. Weber, M. Zuend, M. J. P. Barrett, K. D. Ferrari, P. Maechler, V. Revol, C.-D. Schuh, C. Urban, A. Hall, M. E. Larkum, E. Rutz-Innerhofer, H. U. Zeilhofer, U. Ziegler, B. Weber, *Biomed. Opt. Express* **2015**, 6, 4228.
- 3 T. Nguyen, M. B. Francis *Org. Lett.* **2003**, 5, 18, 3245
- 4 J. C De Mello *Adv. Mater.* **1997**, 9, No. 3

Appendix

A.1 Principles of photophysics

Electromagnetic radiation and matter can interact in different ways. Photochemistry is interested in the conversion of the energy ($h\nu$) of a photon absorbed by a chemical species in electronic energy, causing the transfer of an electron toward an orbital possessing higher energy. The species turns from its electronic ground state A to an electronic excited state A*, which possesses a different electronic configuration:



This different electronic distribution causes the excited states of a chemical species to have physicochemical properties so different from those of the ground state that they can be considered different chemical species. For this reason, it is possible to define photochemistry as the chemistry of excited states. A photon can be absorbed and provoke the formation of an electronic excited state only if its energy $h\nu$ exactly corresponds to the energy difference between the excited and the ground state. Absorption electronic transitions occur in a time scale of the order of femtoseconds (10^{-15} s), creating excited states which are transient and can deactivate in different ways, shown in the Jablonski diagram (Figure A.1). In this diagram electronic states (the singlets S0, S1

and the triplets T1 and T2) are represented by thicker lines. The distinction between states with different spin multiplicity is due to the fact that transitions between these states are partially not allowed. Thinner lines represent the vibrational levels of the electronic states. After the energy absorption and reaching an excited vibrational level of an S2 electronic excited state, the molecule goes rapidly ($< 10^{-12}$ s) to the ground vibrational level of that excited state (vibrational relaxation); then internal conversion occurs, passing from the ground vibrational level of S2 to the isoenergetic vibrational level of S1, the electronic state at lower energy ($< 10^{-12}$ s). Another vibrational relaxation is then observed toward the ground vibrational state of S1, and at this stage the excited molecule can deactivate in two ways:

- 1- *Non-radiative deactivation*: the energy is released as vibrational energy generating heat. If this process occurs between two states with the same spin multiplicity we speak about internal conversion (10^{-12} - 10^{-6} s), while if the states have different spin multiplicity, we have intersystem crossing (10^{-11} - 10^{-6} s). The successive vibrational relaxation leads in the first case to the ground vibrational level of S0, in the second case to that of T1;
- 2- *Radiative deactivation*: it is a process that generates luminescence and it is defined fluorescence if it occurs between states with the same spin multiplicity, phosphorescence if it occurs between states with different spin multiplicity. Similarly, to S1, T1 can deactivate to S0 by radiative deactivation (phosphorescence, 10^{-4} - 10^2 s) or by nonradiative deactivation (intersystem crossing, 10^{-3} - 10^{-6} s, and successive vibrational relaxation to S0). Long-lived states such as T1 can undergo photochemical reactions, for example with oxygen, producing other chemical species. Generally speaking, since the time scale to decay to S1 and T1 are shorter than that necessary to pass from S1 and T1 to S0, only lowest energetic states of each spin multiplicity (that is S1 and T1) live enough to undergo luminescence (Kasha's rule) or photochemical reactions.

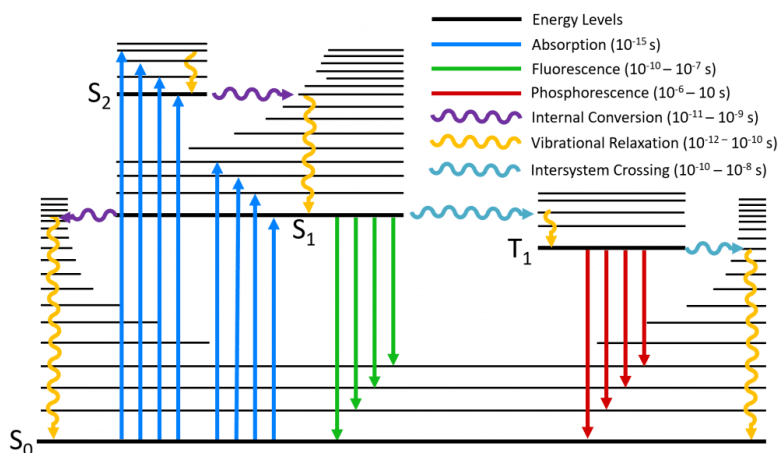
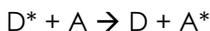


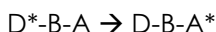
Figure A1 Jablonski diagram for a generic molecule

A.2 Electronic Excitation Energy Transfer

With the term electronic excitation energy transfer we indicate the process in which an excited molecule of a donor D* decays to its ground state D with the simultaneous transfer of its excitation energy to a molecule of acceptor A, which is thus led to an excited state A*:



It is possible to observe this phenomenon exciting D in a spectral region in which it absorbs but A does not: if energy transfer occurs, D* emission is quenched and at the same time the appearance of the emission of A* is observed, which is called sensitized emission. In the case in which D and A are different molecules of the same chemical species we speak about homo energy transfer. It is possible to observe also intramolecular energy transfer in the case of a (super)molecule containing a donor and an acceptor, separated by a spacer B:



Two possible mechanisms of energy transfer exist, radiative one and non-radiative one. The radiative mechanism (also called trivial energy transfer) does not require the direct interaction of D and A, but it occurs via the electromagnetic field produced from the photons emitted by D, which can be absorbed by A, provided that an overlap between the

emission spectrum of D and the absorption one of A exists. This mechanism consist of two different steps:



It is possible to correlate the probability of absorption of A of a photon emitted by D*, that is the probability of energy transfer ($a_{D^* \rightarrow A}$), with the overlap between the emission spectrum of D and the absorption one of A. In particular a relation stands between $a_{D^* \rightarrow A}$ and the overlap integral J , defined as

$$J = \int_0^\infty F_D(\lambda) \epsilon_A(\lambda) \lambda^4 d\lambda$$

where is the normalized emission spectrum of D (the area under the spectrum is equal to 1) and is the absorption spectrum of A in $\text{dm}^3 \cdot \text{mol}^{-1} \cdot \text{cm}^{-1}$. So as J increases, the probability of radiative energy transfer linearly increases. This probability is also directly proportional to the concentration of A, to the optical path length and inversely proportional to the luminescence quantum yield of D. The radiative energy transfer can occur over extremely long distances: solar irradiation on Earth is a striking example. It is necessary that the transition of absorption in the acceptor is spin-allowed so that the radiative energy transfer can occur: thus singlet(D*)-singlet(A*) and triplet(D*)-singlet(A*) transfers are allowed, while singlet(D*)-tripletto(A*) and tripletto(D*)-tripletto(A*) transfers are not allowed. The non-radiative mechanism, on the other hand, requires an intermolecular interaction between D and A mediated by the electromagnetic field. The energy transfer between the partners occurs in resonance conditions, involving isoenergetic non-radiative transitions between D* and A. Also, in this case the probability of energy transfer is directly proportional to J . The theoretical description of the process leads to obtain that the interaction between D* and A consists of a Coulombic term (Förster mechanism) and of an exchange term (Dexter mechanism) (Figure A.2)

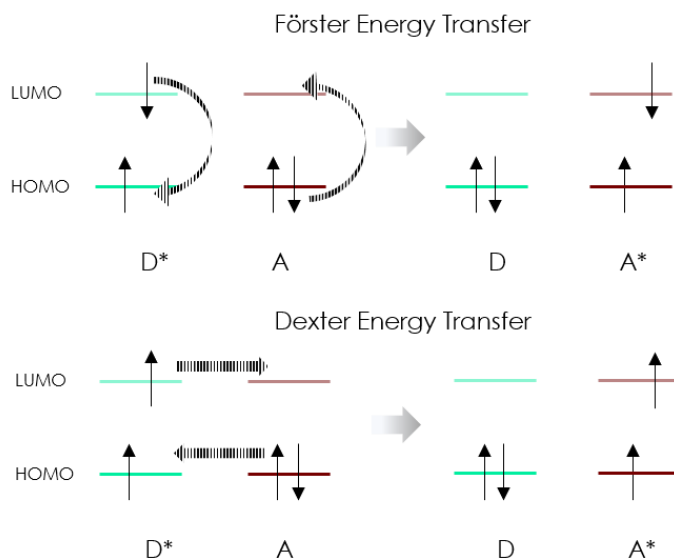


Figure A2 Energy transfer via coulombic mechanism (Foster) and with exchange mechanism (Dexter)

The Coulombic mechanism arises from the coupling of the electronic transition moments of electric dipole of the transitions and . This interaction is governed by Förster's equation, which correlates the energy transfer kinetic constant with the distance R_{DA} :

$$k_{ET} = \frac{1}{\tau_d} \left(\frac{R_0}{R_{DA}} \right)^6$$

Where τ_D is the lifetime of the donor in the absence of the acceptor and is the Förster distance, that is the distance between D and A at which the energy transfer rate (k_{ET}) is equal to the decay rate of the donor in the absence of the acceptor ($k_{ET} = \frac{1}{\tau_d}$). At this distance half of the molecules of D decay via energy transfer. Förster distance is correlated to the overlap between the emission spectrum of D and the absorption spectrum of A by means of the following relation:

$$R_0^6 = 2.303 \frac{9000 \cdot \chi^2 \cdot \Phi_D}{n^4 \cdot N_A \cdot 128 \pi^5} \int F_D(\lambda) \epsilon_A(\lambda) \lambda^4 d\lambda$$

where is the orientational factor which describes the relative orientation of the electric dipole moment of D and A (it is assumed to be equal to 2/3 in the case of freely rotating D and A), is the fluorescence quantum yield of D in the absence of A, is the refractive index of the solvent, is the

Avogadro's constant, is the luminescence spectrum of D normalized to 1, is that absorption spectrum of A expressed in $\text{dm}^3 \cdot \text{mol}^{-1} \cdot \text{cm}^{-1}$. The higher the overlap between the emission spectrum of A and the absorption spectrum of A, the higher the value of R_0 . Typical values are about 20-100 Å.

It is possible to define an efficiency of energy transfer

$$\eta = \frac{k_{ET}}{k_{ET} + k_D}$$

which is linked to R_{DA} by means of the following relation

$$\eta = \frac{R_0^6}{R_0^6 + R_{DA}^6}$$

which highlights that the efficiency of the energy transfer process is equal to 0.5 when $R_{DA} = R_0$. It is possible to experimentally obtain η from the fluorescence quantum yield of D in the presence of A (ϕ_{DA}) and in its absence (ϕ_D), or from lifetimes in the two conditions (τ_{DA} , τ_D):

$$\eta = 1 - \frac{\phi_{DA}}{\phi_D}$$

$$\eta = 1 - \frac{\tau_{DA}}{\tau_D}$$

The processes of Förster type energy transfer are generally allowed if the transition in D and in A does not involve spin changes of the single species. On the contrary Dexter type energy transfer dominates. The exchange interaction requires a simultaneous double electronic exchange involving the LUMO of D and the HOMO of A (Fig. A2) and it is a short-range interaction, becoming important when R_{DA} is ≤ 5 Å. According to Dexter model, the kinetic constant for the exchange mechanism decays exponentially with R_{DA} :

$$k_{ET}^{ex} = \frac{2\pi}{h} K J^{ex} \cdot e^{-\frac{2R_{DA}}{L}}$$

where K is a factor related to the specific orbitalic interaction, J^{ex} is the normalized overlap and L is an average Van der Waals radius which simulates molecular dimensions.

List of Symbols & Abbreviation

k	Kinetic constant
τ	Lifetime
ϵ	Absorption coefficient
λ	Wavelength
Φ	Quantum yield
A	Absorbance
2PA	Two photon absorption
2PLSM	
AFM	Atomic force microscopy
AIP	Aggregation induced phosphorescence
APTES	(3-Aminopropyl)triethoxysilane
CDMT	6-Chloro-2,4-dimethoxy-s-triazine
CmC	Critical micellar concentration
DCHQ	diaza-18-crown-6 8-hydroxyquinoline
DCM	Dichloromethane
DDS	Drug Delivery System
DMF	Dimethyl formamide
DMSO	Dimethyl sulfoxide
EPR	Enhanced permeability and retention
FDA	Food and drug administration
HQ	8-hydroxyquinoline
MRI	magnetic resonance imaging
NMM	N-methyl-morpholine
NP	Nanoparticle

PBS	Phosphate buffer
PDT	Photo dynamic therapy
PEG	polyethylene glycol
PET	Positron emission tomography
PET	Photo electron transfer
PF127	Pluronic F127
PLGA	Poly lactic co glycolic acid
PluSNPs	Pluronic Silica Nanoparticle
PPT	photoinduced proton transfer
PS	Photosensitizer
PVP	Polyvinylpyrrolidone
ROS	Reactive oxygen species
SEC	Size exclusion chromatography
TEOS	Tetraethyl orthosilicate
TGA	thermogravimetry
THF	Tetrahydrofuran
TMSCl	Trimethylsilyl chloride
TOAB	Tetraoctylammonium bromide
TPM	3-(Trimethoxysilyl) PropylMethacrylate
UF	ultrafiltration
UV	Ultraviolet

List of Scientific Contributions

Original research papers

- T. Auvray, B. Del Secco, A. Dubreuil, N. Zaccheroni*, G. S. Hanan* *In depth study of the electronic properties of NIR emissive κ 3N terpyridine rhenium(II) dicarbonyl complexes*
Under submission
- M. Villa, B. Del Secco, I. Ravotto, M. Roy, E. Rampazzo, N. Zaccheroni, L. Prodi, M. Gingras, S. Vinogradov, P. Ceroni *Bright Phosphorescence of All-Organic Chromophores Confined within Water-Soluble Silica Nanoparticles*
J. Phys. Chem. C 2019, 123, 49, 29884-29890
- M. Visconti, S. Maggini, G. Ciani, P. Mercandelli, B. Del Secco, L. Prodi, M. Sgarzi, N. Zaccheroni, L. Carlucci* *New Lanthanide Metalloligands and Their Use for the Assembly of Ln-Ag Bimetallic Coordination Frameworks: Stepwise Modular Synthesis, Structural Characterization, and Optical Properties*
Cryst. Growth Des. 2019, 19(9), 5376-5389
- B. Del Secco, L. Ravotto, T. V. Esipova, S. A. Vinogradov*, D. Genovese, N. Zaccheroni, E. Rampazzo*, L. Prodi* *Optimized synthesis of luminescent silica nanoparticles by a direct micelle-assisted method*
Photochem. Photobiol. Sci., 2019, 18, 2142-2149
- A. Baschieri, B. Del Secco, N. Zaccheroni, L. Valgimigli, R. Amorati *The Role of Onium Salts in the Pro-Oxidant Effect of Gold Nanoparticles in Lipophilic Environments*
Chemistry 2018; 24(36), 9113-9119
- S. Nuti, J. Fernandez-Lodeiro, B. Del Secco, E. Rampazzo, B. Rodriguez-Gonzalez, J. L. Capelo, V. Silva, G. Igrejas, P. Poeta, C. Torres, N. Zaccheroni, L. Prodi, E. Oliveira, C. Lodeiro *Engineered Nanostructured Materials for Ofloxacin Delivery*
Front Chem. 2018; 6: 554
- B. Del Secco, G. Malachin, L. Milli, N. Zanna, E. Papini, A. Cornia, R. Tavano, C. Tomasini* *Form Matters: Stable Helical Foldamers Preferentially Target Human Monocytes and Granulocytes*
ChemMedChem 2017, 12(4), 337-345

- N. Zanna, L. Milli, B. Del Secco, C. Tomasini* *Factors Affecting the Stabilization of Polyproline II Helices in a Hydrophobic Environment* *Org. Lett.* 2016, **18**(7), 1662-1665
- L. Gentilucci, F. Gallo, F. Meloni, M. Mastandrea, B. Del Secco, R. De Marco *Controlling Cyclopeptide Backbone Conformation with β/α -Hybrid Peptide-Heterocycle Scaffolds* *EurJOC* 2016, **19**, 3243

Conferences Contributions

Oral communications

- E-MRs Fall meeting 2019, Warsaw
Luminescent chemosensors for Oxygen
- NanoBio 2018, Heraklion, crete
Luminescent Nanoparticles release from biocompatible polymeric fibers
- *Chimica Supramolecolare: giornata dei dottorandi 2018, Rome, Italy*
Luminescent chemosensors for molecular Oxygen
- *IPM 2017, Perugia, Italy*
Luminescent Nanoparticles release from biocompatible polymeric fibers
- *XVII giornata della chimica dell'emilia Romagna, Bologna, Italy*
Luminescent chemosensors for Oxygen

Poster Presentations

Synthesis and biomedical applications of tumor-targeting peptidomimetics (2016)
Fluorescent peptides as molecular probes for imaging

XXXVI Meeting of Italy Organic chemistry division, Bologna 2015
Synthesis, conformational analysis and biological evaluation of pseudopeptide foldamers»

Awards

Best Oral presentation, Bologna
Luminescent chemosensor for O₂

Co-relator

Master thesis work

*Candidate Cecilia Velino
Tissue Engineering of biocompatible nanostructured materials for
biomedical applications*

*Bachelor thesis work, Bologna July 2018
candidate Nicola Bogo
"Chemosensors for oxygen, from molecules to nanostructures"*

*Bachelor thesis work, Bologna September 2015
candidate Valentina Fiumi
"Preparation of pseudopeptides decorated with fluorophores"*

Acknowledgments

I wish to sincerely thank Nelsi, my PhD supervisor, for giving me a chance to pursue this so much desired PhD. Thanks are due for Enrico, my co-supervisor, for the always punctual support to my questions. Thanks to Luca and Damiano, active participants of this amazing adventure. A special thank also to Francesco, Liviana and Matteo, my group PhD colleagues, for anything that can come to your mind just thinking about our work.

A special thanks to Stefano Sacanna, who hosted me in his group for my research stay, giving me the possibility to fulfill the desire to spend some time of my life doing what I like in the city of my dreams.

I am also grateful to all people and professors in the magara place, ever ready to help and give many smiles, interrupted sometimes by good scientific interaction.

Finally, I thank our coworkers, Professors Sergei Vinogradov (UPenn), Bruno Weber (Zurich University), Marco Lombardo, Stefano Iotti&group, Maria Letiza Focarete and Chiara Gualandi, Riccardo, Paola Ceroni Amorati and Luca Valgimigli (University of Bologna), Garry Hanan (Montreal University) , Lucia Carlucci (Unimi) for the fruitful collaborations

The End.